INSTITUTE OF NATURAL AND APPLIED SCIENCES
UNIVERSITY OF ÇUKUROVA

PhD. THESIS

Pelin KURT

JET SHAPES AT CMS IN PROTON-PROTON COLLISIONS AT $\sqrt{s}$=14 TeV

DEPARTMENT OF PHYSICS

ADANA, 2009

INSTITUTE OF NATURAL AND APPLIED SCIENCES
UNIVERSITY OF ÇUKUROVA

JET SHAPES AT CMS IN PROTON-PROTON COLLISIONS AT $\sqrt{s}$=14 TeV

By Pelin KURT

A THESIS OF DOCTOR OF PHILOSOPHY
DEPARTMENT OF PHYSICS

We certify that the thesis titled above was reviewed and approved for the award of degree of the Doctor of Philosophy by the board of jury on ....

Signature............................	Signature............................	Signature............................
Doç.Dr. İsa DUMANOĞLU	Prof.Dr. Gülsen ÖNENGÜT	Prof.Dr. Sefa ERTÜRK
SUPERVISOR	MEMBER	MEMBER
Signature............................	Signature............................	
Prof.Dr. Ayşe POLATÖZ	Assoc.Prof.Dr. Mustafa TOPAKSU	
MEMBER	MEMBER	

This PhD Thesis is performed in Department of Physics of Institute of Natural and Applied Sciences of Cukurova University
Registration Number:

Prof.Dr. İlhami YEĞİNGİL
Director
The Institute of Natural and Applied Sciences

This Study was supported by Cukurova University Scientific Research Fund.
Project Number: FEF2009D10.

ÇUKUROVA ÜNİVERSİTESİ
FEN BİLİMLERİ ENSTİTÜSÜ

CMS'DE $\sqrt{s}$ = 14 TeV'LİK PROTON-PROTON ÇARPIŞMALARINDA JET BİÇİMLERİ

Pelin KURT

DOKTORA TEZİ
FİZİK ANABİLİM DALI

Bu tez .... tarihinde aşağıdaki jüri üyeleri tarafından oybirliği/oyçokluğu ile kabul edilmiştir.

İmza............................
Doç.Dr. İsa DUMANOĞLU
DANIŞMAN

İmza............................
Prof.Dr. Gülsen ÖNENGÜT
ÜYE

İmza............................
Prof.Dr. Sefa ERTÜRK
ÜYE

İmza............................
Prof.Dr. Ayşe POLATÖZ
ÜYE

İmza............................
Doç.Dr. Mustafa TOPAKSU
ÜYE

Bu tez Enstitümüz Fizik Anabilim Dalında hazırlanmıştır.
Kod No:

Prof.Dr. İlhami YEĞİNGİL
Enstitü Müdürü
İmza ve Mühür

Bu Çalışma Ç.Ü. Bilimsel Araştırma Projeleri Birimi Tarafından Desteklenmiştir.
Proje No: FEF2009D10

ABSTRACT

PhD. THESIS

JET SHAPES AT CMS IN PROTON-PROTON COLLISIONS AT $\sqrt{s}$=14 TeV

Pelin KURT

DEPARTMENT OF PHYSICS
INSTITUTE OF NATURAL AND APPLIED SCIENCES
UNIVERSITY OF ÇUKUROVA

Supervisor: Assoc. Prof. Dr. İsa DUMANOĞLU
Year: 2009, Pages: 217
Jury: Assoc. Prof. Dr. İsa DUMANOĞLU
Prof.Dr. Gülsen ÖNENGÜT
Prof.Dr. Sefa ERTÜRK
Prof.Dr. Ayşe POLATÖZ
Assoc.Prof.Dr. Mustafa TOPAKSU

The CMS (Compact Muon Solenoid) detector will observe high transverse momentum jets produced in the final state of proton-proton collisions at the center of mass energy of 14 TeV. These data will allow us to measure jet shapes, defined as the fractional transverse momentum distribution as a function of the distance from the jet axis. Since jet shapes are sensitive to parton showering processes they provide a good test of Monte Carlo event simulation programs. In this thesis we present a study of jet shapes reconstructed using calorimeter energies where the statistics of all distributions correspond to a CMS data set with 10 pb^{-1} of integrated luminosity.We compare the predictions of the Monte Carlo generators PYTHIA and HERWIG++. In this work we present a study of jet shapes reconstructed using calorimeter energies.

Key Words: QCD, CMS, Monte Carlo, PYTHIA, HERWIG++

ÖZ

DOKTORA TEZİ

CMS'DE $\sqrt{s}$ = 14 TeV'LİK PROTON-PROTON ÇARPIŞMALARINDA JET BİÇİMLERİ

Pelin KURT

ÇUKUROVA ÜNİVERSİTESİ
FEN BİLİMLERİ ENSTİTÜSÜ
FİZİK ANABİLİM DALI

Danışman: Doç.Dr. İsa DUMANOĞLU
Yıl: 2009, Sayfa: 217
Jüri: Doç.Dr. İsa DUMANOĞLU
Prof.Dr. Gülsen ÖNENGÜT
Prof.Dr. Sefa ERTÜRK
Prof.Dr. Ayşe POLATÖZ
Doç.Dr. Mustafa TOPAKSU

Bu tez çalışması, CMS (Compact Muon Solenoid) detektöründe 14 TeVlik kütle merkezi enerjisinde proton-proton çarpışmasından sonra son durumda oluşacak olan yüksek dik momentumlu jetlerin biçimlerinin araştırılması üzerine yapılmıştır. CMS detektörü tarafından alınacak olan veriler bu jetlerin biçimlerinin ölçülmesini sağlayacaktır. Jet biçimleri kısaca jetin ekseninden olan uzaklığın bir fonksiyonu olarak kesirli dik momentum dağılımı olarak tanımlanır. Jet biçimleri parton duş proseslerine karşı duyarlı olduklarından Monte Carlo olay simülasyon programlarının test edilmesini sağlarlar. Bu tez çalışmasında jetler kalorimetre enerjileri kullanılarak tekrardan yapılandırıldılar. PYTHIA ve HERWIG++ Monte Carlo olay jeneratörlerinden alınan veriler kullanılarak jet biçimlerinin karşılaştırması yapıldı. Sunulan sonuçlar 14'TeV de gercekleşek olan pp çarpışması ve 10 pb^{-1} lik bir ışıklılık senaryosu temeline dayanmaktadır.

Anahtar Kelimeler: CMS, Monte Carlo, PYTHIA, HERWIG++

ACKNOWLEDGMENTS

No project can be considered accomplished without sharing it with the others. Sometimes people and events intersect in the right point, such that it can truly inspire someone's creativity. And it did, in the surrounding of the right ones.

Foremost I would like to thank my supervisor Assoc. Prof. Dr. İsa Dumanoğlu who is a mentor with the guidance, motivation and encouragement he provided me. I am thankful for his patience and confidence in my work for the last couple of years.

I am also grateful to our group adviser, Prof. Gülsen Önengüt for her encouragement and infinite support during my graduate studies.

I also would like to thank all the LHC Physics Center staff at Fermilab for their support. Having had the possibility of working in a scientifically challenging environment such as the community of the CMS experiment at CERN cannot be taken for granted. I am grateful to Dan Green and Jim Freeman, without them I would not have had the chance to work at the fruitful research atmosphere at Fermilab. Thank you all for letting me participate so intensively.

Further I owe an extraordinary thank to Prof. Anwar Bhatti who has given me the possibility to work in this exciting subject of Particle Physics and to write this thesis for his guidance and for the constant dedication that he showed in following my work. Working under the inspiring supervision and collaborating with him has been very interesting and fruitful.

Further I owe an other debt of thanks to Dr. Marek Zielinski, not only for the intense collaboration, but also for many helpful suggestions anytime I needed, by far not only, but especially concerning my main thesis topic. We collaborated on the several projects that I am really appreciated to work with him.

Further thanks go to Prof. Nikos Varelas, Prof. Klaus Rabbertz, Dr. Kostas Kaosuorius, Prof. Kenichi Hatakeyama not only for their constructive criticisms in any step of my analysis but also collaborated on the several projects. Their fruitful discussions has contributed a lot to my analysis.

I am indebted to Shuichi Kunori who has been teaching and guiding me through every step of the research that I have done at Fermilab. His expertise, understanding and patience added considerably to my research.

I also am obliged to Prof. Sefa Ertürk for starting my acquantiance with my recent group some years ago, and for giving me chance to start for my first scientific research with him. I do always appreciate for his encouragement, and grateful for showing how big the science world is, and we are the only very small part of this huge collaboration.

I also would like to thank to our high energy group members, Prof. Ayşe Polatöz, Prof. Eda Eşkut, Prof. Aysel Kayış Topaksu for their moral support and encouragement during my studies.

I also would like to thank all the people sharing time with me at Fermilab and CERN. Especially I would like to thank to Selcuk Cihangir for his beautiful heart and hospitality. A special thanks goes to my dear friend Huseyin who not only shared office with me for the past three years but also helped me in many situation, whether related to physics or not, and his wife Seher, you were my closest support at Fermilab. I also thank to my other colleagues/friends Numan, Ayşenur, Kenan and Fatoş for their infinite moral support, since the beginning of my PhD.

Last but not least I owe gratitude to my other friends, who have shown great understanding and support for my work, especially my dear friends at Fermilab, Agata, Cosmin, Suvadeep, and Sheema. Friday launches would not be so colorful without you, we had wonderful times together, talking on anything and to simply laugh. I also thank to my tennis league friends at Fermilab, especially Rick and John, will always appreciate for your patience and modesty. I do still lose in the games but certainly show higher performance.

A gratitude also goes to Fadim and Hakan who have shared my life for the last several years, with me anytime, no matter what. You are my second family, and were closest support to me wherever I go. I do love both of you now and forever.

A special thank goes to Dr. Martin Djongolov for his support on my English on the very beginning just after we meet and the conversations we had from physics to music. The Ocean's have never could been an obstacle for our beautiful friendship even though it's rough time to time. Your patience is admirable, I am very happy to have your friendship for the last 7 years, and would like to have you in my life at least for the next 70 years too, may be closer, may be not, but will have space and time for you through all my life.

Most of all, I am deeply grateful to my dear mother, father, sister and brother for their understanding and unique support on my passion for physics. I am especially grateful to my mother who was always there whenever I need her love. I am still your little daughter, and will need your support anytime for my future accomplishments.

CONTENTS **PAGE**

LIST OF TABLES **PAGE**

LIST OF FIGURES **PAGE**

ABBREVIATIONS

ALICE	A Large Ion Collider Experiment
ATLAS	A Toroidal LHC Apparatus
BFKL	Balitski-Fadin-Kuraev-Lipatov
BSM	Beyond Standard Model
CDF	Collider Detector at Fermilab
CERN	Conceil Europeenne pour la Recherche Nucleaire
CMS	Compact Muon Solenoid
CTEQ	Coordinated Theoretical-Experimental project on QCD
DAQ	Data AcQusition
DGLAP	Dokshitzer-Gribov-Lipatov-Altarelli-Parisi
ECAL	Electromagnetic CaLorimeter
GUT	Grand Unified Theory
HCAL	Hadronic CALorimeter
HF	Hadronic Forward
HLT	High Level Trigger
LEP	Large Electron Positron Collider
LHC	Large Hadron Collider
LAPDF	Les Houches Accord PDF for Parton Distribution Function
PDF	Parton Density Function
QCD	Quantum ChromoDynamics
QED	Quantum ElectroDynamics
SM	Standard Model

1. INTRODUCTION

The Standard Model of particle physics is a compendium of several different quantum field theories following the laws of quantum mechanics and special relativity. In a very precise way, it describes all known particles together with three out of four fundamental forces: the strong, the weak and the electromagnetic force. Each possesses its own characteristics in terms of symmetries and coupling strengths, governing different spatial and time scales, and contributing to the enormous number of phenomena observed today with modern scientific tools. During the last decades, various experiments have verified the predictions of the Standard Model with incredible precision up to energies of the order of 1 TeV, strengthening our comprehension of the universe. Although the lack of the gravitational force prevents the Standard Model from being a complete theory of fundamental interactions it nevertheless became an effective theory due to the negligible strength of the gravitation with respect to the other interactions at the small scales at which particle physics experiments are taking place.

Originally, the Standard Model predicted massless bosons as mediating particles for the electromagnetic, strong and weak force. However, the limited strength of the latter one was a sign on massive vector bosons which was confirmed at CERN in 1983 through the discovery of heavy W and Z bosons. The simplest approach in order to explain massive gauge bosons was the introduction of a scalar field which is assumed to be responsible for creating the masses through spontaneous symmetry-breaking of the electroweak gauge symmetry. The mediator of this field, the Higgs boson, is the only particle predicted by the Standard Model that has not been observed yet. Its discovery at former and present particle accelerators was quite unlikely due to its relatively high mass, low production probability and inconsiderable decay modes.

The next consequent step on a way to fully confirm the Standard Model is the design and construction of a more powerful machine in order to enable the investigation of a larger energy scale and to detect and analyse yet unknown or theoretical expected particles. After a long phase of development, the Large Hadron Collider (LHC) is currently being assembled in the former LEP tunnel at CERN. Its completion is expected for November 2009 and proton-proton collisions at an energy of 14 TeV will take place after the initial phase at lower energies is over. The LHC will exceed the worlds most energetic particle accelerator, the TEVATRON, by a factor of seven in energy and more than two orders of magnitude in collision rate.

The LHC design leads to about 40 million interactions per second and thus an enormous amount of data has to be handled by each of the four participating experiments. Since they will produce roughly 15 Petabytes of data per year, a new concept in terms of storage resources and computing power was developed. In order to ensure a proper processing and analysis of the collected data by thousands of scientists all around the globe, the LHC Computing Grid was born. It consists of so-called computing centres ordered in tiers which are hierarchically linked. The Tier-0 centre at CERN is followed by eight Tier-1 centres equally distributed among the participating countries and several Tier-2 and Tier-3 centres attached to them.

At the startup of LHC, proton-proton collisions at $\sqrt{s}$ = 10 TeV will take place and the CMS detector is expected to accumulate 10pb^{-1} of data at this energy. Given the boost of the center-of-mass energy of the colliding protons, the TeV scale will be prompted immediately. With only about 1 pb^{-1} of integrated luminosity, the transverse momentum will reach beyond any previous collider experiment and the new energy scale can be explored.

In proton-proton collisions, interactions take place between the partons of the colliding protons. Due to the high center-of-mass energy available, the partonic interactions can be in good approximation considered as 2→2 scattering processes. Most of the time, the partonic interactions are soft, leading to small momentum transfer. In those rare cases where the scattering is hard (large momentum transfer), the scattered partons will hadronize into highly collimated bunches of particles that will be measured in the calorimeter as high transverse momentum jets.

The study of the high p_T jets is crucial in order to test the QCD predictions and look for Physics beyond the Standard Model. Since the parton scattering is practically an elementary QCD process, the jet distributions can be calculated from first principles, provided that reasonable hadronization modeling is available. Therefore, the high p_T jets serve as a direct test of perturbative QCD (pQCD). Also, their production is sensitive to the strong coupling constant α_s and precise knowledge of the jet cross section can help reduce the uncertainties of the parton distribution functions (PDFs) of the proton. Particularly important is the constraint of the gluon PDF at high momentum fraction. In general, the reduction of the PDFs uncertainties will be critical for LHC studies looking for Physics beyond the Standard model. However, it should be noted that PDFs constraints can only be achieved with small theoretical and systematic uncertainties and in that sense it will take considerable amount of time for LHC experiments to collect enough data (1000 pb^{-1}) to reach the Tevatron experiments precision. High p_T jets are furthermore sensitive to new Physics (e.g quark compositness, resonances) and given the much higher reach in p_T at LHC with respect to the Tevatron, current limits can be improved and discoveries are possible even at startup.

These jets have an extended structure which can be studied experimentally and theoretically. A possible measure of this structure is the jet shape or jet profile, which depends on variables like transverse momentum and rapidity of the jets, the jet algorithm, and the extension of jets. The jet shape measure is the function $\rho(r,R,P_T,y)$ where P_T is the transverse momentum of the jet and y is its rapidity with ϕ, its azimuthal angle, integrated out. This function ρ measures the fractional P_T profile, i.e. given a jet sample with transverse energy P_T defined with a cone radius R, $\rho(r,R,P_T,y)$ is the average fraction of the jets transverse energy that lies inside an inner cone with radius $r < R$. We demonstrate that jet shape and jet cross section measurements become feasible as a new, differential and accurate test of the underlying QCD theory. We present a first step in understanding these shapes in pp collisions at 14 TeV for an integrated luminosity 10fb^{-1} using the transverse momentum of the hard jets. Our detailed simulation shows that one can evaluate the feasilbility of the jet shape measurement at the LHC. During the first three years of running, event at a fraction of the designed $\mathcal{L} = 10^{34}$ cm^{-2}s^{-1}, LHC is expected to deliver an integrated luminosity 10fb^{-1} per year.

Previously, measurements of jet shapes have been made in $p\bar{p}$ collisions at Tevatron at $\sqrt{s}$=1.8TeV and $\sqrt{s}$=1.96TeV for inclusive and b-jets in different integrated luminosities (Abe, 1993), respectively as well as both neutral and charged particles (Abachi, 1995), and a qualitative aggreement with NLO QCD calculations (Ellis, 1992; Giele, 1993). Similar measurements have been made in e^+e^- interactions at LEP1 using both neutral and charged particles (Akers, 1994) and found to be well described by leading-logarithm parton-shower Monte Carlo calculations. It was observed that the jets in e^+e^- are significantly narrower than those in $p\bar{p}$ (Adloff, 2000; Breitweg, 1999). This is due to the different mixtures of quark and gluon jets in these two environments (Akers, 1994). Measurements of the jet width at LEP1 have shown that gluon jets are indeed broader than quark jets (Alexander, 1991; Acton, 1993; Akers, 1995; Alexander, 1996; Abreu, 1996; Buskulic, 1996).

In this thesis, measurements are presented of the jet shapes in QCD dijet events at centre-of-mass energies $\sqrt{s}$=14 TeV in the range $50 < p_T^{jet} < 1400$ GeV. The data sample used in this analysis was collected from various Monte Carlo (MC) samples, PYTHIA 6.4.2 (Sjostrand, 2006), HERWIG (Bahr, 2008) and ALPGEN (Mangano, 2003) which are generated with the same simulation program in CMS at the LHC. Results of this analysis extend up to jet p_T= 1.4 TeV which is the approximate sensitivity limit for a 10 pb^{-1} integrated luminosity sample of LHC collisions at 14 TeV. Jets are selected with $p_T >$50 GeV in the central region of the CMS detector, $|\eta| < 1$. The jet shape is measured using the CMS calorimeter and corrected to the hadron level. The measurements are presented as a function of the jet transverse energy. Measurements of jet shapes are compared to QCD calculations based on different approaches.

These comparisons allow the study of the relative importance of parton radiation and fragmentation in the formation of a jet as well as the differences between quark and gluon jets. It should be noted that these two predictions refer to the hadron level. For these predictions, jets are searched for in the final state hadronic system using the same jet algorithm as in the simulated data.

2. THEORETICAL BACKGROUND

Several theoretical concepts described nature and especially observations in the field of particle physics quite well during the past few centuries. In the beginning, an idea of small and indivisible particles, called atoms, became one of these models which had to be adjusted in the same manner as the experiments trying to prove these theories evolved during time. Due to higher probing energies, new phenomena arose and modifications had to be made to the theories in order to reflect these new observations correctly. Today, a collection of different quantum field theories called the Standard Model (SM) of particle physics is widely used and precisely describes three out of four known fundamental forces and the participating particles. The lack of gravity prevents the Standard Model from being a complete theory of fundamental interactions, but since the strength of the gravitational force is negligible with respect to microscopic phenomena arising in particle collisions it can be disregarded for our purpose. This chapter gives a short overview of the Standard Model and describes the necessity for a precise identification of so-called particle jets in order to verify and measure several SM parameters, get evidence for the Higgs boson or even indications for new physics beyond the Standard Model. More details can be found in (Griffiths, 2004; Perkins, 1991).

2.1 The Standart Model of Particle Physics

The knowledge of our environment and all observed processes in nature can be reduced to four fundamental forces: gravitational, electromagnetic, weak and strong force. The Standard Model combines the latter three underlying models as well as all known elementary particles and forms a quantum field theory which is consistent with quantum mechanics and special relativity. The mathematical framework of the SM is based on group symmetries with the gauge groups $SU(3) \otimes SU(2) \otimes U(1)$. The gauge group $U(1)$ corresponds to quantum electrodynamics (QED) and provides one generator for the represented gauge field. The $SU(2)$ and $SU(3)$ groups are a bit more complicated and belong to the weak interaction (quantum flavourdynamics, QFD) and to the strong interaction (quantum chromodynamics, QCD) and provide three and eight generators for the quantum fields, respectively. Table 2.1 gives an overview of these four fundamental forces ordered by their strength, relative to each other.

Table 2.1. Fundamental forces ordered by decreasing strength.

Fundamental Force	Strength	Underlying Theory	Mediating Particles
Strong	10	Quantum chromodynamics	8 Gluons
Electromagnetic	10^{-2}	Quantum electrodynamics	Photon (γ)
Weak	10^{-13}	Quantum flavourdynamics	$W^{\pm}$ and Z^0
Gravitational	10^{-42}	Quantum geometrodynamics	Gravitation

There are only two types of particles forming the world we live in. Following the laws of quantum mechanics, only particles with whole- or half-numbered spin quantum numbers J are allowed.

2.1.1 Fundamental Bosons

Particles with an integer spin, $J = n\hbar$ are called bosons. Among them are four fundamental bosons which act as mediating particles for the weak, strong and electromagnetic force. They are called gauge bosons and are mathematically described as field equations for massless particles in the first place. All bosons are indistinguishable particles which follow the Bose-Einstein statistics and therefore can populate the same quantum states at the same time. The gauge bosons which act as force carriers in case of the electromagnetic interaction are called photons, γ. The weak and strong interactions provide three and eight mediating particles according to their field generators, respectively. The three heavy vector bosons $W^{\pm}$ and Z^0 correspond to the weak interaction, whereas eight gluons g act as mediators for the strong force. Table 2.2 gives an overview of these field quanta and shows some properties of these elementary particles.

Table 2.2. Fundamental bosons which act as field quanta for the weak, strong and electromagnetic interaction and several particle properties like their mass m, electric charge q, spin parity J^P and third component of the weak isospin $T-3$.

Bosons	mass $m[GeV/c^2]$	electric charge q	$J^P[\hbar]$	$T_3[\hbar]$
Photon (γ)	0	0	1	0
$W^{\pm}$	80.40	$\pm e$	1	± 1
Z^0	91.19	0	1	0
Gluon (g)	0	0	1	± 1

2.1.2 Fundamental Fermions

On the other hand, particles with spin $J = (n + \frac{1}{2})\hbar$ are called fermions. They follow the Pauli exclusion principle, thus rely on the Fermi-Dirac statistics. The fundamental fermions are divided into two subgroups, namely quarks and leptons and are summarised in Table 2.3. There are 12 fundamental fermions, 6 quarks and 6 leptons as well as the same number of anti-particles associated to them which have the same mass but opposite quantum numbers. The quarks and leptons occur pair-wise and therefore can be grouped into three generations (also called families), where particles within one family have similar properties.

Table 2.3. The fundamental fermions are divided into quarks and leptons. Each of them consists of three generations with similar properties, e.g. electric charge q, spin J and third component of the weak isospin T_3.

Fermions	Generation			electric charge q [e]	$J[\hbar]$	$T_3[\hbar]$
	1	2	3			
Quarks	u	c	t	$+\frac{2}{3}$	$\frac{1}{2}$	$+\frac{1}{2}$
	d	s	b	$-\frac{1}{3}$	$\frac{1}{2}$	$-\frac{1}{2}$
Leptons	ν_e	ν_μ	ν_τ	0	$\frac{1}{2}$	$+\frac{1}{2}$
	e	μ	τ	-1	$\frac{1}{2}$	$-\frac{1}{2}$

The electron e, muon μ and tauon τ together with their three corresponding neutrinos ν_e , ν_μ and ν_τ represent the three known lepton avours. According to their generation, each flavour has a characteristic quantum number Q_e, Q_μ, Q_τ assigned to the different leptons. Due to differences in the mass and energy eigenstates of the neutrinos, oscillations occur between the different families which lead to non-conserved lepton numbers. However, the sum of the lepton numbers is conserved by all interactions. The six quarks, up, down, charm, strange, top and bottom can also be grouped into pairs and carry a charge of either $+2/3$ or $-1/3$, respectively. Corresponding to their names, each quark flavour has an assigned quantum number U, D, C, S, T and B which are each conserved by all known interactions, except the weak force. Responsible for possible weak interactions which violate the quark flavour quantum numbers are the differences between the mass eigenstates $|b\rangle$, $|s\rangle$, $|d\rangle$ and the eigenstates$|d'\rangle$, $|s'\rangle$, $|b'\rangle$ of the weak interaction. This issue is described by the Cabibbo-Kobayashi-Maskawa (CKM) matrix which is defined as

$$\begin{pmatrix} V_{ud} & V_{us} & V_{ub} \\ V_{cd} & V_{cs} & V_{cb} \\ V_{td} & V_{ts} & V_{tb} \end{pmatrix} \begin{pmatrix} |d\rangle \\ |s\rangle \\ |b\rangle \end{pmatrix} = \begin{pmatrix} |d'\rangle \\ |s'\rangle \\ |b'\rangle \end{pmatrix} \tag{2.1}$$

and connects both representations. The matrix elements V_{ij} represent the weak coupling constants for transitions from up-type quark flavours i to down-type flavours j under emission of a $W^{\mp}$ boson, normalised to the square root of the Fermi coupling constant, $\sqrt{G_F}$. The diagonal elements have much higher values (The Particle Data Group, 2006) and thus, transitions within the same families are much more privileged. However, the non-zero values of the remaining elements reflect the above mentioned violation of the quark flavour quantum number conservation.

2.2 Quantum Chromodynamics

Quantum Chromodynamics (QCD) is the universally accepted theory of strong interaction physics. The theory of QCD has a remarkable simplicity and elegance at the classical level, with its underlying non-Abelian SU(3) color symmetry; and unmatched richness after quantization, as revealed by a whole spectrum of contrasting behaviors over a wide range of energy scales, from confinement to asymptotic freedom, in addition to various possible phase transitions under extreme conditions. But the faith in QCD as a true physics theory ultimately is founded, at least up to now, on the successes of perturbative quantum chromodynamics (pQCD) where its wide-ranging predictions are compared to the wealth of experimental data on high energy hard processes, accumulated in the last thirty years at a variety of experimental facilities, covering numerous physical processes in lepton-lepton, lepton-hadron, and hadron-hadron collisions. As is well known, the unique feature of the underlying quantum field theory which makes the perturbative approach useful in QCD, is asymptotic freedom. Equally important are the crucial concepts of infrared safety and factorization, without which it would not be possible to apply the results of perturbative calculations on partons (quark, gluons, vector bosons, . . . etc.) to the world of observed hadrons, electro-weak bosons, Higgs and other new physics particles. In fact, the proof of factorization establishes the theoretical foundation of the QCD parton model, which provides the basic language, and picture, for describing all high energy interactions involving hadrons nowadays in particle physics.

This theory of strong interaction physics describes how particles that carry a colour charge interact. Quarks carry one unit of colour charge, antiquarks carry anticolour and gluons each carry both a colour and an anticolour. There are three colour charges which are traditionally called red (r), green (g) and blue (b). The colour quantum number is never observed in nature so all interactions must be invariant under colour interchange. This discrete symmetry under colour interchange is a special unitary group symmetry in three dimensions, SU(3) symmetry. One of the consequences of this group symmetry is the self-coupling of the mediators of the strong force, i.e. the self-coupling of gluons. We would expect $3^2 = 9$ combinations of colour-anticolour pairs for the gluons but one of the eigenstates ($\frac{1}{\sqrt{3}}(r\overline{r}+g\overline{g}+b\overline{b})$) is a totally symmetric colour singlet which carries no net colour charge so it is decoupled. The remaining eight colour eigenstates of the gluons are

$$r\overline{b}, r\overline{g}, b\overline{g}, b\overline{r}, g\overline{r}, g\overline{b}, \frac{1}{\sqrt{2}}(r\overline{r}-b\overline{b}), \frac{1}{\sqrt{6}}(r\overline{r}+b\overline{b}-2g\overline{g}) \tag{2.2}$$

The fact that the colour quantum number is not an observable (unlike the electric charge) implies that quarks can never be found as free particles but are connected to colour neutral bound states called hadrons. Hadrons can contain either two ($q\overline{q}$) or three (qqq) quarks whose total colour charge must be zero. The former are called mesons, the latter baryons. Other possibilities such as qq or $qq\overline{qq}$ are not bound, i.e. the potential is found to be repulsive.

The colour charge of the strong interaction is analogous to the electric charge in electromagnetic interactions in that both forces are mediated by a massless vector boson. However, the photon itself does not carry any electric charge whereas the gluon is (colour) charged. This difference, which makes the theory non-Abelian, i.e. it allows the self-coupling of gluons, turns out to be crucial in the understanding of the features of quark interactions at short distances. Since gluons are massless particles, one might expect the QCD potential to have a similar $1/r$ form to the Coulomb potential between elementary charges. In fact the quark-antiquark potential is often taken to be of the form

$$V_s = -\frac{3}{4}\frac{\alpha_s}{r} + kr \tag{2.3}$$

where α_s is the strong coupling constant, of the order of 1 . However, in very high collisions , $\alpha_s \approx 0.1$ and single gluon exchange is a good approximation. The first term, dominant at small separations, arises from this single gluon exchange. The second, linear, term is associated with the quark confinement at large separations. Because of the linear term, attempts to free a quark from a hadron simply result in the creation of a new $q\overline{q}$ pair. Several models exist to explain this process. One of these models is that the force lines of the colour field can be imagined to be pulled together by the gluon-gluon interactions so that they form a tube. Pulling apart this tube, the stored energy (kr) eventually reaches the point where it is more favourable, energetically, to create a new $q\overline{q}$ pair resulting in two short tubes instead of one long one. From the sizes and masses of the hadrons, we expect $k \approx 1$ GeV/fm. This corresponds to a force between the quarks of 14 tons weight! The process by which new $q\overline{q}$ pairs are produced is called fragmentation.

2.2.1 The QCD Lagrangian

Formally, QCD interactions can be expressed, in a similar way to QED, by a Lagrangian. The QCD Lagrangian has the form

$$L_{QCD} = -\frac{1}{4}F^{\mu\nu,a}F^{a}_{\mu\nu} + \overline{q}(i\,\partial\!\!\!/ - m_q)q - g_s\overline{q}\gamma^{\mu}T^{a}qA^{a}_{\mu} \tag{2.4}$$

The first term is the kinetic term of the gluon field, A^a_μ , expressed in terms of the gluon field tensor, $F^a_{\mu\nu}$, which is expressed as

$$F^a_{\mu\nu} = \partial_\mu A^a_\nu - \partial_\nu A^a_\mu - g_s f^{abc} A^b_\mu A^c_\nu. \tag{2.5}$$

The last term of equation 2.5, which is non-Abelian, is required by the gauge invariance constraint under local SU(3) transformations of the gluon field. The second term of equation 2.4 is the free Dirac field equation for the quarks whereas the third term is the colour interaction current term between quarks and gluons.

2.2.2 Perturbative QCD and the Simple Parton Model

QCD is a quantum field theory of quarks and gluons endowed with a non-abelian gauge symmetry group SU(3) of color. The classical Lagrangian which explicitly exhibits this symmetry is given by the Yang-Mills formula.

There are many ways in which perturbative QCD can be tested in high-energy hadron colliders. The quantitative tests are only useful if the process in question has been calculated beyond leading order in QCD perturbation theory. The production of hadronic jets with large transverse momentum in hadron-hadron collisions provides a direct probe of the scattering of quarks and gluons:$qq \to qq$, $qg \to qg$, $gg \to gg$, etc.

2.2.3 The Running of the Coupling and Asymptotic Freedom

However the strong interaction exhibits two unique properties which make it behave unlike any other fundamental interaction. The first is color confinement: quarks cannot exist singly, but must always be bound into color-neutral hadrons, either as three quarks in a baryon, or one quark and one antiquark in a meson. Attempting to separate the quarks in a hadron will simply result in more quarks being created from the vacuum, resulting in the production of more hadrons. This has a very significant experimental implication: while we can speak of a given process producing a quark, that quark will not be directly observed in our detector; rather, it will hadronize into a number of collimated hadrons, known as a jet. Measuring the momentum or energy of these jets, as we will see in chapter

5, is a very difficult task.

The second is asymptotic freedom, in which interactions become negligibly weak at large momenta or short distances. An important consequence of this fact is that it is possible to analyze QCD processes (e.g., scattering cross sections) by treating partons (i.e., quarks and gluons) as free particles independent from others in the event.

The asymptotic freedom is responsible for the Bjorken scaling (Bjorken, 1969) which was for the first time observed in a famous SLAC experiment on deep inelastic scattering (Breidenbach, 1969; Friedman and Kendall, 1972). Both asymptotic freedom and confinement are the consequences of unusual (different from electroweak interaction) behavior of the QCD coupling α_s. The dependence of the coupling $\alpha_s(Q)$ on the energy scale Q (also known as running of α_s) is given by the solution of the renormalization group equation (Ellis, Stirling and Webber, 1996):

$$\alpha_s(Q^2) = \frac{4\pi}{b\ln(Q^2/\Lambda^2_{QCD})^2} \tag{2.6}$$

where $b = (33-2n_f)/3$, n_f is the number of active quark flavours (for which $m_q < Q$, Q is the energy scale or momentum transfer and Λ_{QCD} is a parameter with dimension of energy at which the coupling would diverge if extrapolated down to small Q. The value of Λ_{QCD} depends on the renormalization scheme, number of active flavors and can also be defined to leading or next-to-leading order. Experimentally measurements of Λ_{QCD} yield values of around 200 MeV (PDG, 2002). The form of equation 2.3 suggest that the $\alpha_s(Q)$ becomes large and perturbative QCD breaks down, for scales comparable with the masses of the light hadrons, i.e. $Q \approx 1$ GeV. This is an indication that the confinement of quarks and gluons inside hadrons is actually a consequence of the growth of the coupling at low scale, which is opposite to the decrease at high scales that leads to asymptotic freedom. This behavior of the QCD coupling is the result of the non-Abelian nature of the strong interaction which is characterized by the presence of self interaction of gauge bosons.

Since the strong coupling enters into the calculation of all processes beyond the leading order, it can be measured, in principle, in all processes involving hadronic particles. The universality of the function $\alpha_s(\mu)$ provides the most powerful and decisive test of the validity of QCD. Figure 2.1(a) shows a compilation of many measurements of $\alpha_s(\mu)$

made in a variety of physical processes, at energy scales ranging from just above 1 GeV to 200 GeV. As can be seen from the Figure 2.1 (a), the QCD coupling constant α_s approaches zero in the asymptotic limit, $Q^2 \to \infty$. The small coupling at high Q^2 makes perturbative QCD (pQCD) possible and credible.

The universality of these measurements of the running coupling at different scales can be tested by converting all the values to the same scale. The standard scale is usually chosen to be $\mu = M$. The result is shown in Figure 7(b). The agreement is clearly remarkable.

It is important to note that the asymptotic freedom property allows the application of perturbation theory to calculate cross section measurements in scattering processes where quarks and gluons are involved. Moreover, this property explains the partial success of naive Quark Parton Model approach.

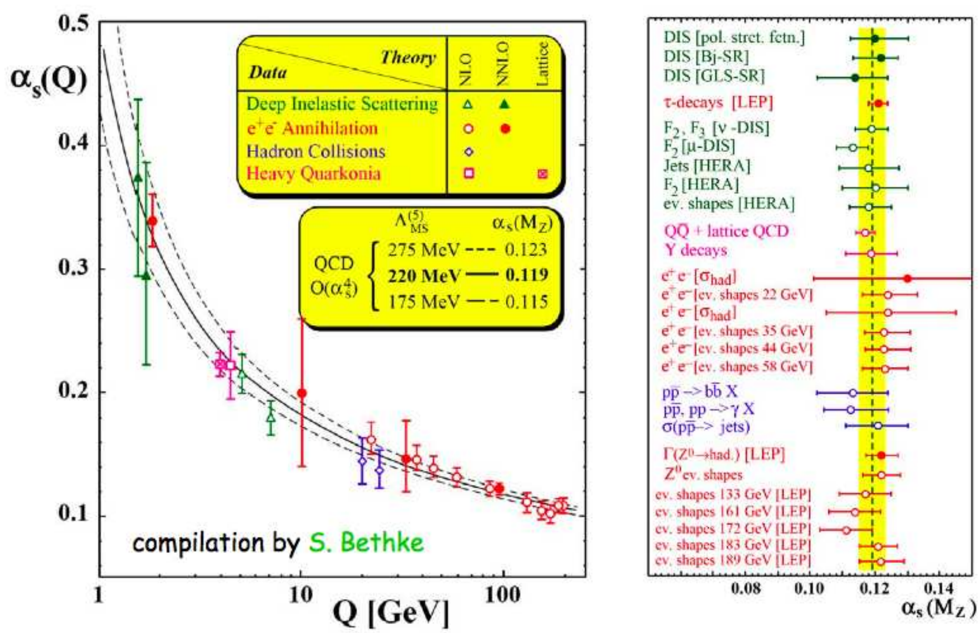

Figure 2.1. Experimental measurements of the universal QCD running coupling function $\alpha_s(Q)$: (a) as a function of Q; (b) all measurements converted to an equivalent $\alpha_s(M_Z)$ (Handbook of QCD, 2001).

.

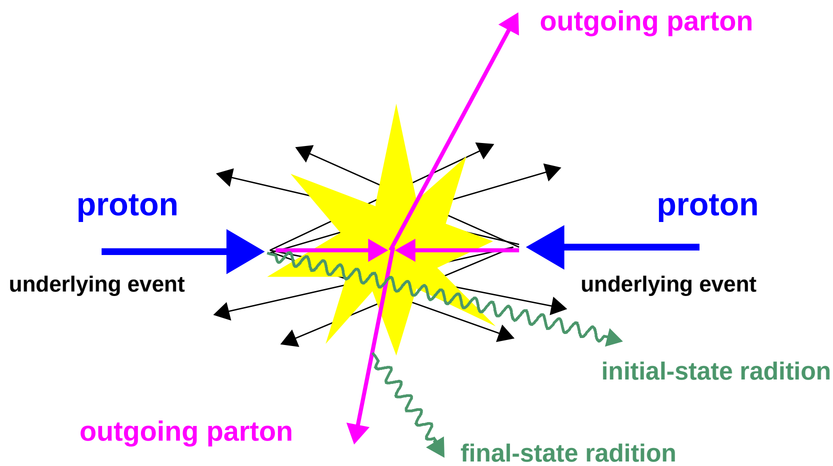

Figure 2.2. llustration of a typical proton-proton two parton hard scattering event including initial and final state radiation and beam-beam remnants (Kurt, Bhatti and Zielinski, 2008; Kurt, 2009).

2.2.4 Factorization

The fundamental challenge when trying to make theoretical predictions or interpret experimentally observed final states is that the theory of the strong interactions (QCD) is most easily applied to the short distance ($\ll 1$ fermi) degrees of freedom, i.e., to the color-charged quarks and gluons, while the long distance degrees of freedom seen in the detectors are color singlet bound states of these degrees of freedom. Figure 2.3 represents the overall scattering process, evolving from the incoming long distance hadrons in the beams to the short-distance scattering process to the long distance outgoing states, as occurring in several (approximately) distinct steps. The separation, or factorization, of these steps is essential both conceptually and calculationally. It is based on the distinct distance (or momentum) scales inherent at each step. We imagine as a first step picking out from the incident beam particles the short distance partons (defined by an appropriate factorization scale) that participate in the short distance scattering. The relative probability to find the scattering partons at this step is provided by the parton distribution functions

(PDFs), which are functions of the partons color and flavor, the longitudinal momentum fractions x_k carried by the partons and the factorization scale μ, all of which serve to uniquely define the desired partons. The pdfs are themselves determined from global fits (See, e.g., Pumplin, 2002; Stirling, 2006) to a wide variety of data, all of which can be analyzed in the context of perturbative QCD (pQCD) essentially as outlined here. The partons selected in this way can emit radiation prior to the short distance scattering yielding the possibility of initial state radiation (ISR). The remnants of the original hadrons, with one parton removed, are no longer color singlet states and will interact, presumably softly, with each other generating (approximately incoherently from the hard scattering) an underlying distribution of soft partons, the beginning of the underlying event (UE).

2.2.5 Soft and Collinear Effects: Parton Evolution and Parton Shower

Above it has been assumed that the PDFs are independent of the scale of the hard scattering process Q. In the parton model picture this means that the structure of the proton looks the same, whatever the energy scale might be at which the proton is probed (e.g. in deep inelastic scattering experiments (DIS)). However, this behavior, known as Bjorken scaling, is only true at leading order. The approximative character of the Bjorken scaling says that as the probing scale Q is increased, the previously point-like observed parton is resolved into several, softly interacting particles. As the number of constituent partons is increased, while the hadron momentum stays constant, each of the constituents has to carry less of the total momentum. This leads to an increase in the parton densities at low and a decrease of the densities at high x values. This scale dependence, known as the breaking of the Bjorken scaling, is experimentally observed.

This scale dependence arises obviously from the interactions within the hadrons during the scattering process, and is thus a higher order correction to the leading order parton picture. The diagrams of these corrections contain singularities in the soft and collinear limit of the additional radiation. The large corrections due to these singular regions in the phase-space can be absorbed into the parton density functions using parton evolution, which by this procedure become scale dependent. The evolution of the parton densities with varying scale Q for the constituents of hadrons are described by the $Altarelli-Parisi$

equations (Altarelli and Parisi, 1977) as

$$\begin{aligned}
\tfrac{d}{dlogQ} f_g(x,Q) &= \frac{\alpha_s(Q^2)}{\pi}\int_x^1 \frac{dz}{z}\left[P_{qg}(z)\sum_f \Big((f_f(x/z,Q)+(f_{\bar{f}}(x/z,Q)\Big)+P_{gg}(z)f_g(x/z,Q)\right]\\
\tfrac{d}{dlogQ} f_f(x,Q) &= \frac{\alpha_s(Q^2)}{\pi}\int_x^1 \frac{dz}{z}\left[P_{qq}(z)f_f(x/z,Q)+P_{gq}(z)f_g(x/z,Q)\right]\\
\tfrac{d}{dlogQ} f_{\bar{f}}(x,Q) &= \frac{\alpha_s(Q^2)}{\pi}\int_x^1 \frac{dz}{z}\left[P_{qq}(z)f_{\bar{f}}(x/z,Q)+P_{gq}(z)f_g(x/z,Q)\right],
\end{aligned}$$

with the splitting functions

$$\begin{aligned}
P_{qq}(z) &= \frac{4}{3}\left(\frac{1+z^2}{(1-z)_+}+\frac{3}{2}\delta(1-z)\right)\\
P_{qg}(z) &= \frac{4}{3}\left(\frac{1+(1-z)^2}{z}\right)\\
P_{qg}(z) &= \frac{1}{2}\left(z^2+(1-z)^2\right)\\
P_{gg}(z) &= 6\left(\frac{1-z}{z}+\frac{z}{(1-z)_+}+z(z-1)+\left(\frac{11}{12}-\frac{n_f}{18}\right)\delta(1-z)\right)
\end{aligned}$$
,

where the plus-distribution is defined as

$$\int_0^1 dx f(x)g(x)_+ = \int_0^1 dx\Big(f(x)-f(1)\Big)g(x). \qquad (2.7)$$

The spitting functions $P_{ab}(z)$ are directly related to the probability for the splitting of a parton a with momentum p into a parton b with longitudinal momentum zp. By using the above evolution equations to define the parton densities at some scale Q all the leading logarithmic terms introduced by soft and collinear radiation at higher orders are re-summed. A detailed derivation of the evolution equations can e.g. be found in (Dissertori, Knowles and Schmelling, 2003). Since factorization is scale dependent, the so called factorization scale, μ, has to be introduced. The hadronic cross-section becomes then

$$\sigma(pp\to X) = \sum_{ff^{,}}\int_0^1 dx_1 dx_2 f_f(x_1,\mu_F)f_{f^{,}}(x_2,\mu_F)\hat{\sigma}(x_1,x_2,s,\mu_F) \qquad (2.8)$$

where the partonic cross-section $\hat{\sigma}$ can also become factorization scale dependent. For LO cross-sections the partonic cross-section is typically independent of the factorization scale. The above description is very important for computing inclusive observables such as cross-sections. However, it does not describe the kinematics of the final state particles properly. To do this a similar, alternative approach can be used, the Parton Shower approach. We just briefly describe the idea and refer the reader to the literature (e.g. Dissertori, Knowles and Schmelling, 2003) for more details.

The evoultion of partons and partons showers were discussed till this part. Lets now concantrate on the later steps of the hadron scattering process fragmentation and hadronisation (part (2) and (3) of Figure 2.2). In part (1) in Figure 2.3, first the hard-scattering occurs which could include some initial and final state radiation. It has a decay of two photons (wavy lines) to two pairs of quarks (straight lines) is shown. Then the fragmentation process occurs (2): many gluons (spring like lines) can be emitted which can in turn decay to quark-antiquark pairs. This process occurs until the energy scale of each parton is close to t_0 . The non-perturbative hadronisation process then occurs (3) which turns the partons into hadrons. The latter can decay into a series of final state particles (4) which are measured by the detector (5). Finally objects such as jets are reconstructed from what is observed in the detector (6). In this case four jets would be observed.

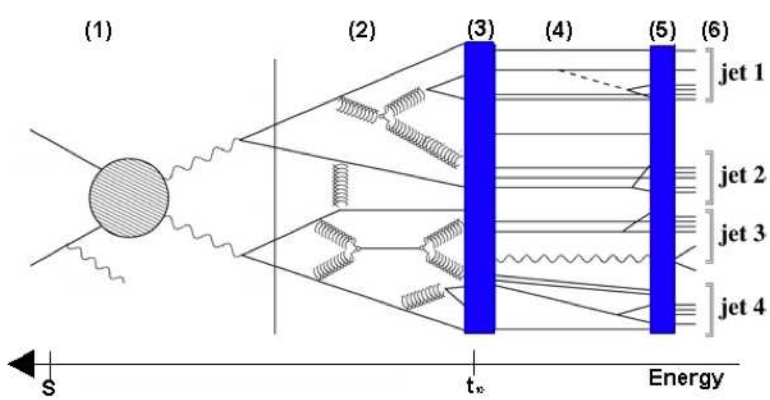

Figure 2.3. Schematic drawing of an interaction involving quarks, (Lister, 2006).

The process whereby the initial partons create many more partons is known as the fragmentation process. This process is illustrated in the part (2) of Figure 2.3. A quark can emit a gluon or, with the help of a nearby quark, create a new quark-antiquark pair. A gluon can emit another gluon or decay into a quark-antiquark pair. This process continues until the virtual masses squared of the partons are of the order of the infrared cut-of scale, t_0 , taken to be of the order of 1 GeV^2. After this, the low-momentum-transfer, long-distance regime is entered, in which non-perturbative effects become important which will be discussed on the next section separately. The most important of these effects is hadronisation which converts the partons into the observed hadrons (part (3) of Figure 2.3). Most models of these phenomena, when implemented in Monte Carlo simulations, assume that the two processes, fragmentation and hadronisation, occur in sequence and can thus be treated independently (Ellis, Stirling and Webber, 1996). Fragmentation models focus on the calculation of approximate results of parton showering where the enhanced terms, such as soft or collinear parton emission from the primary parton, are taken into account for all orders of the perturbative expansion in terms dependent on α_s . The parton shower models represent an approximate perturbative treatment of QCD dynamics at scales larger than t_0 . The implementation of fragmentation models in Monte Carlo simulations mostly use Sudakov form factors, with or without the requirement of angular ordering. These form factors determine the probability of evolving from scale t to the shower cut-off scale, t_0 , without branching. Each parton species has its own form factor, $\Delta(t)$. The form factors are expressed as

$$\Delta_f(t) \equiv exp\left[-\sum_{f;\prime}\int_{t_0}^{t}\frac{dt'}{t'}\int dz\frac{\alpha_s}{2\pi}\hat{P}_{f'f}(z)\right], \tag{2.9}$$

where $\hat{P}_{f'f}(z)$ are the un-regularized splitting functions and the substitution $t \equiv Q^2$ has been applied. These form factors can be interpreted as the probability of a parton not to split when evolving from scale t_0 to scale t. Together with the Altarelli-Parisi Equations they can be employed to define an iterative algorithm to radiate/split partons in a cascade up to some cut-off scale. After this procedure (parton-shower) the final-state consists of a multi-parton configuration and again, similarly as in the case of the PDFs, the leading logarithmically enhanced contributions of the higher-order corrections are included up to all orders.

2.2.6 Long Distance Effects: Hadronization

Hadronization is a non perturbative process that follows parton showering and yields to the production of collimated beams of particles called **jets**. These colorless objects, which move away from the interaction point in the direction of their parent partons, are the experimental signature of the hard collision. The hadronization takes place at low momentum transfer and long distances where the strong coupling is large. Therefore there are only phenomenological models available to describe the hadronization effects. The commonly used models are the String Model, used in PYTHIA, and the Cluster Model, used in HERWIG. The main idea of the String Model is that, when an oppositely color-charged quark-anti-quark pair moves apart, the color-field between them can be described as a narrow flux tube of uniform energy density (string tension). Gluons form so called kinks in these flux tubes. At the end of the perturbative parton-shower colorless strings form between quark-anti-quark pairs (as shown in Figure 2.4(a)). The motion of these strings is then described classically, with the possibility of breaking a string into a $q\bar{q}$ pair, when the field energy in the string allows for it. These quarks are combined into the final-state hadrons, which, if not stable, proceed in decaying until a set of stable final-state hadrons is obtained. In the Cluster Model the quarks after the parton-shower are combined as quark-antiquark pairs into clusters, where beforehand gluons at the end of the shower are forced to split into $q\bar{q}$ pairs (illustrated in Figure 2.4(b)). The clusters are then associated with so called super-resonances, that subsequently decay into the known set of hadronic resonances. A detailed description and comparison of these and other hadronization models can e.g. be found in (Dissertori, Knowles and Schmelling, 2003).

The outcome of the previous discussion is that for any process involving outgoing partons, a large number of hadrons are seen in the detectors because of the fragmentation and hadronisation processes. Due to the higher probability of emitting partons with small angles with respect to the initial parton, most of the final hadrons will be concentrated in a direction close to that of the initial parton. This shower of final state hadrons is what is called a jet. At hadron colliders the situation is complicated by a number of different phenomena. Unlike at lepton colliders, the total centre of mass energy of the hard interaction, s, is not known for each interaction. This is schematically illustrated

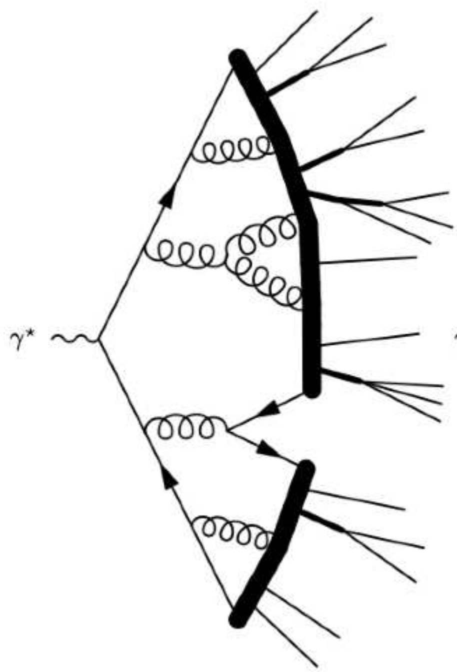

Figure 2.4. Schematic drawing of the hadronisation process whereby partons become a final set of hadrons. The left hand diagram represents the string model whereas the right hand diagram represents the cluster model. In both cases, the decay represented is that of a photon (wiggly line) decaying to a quark-antiquark pair (straight lines) which then fragments to other partons including gluons (cork- screwed lines). This figure is reproduced from (Dissertori, Knowles and Schmelling, 2003).

in Figure 2.5. Only one parton (a and b in Figure 2.5) from each of the hadrons (h1 and h2) participate in the hard-scattering. The partons carry an unknown fraction of the total hadrons energy (f1 and f2). The fractional momentum carried by the partons is described by Parton Distribution Functions (PDFs). These are discussed in reference (Dissertori, Knowles and Schmelling, 2003). The remaining partons inside the colliding hadrons participate only minimally in the interaction.

Moreover, the presence of a significant amount of soft interactions between the colliding hadrons (beam-beam remnant interactions), possible multiple parton interactions and gluon radiation from the initial partons before the hard interaction (initial state radiation) complicate things even further. These additional processes are collectively known as the underlying event. The underlying event, along with the finite detector resolution, leads to the fact that it is not possible to unambiguously determine, even in Monte Carlo simulation, which hadrons came from which initial parton, i.e. which hadrons belong to

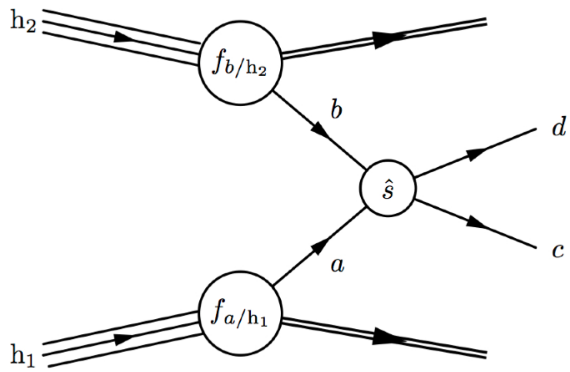

Figure 2.5. Schematic drawing of the hard-scattering component of a hadron-hadron collision. Two initial hadrons (h1 and h2) are collided but only one parton from each of the hadrons (a and b) participate in the hard interaction. The centre of mass energy of the interaction s is therefore unknown. This leads to the fact that the total energy of the outgoing partons (c and d) is also unknown. This figure is reproduced from (Dissertori, Knowles and Schmelling, 2003).

which parton jet. Jet algorithms are used to group the final state hadrons into jets whose properties are as close to the initial parton ones as possible. Some common jet algorithms with their benefits and limitations will be discussed later, in chapter 5. It is sufficient at this stage to mention that in this thesis a cone algorithm is used. A jet is therefore defined by a direction, an energy and a cone size that corresponds to the jet opening angle.

The next section describes the jets in hadron colliders and jet profile that is studied in this thesis, namely jet shapes.

2.2.7 Underlying Event and Multi-Parton Interactions

Hadron-hadron interactions ($p\bar{p}$ or pp) are not as simple as the interactions in ep colliders. In addition to the hard scattering producing dijets, high p_T leptons..., spectator partons produce additional soft interactions called underlying events. The main consequence is that it introduces additional energy in the detector not related to the main interaction which need to be corrected.Another effect is Multi-Parton interaction, where more than two of the constituent quarks of the protons undergo a hard scattering. There are several models available for these effects; we will explicitly use the JIMMY model (Bahr, 2008a; Seymour, 2008) for the HERWIG generator in upcoming sections of this thesis.

Hovewer many of the important observables at a hadron collider, including jets, are

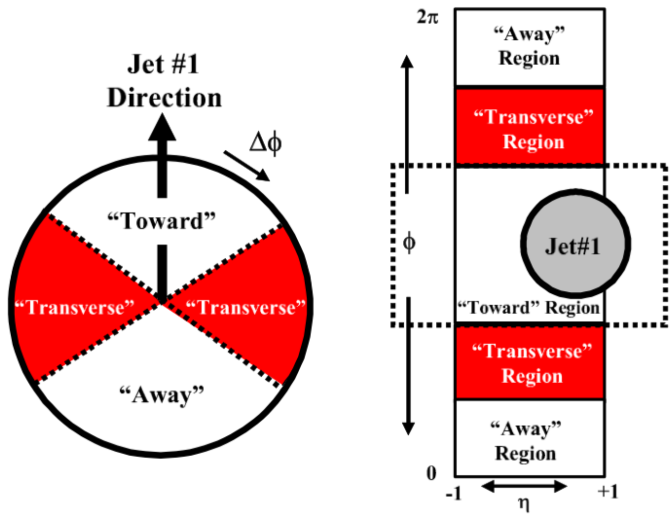

Figure 2.6. Definitions of the toward, away and transverse regions. The angle $\Delta\phi = \phi_{jet=1}$ is the relative azimuthal angle between charged particles and the direction of the leading jet. The transverse region is defined by $60^0 < |\Delta\phi| < 120^0$ and $|\eta| < 1$ (TeV4LHC QCD Working Group, 2006).

sensitive to the underlying event, and so a good understanding of the underlying event is needed for precision measurements. A series of studies have been made on underlying events by CDF in Run I (Aolder, 2002; Acosta 2004; TeV4LHC QCD Working Group, 2006; Field, 2006). These studies made use of the topological structure of hadron-hadron collisions to study the underlying event. The measurements were made on event activities in the transverse region with respect to the jet axis in jet events; this region is most sensitive to the underlying event.

To study this kind of events, the idea is quite simple. It is for instance possible to use dijet events and we can distinguish in azimuthal angle three different regions: the toward region around the leading jet direction defined by a cone of 60 degrees around the jet axis, the away region in the opposite direction to the jet, and the transverse region the remaining regions far away from the jet and the away region. In dijet events, the transverse region will be dominated by underlying events. The geometry of this study is shown in Figure 2.6, where the transverse, towards and away regions have been defined with respect to the direction of the leading jet.

At the LHC, one of the first measurements to be performed will be related to the tuning of underlying events in the generators since it is crucial to tune the Monte Carlo to accomplish fully the LHC program.

2.3 Jets in Hadron Colliders

The experience gained at the Tevatron is extremely useful in the preparation for physics analysis with jets at the LHC. However, hard scattering at the LHC is not just re-scaled scattering from the Tevatron. Many of the interesting physics signatures will take place with relatively low x partons and thus there will be a dominance of gluon and sea quark interactions, as compared to interactions involving valence quarks. In addition, as the initial state partons are at low x, there is enormous phase space for gluon emission, and so a large probability for additional jets from initial state radiation. The underlying event is also expected to be enhanced compared to the activity observed at the Tevatron, largely through an increased rate of semi-hard multiple-parton interactions. These interactions will contribute to the energy measured in jets produced in the hard scatter, and may often lead to the production of extra low transverse momentum jets in their own right. Thus, the LHC will be a very jetty environment and accurate measurements of the dynamics of the hard scattering may be challenging (Campbell, 2007). There is then a need for tools even more powerful than the ones used at the Tevatron to reconstruct jets. The most interesting tools focus on the reconstruction of jet shapes, thus exploiting the significantly finer readout granularity of the LHC detectors.

In high energy interactions partons are produced in the final state with large transverse momenta as a result of the hard scattering process. Jets are experimental signatures of these partons namely quarks and gluons from the hard collisions, see the Figure 2.3. Most of the interesting physics processes in pp collisions at the LHC include jets in the final state. Therefore, the reconstruction and precise measurement of jets serve as key ingredients for the better understanding of hard scattering processes and for new physics searches at the LHC.

Hadron collisions at the LHC are a profile source of high transverse momentum jets as well as for TEVATRON. The essential difference in going from the Tevatron to the LHC is in the production of the hard jets. At the higher collision energy we observe a greater contribution from gluon jets relative to quark jets, for the same E_T, jets at the LHC are expected to be slightly wider than at the Tevatron.

At present, perturbative calculations exist to next-to-leading order ($Q(\alpha_s^3)$) only for the inclusive and dijet rates. These allow quite precise studies of QCD, albeit for very inclusive quantities. At NLO, the cross sections begin to depend on the exact definition of the jets, since the jets begin to develop internal structure. The experiments at the Tevatron and HERA have used measures of internal structure of jets as a cross-check on the reliability of the calculations, as well as a study of QCD in its own right. In fact these more exclusive event properties contain considerably more information aboout QCD dynamics, and make an ideal place to study QCD.

One of the most popular tool to define the internal structure of jets in hadron collisions is the ”jet shapes”. Jet shapes can be defined as the energy flow inside the jet as a function of the radius from the jet axis. This has been measured by both CDF (Abe, 1993; Abulencia, 2008) and D0 (Abachi, 1995) over wide ranges of phase space. The CDF results are presented for both inclusive and b-jets in different integrated luminosities.

This thesis work is mainly based on jet shapes analysis at CMS in proton-proton collisions at 14 TeV. A short introduction related to jet shapes will be given in section 2.3.3 . Before that I would like to concentrate little bit on jet definition and reconstruction of the jet objects on the hadron colliders.

2.3.1 Jet Definition

Standard model processes in proton-proton collisions involving large momentum transfers are described by the scattering of partons namely quarks and gluons. While partons are not directly observable they manifest themselves through hadronization as stable particles, which then produce signals in the electromagnetic- (ECAL) and hadronic- (HCAL) calorimeters and, if they are charged, the pixel- and silicon-strip tracking detectors. These signals are subsequently clustered into collimated objects composed of stable particles, called jets, which are expected to yield a good representation of both the parton-level and the hadron showers emerging from the hard interaction. Perturbative theory and the hadronization model describe the interaction between constituent partons of the protons and the subsequent showering into stable particles. In addition to the hard interaction effects such as the underlying event and multiple pp interactions, which will change the observable energy flow, also have to be modeled. The evolution of a jet from the hard interaction to observable energy deposits is shown schematically in Figure 2.7.

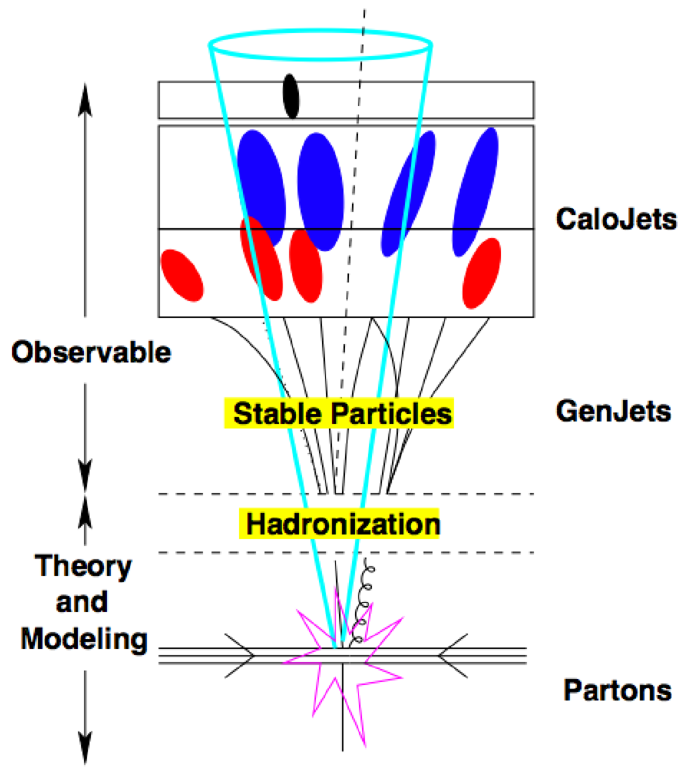

Figure 2.7. Evolution of a jet, (Bhatti, 2008)

Jet algorithms are used to reconstruct the jets. These algorithms cluster energy deposits in the calorimeter or four-vectors of particles. A successful jet algorithm will provide a good correspondence between the parton level and the particle level, where particle level refers to the stable particles remaining after the hadronization stage. Briefly, it should be collinear-safe, such that the outcome remains unchanged if e.g. the energy carried by a single particle is instead distributed among two collinear particles. Collinear safety is typically endangered if the jet finding is based on energetic seeds and a threshold is applied to these seeds. The algorithm should be infrared-safe, such that the result of the jet finding is stable against the addition of soft particles. Jet algorithms which do not comply with either or both of these requirements yield ambiguous results and lead to unnecessary uncertainties when applied to calculations in perturbation theory.

Traditionally at hadron colliders, jets have been defined using cone based clustering algorithms which search for stable cones around the direction of significant energy flow. The steps in a typical cone based algorithm are shown in Figure 2.8 Initially, a cone is defined using the highest E_T particle (or four-vector) and the summed four-vector is calculated for all particles within the cone resulting in a proto-jet. The procedure is repeated until a stable proto-jet is found such that the proto-jets four- vector coincides with the sum of the four-vectors of all the particles within the cone. Once all stable proto-jets are found, a splitting/merging procedure is applied to ensure that all particles will end up in only one jet. Iterative cone algorithms that consider every tower as the starting direction for the initial cone take a prohibitively long time to execute. In order to reduce the computation time, a minimum p_T requirement is applied to the four- vectors resulting in a subset referred to as seeds for the initial trial cone direction. If a p_T cut is applied to the particles used as seeds, then the procedure becomes collinearly unsafe at pQCD parton level and different sets of stable jet configurations can be found depending on the p_T cut. Cone algorithms which use seeds also have the problem of being infrared unsafe at pQCD parton level. The addition of a soft parton can lead to a new stable cone configuration. These two effects are illustrated in Figure 2.9.

2.3.2 Jet Kinematics

The coordinate system used at CMS is defined as follows: the x-axis points horizontally outside the LHC ring, the y-axis points upwards, and the z-axis is aligned with the nominal beam direction. The azimuthal angle is ϕ and the polar angle is θ.

The transverse momentum p_T is defined as a projection of a particle momentum p on the xy-plane,

$$p_T = p \cdot \sin\theta \tag{2.10}$$

It is obvious that both p_T and ϕ are boost-invariant. The transverse energy is defined similiary to the transverse momentum as

$$E_T = E \cdot \sin\theta. \tag{2.11}$$

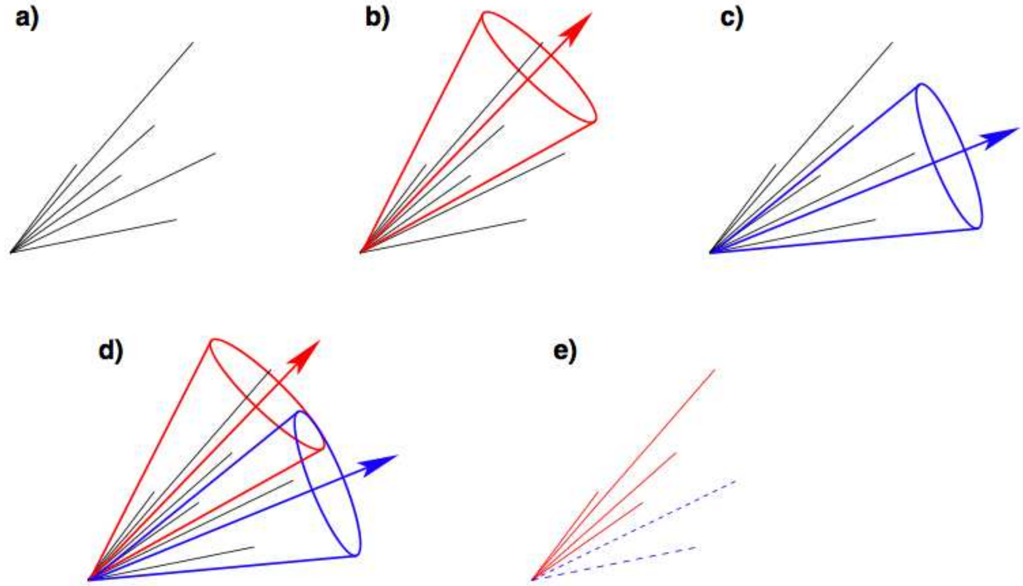

Figure 2.8. Steps in a jet clustering algorithm. a) Starting from an ordered list of four-vectors. b) and c) Stable cones are found. d) A splitting/merging algorithm is applied so that any four-vectors within the overlap region of cones is assigned to a single jet. e) We end up with a final list of jets (Bhatti, 2008).

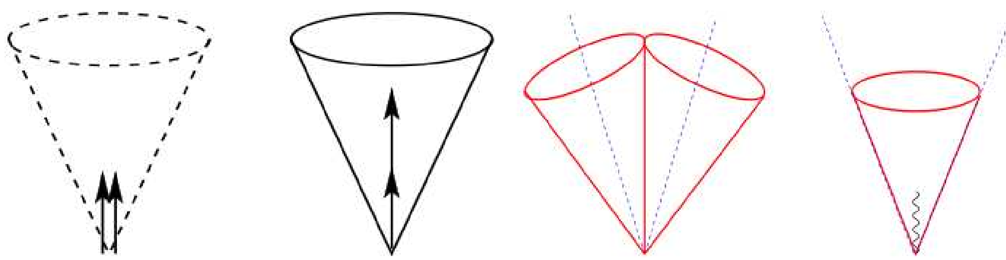

Figure 2.9. Two figures on the left points the case for the Collinear unsafe. Changing the pcut used for the seeds can lead to different stable cone congurations. The other two figures on the right points the Infrared unstable case. The addition of a soft particle can lead to new stable jet configurations (Bhatti, 2008).

The rapidity of a particle of momentum is defined to be

$$y = \frac{1}{2} ln \frac{E + p_z}{E - p_z} \tag{2.12}$$

where E denotes the energy and p_Z is the component of the momentum along the z direction. The advantage of using rapidity is that under an arbitrary boost along the z -axis, rapidity differences remain invariant, i.e. they directly measure relative scattering angles in the partonic center of mass frame (for more details on the kinematics at Hadron collider look at appendix1). Hovewer, the pseudo-rapidity is defined as

$$\eta = -\ln[\tan\frac{\theta}{2}]. \tag{2.13}$$

It is desirable to use the kinematical variables p_T, η, ϕ to describe events in hadronic collisions since these are the directly measured jet quantities. In collider experiments, most often, electromagnetic and hadronic calorimeters provide the energy measurements for (essentially) massless particles, such as $e^{\pm}$, γ, and light quark or gluon jets. Thus

$$E_T = p_T = E\cos\theta. \tag{2.14}$$

A commonly adopted presentation for an electromagnetic or hadronic event is on an $\eta - \phi$ plane with the height to indicate the transverse energy deposit E_T called the lego plot. We show one typical di-jet event from CMS by a lego plot in Figure 2.10. Of particular importance for a lego plot is that the separation between to objects on the plot is invariant under longitudinal boosts. This is seen from the definition of separation

$$\Delta R = \sqrt{\Delta\eta^2 + \Delta\phi^2}. \tag{2.15}$$

As a quantitative illustration, for two objects back-to-back in the central region, typically $\Delta\eta < \Delta\phi$ and $\Delta R \approx \Delta\phi \sim \pi$.

2.3.3 Jet Shapes

The transverse momentum profile of a jet, or jet shape (Ellis, 1992; Seymour, 1998), is sensitive to multiple parton emissions from the primary outgoing parton and provides a good test of the parton showering description of Quantum Chromodynamics (QCD), the theory of strong interactions. Historically the jet shape has been used to test perturbative QCD α_s^3 calculations (Abe, 1993; Abachi, 1995). These leading order calculations, with only one additional parton in a jet, showed good agreement with the observed jet shapes.

While confirming the validity of pQCD calculations, jet shape studies also indicated that jet clustering, underlying event contribution and hadronization effects must be considered. These effects can be modeled accurately within the framework of full-event generators. Current Monte Carlo (MC) event generators use pQCD inspired parton shower

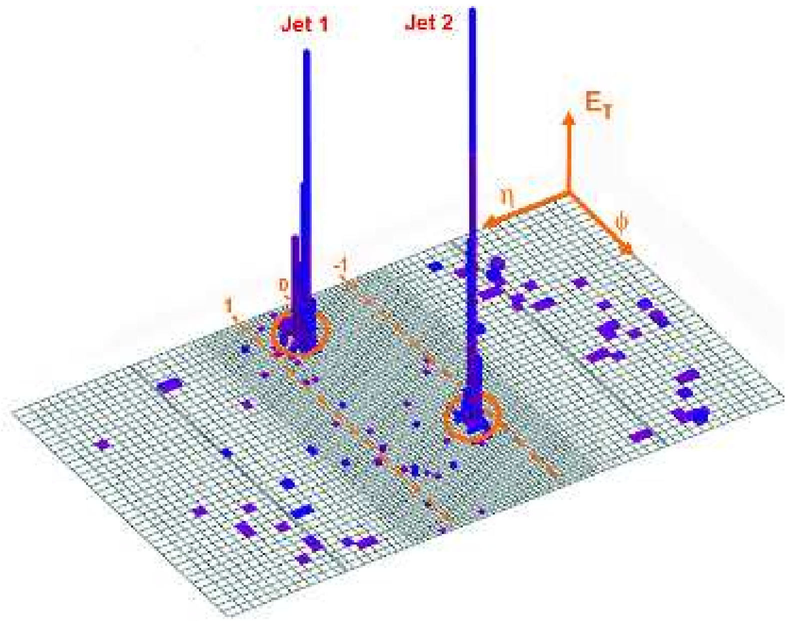

Figure 2.10. CMS simulation: dijet view in (η, ϕ) space

.

models, in conjunction with hadronization and underlying event models, to generate final state particles. MC generators are used extensively to model signal and background events in most analyses at hadron colliders. Jet shapes can be used to tune phenomenological parameters in these MC generators. These parameters control the initial and final state radiation, jet fragmentation, hadronization, and underlying event. Well-tuned Monte Carlos are essential for a precise measurement and proper comparison with theoretical predictions. The good modeling of jet fragmentation properties and of the underlying event in Monte Carlo events is crucial for corrections of jet energies from the calorimeter level to the hadron level. Moreover, the underlying event, an important component of any hadronic collision, plays a non-negligible role in the internal structure of jets.

Jet shapes are sensitive to whether the initial hard-scattered parton is a quark or a gluon. QCD predicts broader gluon jets than quark jets (see Figure 2.11) because the strength of the gluon-gluon coupling is larger than that of the quark-gluon coupling. The structure of quark and gluon jets can be investigated by comparing measurements of the jet shapes in different processes enriched with either quark or gluon initiated jets in the final state. Previously, jet shapes have been measured in $p\bar{p}$ collisions at Tevatron and

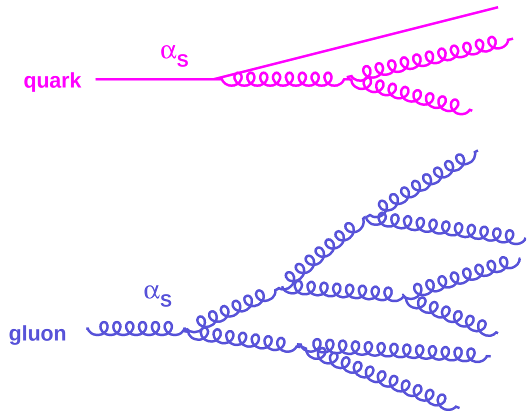

Figure 2.11. Examples of the structure of quark and gluon initiated jets (Kurt, Bhatti and Zielinski, 2008).

ep collisions at HERA (Abe, 1993; Abachi, 1995; Acosta, 2005, Adloff, 2000; Breitweg, 1999).

Jet shapes look at the fractional transverse momentum (p_T) distribution inside the jets as a function of the distance away from the jet axis. This can be expressed either as a differential or integrated quantity. The differential jet shape is the rate of change of p_T with increasing distance away from the jet axis, whereas the integrated shape is the fractional p_T inside a cone around the jet axis as illustrated in Figure 2.12 and Figure 2.13, respectively. This quantity can be computed at parton or hadron level in the Monte Carlo (MC) simulations and by using either the tracks or the calorimetric towers at detector level. Formally, the distance away from the jet axis is defined as

$$r = \sqrt{(\Delta y)^2 + (\Delta\phi)^2} \tag{2.16}$$

where $\Delta\phi$ and Δy are the angular distances in the (ϕ, y)-plane between the objects and the jet direction. y is the rapidity which is described in the jet kinematics section 2.3.2, and ϕ is the direction in the plane orthogonal to the beam-direction relative to the vertical as described in section 2.3.2. The integrated jet shape is expressed as

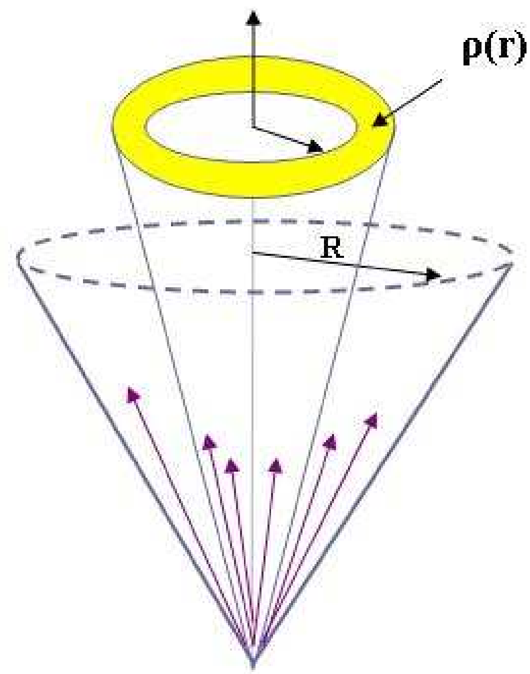

Figure 2.12. Definition of the differential jet shape, $\rho(r)$ (Kurt, Bhatti and Zielinski, 2008).

$$\psi(r) = \left\langle \frac{P_T(0,r)}{P_T(0,R)} \right\rangle \tag{2.17}$$

where R is the jet cone radius and $P_T(0,r)$ is the sum of the transverse momentum of all objects inside a sub-cone of radius r around the jet axis. Similarly, the differential jet shape is defined as

$$\rho(r) = \frac{\partial \psi(r)}{\partial r} = \left\langle lim_{\Delta r \to 0} \left(\frac{1}{\Delta r} \frac{P_T(r - \Delta r/2, r + \Delta r/2)}{P_T(0,R)} \right) \right\rangle. \tag{2.18}$$

The integrated shapes are normalised such that $\psi(r = R) \equiv 1.$, i.e. the fractional transverse momentum of the objects inside a cone of radius equal to the jet cone radius around the jet axis is unity. Similarly, the differential shapes are normalised such that $\int_0^R \rho(r) dr = 1$. This requirement comes from the fact that the fractional transverse momentum of the objects inside the jet cone must be equal to unity. Jet shapes will be discussed in more detail in chapter 7.

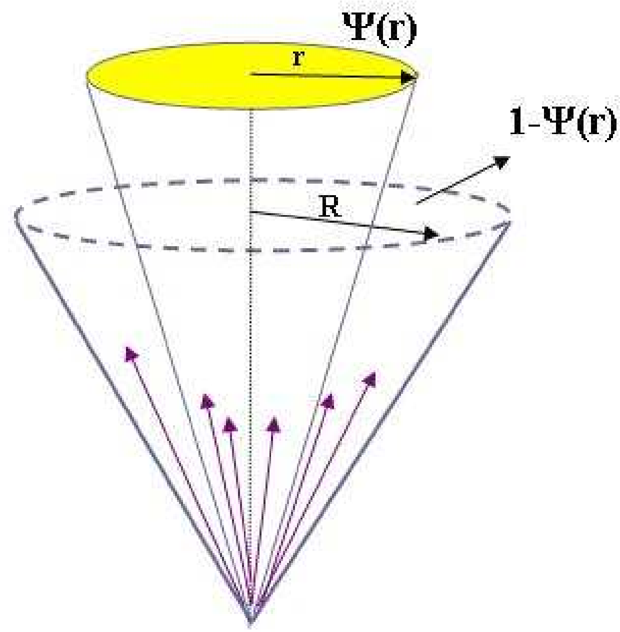

Figure 2.13. Definition of the integrated jet shape, $\psi(r)$ (Kurt, Bhatti and Zielinski, 2008).

2.3.4 Jet Shapes at CDF

The jet shape is dictated by multi-gluon emission from primary partons, and is sensitive to quark/gluon contents, PDFs and running α_S , as well as underlying events. We defined (equation 2.17) ψ which is sensitive to the way the energy is spread around the jet center where R is the jet size. The energy is more concentrated towards the jet center for quark than for gluon jets since there is more QCD radiation for gluon jets (which means that ψ is closer to one for quark jets when $r \approx 0.3R$ for instance. The CDF collaboration measured $\psi(0.3/R)$ for jets with $0.1 < |y| < 0.7$ as a function of jet p_T and found higher values of ψ at high p_T as expected since jets are more quark like (Acosta, 2005). This measurement also helps tuning the PYTHIA and HERWIG generators since it is sensitive to underlying events in particular. The CDF collaboration also studied the jet shapes for b-jets in four different p_T bins (Abulencia, 2008), and the result is given in Figure 2.14. The default PYTHIA and HERWIG Monte Carlo in black full and dashed lines respectively are unable to describe the measurement. Compared to the inclusive jet shape

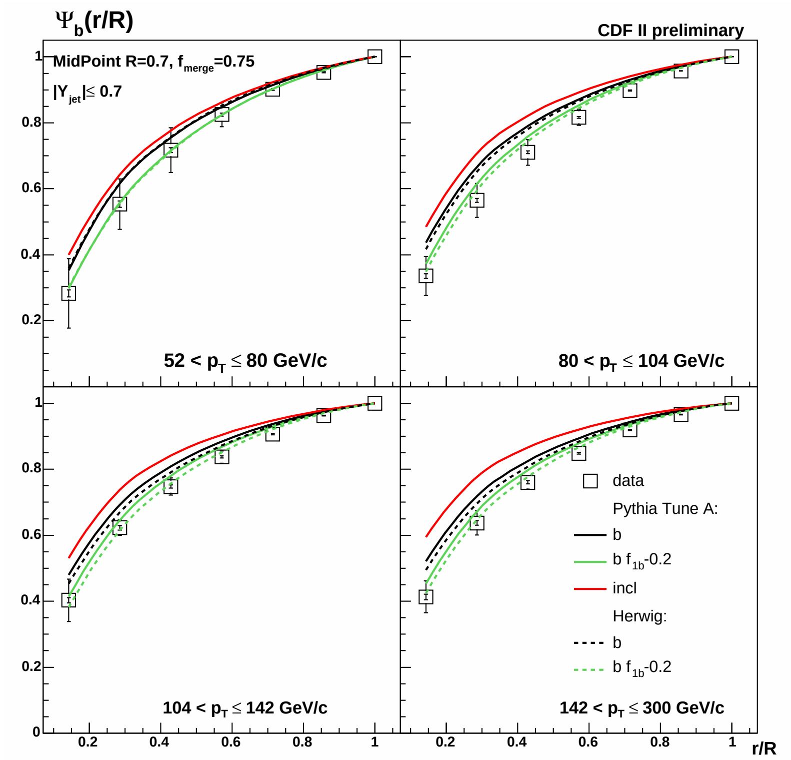

Figure 2.14. Measurement of the b-jet shapes and comparison with the predictions of the PYTHIA and HERWIG Monte Carlo (Lister, 2006).

depicted in Figure 2.14 in full red line for PYTHIA, the tendency of the b-jet shape is definitely the right one, leading to smaller values of ψ as expected, but the measurement leads to a larger difference. The effect of reducing the single b-quark fraction by 20% leads to a better description of data as it shown in green in Figure 2.15. The fraction of b-jets that originate from flavour creation (where a single b-quark is expected in the same jet cone) over those that originate from gluon splitting (where two b-quarks are expected in the same jet cone) is different in Monte Carlo and data.

Figure 2.16 presents the measured integrated jet shapes, $\psi(r/R)$, in bins of P_T^{jets} , for jets with $0.1 < |Y^{jet}| < 0.7$ and 37 GeV/c $< P_T^{jet} <$ 148 GeV/c, compared to HERWIG, PYTHIA-Tune A, PYTHIA and PYTHIA-(no MPI) predictions, to illustrate the importance of a proper modeling of soft-gluon radiation in describing the measured jet shapes.

Figure 2.17 shows, for a fixed radius $r_0 = 0.3$, the average fraction of the jet transverse momentum outside $r = r_0$, $(1 - \psi(r_0/R))$, as a function of P_T^{jet}. The points are located at the weighted mean in each P_T^{jet} range. The measurements show that the fraction of jet transverse momentum inside a given fixed r_0/R increases ($1-\psi(r_0/R)$ decreases) with P_T^{jet} , indicating that the jets become narrower as P_T^{jet} increases. PYTHIA with default parameters produces jets systematically narrower than the data in the whole region in P_T^{jet}. The contribution from secondary parton interactions between remnants to the predicted jet shapes (as shown by the dierence between PYTHIA and PYTHIA-(no MPI) predictions) is important at low P_T^{jet} . PYTHIA-Tune A predictions describe all of the data well. HERWIG describes the measured jet shapes well but produces jets slightly narrower than the data at low P_T^{jet} .

Figure 2.18 presents the measured integrated jet shapes, $\psi(r/R)$, in bins of P_T^{jets} , for jets with $0.1 < |Y^{jet}| < 0.7$ and 37 GeV/c $< P_T^{jet} <$ 148 GeV/c, compared to PYTHIA-Tune A predictions. In these figure, predictions are also shown separately for quark- and gluon-jets. Each hadron-level jet from PYTHIA is classied as a quark- or gluon-jet by matching ($y-\phi$ plane) its direction with that of one of the outgoing partons from the hard interaction. The Monte Carlo predictions indicate that, for the jets used in this analysis, the measured jet shapes are dominated by contributions from gluon-initiated jets at low P_T^{jets} while contributions from quark-initiated jets become important at high P_T^{jets} . This can be explained in terms of the different partonic contents in the proton and antiproton contributing to the low- and high-P_T^{jets} regions, since the mixture of gluon- and quark-jet in the final state partially reflects the nature of the incoming partons that participate in the hard interaction.

Figure 2.19 shows the measured $1-\psi(r_0/R)$, r_0 = 0.3, as a function of P_T^{jet} compared to PYTHIA-Tune A predictions with quark- and gluon-jets shown separately. The trend with P_T^{jet} in the measured jet shapes is mainly attributed to the different quark- and gluon-jet mixture in the final state and perturbative QCD effects related to the running of the strong coupling, $\alpha_s(P_T^{jet})$ (Akers, 1994; Ackersta, 1998). The Monte Carlo predicts that the fraction of gluon-initiated jets decreases from about 73 % at low P_T^{jet} to 20 % at very high P_T^{jet} , while the fraction of quark-initiated jets increases.

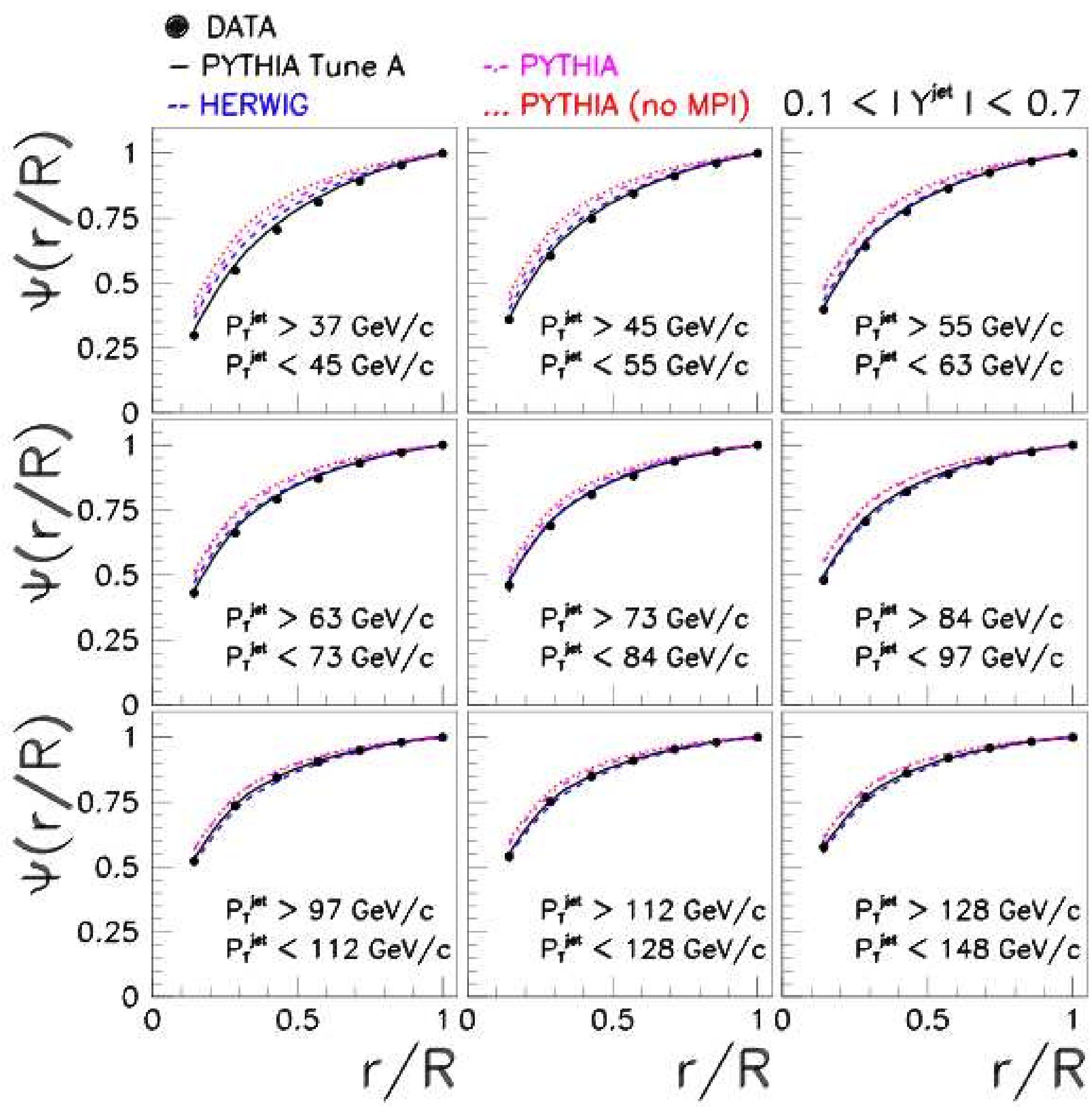

Figure 2.15. The measured integrated jet shape, $\psi(r/R)$, in inclusive jet production for jets with $0.1 < |Y^{jet}| < 0.7$ and 37 GeV/c $< P_T^{jet} <$ 148 GeV/c, is shown in different P_T^{jet} regions. Error bars indicate the statistical and systematic uncertainties added in quadrature. The predictions of PYTHIA-Tune A (solid lines), PYTHIA (dashed-dotted lines), PYTHIA-(no MPI) (dotted lines) and HERWIG (dashed lines) are shown for comparison (Abe, 1993).

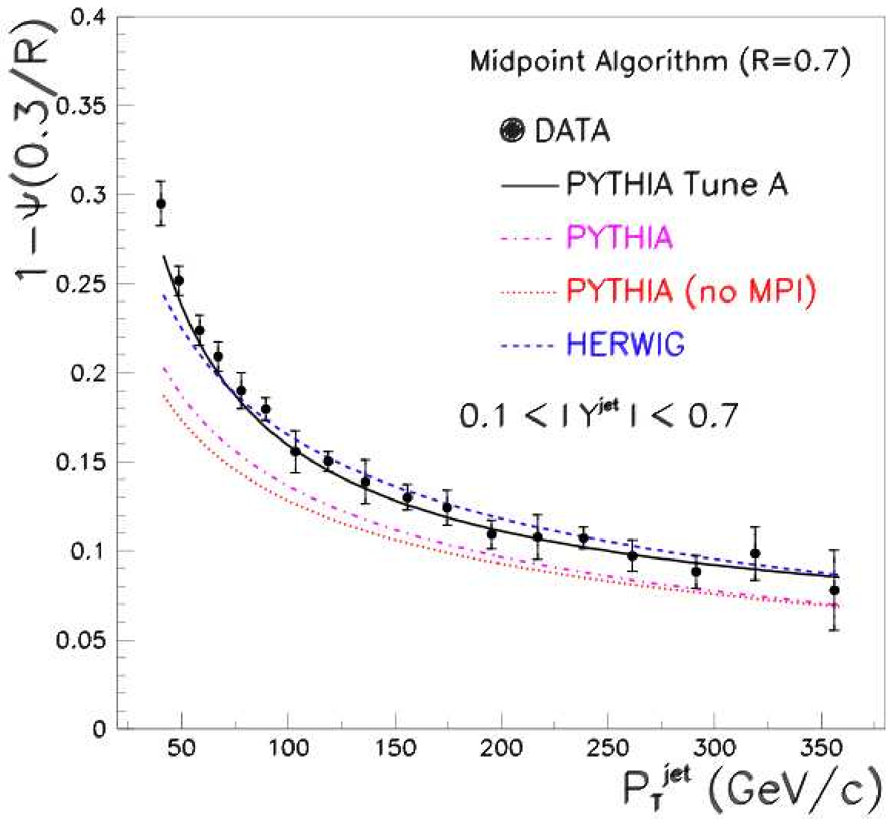

Figure 2.16. Measurement of the b-jet shapes and comparison with the predictions of the PYTHIA and HERWIG Monte Carlo (Abe, 1993).

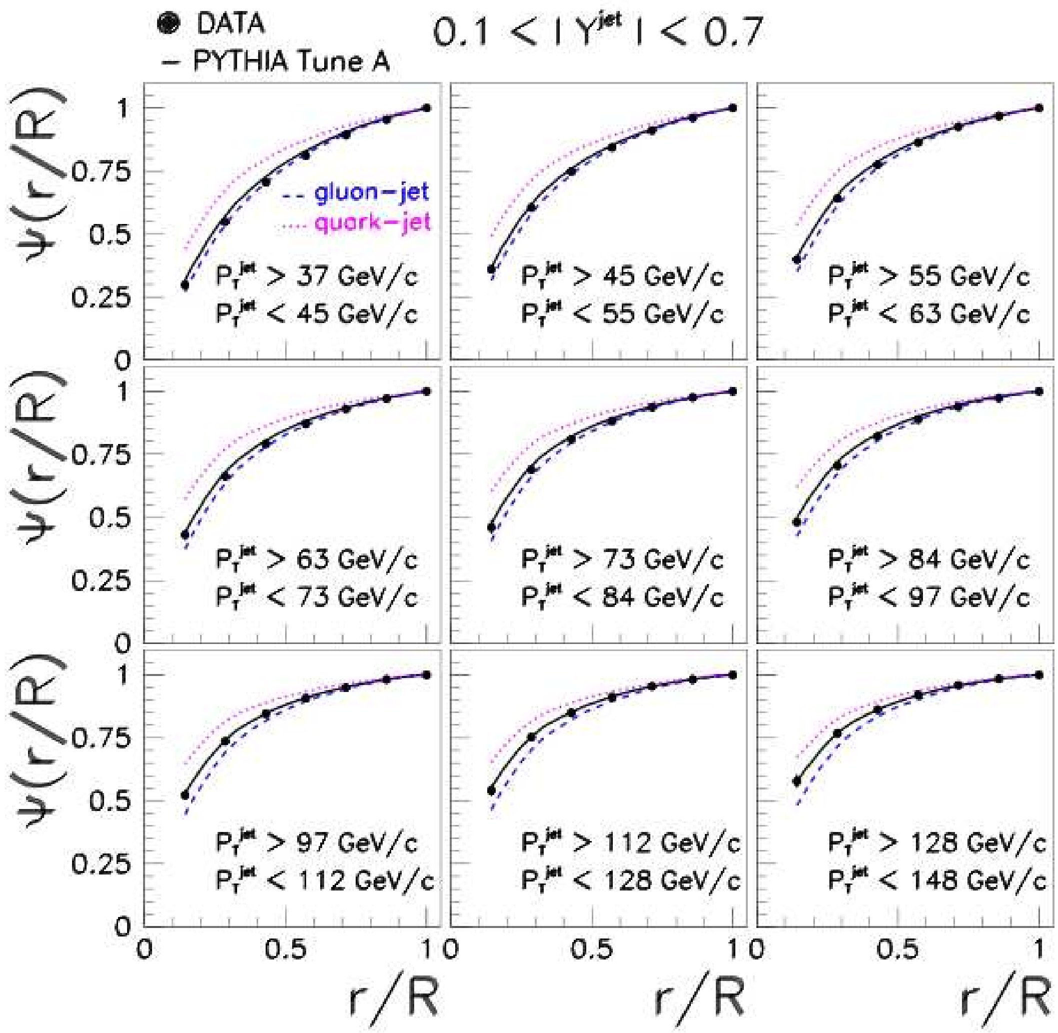

Figure 2.17. The measured integrated jet shape, $\psi(r/R)$, in inclusive jet production for jets with $0.1 < |Y^{jet}| < 0.7$ and 37 GeV/c $< P_T^{jet} <$ 148 GeV/c, is shown in different P_T^{jet} regions. Error bars indicate the statistical and systematic uncertainties added in quadrature. The predictions of PYTHIA-Tune A (solid lines) and the separate predictions for quark-initiated jets (dotted lines) and gluon-initiated jets (dashed lines) are shown for comparison (Abe, 1993).

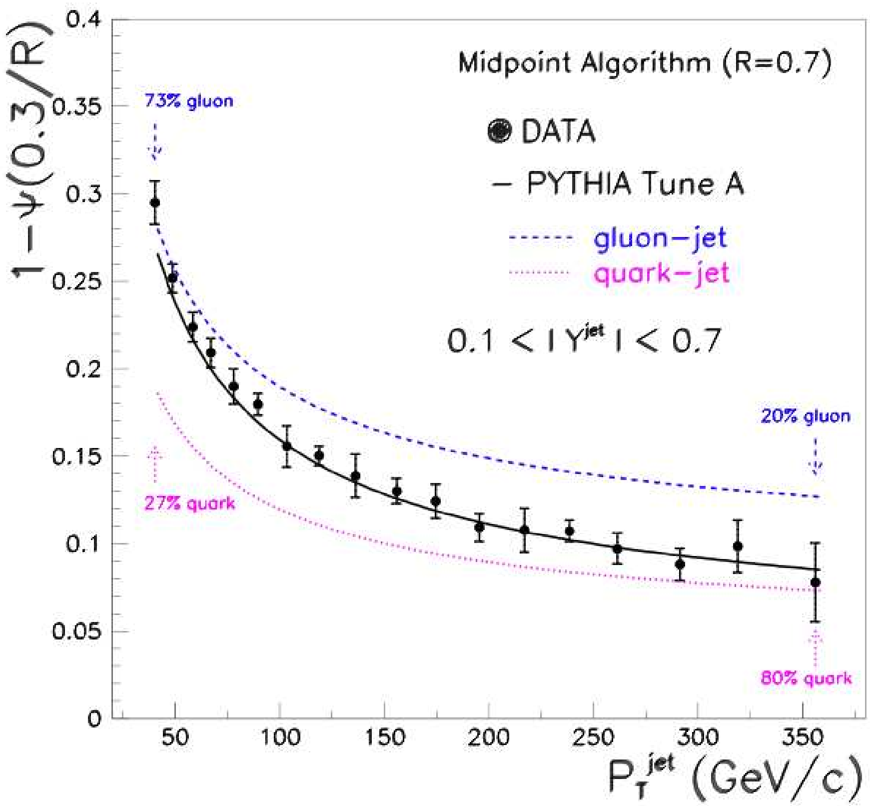

Figure 2.18. Measurement of the b-jet shapes and comparison with the predictions of the PYTHIA and HERWIG Monte Carlo (Abe, 1993).

3. LHC

The Large Hadron Collider (LHC) (Bruning, 2004) is presently being constructed in the already existing 27-km LEP tunnel in the Geneva region. The LHC will yield head-on collisions of two proton (ion) beams, circulating in apposite directions, at an energy of 7 TeV (2.75 TeV per nucleon) each (center-of-mass $\sqrt{s}$ = 14 TeV and $\sqrt{s}$ = 5.5 TeV, respectively) with a design luminosity of $10^{34}cm^{-2}s^{-1}$ ($10^{27}cm^{-2}s^{-1}$). The LHC will be the highest energy accelerator in the world for many years following its completion after Tevatron which is operating on center of mass energy $\sqrt{s}$ = 2 TeV. Figure 3.1 shows a variety of SM cross section for hadron collisions of various energy, and marks off in particular Tevatron and LHC. The prime motivation of the LHC is to elucidate the nature of electroweak symmetry breaking for which the Higgs mechanism is presumed to be responsible. The experimantal study of the Higgs mechanism can also shed light on the mathematical consistency of the Standart Model at energy scales above about 1 TeV. Various alternatives to the Standart Model invoke new symmetries, new forces or constituents. Furthermore, there are hight hopes for discoveries could take the form of supersymmetry or extra dimensions, the latter often requiring modification of gravity at the TeV scale. Hence there are many compelling reasons to investigate the TeV energy scale. The LHC will also provide high-energy heavy ion beams at energies over 30 times higher than at the previous accelerators, allowing us to further extend the study of QCD matter under extreme conditions of temperature, density, and parton momentum fraction (low-*x*).

The Compact Muon Solenoid (CMS) is one of the largest detector located on LHC, and installed about 100 meters underground close to the French village of Cessy, between Lake Geneva and Jura mountains. The CMS is a general purpose experiment, designed to study the physics at TeV scale at the LHC (Chatrchyan, 2008). It currently involves more than 2000 physicists from more than 150 institutions and 37 countries. CMS will also be an instrument to perform precision measurements of the parameters of the Standard Model, mainly the result of the very high event rates for a luminosity of $2 \times 10^{33}cm^{-2}s^{-1}$.

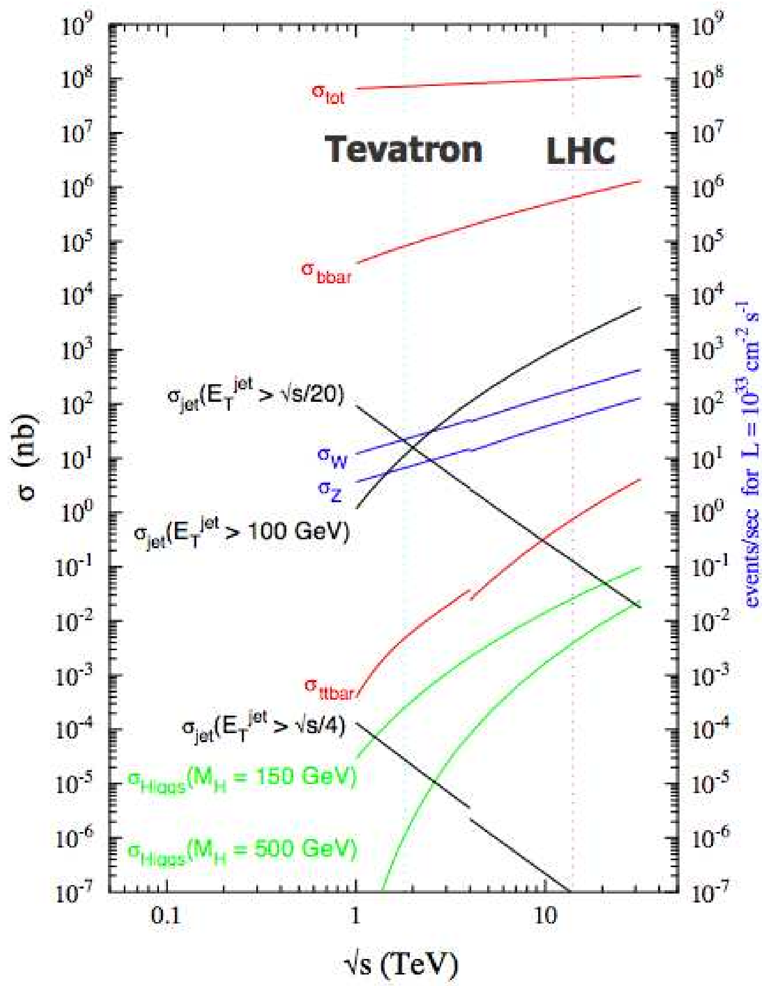

Figure 3.1. Various SM standart candle" cross sections at hadron colliders of varying energy, with Tevatron and LHC marked in particular. Discontinuities are due to the difference between $p\bar{p}$ for Tevatron and pp for LHC (Gianotti, 2004).

3.1 Collider Physics

The development of accelerators and storage rings has allowed to collide particles at higher and higher energies. In accordance with Einstein's famous equation, $E = mc^2$, several hundreds of short-lived particles could be found at the various accelerators, in addition to the few stable particles (like protons and electrons) of which the universe is built. The particles that can be accelerated are usually electrons, positrons, protons, antiprotons, and ions. There are different motivations why to choose to collide protons or leptons in an experiment. As leptons are point-like, the energy of the interacting particles is known. The event kinematics is thus completely constrained. Leptons are therefore chosen, if i.e. the mass of the particle to discover is already predicted rather precisely by theory. In a hadron beam the hadron energy is shared between its constituent partons, the quarks and gluons; these are the interacting particles at high energies, and the energy of the two colliding partons is therefore not fixed. The event kinematics is thus only partially known and only part of the beam energy is used. In order to discover a particle which mass is not known, it is more convenient to use protons, as automaticlly a larger mass range is addressed. On the other hand, leptons have the advantage that the signatures are produced in a clean environment, while in a proton collider there are a lot of minimum bias events.

A disadvantage of colliding beams is, however, that the luminosity is much lower than with a fixed target, as the target is much smaller. Besides the type of the particle collisions, one can also distinguish between linear and circular accelerators. In a linear accelerator (so-called Linacs), particles are accelerated in a straight line. In a circular accelerator, particles move in a circle until they reach the desired energy. The advantage of circular accelerators over linear accelerators is that the ring topology allows continous acceleration, as the same particles pass through the same accelerating elements many times. Dipole magnets keep particles in a circular orbit while quadrupole magnets focus the beam. However, circular accelerators have the disadvantage that the particles emit synchrotron radiation. Synchrotron radiation occurs when any charged particle is accelerated; it emits electromagnetic radiation and secondary emissions. As a particle travelling in a circle is always accelerating towards the center of the circle, it continuously radiates towards the tangent of the circle. The energy loss due to synchrotron radiation for highly relativistic particles is described as:

$$E = \frac{4\pi\alpha\hbar c}{3R}\beta^3\gamma^4 \tag{3.1}$$

where $\gamma = \frac{E}{mc^2}$ and $\beta = \frac{v}{c} \approx 1$, with R the radius of the accelerator, E the energy of the particle and m its mass. To reduce the energy loss due to synchrotron radiation, there are two possibilities: either to increase the radius of the collider or to increase the mass of the accelerated particles. Cyclic leptonic machines suffer such large synchrotron losses that they cannot be realistically constructed much larger than the LEP2 - at a LEP center-of-mass-energy of about 200 GeV, all the energy that was added to the beam in the radio frequency cavities was radiated again by synchrotron radiation.

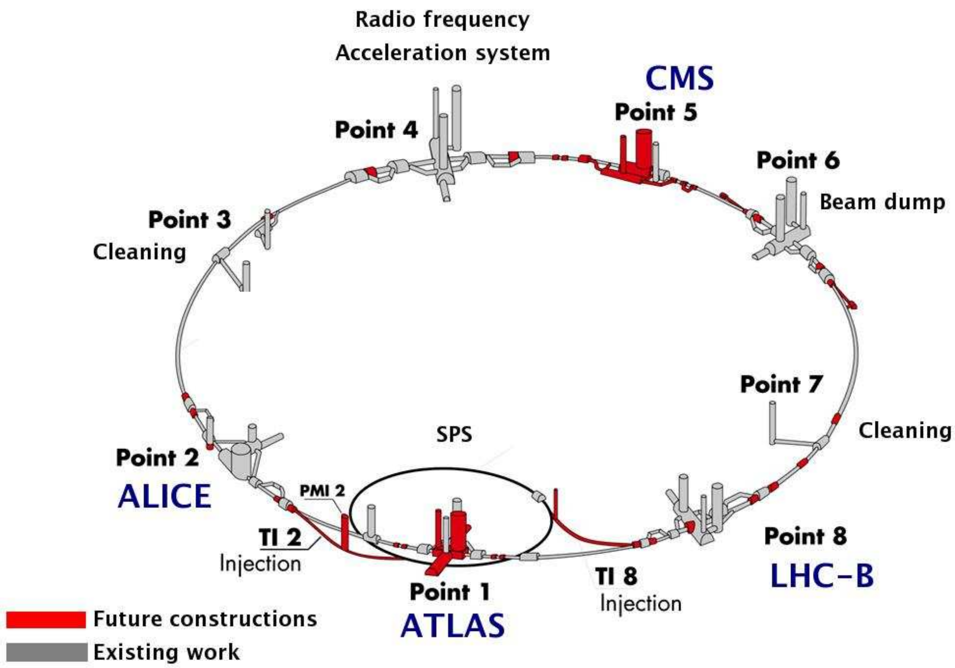

Figure 3.2. The Large Hadron Collider at CERN

3.1.1 Hadron Colliders

The highest center of mass energies and, hence, the best reach for new heavy particles is provided by hadron colliders, the Tevatron with its 2 TeV and pp collisions at present, and the LHC with 14 TeV $p\bar{p}$ collisions after 2009. The LHC is expected to do detailed investigations of the Higgs sector, and should answer the question whether TeV scale supersymmetry is realized in nature. Proton and electron beams have been used to investigate new physics signatures to test the SM.

Protons are composite particles, made of partons of quark and gluons. The quarks and gluons are the fundamental degrees of freedom to participate in strong reactions at high energies according to QCD (Sterman, 2004). The proton is much heavier than the electron. These lead to important differences between a hadron collider and an $e^+ e^-$ collider.

- Due to the heavier mass of the proton, hadron colliders can provide much higher center of mass energies in head-on collisions.

- Higher luminosity can be achieved also, by making use of the storage ring for recycle of protons and antiprotons.

- Protons participate in strong interactions and thus hadronic reactions yield large cross sections. The total cross section for a proton-proton scattering can be estimated by dimensional analysis to be about 100mb, with weak energy-dependence.

- At higher energies, there are many possible channels open up resonant productions for different charge and spin states, induced by the initial parton combinations such as $\bar{q}$, q, qg, and gg. As discussed in the last section for gauge boson radiation, there are also contributions like initial state WW, ZZ and WZ fusion.

While proton colliders can reach very high energies, the design introduces some extra challenges. Colliders that use antiparticles must find ways of producing them in large numbers and then storing them while the beam is brought up to full energy. Unless the beams are very tightly focused there will only be a few collisions per revolution so the antimatter may have to be stored for hours. In addition, to bend high-energetic protons in the ring, very strong beam magnets are needed. LHC therefore uses superconducting magnets (Chatrchyan, 2008).

3.2 The Large Hadron Collider

The Large Hadron Collider (LHC) was approved by the CERN council in December 1994. It is scheduled to start operation in November 2009. The LHC is a circular proton collider. The nominal energy of 14 TeV in the center-of-mass frame should be reached in 2010. The LHC is built in the former LEP tunnel, and has a circumference of 26.7 km. Four experiments will be located in the LHC tunnel: ATLAS (A Toroidal LHC ApparatuS) (Armstrong, 1994), CMS (Compact Muon Solenoid) (Chatrchyan, 2008), LHCb (Amato, 1998), and ALICE (A Large Ion Collider Experiment) (ALICE Collaboration, 1995) (Figure 3.2).

ATLAS and CMS are general multipurpose detectors. The three main topics of the physics program of CMS and ATLAS are to investigate electroweak symmetry breaking through the detection of one or more Higgs bosons (or, in case they do not exist, to study alternative electroweak symmetry breaking mechanisms); to search for phenomena beyond the Standard Model, such as supersymmetric particles; and to study the high-Q^2 region in more detail. LHCb is dedicated to *B*-physics and *CP*-violation studies, while ALICE investigates heavy ion physics. The aim of such high energy heavy ion collisions is to study the properties of a quark-gluon plasma. In order to achieve such high energies, the protons have to pass through different acceleration stages whereas the LHC itself is just the final part. These stages are explained below in detailed.

3.2.1 Proton Production and Linear Acceleration

The LHC has the ability to collide either protons or heavy ions (e.g. lead) at several given interaction points around the main ring. Since the main LHC operation mode will be the collision of two proton beams, the production and acceleration of heavy ions is to be ignored here. The first step of the proton production is the ionisation of hydrogen gas through a Radio Frequency Quadrupole (RFQ) duoplasmatron creating a negatively charged ion beam of 750 keV. This beam is furthermore accelerated by a linear accelerator (LINAC2) and passes through a carbon foil at the end of the machine. The foil strips off all orbiting electrons to generate a pure proton beam at an energy of 50 MeV and a current of 180 mA which is the requirement for the LHC at the stage of the next injection step.

3.2.2 Booster and Proton Synchrotron

The proton beam is fed into the Proton Synchrotron Booster (PSB) increasing its energy to about 1.4 GeV and then, in the next step of the acceleration chain, injected to the Proton Synchrotron (PS) itself, a circular accelerator with a circumference of about 630 meters. The PS served as beam source for several CERN experiments, e.g. ISR[1] and LEP. Since its completion in 1959 it has passed through several upgrade stages and is now

[1] Intersecting Storage Rings, the worlds first hadron collider.

capable of accelerating the protons to an energy of 26 GeV.

3.2.3 Super Proton Synchrotron

The last step of the LHC pre-injector chain is the Super Proton Synchrotron (SPS). Since its commissioning in 1976, the SPS has been used to accelerate electrons, positrons, protons, antiprotons and heavy ions for a variety of experiments. Today it provides proton beams for several fixed-target experiments like Compass and NA48[2]. With the start-up of the LHC, the SPS picks up the proton beam from the PS and accelerates it to a final energy of 450 GeV. Afterwards, the beam is split and extracted via two transfer lines into the LHC main ring in opposite directions.

3.2.4 LHC Main Ring

The final part of the proton acceleration is the velocity increase through radio frequency cavities implemented in 1232 superconducting dipole magnets with a length of 15 m inside the LHC. Within one circulation, the beam gains 0.5 MeV of energy and reaches its final state after about 20 minutes of operation. The dipole magnets have to provide a nominal magnetic field of 8.33 T to keep the 7 TeV protons on their circular path around the ring. Reaching such high magnetic fields required the development of new types of superconducting magnets. The coils of the magnets are made up of copper-clad niobium-titanium (NbTi) cables which are chilled to the temperature of superfluid helium of about 1.9 K. In addition to these bending magnets, several other types are required for a proper operation of the LHC, e.g. 392 quadrupole magnets counteracting a defocusing of the beam. Table 3.1 gives a short summary of the accelerator chain and shows the corresponding beam energies in each of the different acceleration stages.

[2] Common Muon and Proton Apparatus for Structure and Spectroscopy: Fixed target experiment in the field of kaon physics.

Table 3.1. Energy of the proton beam at each acceleration step.

Accelerator	Injection Energy	Final Energy
LINAC2	750 keV	50 MeV
PSB	50 MeV	1.4 GeV
PS	1.4 GeV	26 GeV
SPS	26 GeV	450 GeV
LHC	450 GeV	7 TeV

3.2.5 LHC Machine Parameters

The LHC experiments aim at identifying interesting collisions at the different interaction points (IP) around the ring. Most of these events are very rare due to a very small production cross section, σ_{event} . The cross section is a measure for the probability to observe a desired interaction with respect to all events generated by the accelerator. The amount of such events produced per second is given by

$$N_{event} = L\sigma_{event} \tag{3.2}$$

and directly linked to the luminosity L of the machine.

The LHC is therefore a two ring superconducting accelerator and collider. An approximatively 130 m long common pipe is shared by the two beams near the interaction regions. For the dipole magnets, LHC chose an elegant solution and uses twin bore magnets, which consist of two sets of coils and beam channels sharing the same mechanical structure. The maximal energy a proton beam can obtain is determined by the maximal magnetic dipole field which can be achieved to compensate the centrifugal force of the particles, given by E[TeV]$\approx$ 0.84B [Tesla]. To achieve high magnetic fields, new types of superconducting magnets had to be developed, which operate at liquid helium temperatures. By lowering the temperature down to 1.9 K, an extra 1.5 T can be gained over standard superconducting elements. This represents a 20% gain in beam energy. Such a high magnetic field induces huge mechanical constraints on the surrounding material. In order to counter these forces, non-magnetic austenitic steel collars are used to maintain the conductors in place. The luminosity L of an accelerator which collides bunches

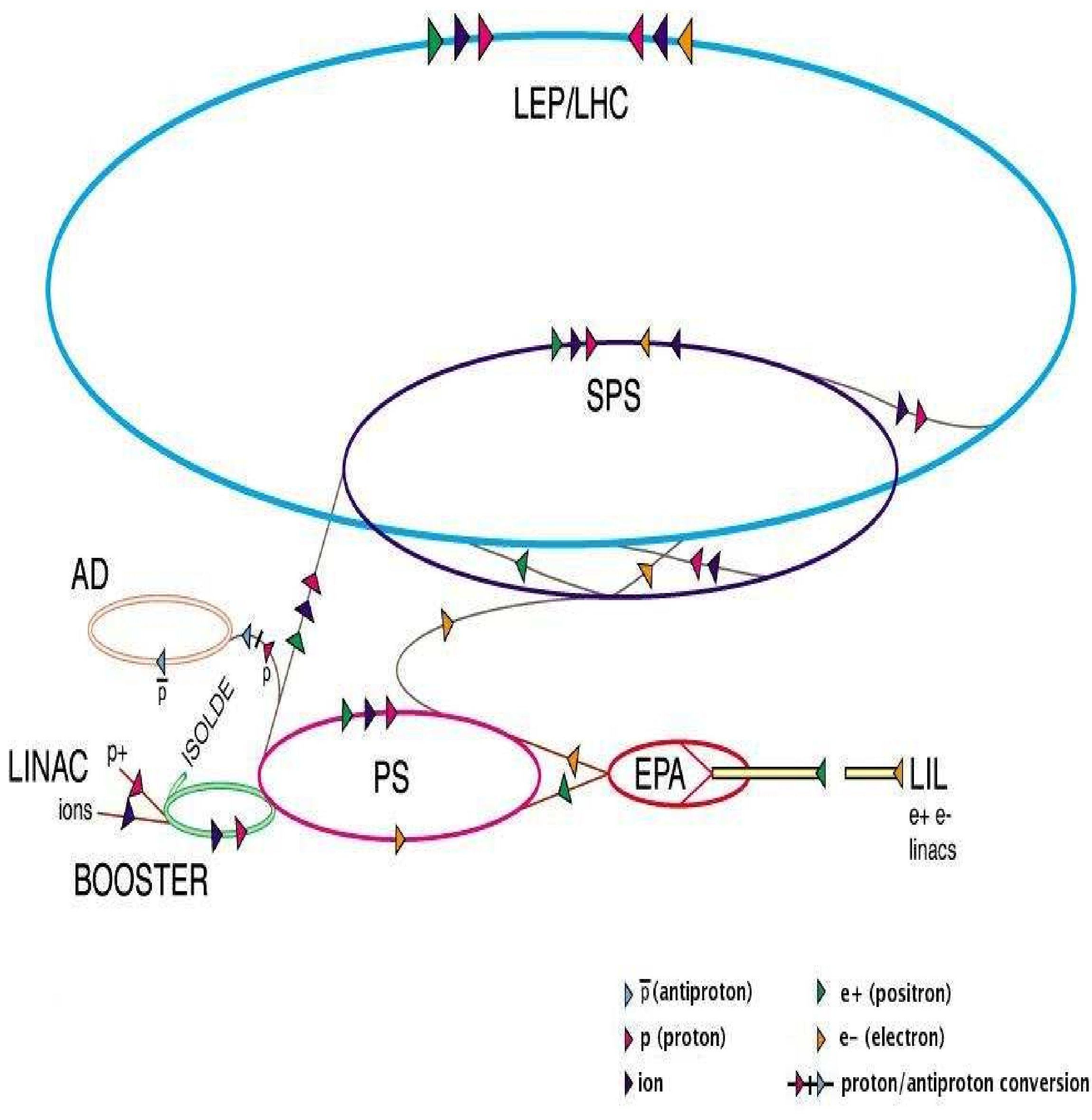

Figure 3.3. Schematic view of the CERN accelerator chain from the proton injection up to the final collision energy inside the LHC main ring (CERN Communication Group. 2008).

containing n_1 and n_2 particles at a frequency f is given by

$$L = f\frac{n_1 n_2}{4\pi\sigma_x\sigma_y} \tag{3.3}$$

where σ_x and σ_y characterize the Gaussian transverse beam profiles. To achieve a high luminosity, a small transverse beam profile, high bunch collision frequency and a large number of particles per bunch are required. The nominal number of protons per bunch at injection is about 10^{11} for a nominal luminosity of 10^{34}cm^{2}s^{-1}, which is the LHC design luminosity.

Because of this large number, the average number of inelastic pp collisions (minimum bias events) per bunch crossing is high, up to 25 for the design luminosity. This imposes difficult experimental conditions, since the rare interesting events that may occur in a bunch crossing are superimposed (piled-up) on top of many minimum bias events. A way to minimize the number of pile-up events while keeping the luminosity constant is to operate at a high collision frequency. The LHC bunch crossing rate will be 40 MHz, which means that a bunch crossing will occur every 25 ns. Such a high frequency, however, imposes stringent requirements on the response times of the LHC detectors.

The LHC luminosity is not constant over a physics run, but decays exponentially $L = L_o e^{-i\tau_L}$ due to the degeneration of the circulating beams. As the total cross section is large, the collisions themselves limit significantly the beam life-time. The decay time of the bunch intensity due to this effect is written as

$$\tau_{col} = \frac{N_{tot,0}}{L\sigma_{tot}k} \tag{3.4}$$

where $N_{tot,0}$ is the initial number of particles in the beam, L the luminosity, σ_{tot} the total cross section (σ_{tot} =110 mb at 14 TeV), and k the number of interaction points. For nominal LHC conditions, the resulting decay time is 44.9 h. The time required to reach $1/e$ of the luminosity is written $\tau_{col,1/e}$. In addition, other sources of luminosity loss have to be taken into account, which are intra-beam scattering (IBS)[4] and beam-gas interactions. Since all these effects induce an exponential luminosity drop, the net luminosity lifetime can be approximated as

$$\frac{1}{\tau_L} = \frac{1}{\tau_{col,1/e}} + \frac{1}{\tau_{IBS}} + \frac{1}{\tau_{gas}} \tag{3.5}$$

which gives τ_L = 15 h. To get the integrated luminosity per year, an estimate of the number of luminosity fills per year is needed. From PS and SPS experience, the time before physical data can be taken, τ_{fill}, which is time to fill the LHC, to ramp magnets etc., can be estimated to be around 70 minutes. From HERA, it is known that this time could also be six times larger thus in the following the upper limit of 7 hours and lower limit of 70 minutes are considered and the resulting luminosities compared. With an estimated run time of X days per year, the total luminosity per year is

$$L_{tot} = \frac{X \times 24}{T_{run}[h] + T_{fill}[h]} L_o \tau_L (1 - e^{-T_{run}/\tau_L}) \tag{3.6}$$

with T_{run} the total length of the luminosity run which can be used for physics, and L_o the initial luminosity. For a design luminosity of $10^{34}\text{cm}^2\text{s}^{-1}$ and an estimated run time of X =200 days, this leads to a total luminosity between 80 fb^{-1} and 120 fb^{-1} per year (for the lower and upper limit of τ_{fill}, respectively), which meets the original objectives of the machine.

A summary of LHC parameters is given in Table 3.1.2 The chain of accelerators is shown in Figure 3.3. In addition to the proton-proton collision, heavy ions will be accelerated and brought to collisions in the LHC. In Pb Pb collisions, the center-of -mass energy reaches 1140 TeV, which is almost 30 times the center-of-mass energy of todays most energetic heavy ion collider RHIC in Brookhaven (The CMS Collaboration, 2007). If particles with same mass and electric charge are accelerated in opposite directions, it is no longer possible to convey particles in a unique vacuum tube (as was the case at LEP).

3.3 The CMS Detector

Most of the particles produced in high-energy collisions are unstable. One would need a very sophisticated modern detector complex and electronic system to record the events for further analyses. We now briefly discuss the basic components for collider detectors.

The Compact Muon Solenoid (CMS) is one of the multi-purpose apparatus due to operate at the LHC. The CMS is located 100 m below surface at Cessy in France, and has a cylindrical structure, covering almost 4π, in order to detect a large fraction of high

Table 3.2. Some of the LHC Paramters.

Circumference	26659 m
Dipole operating temprature60	1.9 K (-271.3 C)
Number of dipoles	1232
Number of RF cavities	8 per beam
Nominal energy, protons	7 TeV
Energy at injection	450 GeV
Nominal energy, ions (energy per nucleon)	2.76 TeV/u
Peak magnetic dipole field (at 7 TeV)	8.83 T
Minimum distance between bunches	$\approx$ 7m
Design luminosity	$10^{34}\mathrm{cm}^{-2}\mathrm{s}^{-1}$
Collision rate	45 MHz
Number of bunches per proton beam	2808
Number of protons per bunch (at start)	1.1×10^{11}

p_T particles produced in a collision. It has an overall length of 21.6 m and a diameter of 15 m. The detector is divided into barrel and endcaps, and weights in total 12500 tons. It contains subsystems which are designed to measure the energy and momentum of photons, electrons, muons, and hadrons. In addition, the aim is to be as hermetic as possible, in order to measure the missing energy of an event. A trajectory of particles through the CMS detector is shown in Figure 3.4, starting from the beam pipe. The tracker allows precise momentum measurement and the impact parameter of charged particles. It is surrounded by a scintillating crystal electromagnetic calorimeter, which is surrounded by a sampling calorimeter for hadrons (Figure 3.5). Outside the solenoid lies the return yoke of the magnet, interleaved by four layers of muon chambers. The barrel covers a pseudorapidity range $|\eta| < 1.5$, while endcaps cover the range $1.5 < |\eta| < 3$. The relative error on the particle p_T measurement by a tracker goes like

$$\frac{\Delta p_T}{p_T^2} \approx \frac{1}{BR^2} \tag{3.7}$$

where B is the magnetic field in a direction orthogonal to the particle momentum, and R is the tracker radius. The magnetic field of the solenoid is about 4 T with a diameter of roughly 6m and a length of 13 m. To create such a high magnetic field a very high current (20 kA) has to be generated, circulating in superconducting strands. To allow superconductivity, the magnet will be cooled down to 4.2 K with liquid helium. At the

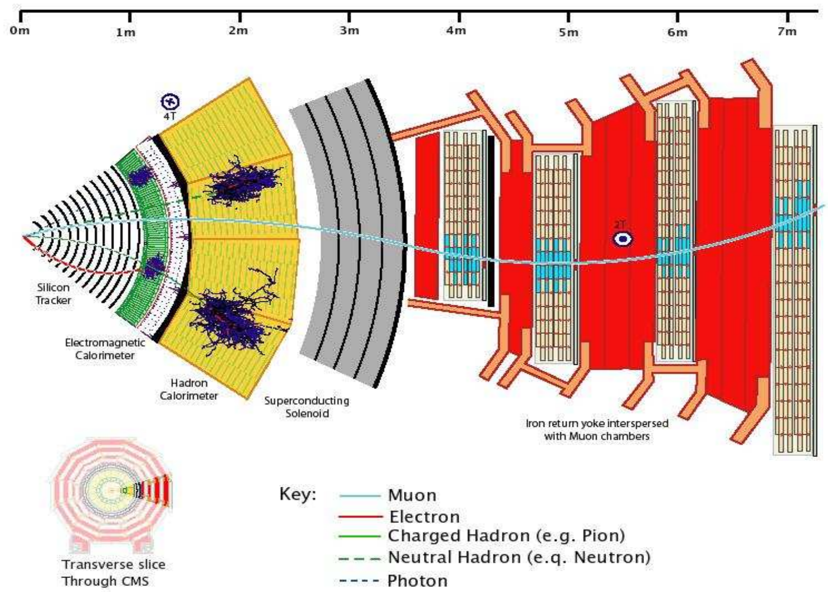

Figure 3.4. A slice of the CMS detector. The traces of particles to be detected are shown

nominal current of 20 kA, the coil will store 2.7 GJ in the magnetic field. Ramping to this current will take five hours, while discharge will last up to 18 hours. In case of emergency, this energy has to be evacuated quickly or both the coil and the detectors could be damaged. Therefore, a fast discharge in 50 m resistors is used with the decay time is then 280 s. The maximum field of 4 T have been successfully obtained in the magnet test several times since 2006 August. The magnetic flux is returned through a saturated iron yoke, which is split into five barrel rings and two endcap discs housing the muon chambers. Muons are particles with minimal ionizing power, which make them particularly easy to separate from the other particle types. More details about the CMS detector can be found in (Chatrchyan, 2008).

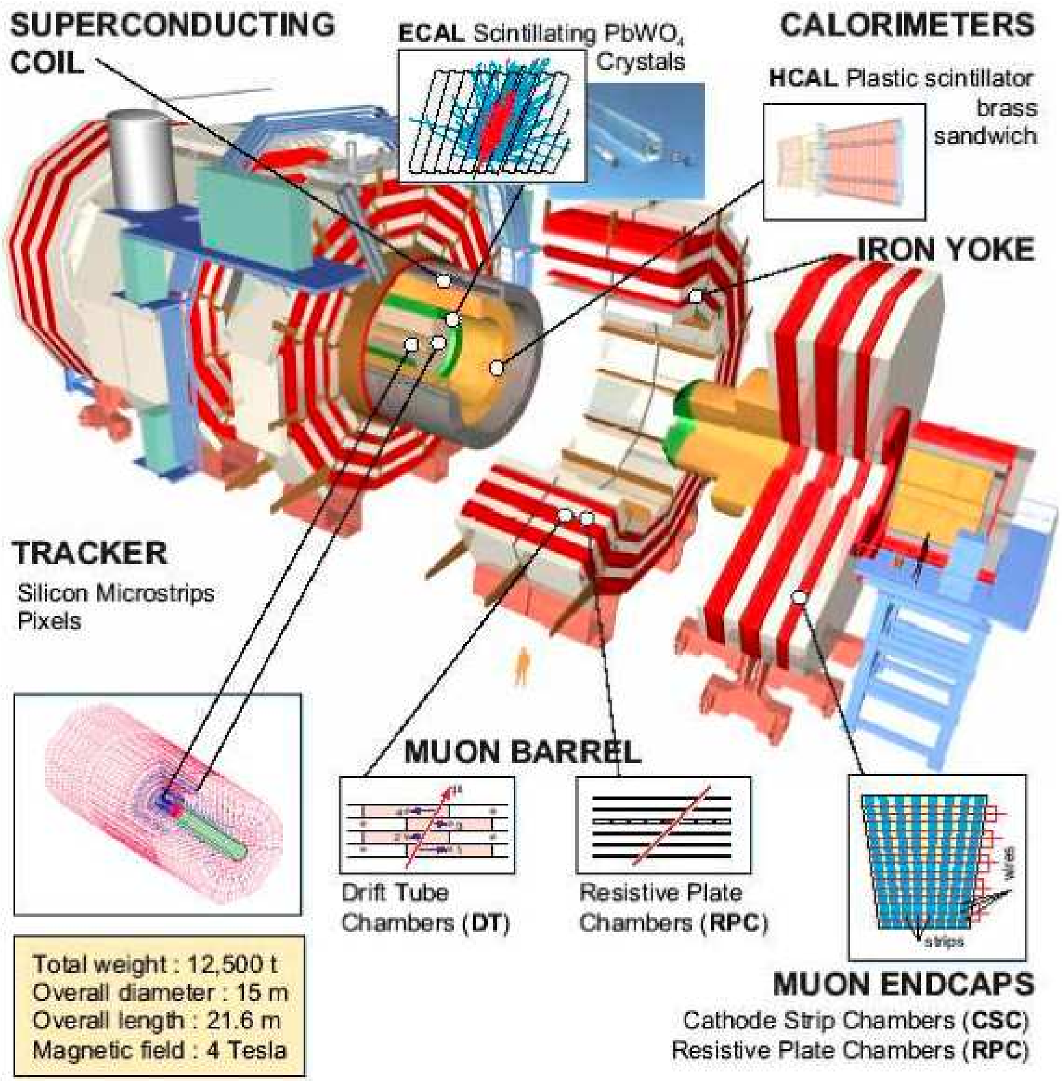

Figure 3.5. Schematic view of CMS Detector.

3.4 Coordinate conventions in CMS

Proton collisions at high energies manifest themselves as inelastic collisions of composite objects, where the actual collisions happen between the constituent quarks and gluons, also called partons. These partons carry a fraction x_1 and x_2 of the total proton momentum. The fractions are statistically distributed according to the so-called parton density functions, which are rigorously introduced in Section 3.1.2. Hence, in general, x_1 and x_2 are not equal and the rest frame of the hard collision will be boosted along the beam line with respect to the lab frame. The reconstruction of the boost of the system on a collision-by-collision basis requires the full reconstruction of the remnants of the colliding protons, which is in practise not possible because of the presence of the beam pipe and instrumentation along the beamline. Because of the unknown energy balance along the beamline, proton collisions are usually studied in a more convenient coordinate frame. The z axis is placed along the beamline, and the x and y axes hence define the transverse plane, perpendicular to the beam. The spherical coordinates (r,θ,ϕ) are replaced with (r,η,ϕ), where r is the radial distance, ϕ is the azimuthal angle in the transverse (x,y) plane, θ is the polar angle measured from the z axis, and the pseudorapidity η is defined as

$$\eta = -\ln[\tan\frac{\theta}{2}] \tag{3.8}$$

The advantage of this coordinate frame is the Lorentz invariance of transverse quantities and differences in η under Lorentz boosts along the beamline. As a consequence, a solid angle in (η,ϕ) space is also invariant under longitudinal boosts.

3.4.1 The Tracking System

The CMS tracking system is an all-silicon detector (Bayatian, 1998; Bayatiyan, 2000). It contains both the strip detector and pixel detector. The inner most component is the pixel detector, consisting of three barrel layers and two end disks on each side. The pixel detector provides precise measurements of space points to allow effective pattern recognition in multitrack environments near the LHC interaction point. The end disks,

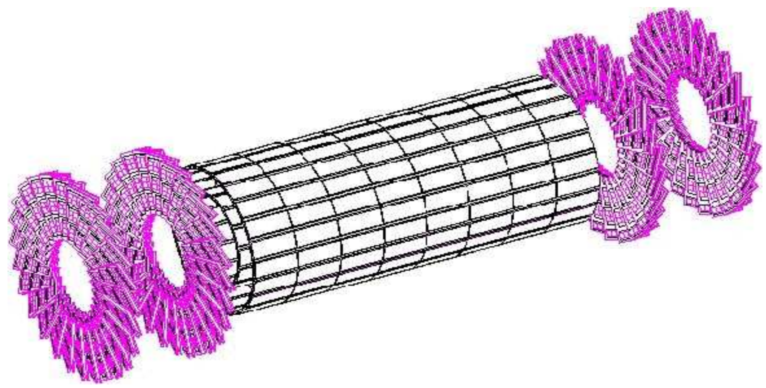

Figure 3.6. The CMS Pixel Detector is shown in 3D.

known as the Forward Pixel detector, was located at a mean distance of 34.5 cm and 46.5 cm longitudinally from the interaction point. One of the main challenges in the design of the pixel detector is the expected high level radiation in LHC environment. The tracker has to fulfill the condition to be radiation hard as well as to offer high granularity. The tracker occupied a cylindrical volume with the length of about 5.4 m and a diameter of 2.4 m. The large volume of the tracker together with the 4 T magnetic field allows a significant bending of the track and therefore an accurate momentum measurement of high energetic charged particles. Placed around the interaction point, the CMS Tracker consists of silicon pixel detectors and silicon micro-strip detectors. Three pixel layers and ten silicon strip layers were installed in the barrel, and two pixel layers, three inner and nine outer forward discs of silicon detectors will be placed in each endcap.

Closest to the beam pipe are the three barrel layers of the pixel detectors. Perpendicular to them, two pixel discs will be positioned at each side (see Figure 3.6). A compromise between cost and accuracy lead to a square pixel shape of 150×150 μm^2. About 16000 readout chips are bump-bonded to the detector modules, adding up to about 44 million readout channels. The pixel detectors will allow a precise vertex reconstruction and provide the first step in the track reconstruction. The expected pixel hit resolution is $\sigma_{r\phi} < 10m$ and $\sigma_{rz} < 17$m. The efficiency to find three pixel hits on a track (in the three-layer geometry) is above 90 % for $|\eta| < 2.2$. The silicon strip detector consists of four tracker inner barrel (TIB) layers, six tracker outer barrel (TOB) layers and in each endcap nine tracker endcap (TEC) layers. On each side of the TIB, there are three tracker inner discs (TID) installed. The expected hit resolution for the silicon strip is $\sigma_{r\phi}$= 10-60 μm and σ_{rz}= 500 μm. Combining these numbers, the expected CMS tracking resolution ranges from $\Delta p_T/p_T^2$ = 0.015% for $|\eta| < 1.6$ up to $\Delta p_T/p_T^2$ = 0.06% for $|\eta|$= 2.5. Thus, a muon with a p_T of 100 GeV can be reconstructed with an accuracy of 1.5 GeV for $|\eta| < 1.6$. To protect the silicon detectors from aging due to the high radiation flux, which causes an increase in leakage current, the full silicon tracker will be operated at 10 °C. A thermal shield placed outside of the tracker volume provides insulation while a cooling system extracts 60 kW of heat dissipated by the front end electronics.

3.4.2 The Electromagnetic Calorimeter

The electromagnetic calorimeter (ECAL) (Bayatian, 1997a) is placed around the tracker. The design of the ECAL is driven by the requirement to provide an excellent di-photon mass resolution for the $H \to \gamma\gamma$ decay mode. A crystal-based scintillating calorimeter (as opposed to sampling calorimeters) offers the best performance for energy resolution from electrons and photons, since most of the energy is deposited inside the active volume. The choice of lead tungstate ($PbWO_4$) was motivated by its fast light decay time, its small Moliere Radius, its high density of 8.28 g/cm^3 (allowing a compact design) and its good radiation resistance, as the crystals have to endure very high radiation doses. After 15 ns, already 60% of the light should be emitted by the crystals (compared to 300 ns for BGO crystals, which were used e.g. in L3), and 100 ns should be enough to collect the emitted light. The small Moliere Radius of 2.19 cm allows for lateral shower containment inside a few crystals.

Furthermore, $PbWO_4$ is a fast scintillator compatible with the high event rate at LHC. The crystal dimension is roughly 2.2 cm x 2.2 cm x 23 cm for the barrel crystals and 2.5 cm×2.5 cm×22 cm in the endcaps. This corresponds to a granularity of $\Delta\phi \times \Delta\eta$ of 0.0175×0.0175 in the barrel. The CMS Detector size of the crystals corresponds to about 26 radiation lengths. For 35 GeV electrons, about 94% of the electron energy is contained a 3×3 crystal array, and 97% in a 5×5 crystal array. A drawback of the lead tungstate is its relatively low light yield, which is about 14 times smaller than the one from BGO crystals. This requires strong amplification within the photodetector at the end of the crystal. The

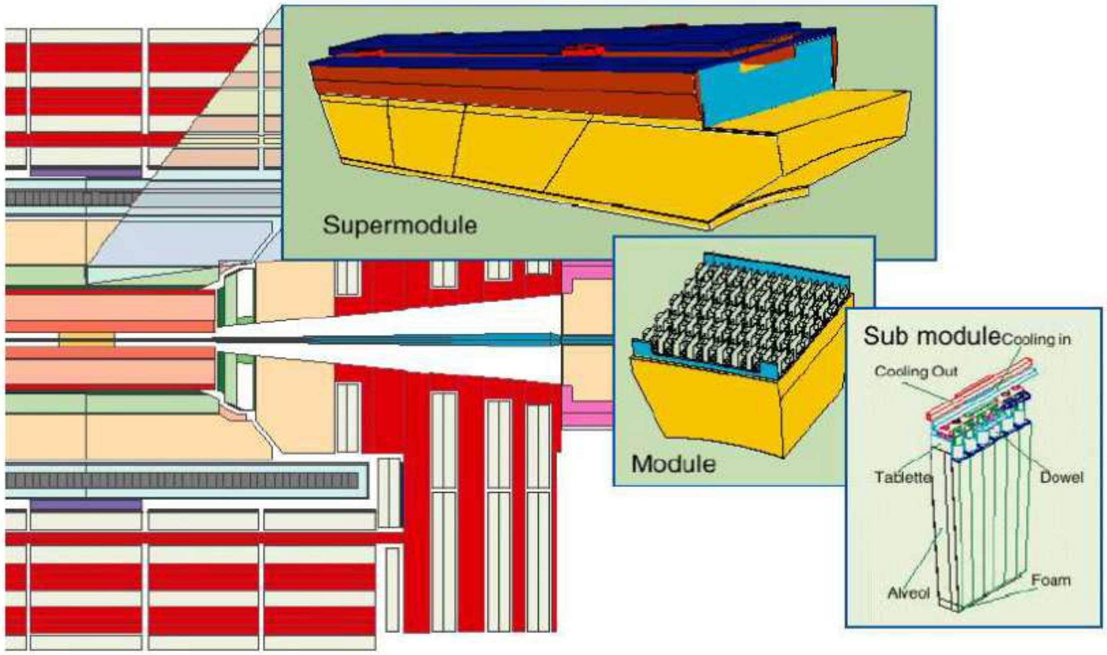

Figure 3.7. The Supermodules, Modules and Submodules of the ECAL detector.

photodiodes have to operate in a rather hostile environment. Photomultipliers can not be used in such a strong magnetic field, and thus avalanche photodiodes, which can operate in strong transverse magnetic fields, were used in the barrel part of the calorimeter, while vacuum phototriodes were used in the endcaps, in order to cope with the higher levels of radiation. The ECAL is built out of $\sim$ 76000 individual crystals. The crystals are mechanically organized into modules and supermodules. In the barrel, the crystals are tilted in the transverse plane by 3 degrees, in order to minimize the probability that particles pass through the inactive area between crystals. The barrel crystals are assembled into 36 supermodules, each consisting of 4 modules with 50 submodules in the first module and 40 in the remaining three modules. This is shown in Figure 3.7. Those submodules are composed of 2$\times$5 crystals assembled into a fiberglass alveolar structure. In total, the barrel contains 61200 crystals. The supermodules have a wedge shape and subtend an angle of 20 degrees. The design guarantees a maximum distance between crystal faces of 0.4 mm within a supermodule and 0.6 mm across two submodules. A crack of about 6 mm is expected between two supermodules in ϕ and 6.8 and 7.8 mm between two modules at different η. The endcap ECAL is built up of identical 5 x 5 crystals, To ensure a hermetic design, the crystals will be oriented toward a point located 1.3 cm away from the interaction point. Thus the crystals are off-pointing to a similar extend as the barrel crystals. A preshower built in front of the endcap calorimeter ($|\eta| > 1.653$) should allow to reject high p_T π^0s by measuring the transverse profile of the electromagnetic shower after roughly three interaction lengths. The preshower is built like a sampling calorimeter with lead as absorber and a layer of silicon strip sensors for the measurement of the charged particles created in the shower. Strips from one plane are orthogonal to these of the second plane, which gives a two-dimensional position measurement with a precision of 300 μm for a 50 GeV π^0. The energy resolution can be parametrized as a function of the energy as

$$\frac{\Delta E}{E} = (a/\sqrt{E})^2 + (b/E)^2 + c^2 \tag{3.9}$$

The first term is the stochastic term, the second the noise, and c^2 is the constant term. The stochastic term includes contributions from photostatistics and fluctuations in the shower containment. The noise term incorporates contributions from the electronics readout and pile-up, and therefore depends on the luminosity. The design goal is to reach a stochastic term of $a = 2.7\%$ in the barrel and $a = 5.6\%$ in the endcap, a constant term of $c = 0.55\%$ and a noise term of b = 210 MeV in the barrel and 245 MeV in the endcap (at high luminosities).

3.4.3 The Hadronic Calorimeter

The Hadronic Calorimeter (HCAL) (Bayatian, 1997b) is a sampling calorimeter with copper absorber plates interplaced with 4 mm thick plastic scintillators. Copper was chosen for its relatively low Z, which minimizes multiple scattering for muons. It is also a non-magnetic metal, which is important since the calorimeter is placed within the 4 T solenoid. The produced blue scintillation light is captured and shifted toward green in wavelength shifting fibers and then transported to photodiodes. The calorimeter granularity of $\Delta\eta \times \Delta\phi$ was chosen with the goal that highly boosted dijets from W and Z decays can still be distinguished. In order to get a good measurement of the missing transverse energy, jets are expected to be reconstructed up to a rapidity of 5. The hadronic calorimeter is designed to measure the direction and energy of hadrons produced either as remnants of the proton, during the hadronization of quarks and gluons from the hard process, or from tau decays. By combining all calorimetric activity, a missing transverse energy is determined. The missing transverse energy is the only variable sensitive to neutrinos and other weakly interacting particles that could be a sign for new physics. Since the longitudinal momentum is not measured in hadron collisions (as it is parallel to the beam axis) only transverse quantities (e.g. transverse momentum or transverse mass) are generally considered.

The HCAL is the last detector inside magnetic coil and therefore it surrounds the ECAL as well as the tracking system. The HCAL provides the energy and direction measurements of the jets in conjunction with ECAL system. It also measures the total visible transverse and missing transverse energy due to hermetic coverage. The hadron calorimeter will also help in the identification of electrons, photons and muons as it is used with the electromagnetic calorimeter and the muon system. The HCAL consists of three subdetectors: barrel and endcap detectors cover up to psuedorapidity range $|\eta| < 3.0$ and is placed in 4 T magnetic field, forward calorimeters (HF) which are located outside the magnet return yokes cover up to $|\eta| < 5.0$. The barrel is 9m long and covers a pseudorapidity region $|\eta| < 1.48$. The endcaps are 1.8 m thick, and cover the pseudorapidity range $1.48 < |\eta| < 3$. The thickness corresponds to at least ten nuclear interaction lengths, enough to contain a large fraction of the hadronic showers.

The layout of the HCAL is given in Fig. 3.8. The HCAL is a sampling calorimeter in which active and passive layers alternate. The passive material that acts as an absorber is chosen as brass in the central region, it is non-magnetic and low Z material to prevent it from magnetization in high magnetic field and avoid multiple scattering of muons (affect muon reconstruction) inside the HCAL. The active material is plastic scintillator and readout with wave-length shifting fibers. In the pp collisions there will be frequently boosted objects that will later decay as two close jets. Reconstruction of these two jets separately requires a small lateral granularity. The sufficient lateral granularity is introduced by reading out the calorimeter as towers with a size of $\Delta\eta \times \Delta\phi$= 0.087 for $|\eta| < 2.0$, providing a matching with ECAL and muon chamber cell size. Although HCAL is designed to contain all of the hadronic showers the thickness of the calorimeter at $|\eta| = 0$ is about 5 nuclear

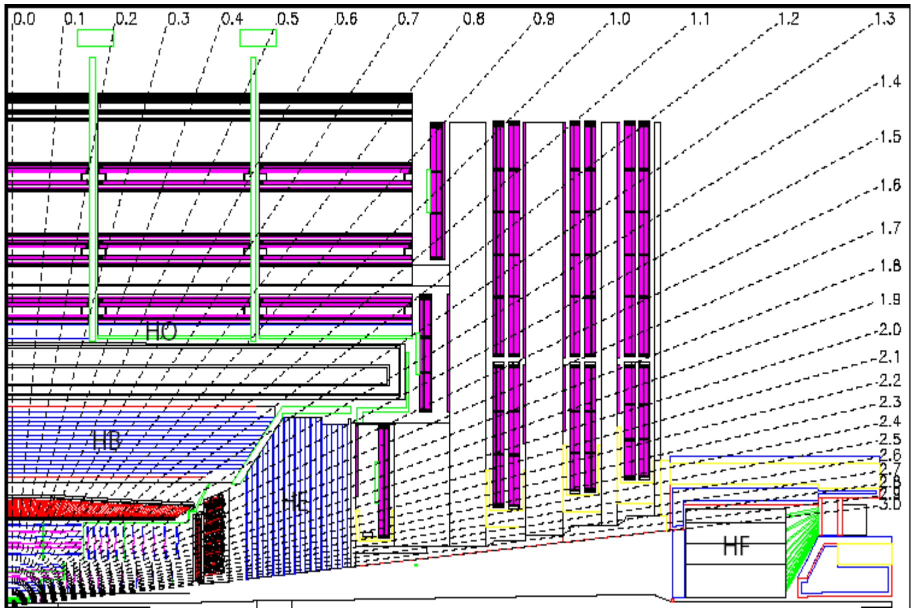

Figure 3.8. The HCAL Side view.

interaction lengths for charged pions and is not enough to contain the low-energy tails of hadronic shower development. This causes mismeasurements of the jet energies and therefore effects the missing transverse energy measurements which is very sensitive for new physics discoveries. To avoid that problem and catch the tails of energy distribution in the hadronic showers, a layer of scintillator (referred as HO, hadronic outer calorimeter) is placed between super-conducting coil and muon chambers up to $|\eta| < 1.4$ (See Figure 3.8). The HF detectors are located at a distance of 11 meters from the interaction point to extend the coverage up to $|\eta| < 5$. The HF calorimeters reduce the fake missing transverse energy measurements with the increased coverage and also help identification and reconstruction of high-p_T forward jets.

3.4.4 The Magnet

In the hadron colliders often muons are present in the final state, therefore selection of interesting events over ten times bigger background events is crucial. Establishing very strong magnetic field enable to trigger for such interesting events. Bending the trajectory of the muons (and other charged particles) gives momentum measurements and charge information. The design of the magnet system also defines the design of the detector. The CMS experiment has chosen to use a solenoidal type (see Figure 3.9) of magnetic field to achieve a compact design with strong field inside the coil (Bayatian, 1997c). The tracking system, electromagnetic and hadronic calorimeters (except from HO) are accommodated by the inner coil. 4 T magnetic field produced by the superconducting magnet system bends the particle trajectories in the transverse plane and therefore provides precise measurements of transverse momentum with the combination of central tracking system and muon chambers. There is a drawback of having strong field: charged particles with low momentum do not reach to the calorimeters in the barrel region or can be separated from other particles and hit calorimeter cells resulting out of cone particles in the jet reconstruction algorithms. The relation between the curvature of charged particle trajectory with the magnetic field strength is given by

$$P_T = 0.3 \times B \times R \tag{3.10}$$

where P_T is the transverse momentum of the particle in GeV/c, B is the magnetic field in T and R is the radius of curvature of the particle in meters. Particles that have less than $\approx$ 0.9 GeV/c transverse momentum can not reach to the calorimeters. The CMS superconducting solenoid is 13 m long and has a 5.9 m inner diameter. The ratio length/radius of the solenoid and the high field allow efficient muon detection and measurement up to a η of 2.4. The magnetic flux is returned with a 1.5 m thick iron yoke (return yoke) where the field is 1.8 Tesla. The return yoke is divided into barrel and endcap yoke. The barrel yoke is designed as a 13.2 m long 12-sided cylindrical structure.

3.4.5 Muon system

The CMS muon system (Bayatian, 1997d) is placed outside the magnet, embedded in the iron return yoke to make full use of the 1.8 T magnetic return flux, a schematic view of this subdetector is shown in Figure 3.10. It plays an essential role in the CMS Trigger system, because high p_T muons are clear signatures of many physics processes. The main goal of this system is to identify muons and measure, when combined with the Tracker, their transverse momentum p_T . Three different and complementary detection

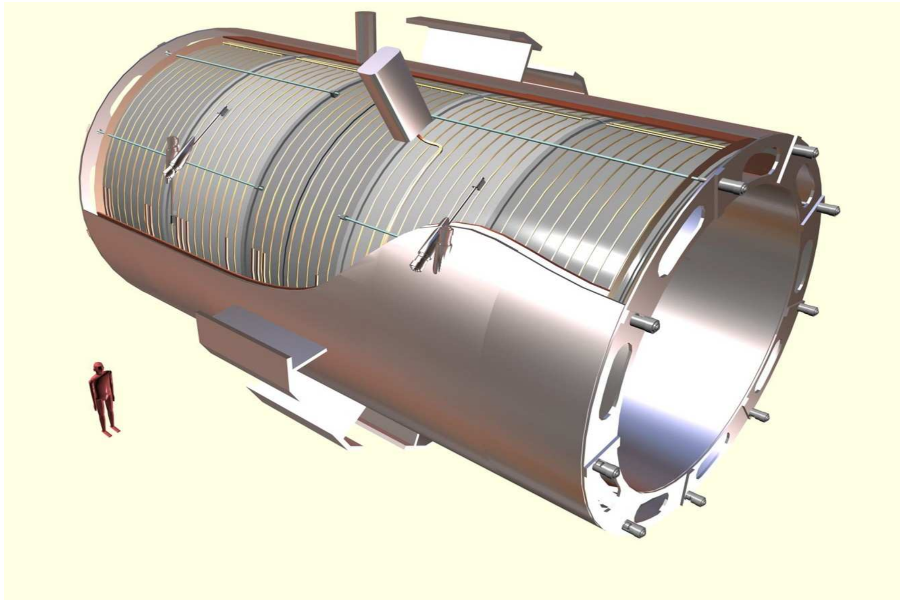

Figure 3.9. The CMS superconducting magnet.

technologies have been used: Drift Tube Chambers (DT) in the barrel region ($0 < |\eta| < 1.1$), Cathode Strip Chambers (CSC) in the endcap region ($0.9 < |\eta| < 2.4$) and Resistive Plate Chambers (RPC) in both barrel and endcap regions.

In the barrel region, the expected occupancy is low ($<$ 10 Hz/cm^2), allowing for the use of drift tubes as detection element. In Figure 3.10 a layout of the CMS Barrel Muon Drift Tube Chamber is shown. The amount of iron in the return yoke was dictated by the decision to have a large and intense solenoidal magnetic field at the core of CMS. Two detector layers, one inside the yoke and the other outside, would be insufficient for reliable identification and measurement of a muon in CMS. Therefore, 2 additional layers are embedded within the yoke iron. In each of the 12 sectors of the yoke there are 4 muon chambers per wheel, labeled MB1, MB2, MB3, and MB4 (Figure 3.10). The yoke-iron supports that are between the chambers of a station generate 12 unavoidable dead zones in the ϕ coverage, although the supports are placed so as not to overlap in ϕ.

The chamber design is very redundant: each chamber is made up of twelve layers of drift tubes, packed in three independent subunits called superlayers (SL), two of them with the anode wires parallel to the beam axis for measuring the transverse coordinates (r, ϕ) and the remaining SL orthogonal to the other two for determining the longitudinal

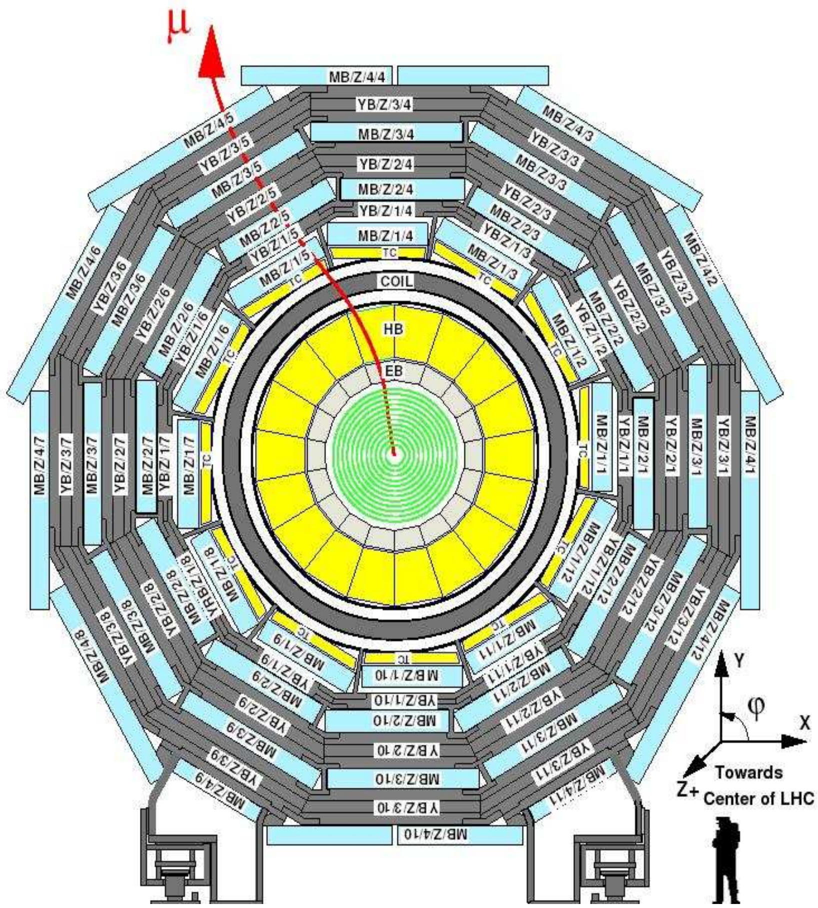

Figure 3.10. Layout of the CMS barrel muon DT chambers in one of the 5 wheels. The chambers in each wheel are identical with the exception of wheels -1 and +1 where the presence of cryogenic chimneys for the magnet shortens the chambers in 2 sectors. Note that in sectors 4 (top) and 10 (bottom) the MB4 chambers are cut in half to simplify the mechanical assembly and the global chamber layout.

coordinate (z). The Drift Tubes are parallel aluminum plates insulated from perpendicular "I" shaped aluminum cathodes by polycarbonate plastic profiles. The anodes are 50μm diameter stainless steel wires placed between the cathodes. The internal volume is filled with a gas mixture of Ar(85%) + CO2(15%) at atmospheric pressure, because this gas is non-flammable and can be safely used in underground operations in large volumes, as required in CMS. The single hit position resolution is better than 200 μm at nominal voltage values. The position and angular resolution of the full chamber are 98 μm ($r\phi$) and 570 μrad respectively. Due to the larger occupancy of the endcap regions, from few Hz/cm^2 to more that 100 Hz/cm^2, and the intense and non uniform magnetic field, Cathode Strip Chambers (CSC) have been chosen in this region.

The CSCs are multiwire proportional chambers with one cathode plane segmented in strips running orthogonal to the wires. The chosen gas mixture is $Ar(40\%)$ + $CO_2(50\%)$ + $CF_4(10\%)$. In the CMS endcap muon system each chamber is formed by six trapezoidal layers, with strips in the radial direction for a precise measurement of the azimuthal direction. The single plane spatial resolution is between 150 and 350 μm depending on the location of the hit on the strip position. The estimated overall chamber resolution is calculated to be 80-85 μm independently of the hit position. Resistive Plate Chambers are installed both in the barrel and endcap regions. They have a limited spatial resolution but thanks to their fast response ($\sim 3ns$) they are used as a dedicated Trigger subsystem, mainly for unambiguous bunch crossing identification. The RPCs used in CMS are double gap RPCs filled with a $C_2H_2F_4$ and C_4H_{10} gas mixture, with common pickup strips in the middle and work in avalanche mode to sustain the high event rate.

3.5 Triggers

The LHC bunch crossing rate is 40 MHz. About 20 inelastic pp events are produced at each bunch crossing at the design luminosity of 10^{34} cm^{-2}s^{-1} . This produces $\approx$ 1 MB of data at each crossing. Only a small portion of the data can be kept since current storage capacity is limited to about $\approx$ 100 MB/s or about 100 crossings per second. Therefore, a Trigger and Data Acquisition(DAQ) system is required that selects the interesting data with a rejection factor of $\approx 10^6$. The CMS trigger system consists of a level-1 (L1) trigger followed by a high level trigger (HLT) performed completely at the software level. The total time needed for the L1 trigger to come to a decision to store or not to store the data is 3.2 μs. This is mainly determined by the time needed for a signal to be transferred from the front-end electronics to the L1 logic system, since the time needed for the trigger calculations is less than about 1 μs. The data waits in the pipe-line buffers for 3.2μs/25 ns = 128 bunch crossings before it is decided that it will be kept or not. The L1 trigger reduces the event rate to 100 kHz for the design luminosity. The L1 trigger uses calorimeter, muon system, and global (combination) triggers, that combine the data from calorimeters and the muon system. The trigger-primitive objects (photons, electrons, muons and jets) are constructed using the detector systems. These objects are created only

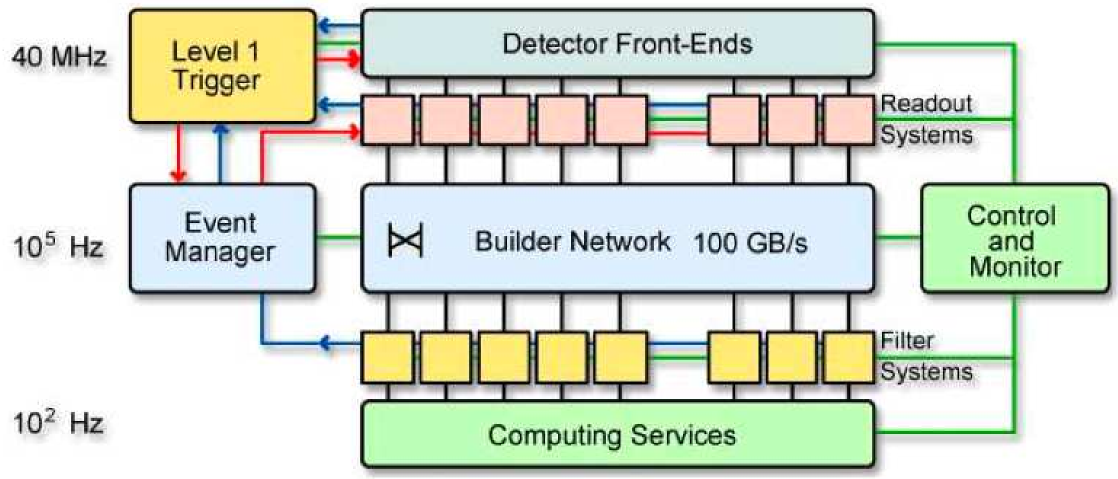

Figure 3.11. The CMS DAQ system (Bayatiyan, 2006).

if the p_T or E_T are above some thresholds. Also, the sum E_T and missing E_T which are determined globally, are included as trigger primitive objects.

HLT reduces the 100 kHz L1 event rate to $\approx$ 100 Hz. All calculations beyond L1 are performed in a single filter farm of about 1000 dual-CPU computers. The HLT is highly flexible when it comes to changes in the decision trees. HLT first does partial event reconstruction using the calorimeters and the muon system. At this stage, it refines the objects created at L1. Then it combines the data from pixel and tracker for further rejection. The design of the HLT makes it possible that the offline reconstruction algorithms can be used in the HLT. The schematics of the CMS trigger and DAQ system are displayed in Figure 3.11. For further details, see the trigger CMS technical design reports (Bayatian, 2006; Level-1 Trigger, 2000; DAQ and HLT TDR, 2002).

4. MATERIAL ANALYSIS IN TEST BEAM 2006

4.1 Introduction

In this chapter, some analysis performed during the Test Beam 2006 (TB2006) will be discussed. The Test Beam 2006 mainly tested performance of the combined barrel system of the electromagnetic and hadronic calorimeters. In this particular analysis, uniformity of the energy on the combined system and dead material measurement between electromagnetic barrel (EB) and hadronic barrel (HB) system were studied. Section 4.2 summarizes test beam setup, Section 4.3 discusses beam clean-up and particle identification. Section 4.4 discusses energy uniformity of the calorimeters. Finally section 4.5 outlines the method for the material measurement and shows the results.

4.1.1 Energy Measurements

The energy of a particle can be destructively detected by initiating a series of reactions whereby the total particle kinetic energy is deposited in the detector. The energy is locally deposited so that the particle position is measured to a degree of accuracy specified by the transverse fluctations in the energy deposition. The particle energy is measured to a level of accuracy specified by the uniformity of the detector medium (the ”constant term”) and the level of active sampling of the detector with respect to total volume (the ”stochastic term”). Thus, the calorimetric technique provides a measurement of the incident particle momentum. Calorimetry itself refers to the destructive detection of the energy of an incident particle. The idea is to absorb all the energy in a detecting medium and by that means to record the energy of the incident particle. Redundant measurements of charged particle momenta can be done by first tracking them in a magnetic field and then absorbing them in a calorimeter. This redundacy is often very usefull in cleaning up the backgrounds which are always present in the study of a rare process.

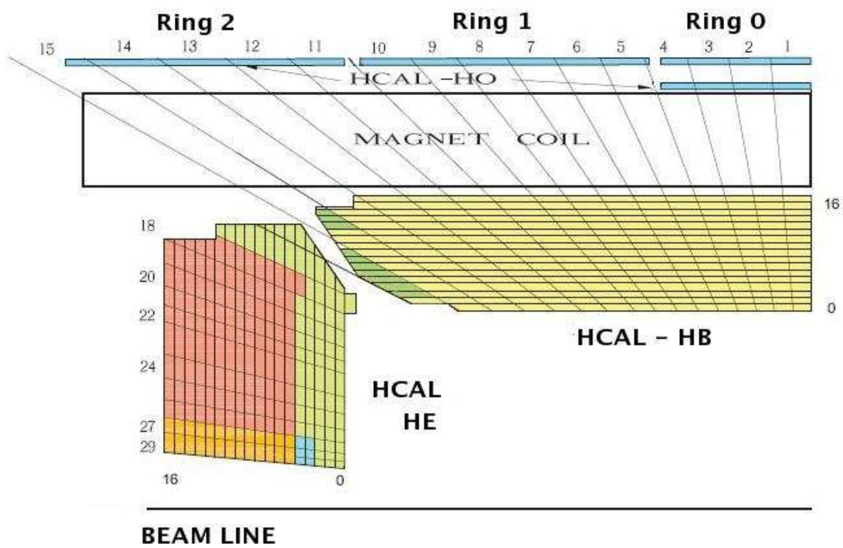

Figure 4.1. Location of the ECAL and the HCAL detectors (quarter slice-longitudinal cross section) in and around the CMS magnet.

4.2 Test Beam Setup

The combined ECAL+HCAL calorimetric system for CMS has been tested in 2006 at the H2 beam line at the CERN SPS. The H2 beam line setup is displayed in Figure 3.1. The tests were done in high (10-350 GeV) and low-energy (1-9 GeV) pion, electron and muon beam configurations. The CMS calorimeters have distinct hadronic (HCAL) and electromagnetic (ECAL) systems. The calorimeters are divided into the barrel (HB and EB) and the end-cap (HE, EE and pre-shower, ES) sections inside a cryostat of 5.9 m inner diameter, containing a superconducting solenoid coil providing a 4 T magnetic field. The electromagnetic calorimeter (ECAL) uses lead tungstate (PbWO4) crystals with coverage in pseudorapidity up to η <3.0. The scintillation light is detected by silicon avalanche photodiodes (APDs) in the barrel region and vacuum phototriodes (VPTs) in the endcap region. A preshower system is installed in front of the endcap ECAL for π^0 rejection. The ECAL is surrounded by a brass/scintillator sampling hadron calorimeter (HCAL) with coverege up to η <3.0. The scintillation light is converted by wavelength-shifting (WLS) fibers embedded in the scintillator tiles and channeled to photodetectors via clear

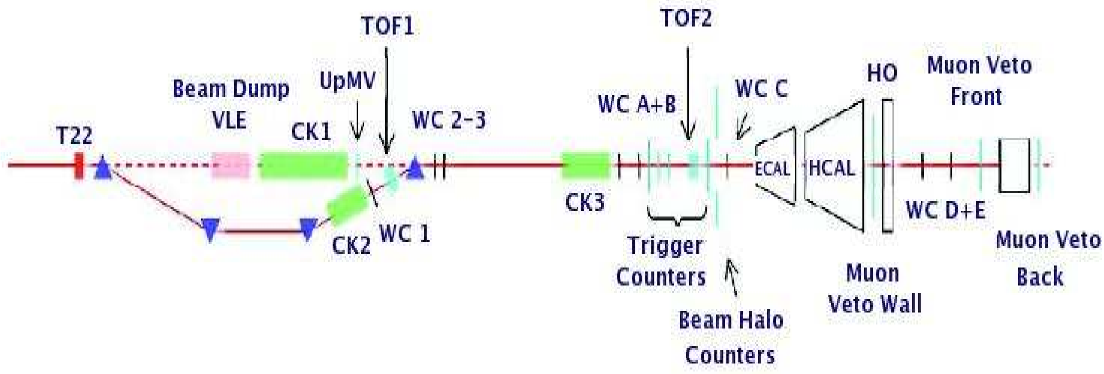

Figure 4.2. Layout of the testbeam line at H2.

fibers. This light is detected by photodetectors (hybrid photodiodes, or HPDs) that can provide gain and operate in high axial magnetic fields. The HB design maximizes the number of interaction lengths (λ_I) inside the cryostat and is limited to 5.8λ_I at η = 0. This central calorimetry is complemented by a tail-catcher in the barrel region (HO) ensuring that hadronic showers are sampled with nearly 11 hadronic interaction lengths (Archaya, 2006). There are also two very forward calorimeters (HF) made of iron and quartz fibers (Abdullin, 2008). Figure 4.1 shows the calorimeters inside and around the solenoid coil.

In the beam line, there are 4 scintillator counters (S1-4) and 4 beam halo veto counters, which have 7$\times$7 cm holes in their centers (BH1-4). There are three Cerenkov counters (CK1-3) and two time-of-flight (TOF1-2) counters dedicated to particle identification. Only CK2 and CK3 were used in the test beam experiment. CK2 is filled with CO_2 and CK3 is filled with Freon gas. As can be seen from the figure μ4.2, there are several wire chambers in various locations in the beam line. Just behind HB1 there are 8 muon veto counters (VM1-8) and far behind the calorimeters there are two muon veto detectors, namely muon veto front (VMF) and muon veto back (VMB), which is separated from VMF by a thick absorber to achieve better muon identification. The HCAL part of the calorimeter system consisted of two HB wedges (HB1 and HB2) corresponding to 8 segments covering 40 degrees in azimuth, four HE segments covering about 20 degrees

Figure 4.3. EB,HB and HE on the rotatable table. The white line represents the beam.

in azimuth, and the Outer Barrel Calorimeter HO. The ECAL part used in the test beam is one of the 36 supermodules, namely SM9. Both ECAL and HCAL detectors were equipped with the final CMS production electronics. The entire calorimeter system was placed on a rotatable table whose pivot mimics the interaction point at LHC as shown in Figure 4.3.

4.3 Beam Clean-up and Particle Identification

To get a clean beam, only single-hit events in the scintillators S1, S2 and S4 were used in the trigger. Moreover, beam halo events and wide-angle secondaries were removed using the beam halo counters (BH1-4). VMB was used in later analysis to tag the muons in the high energy beam. To identify the muons in the low energy beam configuration (VLE), VMB, VMF and the muon veto counters (VM1-8) were utilized. At low beam momentum, electron contamination in the π^- (pion) beam was dominant. Therefore, in addition to CK2, which was dedicated to electron tagging at VLE, also CK3 was used to remove the electrons in the π^- beam since CK3 could identify pions down to 4 or 5 GeV/c, depending on the pressure setting used during the data taking. Protons/antiprotons and kaons in the pion beam were identified using time-of-flight counters and CK3.

4.4 Calibration of Calorimeters

Both the EB and HB calibrations were carried out with 50 GeV/c e^{-}s. The e^{-} beam was directed at the center of each HB tower. Similarly, the EB calibration data were collected by pointing the beam to a selected set of crystals that formed a tight grid pattern. For the EB, the signals from 7×7 crystals, and for the HB the signals from 3×3 towers were summed. In the case of the HO, the total energy was estimated by adding signals from 3×2 towers. The response of each HB scintillator tile of each layer was also measured by using a 5-mCi ^{60}Co moving wire radioactive source (Adams, 2003). The HO modules were first calibrated by 150 GeV/c μ^{-} beam. A clear peak was observed in Ring 0 and Ring 2. In Ring 1 the peak was measurable but not as cleanly separated from pedestal. Next, the HO energy scale was determined by 300 GeV/c π^{-} beam impinging on tower 4 of the HB. For this measurement, it was required that the energy in the EB be less than 1.2 GeV. The energy scale was determined by requiring the best energy resolution in HB+HO, as measured by *rms* width, for the 300 GeV/c π^{-} beam.

4.5 Uniformity on Calorimeter Systems

Linearity of the calorimeter response depends on the instrintic e/h which is the conversion efficiency of electromagnetic and hadron energy to an observable signal (Yazgan, 2007). The linearity of the response of the combined system was studied for pions and muons with momenta 100 GeV/c. The interface region between ECAL and HCAL system has a significant effect on the energy response on the calorimeter systems. Uniformity study has been done by using π^{-} and μ beams at 100 GeV. In order to understand the boundary of ECAL module's response the ECAL was scanned in η and the boundary direction.

In the following discussion we consider two different samples of pion data. The first, which we refer to as MIP in ECAL pions, includes only pions which are minumum ionizing in ECAL, i.e do not interact in ECAL and begin interaction in HCAL. This sample is selected by requiring that energy deposition in ECAL is consistent with minimum ionizing deposition, i.e is less than 2.5 GeV. The second sample which refer to as the full pion sample, includes all pions, i.e interacting either in ECAL or HCAL.

Table 4.1. Masses, lifetimes and main decay modes for pions (W.-M. Yao, 2006).

Particle	Mass[MeV]	Mean Lifetime[s]	Main Decay Modes (Fraction)
π^+	139.57018 ± 0.00035	(2.6033 ± 0.0005) $\times 10^{-8}$	$\mu^+\nu_\mu(99.9877 \pm 0.00004\%)$ $e^+\nu_e(1.230 \pm 0.004 \times 10^{-4}\%)$
π	139.57018 ± 0.00035	(2.6033 ± 0.0005) $\times 10^{-8}$	$\mu^-\overline{\nu}_\mu(99.9877 \pm 0.00004\%)$ $e^-\overline{\nu}_e(1.230 \pm 0.004 \times 10^{-4}\%)$
π^0	134.9766 ± 0.0006	(8.4 ± 0.6) $\times 10^{-17}$	$\gamma\gamma(98.798 \pm 0.032\%)$ $e^+e^-\gamma(1.198 \pm 0.032\%)$

4.5.1 Calorimeter Response to Pions

The pions are the lightest mesons, and are therefore preferentially emitted in hadronic interactions, that can be composed of the Standart Model fundamental particles. They consist of up and down quarks and form a spin-0-triplet with two charged mesons, π^+ ($|u\overline{d}\rangle$), π^- ($|d\overline{u}\rangle$), and one neutral mesons, the π^0 ($\frac{1}{\sqrt{2}}$ ($|u\overline{u}\rangle - |d\overline{d}\rangle$)). Neutral pions quickly decay into two photons which share the parent π^0 energy. These photons then participate in the hadronic cascade as an electromagnetic component. Hadronic showers from pions are quite different from the pure electromagnetic showers created by electrons and photons. However, the non-electromagnetic component of the hadronic shower comes from particles produced in the hadronic interactions with the nuclei of the absorber material. These shower particles carry less than 20% of the shower energy (Wigmans, 2000), and in general, are not fast enough to create Cherenkov photons in quartz. The masses lifetimes and main decay modes for pions are shown in Table 3.1. When a particle traverses matter it will generally interact with that matter and lose (at least a fraction of) its energy. Due to the energy conservation, the traversed medium will be heated up in this process or more precisely, the constituents of the medium are excited into a higher energy state. The actual interaction process that occurs depends strongly on the energy and the nature of the traversing particle. The way muons (and other heavy particles like pions, protons, etc) lose their energy at a given particle energy is substantially different from the way electrons lose their energy due to their much greater restmass, although the mechanisms are the same (ionization and bremstrahlung). The muons lose their energy primarily through ionaziation. Bremstrahlung occurs only at very high energies ($E_{\mu} > 1TeV$). A typical muon loses only 1-2 MeV g^{-1}cm^{2} while transversing an absorber. This is much less than an electron of the same energy and therefore it takes very substantial amount of matter to absorb high energetic muons. Figure 4.4 shows the deposited 100 GeV pion energy on HCAL with MIP in ECAL with/without HO. As can be seen HO makes 10% difference on the average mean value. This is due to the fact that there is a leakage of energy to the HO since it is sitting behind the HCAL.

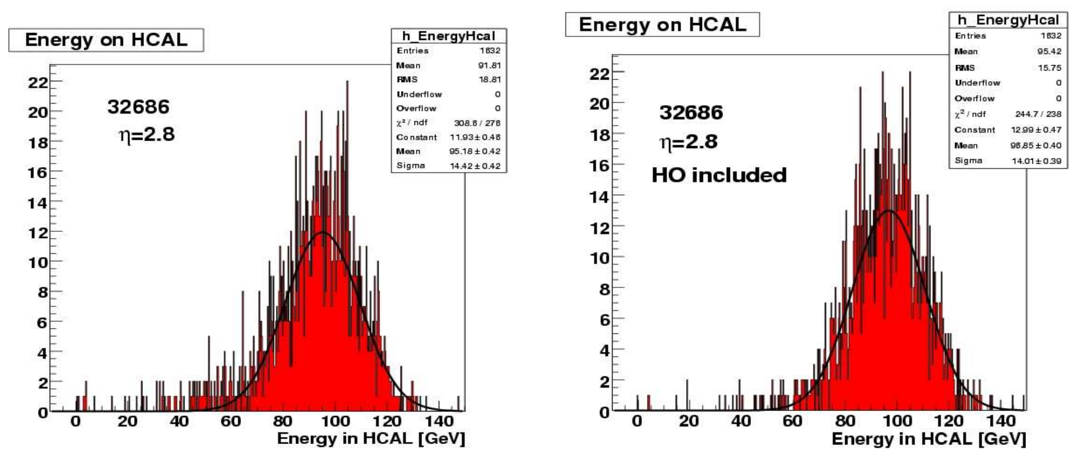

Figure 4.4. 100 GeV pion beam energy response on the HCAL.

Figure 4.5 shows the deposited pion energy at 100 GeV on ECAL without MIP in ECAL. As you can see η scan is shown in the $\phi = 12.8$ while boundary scan is shown in the $\phi = 13$ position. The position difference on the boundaries for both case is a result of the different ϕ positions of the π^{-} beam. The deposited energy on ECAL is $\approx$ 20 GeV. On the other hand, the pion beam energy response on the HCAL was measured. To get a reasonable response of the 100 GeV pions layer 12 (L12) correction was applied since TB2006 wire source results showed that L12 was flipped when it is connected to the RBX and L12 in $\eta 13, 14, 15$ tiles are not connected to the pixels of the HPD. It has also been

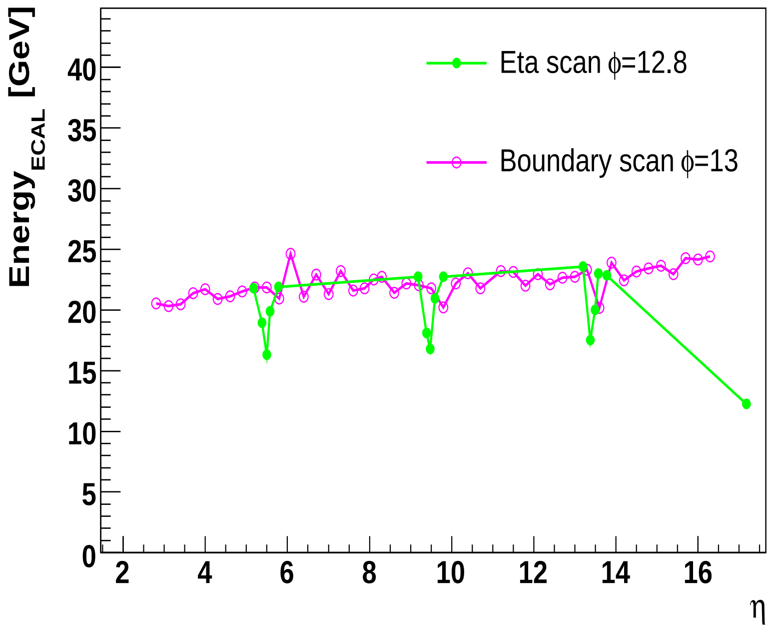

Figure 4.5. Pion energy deposited on the ECAL as a function of η for two different scans.

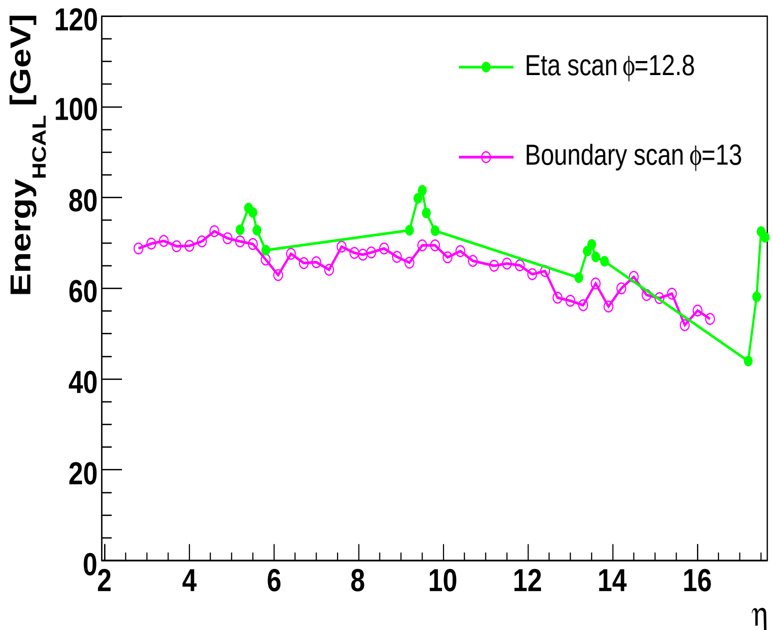

Figure 4.6. Pion energy deposited on the HCAL as a function of η for two different boundary scans.

noticed that there is a leakage to HO as expected about $\approx$ %4, it is shown in Figure 4.4. After all corrections the response of the 100 GeV pions on HCAL as a function of η is shown in figure 4.6. The response of pions on HCAL is decreasing on higher η range, especially in the region $\eta > 12$. The difference in ϕ positions could be a reason for this disharmony.

4.5.2 Calorimeter Response to Muons

Muons traversing homogenous calorimeters lose kinetic energy through the same mechanism as the shower particles produced in electromagnetic shower development, exciting atoms and molecules of the detector medium. Usually, the muons easily penetrate these detectors, losing only a small fraction of their energy in the process. Muon response on HCAL with the 100 GeV π^- data , in ϕ=12.8 direction is shown in Figure 4.7. To choose clean muon events proper scintillator and beam halo cuts were applied in 1$\times$2 towers.

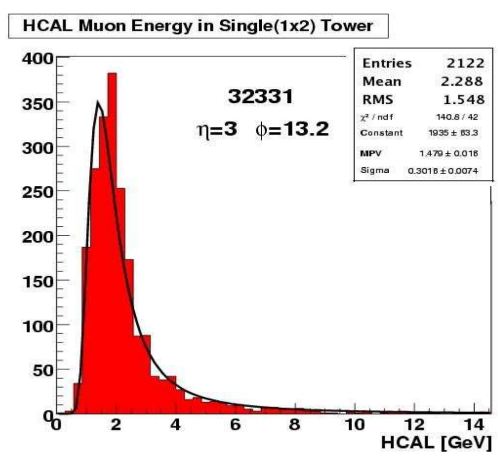

Figure 4.7. Muon energy on HCAL.

4.6 Material Analysis

The ECAL/HCAL interface region effects the combined system in two different ways.

- The magnetic field bends the shower of low energy particles outside the energy

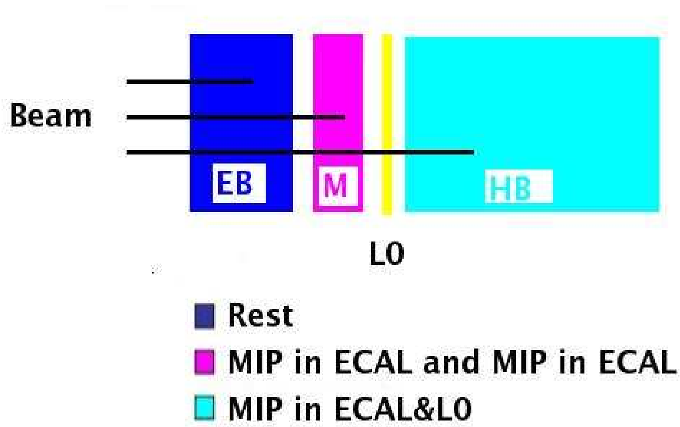

Figure 4.8. First interaction point illustration.

reconstruction cone.

• The dead materials (mechanic structures, electronic, cables etc.) These effects will have an influence on the hadron and jet energy resolution on the electron and photon identification.

In order to measure the amount of the material between ECAL crystals and HCAL 100 GeV pions are identified as first interaction point in ECAL, HCAL and in between respectively by using MIP in ECAL and MIP in ECAL/L0. It is illustrated in Figure 4.8. Once pions going through ECAL without interaction, a half of pions interacted in material between crystals and L0, and rest in HCAL.

Figure 4.9 shows the location of the first interaction point of the pions. The fraction of the events in different part of the test beam setup. As you can see statistically $\approx$ %60 of the pion events interacted in ECAL, $\approx$ %20 in HCAL and the rest interacted in both ECAL and L0. The pion particles decay dominantly to the electron and positrons and this weak interaction happens in mostly in the electromagnetic calorimeters. These numbers will be used to calculate the interaction length in material. Ideally, if the thickness of the material is constant in radial direction similar to the scintillators in HB, particles at higher η range see more material because of the incident angle of the beam. This information was proved in the figure 4.10. It shows that the thickness of material is constant in radial direction, so particles at higher η see more material because of the incidence angle.

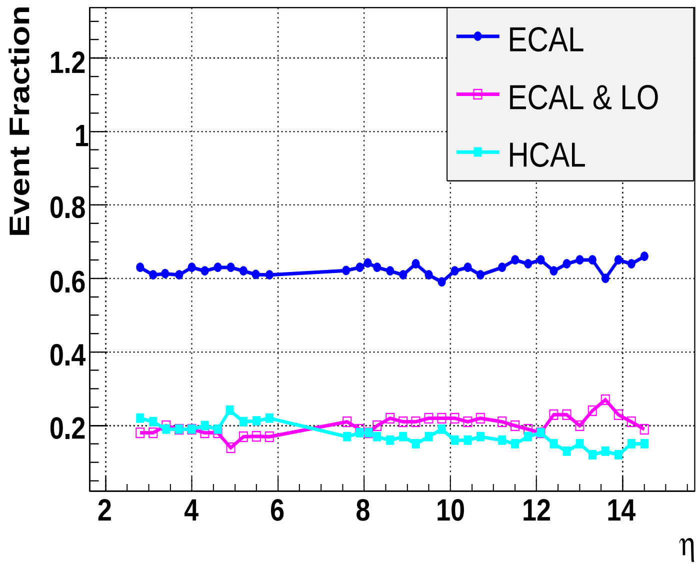

Figure 4.9. First interaction of the pion beams in different part of the test beam setup.

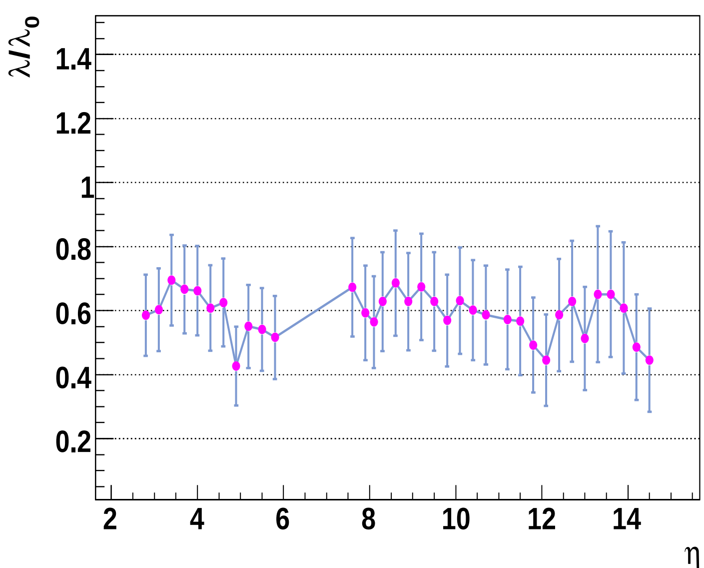

Figure 4.10. Interaction length.

5. JET RECONSTRUCTION in CMS

A very important part of many QCD analyses, event signatures for SUSY, Higgs boson production, and other new physics processes require the reconstruction and measurement of jets coming from high-momentum quarks and gluons (Kodolova, 2005) at the hadron colliders. Some particles, such as charged leptons, or photons, go through the detector without decaying or emitting any other particles. This results in a very clear signature in the detector: a single track in the tracker or no track, for the cases of charged and neutral particles, respectively, and a well-localised energy deposit in the calorimeters. Hadronic particles, on the other hand, are more complicated and complex to study. Because of the nature of the strong interaction, a single hard interaction involving a quark or a gluon will result in a large number of hadrons seen in the detector, as previously discussed in Chapter 2. This evolution from a single particle to a large number of final state particles is governed by QCD processes, in particular by fragmentation processes (radiation of other particles from the primary one) as well as hadronisation (the process by which quarks and gluons are bound into hadrons).

Because of the possibility of having gluon-mediated interactions, which by far dominate the interaction cross section, there is a possibility of having many jets in the event. So the definitions of the jets at the hadron colliders are quite difficult. On the other hand this possibility can lead to the shower of particles from one parton overlapping with those from another. There are also many more processes happening, when protons collide, than just the hard interaction. These other processes are what is referred to as the underlying event as we disccused in Chapter 2. All of these effects result in a large number of tracks and calorimeter energy deposits which must be disentangled into objects such as jets or isolated particles. This disentangling is done using jet algorithms.

In parton shower Monte Carlo events, a jet clustering algorithm can be applied to particles produced after hadronization of the partons, producing hadron level jets; for pQCD parton-level predictions, jets are formed by running the algorithm on partons from the fixed-order (typically next-to-leading order) pQCD event generator. Experimentally, it is extremely challenging to both identify and measure the kinematic properties of the large variety of individual particles produced in high-energy hadronic collisions, especially with the relatively coarse calorimeter segmentation present in the Tevatron experiments. As a result jets are reconstructed by running the jet algorithm on the raw energy depositions in the calorimeter towers, and not on the individual particles. The reconstruction and energy measurement of these calorimeter jets are affected by a variety of instrumental and physics effects. The instrumental effects include (1) calorimeter non-uniformity, (2) resolution effects due to large fluctuations in particle showering in the calorimeter, (3) non-linear response of the calorimeter, especially to hadrons, and (4) low momentum particles not reaching the calorimeter due to materials in front of the calorimeter and the solenoidal magnetic field. Energy from additional pp interactions occurring in the same bunch crossing also affects the jet reconstruction and energy measurement. This has a non-negligible effect especially for low transverse momentum jets and high instantaneous luminosities. The situation is further complicated due to the fact that (a) the underlying event contributes energy to the jet cone, and that (b) the jet cone does not contain all the energy of the parent parton because of the effects of parton showering and hadronization. All of these effects have to be taken into account when comparing experimental data with theoretical predictions or extracting physics quantities of interest from experimental data.

Typically in jet cross section measurements, the data are corrected to the hadron-level (i.e., corrected only for instrumental effects); at this level, the results can be compared with hadron-level theoretical predictions without any knowledge of the detectors. It is strongly encouraged that, where possible, measurements at the LHC produce results at this level; often, instead the predictions from Monte Carlos are themselves passed through a detector simulation program and then directly compared to the raw data distributions.

Sometimes, the theoretical predictions from perturbative QCD calculations are available only at the parton level and then it is necessary to either correct the theory to the hadron level or the data to the parton level. For inclusive jet cross sections, the best theoretical predictions available, as of now, are from next-to-leading order perturbative QCD calculations (Ellis,1992;1990;1989, Giele 1994, Nagy 2002a). When making comparisons between experimental measurements and next-to-leading (NLO) order predictions, non-perturbative QCD effects from the underlying event and hadronization (see Section 4.3 for details) are evaluated based on tuned parton shower Monte Carlos. It should be noted that a correction is not made for out-of-cone energy from hard gluon emission, as such effects are already (at least partially) taken into account in the NLO calculations. In these comparisons, next-to-leading order hard gluon emission is assumed to model the whole parton shower perturbative QCD radiation process. NLO pQCD calculations have been shown to provide a reasonable description of energy flow inside jets (Ellis, 1993), so this is considered to be a reasonable assumption; however, data-theory comparisons will benefit a great deal from higher order QCD calculations or next-to-leading matrix element calculations interfaced with parton shower models, as in e.g., MC@NLO (Frixione, 2002).

The first jet algorithms for hadron colliders were simple cones. Over the last two decades, clustering techniques have greatly improved in sophistication. A perfect detector jet is defined at particle-level through the use of jet algorithms, while a reconstructed jet is formed by applying the same algorithms on a set of energy deposits in calorimeter cells. A reconstructed jet is identified with the particle-level jet through a pseudorapidity, phi (η, ϕ) matching criterion that searches within a cone $R = \sqrt{(\Delta y)^2 + (\Delta\phi)^2}$ to find agreement of the jet axes. The correspondance of a reconstructed jet to the particle-level jet, however, is not always unambiguous. The parameters of the initial parton corresponding to the particle jet depends on a number of factors including final state radiation, which can lead to the splitting of the jet in the detector. For a large cone, the jet reconstruction collects a large fraction of the energy of the initial parton, but such a cone is also susceptible to collecting the energy of non-isolated additional partons in the hard interaction, in addition to energy from the underlying event, pile-up interactions, and electronic noise.

The first step in the reconstruction, before invoking the jet algorithm, is to apply noise and pile-up suppression with either a set of cuts on the tower energies or to apply a pile-up subtraction algorithm (Kodolova, 2005). The choice of the tower energy or E_T cuts is based on a balance between jet reconstruction efficiency and instrumental fake rates. The factors influencing the identification of a reconstructed jet energy with the energy of a scattered parton can be divided into two groups. One is connected with the jet as a physical object, and includes fragmentation model, initial and final state radiation, the underlying event, and particles coming from pile-up events. A second group follows from detector performance and includes electronic noise, the effect of the magnetic field which deflects low energy charged particles out of the jet reconstruction cone, non-compesating responses of the calorimeters to electromagnetic and hadronic showers (electron/hadron ratio), losses due to out-of-cone showering, dead materials and cracks and longitudinal leakage for high energy jets. While some of the corrections for effects in the first group are channel dependent, the bulk of the detector effects are channel independent and common particle-level correction coefficients can be provided. Calibrations are applied to restore equality between reconstructed and particle-level jets. Corrections to the jet energy have a strong dependence on η and E_T. These non-uniformities are due in part from differing detector technologies versus η , granularity changes in η and ϕ, subdetector boundaries, and the intrinsic E-dependence (as opposed to E_T) in the detector response.

5.1 Jet Clustering Algorithms in CMS

High quality and highly efficient jet reconstruction is an important tool for almost all physics analyses to be performed with the CMS detector at the LHC at CERN. Jet clustering algorithms are among the main tools for analysing data from hard collisions. Their widespread use at Tevatron and the prospect of unprecented final state complexity at the upcoming LHC have stimulated considerable debate concerning the merits of different kinds of jet algorithm.

In high energy interactions partons are produced in the final state with large transverse momenta as a result of the hard scattering process as discussed in chapter 2. Partons outgoing from the interaction point produce parton showers and subsequently partons from these showers combine to form hadrons which are color singlets which interact in the detector. Since the transverse energies involved in the hadronization process are much smaller than the hard scattering energies, the final state particles are collimated around the direction of the original parton. These streams of particles are called jets which are defined by their energy deposit E_T measured in the ECAL and HCAL as well as their momentum vector p_T, both in transverse direction. In order to measure the jet energy as well as the direction of the jet, all electromagnetic and hadronic calorimeter cells above a certain signal to noise ratio are grouped into so-called towers which act as basis for the different jet reconstruction algorithms provided by CMS (Heister, 2006).

Jet clustering algorithms are used to associate particles to a particular jet. Direction and energy of a jet are related to the direction and energy of the original parton.

Two broad classes of jet definition are generally advocated (TeV4LHC QCD Working Group et al., 2006) for hadron colliders. One option is to use sequential recombination jet algorithms, such as the k_T which groups calorimeter objects based on their distance relative to each other in the four-momentum space, iteratively (Catani, 1993; Soper, 1993) and Camridge/Aachen algorithms (Dokshitzer, 1997; Wobisch, 2000), which introduce a distance measure between particles, and repeatedly recombine the closest pair of particles until some stopping criterion is reached.

Cone jet algorithms make up the second class, which are inspired by the idea of defining a jet as an angular cone around some direction of dominant energy flow. So it groups the calorimeter towers in a cone around a high energetic seed tower. To find these directions of dominant energy flow, cone algorithms usually take some or all of the event particles as 'seeds', *i.e.* trivial cone directions. Then for each seed they establish the list of particles in the trial cone, evaluate the sum of their 4-momenta, and use the resulting 4-momenta as a new trial direction for the cone. This procedure is iterated until the cone direction no longer changes, *i.e* until one has a stable cone.

Two types of problem arise when using seeds as starting points of an iterative search for stable cones. On one hand, if one only uses particles above some momentum threshold as seeds, then the procedure is collinear unsafe. Alternatively if any particle can act as a seed then one needs to be sure that the addition of an infinitely soft particle can not lead to a new (hard) stable cone being found, otherwise the procedure is infrared (IR) unsafe. These issues will be discussed in detail in section 5.1.4.

The infrared (IR) unsafety problem came to fore in 1990's, when it was realised that there can be stable cones that have two hard particles on opposing edges of the cone and no particles in the middle, e.g. for configurations such as

$$p_{t1} > p_{t2}; \tag{5.1}$$

$$R < D(p_1, p_2) < (1 + p_1/p_2)R \tag{5.2}$$

In traditional iterative cone algorithms, p_1 and p_2 each act as seeds and two stable cones are found, one centred on p_1, the other centred on p_2. The third stable cone, centred between p_1 and p_2 (and containing them both) is not found. If, however, a soft particle is added between the two hard particles, it too acts as a seed and the third stable cone is then found. The set of stable cones (and final jets) is thus different with and without the soft particle and there is a resulting non-cancellation of divergent real soft production and corresponding virtual contributions, i.e. the algorithm is infrared unsafe.

Infrared unsafety is a serious issue, not just because it makes it impossible to carry out meaningful (finite) perturbative calculations, but also because it breaks the whole relation between the (Born or low-order) partonic structure of the event and the jets that one observes, and it is precisely this relation that a jet algorithm is supposed to codify: it makes no sense for the structure of multi-hundred GeV jets to change radically just because hadronisation, the underlying event or pileup threw a 1 GeV particle in between them. The big picture in the story says that iterative cone algorithms should be abondoned due to the IR unsafe caharactreristic problem.

There are four principal jet reconstruction algorithms in CMS: the midpoint cone (Kurt, 2008) which is not supported by CMS simulation software recently, the iterative cone [Kurt, 2008], the inclusive k_T jet algorithm (Kurt, 2007), and a recent algorithm SISCone (Seedless Infrared Safe Cone) (Salam, 2007). The midpoint-cone and k_T algorithms are widely used in offline analysis in current hadron collider experiments while the iterative cone algorithm is simpler and faster and commonly used for jet reconstruction in software-based trigger systems. New Seedles Infrared and collinear safe algorithm SISCone is one of the popular jet reconstruction algorithm currently which is used specifically to focus on the ”Infrared and Collinear Unsafe” problem.

The jet algorithms are used with one of two recombination schemes for adding the constituents. The energy scheme, E-scheme (Blazey, 2000), is used to calculate the 4-momentum of the jet from the 4-momenta of the individual particles. In the E-scheme, constituents are simply added as four-vectors, producing massive jets by equating the jet transverse momentum to the $\sum E_T$ of the constituents and then fixing the direction 2 of the jet in one of two ways: 1) $\sin\theta = \sum E_T/E$ where E is the jet energy (usually used with cone algorithms), or 2) $\eta = \sum E_{Ti}\eta_i/E_T$ and $\phi = \sum E_{Ti}\phi_i/E_T$ (usually used with the k_T algorithm). When using the E_T scheme, the jet E_T is equal to cp_T. The inclusive k_T

algorithm merges, in each iteration step, input objects into possible final jets and so the new jet quantities, the jet direction and energy, have to be calculated directly during the clustering. The cone jet algorithm, SISCone, groups the input objects together based on their distance in (y, ϕ) space, and the determination of the jet quantities is done at the end of the jet finding. The inclusive k_T algorithm iteratively merges input objects into final jets and so the jet kinematic quantities, the jet direction and energy, are calculated directly during the clustering. The rest cone jet algorithms, iterative and midpoint, group the input objects together as an intermediate stage and the final determination of the jet quantities (recombination) is done in one step at the end of the jet finding.

The towers are used as input to several jet clustering algorithms. The energy associated with a tower is calculated as the sum of all contributing readout cells which pass the online zero-suppression threshold and any additional offline software thresholds. For the purpose of jet clustering, the towers are treated as massless particles, with the energy given by the tower energy, and the direction defined by the interaction point and the center of the tower.

5.1.1 MidPoint Cone Algorithm

The midpoint-cone algorithm was designed to facilitate the splitting and merging of jets. The midpoint-cone algorithm also uses an iterative procedure to find stable cones (proto-jets) starting from the cones around objects with an E_T above a seed threshold. Contrary to the iterative cone algorithm described above, no objects is removed from the input list since a single input object may belong to several proto-jets. A second iteration of the list of stable jets is done to ensure the collinear and infrared safety of the algorithm. For every pair of proto-jets that are closer than the cone diameter, a midpoint is calculated as the direction of the combined momentum. These midpoints are then used as additional seeds to find more proto-jets. When all proto-jets are found, the-splitting and merging procedure is appled, starting with the highest E_T proto-jet. If the proto-jet does not share objects with other proto-jets, it is defined as a jet and removed from the prot-jet list. Otherwise, the transverse energy shared with the highest E_T neighbor proto-jet is compared to the total transverse energy of this neighbor proto-jet. If the fraction is greater than 0.5

the proto-jets are merged, otherwise the shared objects are individually assigned to the proto-jet that is closest in η, ϕ space. The procedure is repeated, again always starting with the highest E_T proto-jet, until no proto-jets are left. This algorithm implements the energy scheme to calculate the proto-jet properties, but a different recombination scheme may be used for the final jet. The parameters of the algorithm include a seed threshold, a cone radius, a threshold ratio on the shared energy fraction for jet merging, and also a maximum number of proto-jets that are used to calculate midpoints.

5.1.2 Iterative Cone Algorithm

In the iterative cone algorithm, an E_T ordered list of input objects (particles and calorimeter towers) is created. A cone of size R in η, ϕ space is cast around the input object having the largest transverse energy above a specified seed threshold. The objects inside the cone are used to calculate a proto-jet direction and energy using the E_T scheme. The calculated direction is used as a seed to produce a new proto-jet. The procedure is repeated until the energy of the proto-jet changes by less than 1% between iterations and the direction of the proto-jet changes by $\Delta R \leq 0.01$

When a stable proto-jet is found, all objects in the proto-jet are removed from the list of input objects and the stable proto-jet is added to the list of jets. The whole procedure is repeated until the list contains no more object with an E_T above the seed threshold. The cone size and the seed threshold are parameters of the algorithm.

5.1.3 k_T Algorithm

The k_T algorithm has been widely used for precise QCD measurements at both e^+e^- and $e^\pm p$ colliders and allows a well defined comparison to the theoretical predictions, without introducing into the calculations additional parameters to emulate the experimental procedure governing the merging or splitting of overlapping cones (Soper, 1993), namely is a collinear and infrared safe algorithm, which is suited for hadron colliders. The inclusive k_T jet algorithm is a cluster-based jet algorithm. The cluster procedure starts with a list of input objects, stable particles or calorimeter cells.

In the fallowing discussion, k_{Ti} denotes to the transverse momentum, y_i and ϕ_i are respectively the rapidity and azimuth of particle i and D is the distance or radius parameter. For each object i and each pair (i,j) the fallowing distances are calculated.

$$d_{i,j} = min(k_{Ti}^2, k_{Tj}^2)\frac{[(y_i - y_j)^2 + (\phi_i - \phi_j)^2]}{D^2} \tag{5.3}$$

$$d_i = k_{Ti}^2 \tag{5.4}$$

If, all the values d_{ij}, d_i, d_{kl} is the smallest, then objects k and l are combined into a single new object. If, however, d_k is the smallest, then object k is considered as a jet and is excluded from further clustering. The procedure is repeated until all objects were assigned to jets.

Two external implementations of this algorithm were introduced by CMS. The one is the library k_t jet (Butterworth, 2003) and the other is a version of the algorithm included in the FastJet package (Cacciari and Salam, 2006). The k_T implementation of FastJet includes optimizations that make the jet-finding algorithm much faster than the traditional one so the time spent for the reconstruction of an event is much smaller. The FastJet package also includes additional features such as the pile-up subtraction on an event-by-event.

5.1.4 Seedless Infrared Collinear Safe Cone Algorithm

Partons (quarks and gluons) are the concepts that are central to discussions of the QCD aspects of high-energy hadron collisions. Quarks and gluons, however, are not observable, and in their place one sees jets, collimated bunches of high-energy hadrons which are the result of fragmentation and hadronization of the original hard (high-energy) partons.

Naively, jets are easily identified, one can simply searches for bunches of collimated hadrons. However, to carry out accurate comparisons between parton level predictions and hadronic-level observations one needs a well-defined jet finding procedure.

The SISCone algorithm has been developed specifically to address the IRC problem by removing the use of seeds; as a consequence, the algorithm is IRC safe to all orders. Special techniques have been employed to achieve reconstruction speed comparable to

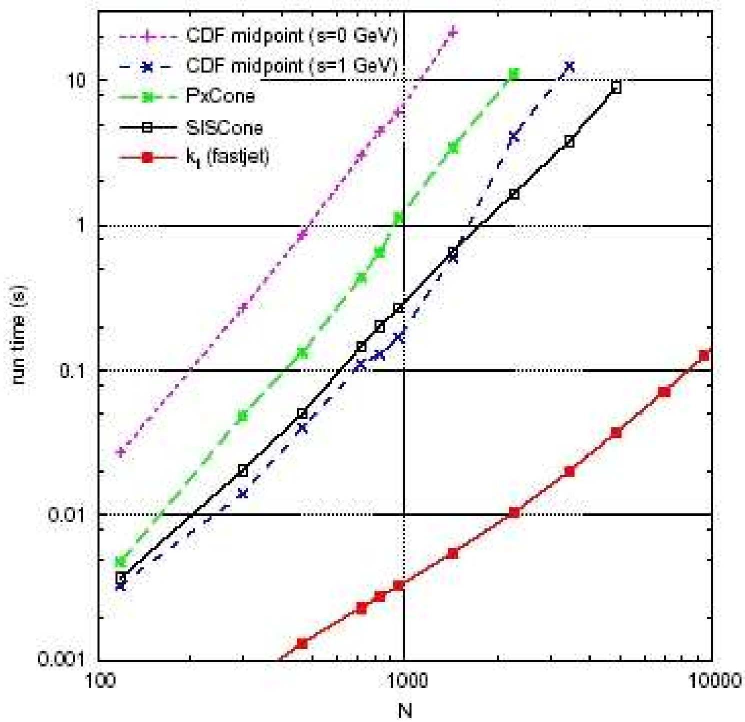

Figure 5.1. Time to cluster N particles, as a function of N, for various algorithms, with R = 0.7 and f = 0.5, on a 3.4GHz Pentium IV processor. For the CDF midpoint algorithm, s is the threshold transverse momentum above which particles are used as seeds.

Midpoint Cone. Therefore, the SISCone algorithm is clearly theoretically preferred for QCD measurements and for other applications where the accuracy of higher-order QCD calculations is desired. The SISCone algorithm also avoids the dark jet problem by implementing the option of sequential multiple passes which cluster the towers/particles left unclustered by the previous pass.

These features make SISCone a superior algorithm for theory predictions and for reconstruction at particle level. For the calorimeter-level reconstruction, the performance of SISCone is similar to Midpoint Cone as can be seen in section 5.3.1, and the increase in the jet reconstruction time is modest, in fact negligible, within the full-event time budget as you can see in Figure 5.1.

5.2 Jet Energy Corrections

Many physics measurements in CMS will rely on the precise reconstruction of jets. Correction of the raw jet energy measured by the CMS detector will be a fundamental step for most of the analysis where hadron activity is investigated.

Due to the non-linear calorimeter response, the measured jet energy is lower than the particle jet energy and therefore needs to be corrected. The plan for the jet corrections in CMS is described in (Bhatti, 2007) and is based on a factorized approach where different levels of corrections are applied sequentially to correct for different effects. The default jet corrections include:

- Level 1 (Offset) correction (Bhatti, 2009) is the first step in the chain of the factorized corrections. Its purpose is to subtract the energy not associated with the high-scattering. So it primarily corrects for energy from electronic noise, pile-up and energy lost by thresholds. Here pile-up refers to the energy from additional proton-proton collisions, occurring close enough in time to the hard scatter to be included in the calorimeter energy within the jet. The electronic noise refers to any noise above the calorimeter cell and tower thresholds for CaloTowers included in the jet. Both pile-up and electronic noise produce an energy offset which is planned to subtract from the jet. The initial plan to estimate the level 1 offset energy is to measure it in zero-bias collisions(proton bunch crossings).

- Level 2 (Relative - η dependence) (Bhatti, 2007) correction aims at removing relative jet response variations in the CMS detector as a function of pseudorapidity. The goal is to make the jet response flat as a function of η.

- Level 3 (Absolute - p_T dependence) (Bhatti, 2007) correction removes the variations in p_T as a function of jet p_T^{jet} which is caused by the CMS calorimeter since the CMS calorimeter energy repsonse to a particle level jet is smaller than unity and varies as a function of jet p_T. It is planned to determine this correction first from MC truth, and subsequently from photon + jet p_T balance in actual collision data (The CMS Collaboration, 2009a) and Z + jet (The CMS Collaboration, 2009b).

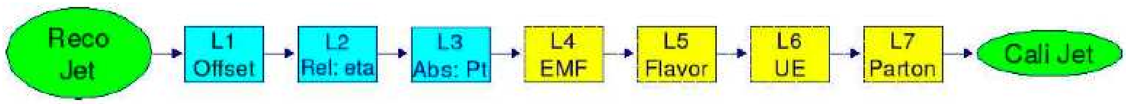

Figure 5.2. Official (factorized) jet energy corrections in CMS (Bhatti, 2007). L1-L3 (L4-L7) are required (optional).

However the standard jet reconstruction applies the Scheme B thresholds (Demina, 2006) on calorimeter cells and an overall tower threshold E_T >0.5 GeV, summarized in Table 5.1 and relevant for all studies presented in this thesis.

Table 5.1. Energy thresholds (in GeV) for calorimeter noise suppression Scheme B. $\sum EB$ and $\sum EE$ refer to the sum of ECAL energy deposits associated with the same tower in the barrel and endcap respectively.

Scheme	HB [GeV]	HO [GeV]	HE [GeV]	EB [GeV]	EE [GeV]
B	0.90	1.10	1.40	0.20	0.45

With the current default reconstruction thresholds (SchemeB), the offset correction is negligible and only the other two (relative, absolute) are applied to jets. According to the plan, data driven techniques will be applied to determine the jet energy corrections when enough collision data will be available. However, at startup, the jet corrections will be derived from MC using MC truth information. The detailed description of the MC truth method for deriving the jet corrections can be found in (Kousouris, 2008).

5.3 k_T Algorithm validation in CMSSW

In this section, the output of two different implementations of the k_T algorithm, the k_T jet and FastJet packages, is compared for a standard setting of parameters. Ideally, the results should be identical, any observed difference will come from details of the implementation. Since current versions of the CMS software only the FastJet package are used, this comparison is crucial to assure a clean transition from old version to the FastJet package.

5.3.1 Analysis Procedure and Event Selection

Standard QCD dijet events were generated with PYTHIA (Sjostrand, 2006) and simulated with CMSSW_1_3_1. In each case two different inputs were used: the four-vectors of the generated stable particles in the event and the four-vectors of the calorimeter towers after the detector simulation. Two output jet-collections were produced which are respectively called generator level jets (GenJets, also particle jets or hadron jets) and calorimeter jets (CaloJets). For both KtJet and FastJet the following parameters were used:

- D-Parameter is set to 0.4, 0.6 and 1.0
- All stable particles are taken as input for reconstructing GenJets
- Calo towers with E_T >0.5 GeV are used as input for the reconstruction of CaloJets
- The output was restricted to jets with $p_T > 1.0$ GeV.

5.3.2 Energy Distribution within a Jet with the k_T Algorithm

Although in k_T jet clustering algorithm the objects (particles, towers, tracks or partons) are combined based on their relative transverse momenta, the resulting jet is mainly localized in $\eta - \phi$ space. In other words, although a k_T clustered jets do not have a precise boundary in physical space, the jet properties are similar to the properties of jets clustered by the cone clustering algorithms. This can be seen by measuring the energy distribution within a jet which is characterized by the differential jet shape, $\rho(r)$, defined as

$$\rho(r) = \frac{\sum P_T(r - \Delta r/2, r + \Delta r/2)}{\Delta r \sum P_T^{Jet}}$$

where the sum is over all the jet constituents in the range $(r - \Delta r/2, r + \Delta r/2)$ in the numerator where $r = \sqrt{(\eta_{jet} - \eta_c)^2 + (\phi_{jet} - \phi_c)^2}$ with (η_{jet}, ϕ_{jet}) and (η_c, ϕ_c) being the position of the jet and the constituents. The denominator $\sum P_T^{Jet}$ is the scalar sum of the transverse momenta of all the jet constituents.

Figure 5.3 shows the jet shape distribution $\rho(r)$ as a function of distance from the jet centroid for k_T-jets from Spring07 dijet dataset generated and simulated using CMS software version CMSSW_1_3_3. The particles and calorimeter towers linked to the reconstructed jets are used for jets with $50 < P_T^{Jet} < 80$ GeV. As expected, in contrast to the cone jets, k_T jets extend to a larger area in physical space and do not have a sharp cut off. However, most of the energy is concentrated at the core of the jets. The particle jets include the particles down to very small momenta and thus have large area. The calorimeter jets are reconstructed from towers which have minimum $E_T > 0.5$ GeV and pass scheme B thresholds. These threshold requirements limit the area of the jets.

The shape of the particle jets is compared with calorimeter jets in Figure 5.4 for the clustering parameter D=0.4, 0.6 and 1.0. The particle jets extend to a larger physical area than calorimeter jets. Quantitatively, 90% of the jet energy is confined to $r < 0.25, 0.38$ and 0.81 for $D = 0.4, 0.6$ and 1.0 particle jets while for calorimeter jets the values are $r < 0.27, 0.37$ and 0.55, respectively. The fraction of jet transverse energy outside $r = 0.5$ is 1%, 10% and 19% for $D = 0.4, 0.6$ and 1.0 respectively for particle jets which can be compared to 1%, 4% and 12% for the calorimeter jets.

5.4 Performance of Jet Algorithms in CMS

Almost every process of interest at the LHC contains quarks or gluons in the final state. The partons can not be observed directly, but fragment into stable hadrons, which can be detected in the tracking and calorimeter systems. This study describes the latest performance studies of several algorithms which cluster energy deposits in the CMS calorimeters into collimated objects of stable particles, CaloJets. Calorimeter jets are expected to yield a good description of both the parton-level and the hadron showers emerging from the hard interaction. For Monte Carlo events, the hadron-level is dened by applying the same clustering algorithms, which are typically formulated to accept any set of four vectors as inputs, to all stable particles from the MC truth record (GenJets). Hadron-level is also referred to as particle-level, and jet energy scale corrections based on MC are derived to correct back to this detector-independent level. Calorimeter jets are reconstructed using energy deposits in calorimeter towers (CaloTowers) as inputs: they

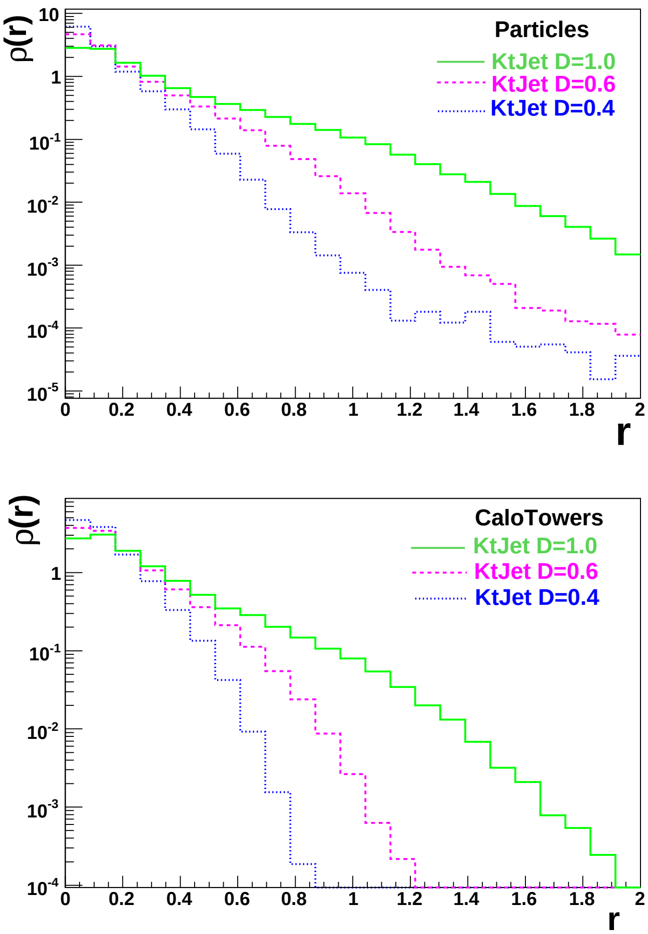

Figure 5.3. Normalized transverse energy density distributions, $\rho(r)$ for particle (left) and calorimeter (right) k_T jets reconstructed using the clustering parameter $D = 0.4$, 0.6 and 1.0. As expected, the jets occupy larger area as the D parameters increases.

are composed of one or more HCAL cells and corresponding ECAL crystals. The unweighted sum of energy deposits of one single HCAL cell and 5x5 ECAL crystals form a projective tower in the barrel ($|\eta|$ <1.0). A more complex association between HCAL cells and ECAL crystals is required in the forward region. The standard jet reconstruction applies the Scheme B thresholds on calorimeter cells and an overall tower threshold E_T >0.5 GeV.

The studies presented in this section are based on QCD dijet Monte Carlo samples without pileup, produced and reconstructed with CMSSW_1_5_2 and analyzed with CMSSW_1_6_X. It is often necessary to associate CaloJets with GenJets in these samples to probe how well the calorimeter-level reconstruction represents the hadron-level of the

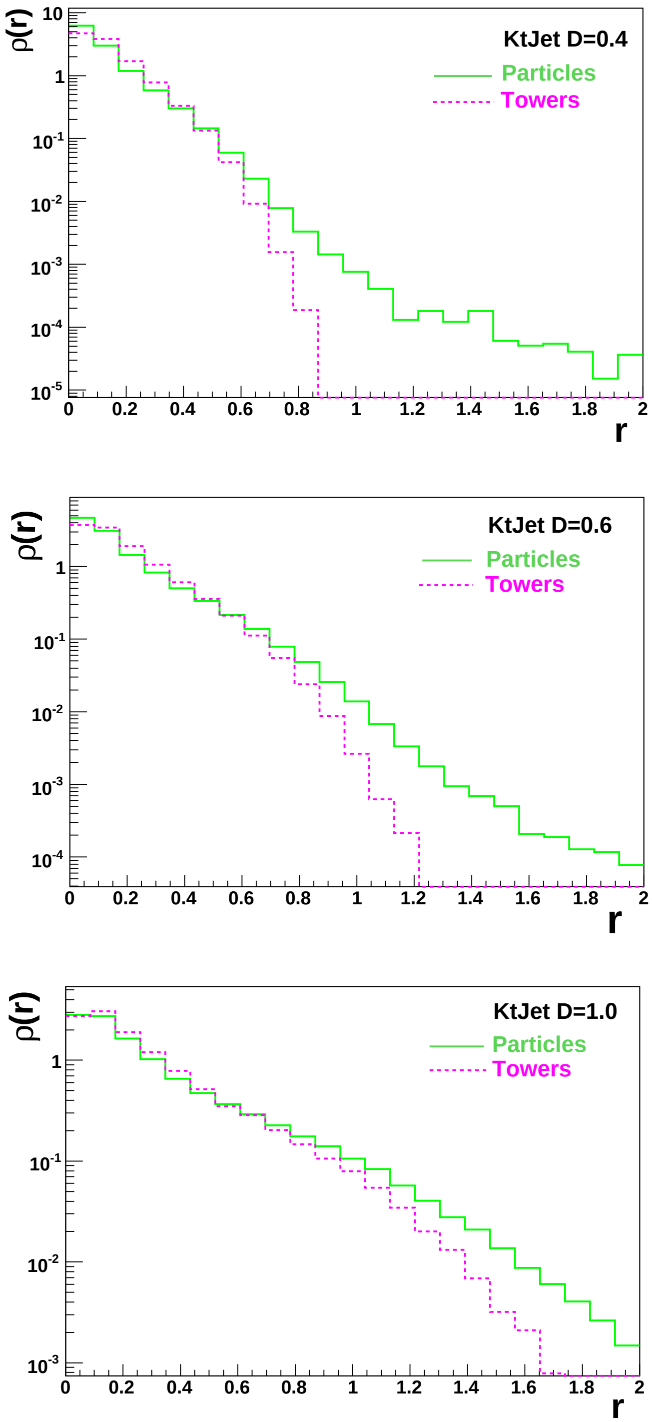

Figure 5.4. Normalized transverse energy density distributions ($\rho(r)$) in k_T jets reconstructed using the clustering parameter D=0.4, 0.6 and 1.0. The particle jet (green solid lines) extend much further than the calorimeter jets (magenta dotted line).

process. This association is based on spatial separation in space between the two jet axes by requiring

$$R = \sqrt{(\Delta y)^2 + (\Delta \phi)^2} \tag{5.5}$$

to be less than a certain value. Similarly, GenJets (and hence their associated CaloJets) are assigned the same parton flavor as the matched MC parton from the hard interaction. These four algorithms can be grouped into two general categories: seeded and seedless. The E-Scheme is used for all algorithms as the recombination scheme: the energy and momentum of a jet are defined as the sums of energies and momenta of its constituents.

5.4.1 Energy Distribution within the Jets using all CMS Jet Algorithms

In this section, we compare the internal properties of the calorimeter and particle jets reconstructed with different algorithms. This study is performed using CMSSW_1_5_2 QCD dijet events. Different $\hat{p_T}$ samples are combined using appropriate weights. The jet collections for Iterative Cone (R=0.5, 0.7), Midpoint Cone (R=0.5, 0.7), and Fast kT (D=0.6) clustering algorithms are taken from official production. The SISCone jets are reconstructed using CMSSW_1_6_0. Only events where the two leading jets are within $|y| <1.0$ are used, where y is the rapidity of the jet. In addition, we use only those calorimeter jets which are within $\Delta R <0.3$ of a particle jet (GenJet), to ensure correspondence between calorimeter and particle level distributions. For all studies in this section,we use only the particles (towers) which are associated with the jet by the clustering algorithm. Multiplicity and p_T distributions for particles (towers) in particle (calorimeter) jets are shown in Figures 5.5 and 5.6 (5.7 and 5.8). As expected, both the particle and tower mean multiplicities in a jet increase logarithmically with jet p_T. The p_T distribution of particles and towers becomes harder with increasing jet p_T. The internal structure of the jet can also be described by the energy distribution within a jet which is characterized by the differential jet shape, $\rho(r)$, defined as in chapter 2.

The jet shapes for different particle and calorimeter jets are shown in Figures 5.9 and 5.10 respectively. Jets become narrower with increasing jet p_T. Note that the Iterative Cone algorithm is based on $\Delta R(\eta)$, while the differential jet energy density is defined using $\delta r(y)$, explaining contributions to the density for r > R. The cone clustering algorithms using the same radius have similar properties. The Iterative Cone and Midpoint Cone algorithms mainly differ due to the splitting-merging stage. This difference has a small effect on the two leading jets in the sample used which is dominated by back-to-back jets. The SISCone algorithm finds all stable cones. The two leading jets produced by splitting and merging of stable cone are expected to be similar to the jets found by the Midpoint Cone algorithm. The k_T clustering algorithm with D=0.6 has similar characteristics as the cone jets with R=0.7 except for jets in the $30 < p_T < 50$ GeV range where k_T jets are slightly narrower.

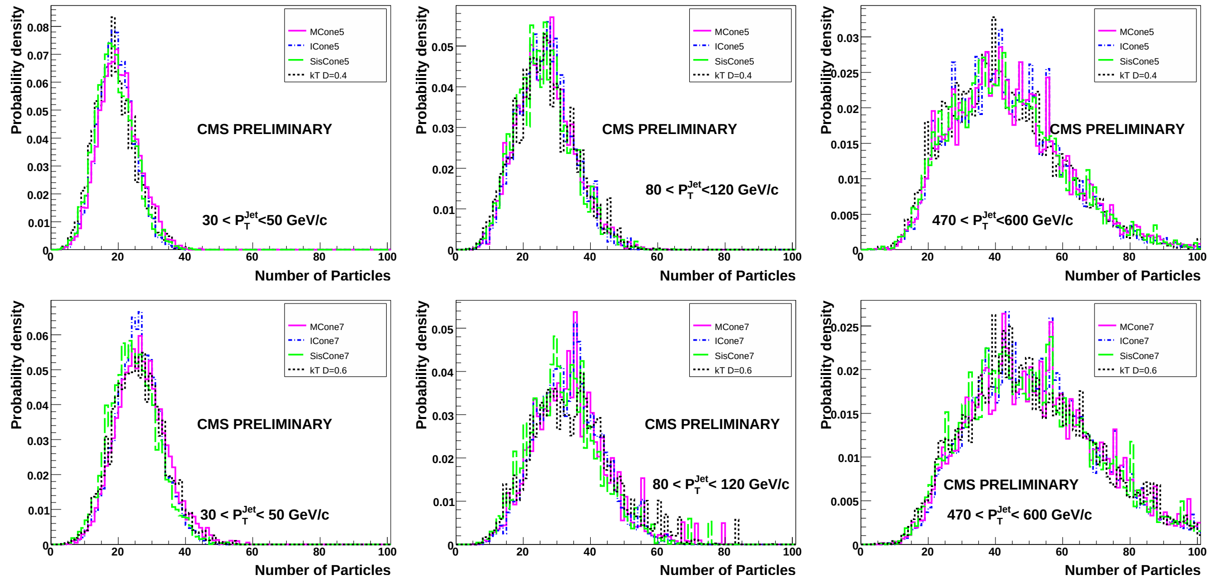

Figure 5.5. The multiplicity of particles in a jet for different algorithms. Different cone algorithms with the same clustering radius have almost the same multiplicity. The multiplicity for Fast k_T D=0.6 jets is close to the observation for cone jets with R=0.7.

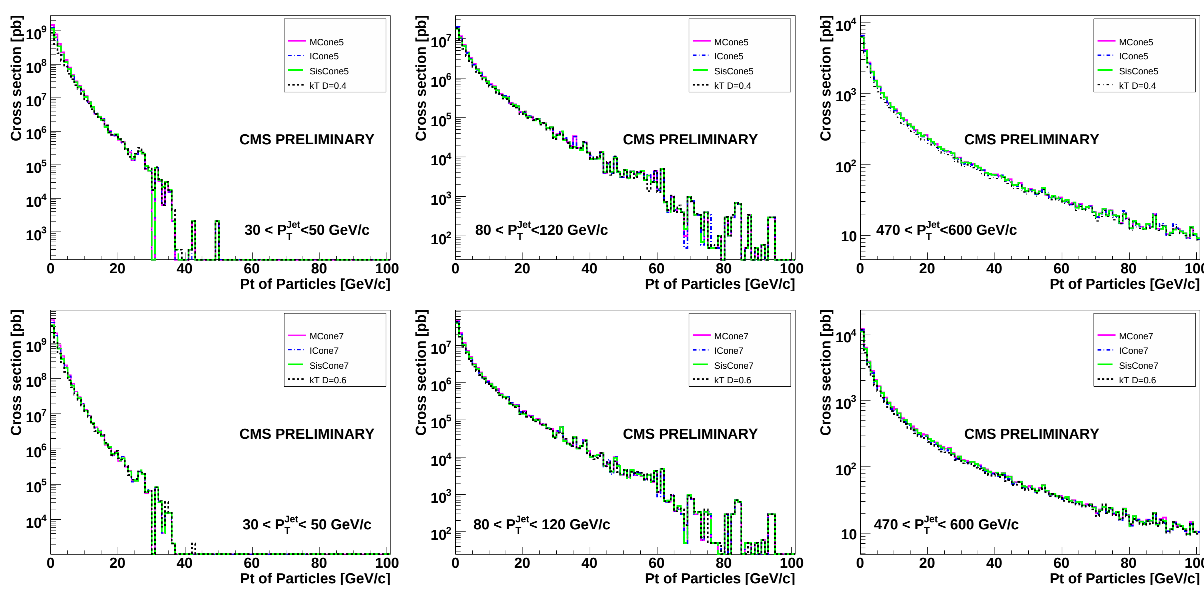

Figure 5.6. The transverse momentum of particles clustered into a jet for different jet clustering algorithms. The p_T distribution for Fast k_T D=0.6 jets is close to the one observed for cone jets with R=0.7. Plots are labeled with corresponding particle jet p_T bins.

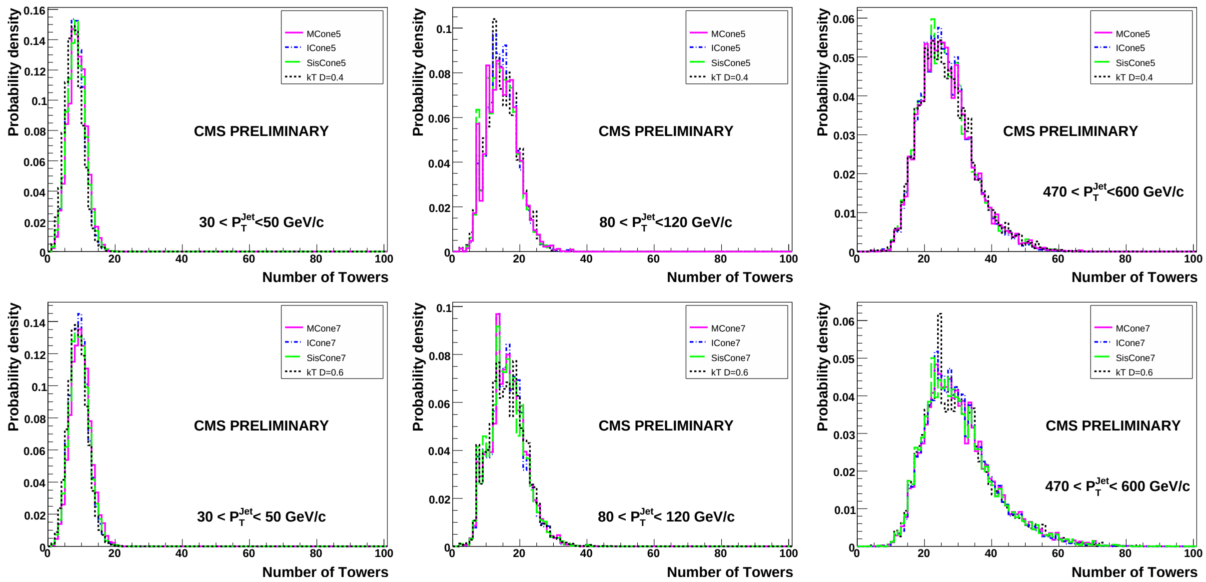

Figure 5.7. The multiplicity of towers in jets reconstructed using different algorithms. Different cone algorithms with the same clustering radius have almost the same multiplicity. The multiplicity of Fast k_T D=0.6 jets is close to the one observed for cone jets with R=0.7.

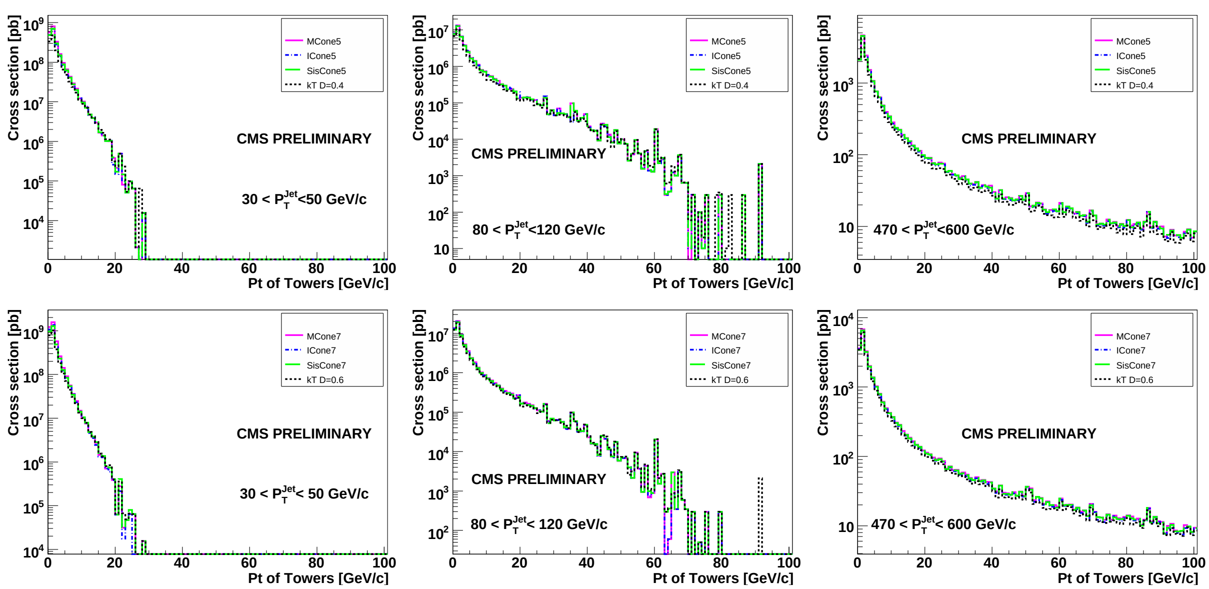

Figure 5.8. The p_T of towers in jets reconstructed using different algorithms. Different cone algorithms with the same clustering radius have almost the same p_T distributions. The p_T of towers clustered into Fast k_T D=0.6 jets is close to the observation for cone jets with R=0.7. Plots are labeled with corresponding particle jet p_T bins.

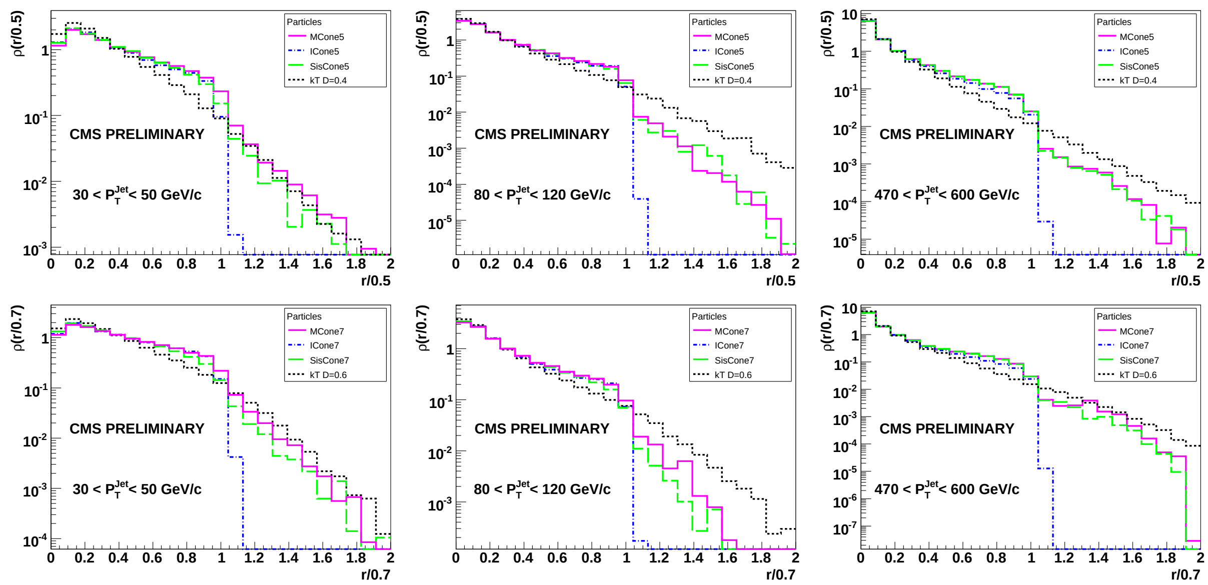

Figure 5.9. Normalized transverse energy density distributions ($\rho(r)$) in particle jets reconstructed using different algorithms.

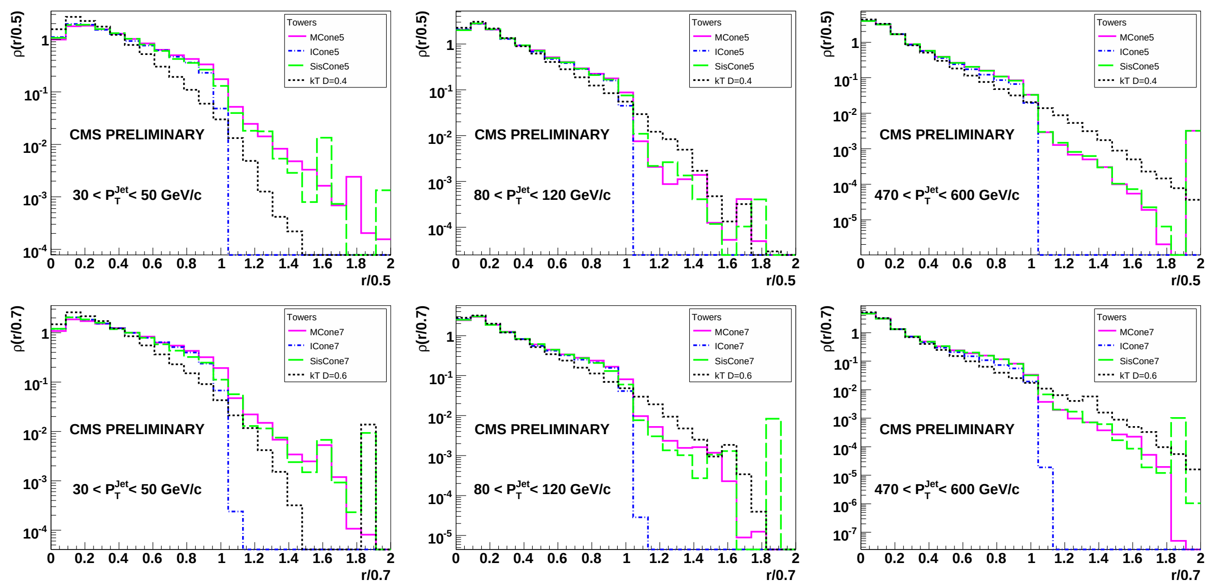

Figure 5.10. Normalized transverse energy density distributions ($\rho(r)$) in calorimeter jets reconstructed using different algorithms. Plots are labeled with corresponding particle jet p_T bins.

6. MONTE CARLO TOOLS AND ANALYSIS FRAMEWORK

Monte Carlo methods are an important tool for understanding the signals of different processes measured in the experiment. This chapter gives a brief introduction on the stages of Monte Carlo production and some important event generators used in this study for producing signal event samples. A summary on the software framework used in the CMS environment is also given.

6.1 Event Generation with Monte Carlo Techniques

The complexity of high energy particle physics processes exceeds the feasibility of a full quantum mechanical treatment, because the number of particles in proton-proton collisions is too large. Furthermore, perturbation theory is not able to handle the transition of partons to hadrons. Hence, Monte Carlo (MC) simulations, which contain the theoretical understanding of the explored model, are used to reproduce the expected signal of an experiment. This is done for developing a design of the experiment, improving analysis strategies, and evaluating measured data. A huge variety of software tools exists for each individual part of the event generation. In the following, each step is explained briefly. The functionality of the Monte Carlo generators is explained, which are used in this study for the production of the simulated data. A more detailed introduction to Monte Carlo generators for hadron colliders is given in reference (Dobbs, 2004).

6.2 The Steps of Monte Carlo Simulation

The generation of a Monte Carlo simulation is subdivided into several steps, which are visualised in Figure 6.1. The simulation has to deal with the hard subprocess, and the evolution of the particles to final state objects. This implies the showering of the partons, the hadronisation process and the decay of unstable particles. In the following each part is explained briefly.

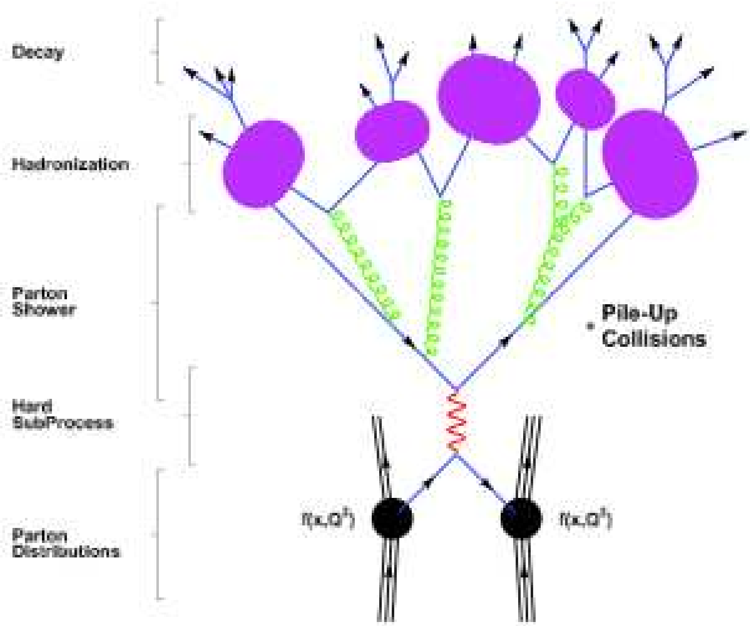

Figure 6.1. The basic steps in the generation of a simulated event. The event generation starts with the hard subprocess of the simulated process, incorporating the parton distribution of the colliding hadrons. The parton shower evolves the partons from the hard interaction to jets, which are afterwards hadronised into compound particles, which decay further if they are not stable. Furthermore, pile up is added to the event, which stems from other beam particle interactions during the same bunch crossing (Dobbs, 2004).

6.2.1 Parton Distribution

As described in chapter 2 the constituents of the hadrons are parameterised by parton distribution functions. The simulation relies on the momentum fraction x of the quarks and gluons, to describe the kinematic range in which the hard scattering process takes place.

6.2.2 Hard Process

In theory the hard process is described by the corresponding matrix element M for the physical event, which can be determined by the Feynman rules. The square of the matrix element $|M|^2$ is proportional to the differential cross section dE of the event occurring in a certain part of the phase space dN. The phase space, a multi dimensional hypercube, is spanned by the degrees of freedom of the matrix element e.g. the coordinates, the momentum, or the spin of the particles considered. Monte Carlo tools exploit the information given by M by sampling the phase space with uniformly distributed random numbers. In the case of a cross section integrator, physical distributions of a certain variable are gained by filling the weight dE into a histogram. In contrast, events generators produce the events with the frequency which the theory predicts. Those events are not weighted by the differential cross section. The individual event then represents what might be observed in the experiment, but has itself no physical meaning in the sense of a distribution of an observable. Only a large number of randomly generated events can be taken to predict an observable.

6.2.3 Parton Shower

The parton shower adds higher order QCD effects to the hard process. Gluon radiation is added to initial- and final-state partons. The evolution of the parton shower is characterised by the momentum fraction z of the radiated particles, its azimuthal angle and the flavour of the emitted particles in case of a gluon splitting. The branching of the partons is described with the DGLAP (Gribov, 1972; Lipatov, 1975; Altarelli and Parisi, 1977; Dokshitzer, 1977) splitting function. The showering of a parton is finished when a certain cutoff point is reached, to avoid infrared singularities. No more particles can be emitted by that parton. The showering of one parton results in a jet of quarks and gluons, moving approximately in the direction of the initial parton. The parton jet is organised in a way, that colour singlets can be formed out of its constituents.

6.2.4 Hadronisation

Since free particles are colourless objects, the partons have to be grouped to colour singlets to achieve a realistic outcome of the simulation. The scale of hadronisation is in the non-perturbative regime, because the strong coupling constant becomes large at low momenta. Therefore, perturbation theory is no more applicable. The hadronisation models are based upon phenomenological assumptions, which are tuned to experimental data. The choice of a hadronisation model has a rather small impact on the topology of the generated event, since this process takes place at low energies compared to the hard scattering process. Currently, two models are the most effective at describing data: the Lund string model, implemented in PYTHIA, and the cluster model implemented in HERWIG.

6.2.5 Hadron Decays

The hadrons grouped together by the hadronisation process often are short lived resonances, which have to be decayed into long living particles. The simulation of the hadron decay is realistic, since the decay rates are well known from various experiments.

6.2.6 Underlying Event and Pile-up

The hadronisation system after the hard scattering process also includes the coloured hadron remnants, which are left behind after the partons are kicked out of the initial hadron. This effect is called underlying event. This also includes multiple parton interactions from the same collision. Events, which stem from other beam particle interactions during the same bunch crossing are called pile-up or minimum bias events. Those have to be added to obtain a realistic simulation.

6.3 Parton Generator

As described before, the generation of simulated events can be subdivided into several steps. In the following an introduction is given to some commonly used Monte Carlo tools for this task. Parton generators compute the hard process on basis of tree-level matrix elements with a fixed number of final states. Those are described in the lowest order of perturbation theory to avoid regularization problems of the matrix element due to virtual loops. The final state consists of bare partons. Usually no hadronisation is performed.

6.3.1 Alpgen

Alpgen (Mangano, 2003.] is an event generator for simulating hard multi-parton processes in hadronic collisions. The matrix elements for many parton processes are calculated in leading order in QCD and electroweak interactions. The parton level events contain full information on the colour and flavour structure. The evolution of the parton shower has to be performed afterwards with external software. Alpgen is specialised for multi-jet final states originating from QCD radiation. Next-to-leading order corrections have to be applied with the parton-shower generator.

6.3.2 MLM matching

After the showering process the produced jets have to be matched against the partons from the hard process. This has to be done to eliminate the dependence of the physical cross section from cuts on generator level and to avoid double counting. Double counting arises from configurations, where jets stem from higher order calculation as well as from hard emission during the shower evolution. The matching procedure also allows to construct inclusive event samples, containing events with all jet multiplicities as well as samples containing only a distinct number of jets. The matching keeps only events when all partons are matched to a single jet without any ambiguities.

6.4 Shower Generator

The hard process generated with the tools mentioned above has to be showered and hadronised to obtain a physical simulation. The shower evolution of a specific parton adds higher order QCD effects to the simulation. The single partons have to be grouped into colour-singlet hadrons, which are decayed to stable particles. The showering and hadronization tools also add the underlying event structure from beam remnants and multiple parton interactions. The evolution of the hard process is based on phenomenological models which have to be tuned to experimental data.

6.4.1 Pythia

Pythia (Sjostrand, 2006) is a tool for the evolution from a few-body hard process to a complex multi-hadronic final state. It is capable of producing the hard process by itself. But events produced with other matrix element generators can be processed also. Pythia models the initial- and final-state parton showers, multiple parton interaction, beam remnants, string fragmentation, and particle decays. The parton shower algorithm is based on a p_T-ordered evolution. The hadronization is based on the Lund string fragmentation, which assumes a linear confinement between two quarks. Between two partons moving apart from each other, a colour flux tube is stretched. The energy stored in the potential increases linearly with the distance of the particles. The string breaks apart when a new quark-antiquark pair can be produced. Consequently, two new colour singlets are produced. A schematic view of the PYTHIA work flow is presented in Figure 6.2.

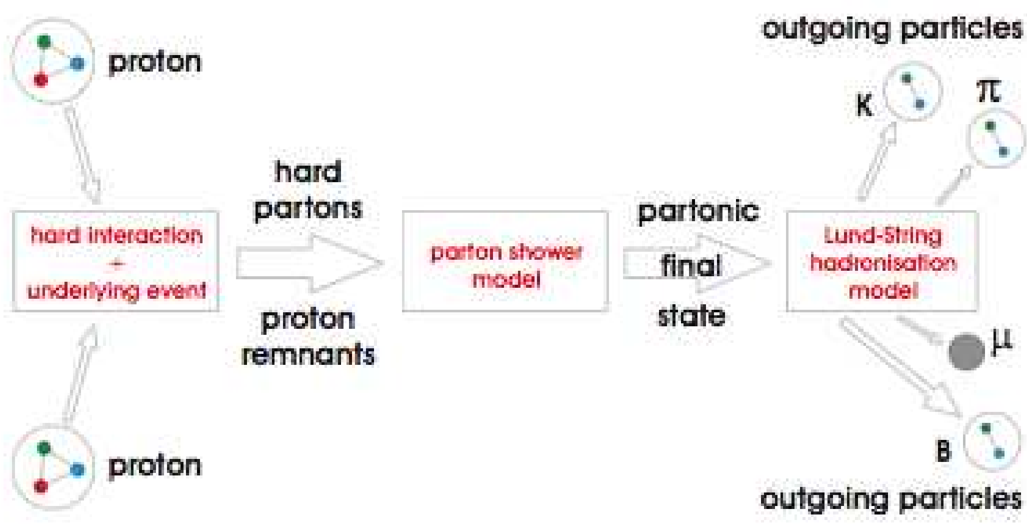

Figure 6.2. Schematic view of the PYTHIA event generation work flow. The hard interaction between two partons of the incident protons is calculated. The outgoing hard partons and the proton remnants are then passed to the parton shower model and the partonic final state is formed. Afterwards, a hadronisation procedure is performed and outgoing hadrons according to the Lund-String model are produced.

6.4.2 Herwig

Herwig (Corcella, 2001) is a comprehensive tool for hard particle collisions. The first-order matrix elements are matched with the corresponding parton shower. Spin correlations and heavy quark decays are also taken into account. The initial- and final-state jet evolution via gluon radiation is achieved with angular ordering. The energy radiated by the parton depends on its space-like virtuallity. The jet hadronisation is performed using the cluster model based on non-perturbative gluon splitting. To form colour neutral objects, the pre-confinement of the perturbative QCD shower is exploited. All gluons are split to quark-antiquark pairs. The colour singlet cluster is formed by the particles next to each other. The clusters are decayed until they are light enough to form a stable particle.

6.5 Analysis Framework

In the following the detector software framework and the Monte Carlo data used in this analysis are described.

6.5.1 CMS Offline Software

In this analysis the CMS software framework CMSSW_1_5_2 and CMSSW_1_6_12 used. The software environment provides all necessary modules for event simulation, reconstruction, detector calibration, and alignment related to the CMS experiment. Data is stored in the Event Data Model (EDM), which is capable to hold different types of data from Monte Carlo simulations, raw detector readout, or reconstructed high level objects needed for the physics analysis. The CMSSW framework is modularised in that way that only those parts of the software are loaded which are necessary for the individual job.

6.5.2 Simulated Event Data

The output of the Monte Carlo simulation for the different processes is handed to a full detector simulation of the CMS detector. The Geant 4 (Dellacqua, 1994) package is used for propagating the particles through the detector and simulating the interplay with the detector matter. Finally, the detector response and expected signals for the individual particles is simulated. These Monte Carlo events can be treated as if they were observed data. Later on, when the experiment is running, those can be compared to the measured signals.

The Monte Carlo QCD samples used in this analysis. The showering of all samples is performed with the Pythia package version 6.2.4. The signal Monte Carlo data of the QCD-2jet production process is generated with PYTHIA. The hard subprocesses of the QCD are generated with Alpgen and HERWIG. The datasets used were produced in the Spring 2007 Monte Carlo generation.

The process is 2→2 parton scattering via the strong interaction, plus a parton shower, hadronization, and a full detector simulation. That gives not just pure clean isolated dijets, but also multijets to the extent that they come from initial and final state radiation on top of a 2→2 process. We call it dijets, because that is the underlying hard scattering process before we add in initial and final state radiation and an underlying event.

This process is not the full standard model, which includes production of photons, W and Z at the vertices (electroweak vertices in addition to strong vertices). It's just production of partons (quarks and gluons) in the 2→2 process.

7. JET SHAPES ANALYSIS AND RESULTS

In this chapter, we present a study of jet shapes at particle and calorimeter levels in the central region of the CMS detector and compare the results obtained with various Monte Carlo generators. The sensitivities of jet shapes to the underlying event models and to the flavor of the initiating parton are also explored.

7.1 Datasets

QCD dijet events were generated with PYTHIA in $15 < \hat{p}_T < 5000$ GeV range, ALPGEN in $20 < \hat{p}_T < 5600$ GeV and HERWIG++ in $50 < \hat{p}_T < 7000$ GeV, where $\hat{p}_T$ refers to the transverse momentum in the hard-scatter of partons. Results of this study extend up to jet p_T= 1.4 TeV which is the approximate sensitivity limit for a 10 pb^{-1} integrated luminosity sample of LHC collisions at 14 TeV. Expected number of events for 10 pb^{-1} of integrated luminosity is summarized in Table 7.1 for different High Level Trigger (HLT) thresholds.

We used calorimeter energy deposits to explore the largest p_T range possible. Tracks can be used to measure jet shapes at low and medium p_T, and to help estimate systematic uncertainties. The calorimeter jet p_T was corrected using CMS standard jet energy corrections (Bhatti, 2007). Calorimeter towers and reconstructed tracks were required to satisfy the E_T=0.5 GeV threshold while no such threshold was applied to particles when reconstructing generator-level jets.

Generated jets were simulated and digitized with CMSSW_1_6_12 for PYTHIA (Sjostrand, 2006) and ALPGEN (Mangano, 2003) and CMSSW_1_8_4 for HERWIG++ (Bahr, 2008b) samples. ALPGEN generated events also were used to verify the PYTHIA correction factors using a different data set. Figure 7.1 shows the quark-gluon jet fraction as a function of jet p_T in the PYTHIA samples. It was determined by matching the two leading p_T jets in the event with the two outgoing partons from the hard scatter within a distance $\Delta R < 0.5$ in (y, ϕ) space.

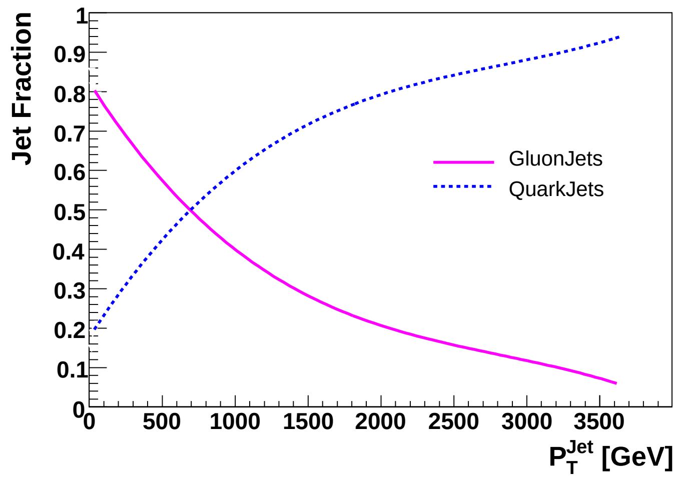

Figure 7.1. Fraction of the quark or gluon initiated jets as a function of jet P_T for $|\eta| < 1$ (from PYTHIA DWT).

7.2 Jet Cleanup

In addition to jets that originate from the hard scattering of partons, we will likely observe large calorimeter signals originating from occasional occurrences of catastrophic noise, beam-halo energy deposits, and cosmic ray air showers. While their rate of occurrence may be small compared to low p_T jets, it could be significant compared to higher p_T jets. One thing all these noise sources share in common is that unlike dijets they most often produce large amounts of missing E_T (MET) compared to the total E_T (ΣE_T) in the event. In Figure 7.2 we show the distribution of $\not{E}_T/\sqrt{\sum E_T}$ for a $\hat{p_T}$ bin of the QCD sample. The distribution is peaked at low MET/ΣE_T, characteristic of a dijet event.

For data, we will use events with one and only one vertex to minimize contribution from pile-up, and to remove some non-physics events. Clean-up selections will be used to reject cosmic ray events and non-physics events such as beam halo and catastrophic noise. In particular, we plan to use cuts on missing E_T relative to total E_T in the event, and fractions of total jet p_T detected in the electromagnetic calorimeter and carried by the associated charged tracks. These cuts are expected to be fully efficient for QCD dijet events and are discussed below. The values of the cuts will be determined by looking at the data.

7.2.1 Missing E_T Significance

This cut will be used to remove cosmic rays and detector related beam background events. Figure 7.2 shows the distribution for $\not{E}_T/\sqrt{\sum E_T}$ in QCD events. It indicates that one can safely require $\not{E}_T/\sqrt{\sum E_T}$ <5.

7.2.2 Event Electromagnetic Fraction

In the preselection of data, to distinguish real jet events from fake events, the Event Electromagnetic Fraction (F_{EM}) cut can be applied. F_{EM} distribution, shown in Figure 7.3, is defined as

$$F_{EM} = \frac{\sum_{j=1}^{N_{jet}} P_T^j \cdot f_{EM}^j}{\sum_{j=1}^{N_{jet}} P_T^j} \tag{7.1}$$

for jets within the acceptance of the electromagnetic calorimeter, $|\eta| < 3$. f_{EM}^j is the jet electromagnetic fraction of the jet j. Normally, events are expected to have the electromagnetic fraction between 0 and 1, but not close to the edges. Non-physics energy, for example energy from a halo muon, may be deposited either in the hadronic or in the electromagnetic calorimeter only, and thus have F_{EM} either close to 0 or 1.

7.2.3 Event Charge Fraction

The Event Charge Fraction is defined as the sum of the P_T of the tracks associated to the jet for jets within $|y| < 1.7$. The event charge fraction is formulated as

$$F_{ch} = \frac{1}{N_{jet}} \sum_j \frac{(\sum_i^{tracks} P_{Ti})^j}{P_T^j} \tag{7.2}$$

where for every jet the sum runs over the tracks that can be matched in (y, ϕ) space to that jet; the average over the charge fraction is taken for all jets within $|y| < 1.7$. Event charge fraction distribution for good events is also shown in Figure 7.3. Background events from beam halo or cosmic rays are expected to have $F_{ch} = 0$, and can be removed by requiring $F_{ch} > 0$, with minimal loss in efficiency.

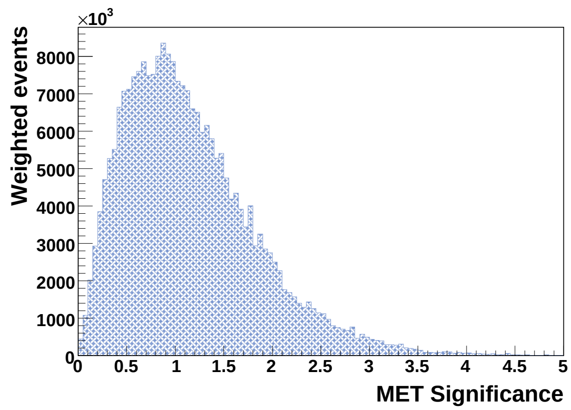

Figure 7.2. Distribution of MET significance $\not{E}_T / \sqrt{\sum E_T}$ in QCD events.

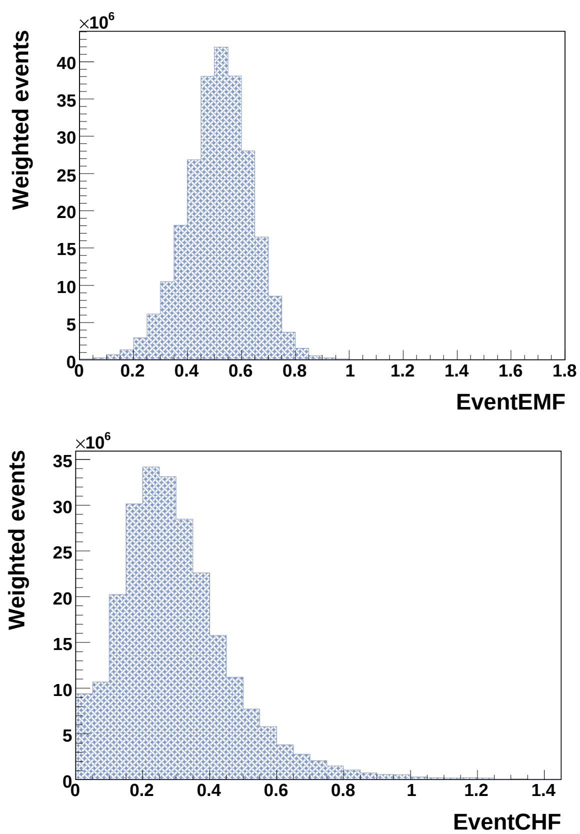

Figure 7.3. Event Electromagnetic Fraction (EventEMF) and Event Charge Fraction (EventCHF) distributions in QCD events.

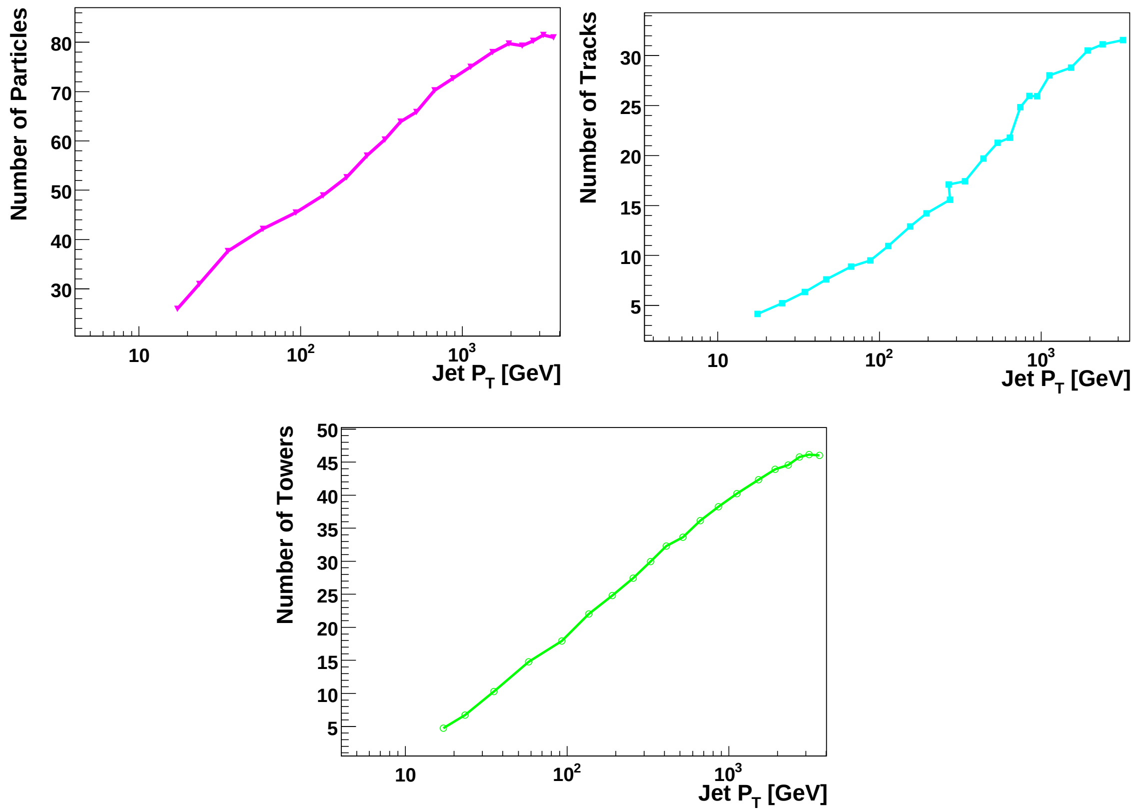

Figure 7.4. Mean multiplicities of particles, tracks and towers in a jet as a function of jet p_T. Statistical errors are too small to be visible.

7.3 Multiplicity of Jet Constituents

Figure 7.4 summarizes the mean multiplicities of particles, tracks and calorimeter towers in a jet as a function of jet p_T. As expected, they increase logarithmically with increasing jet p_T. See the Figures A.1, A.2 and A.3 in appendix A for the multiplicity distributions for particles, calorimeter towers and tracks in a jet, respectively, in some selected P_T bins.

7.4 p_T Distributions of Particles, Tracks and Towers In a Jet

p_T distributions of particles, tracks and towers in a jet are shown in Figures 7.5, 7.6 and 7.7, respectively. These distributions become harder with increasing jet p_T.

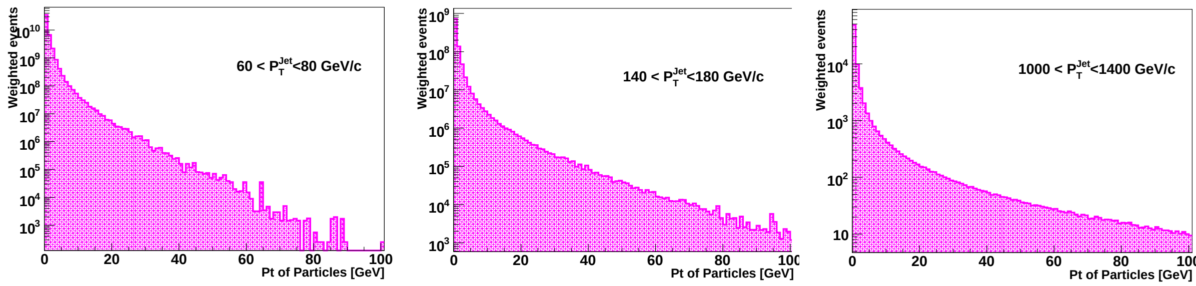

Figure 7.5. p_T distributions of particles in a jet for selected jet p_T bins.

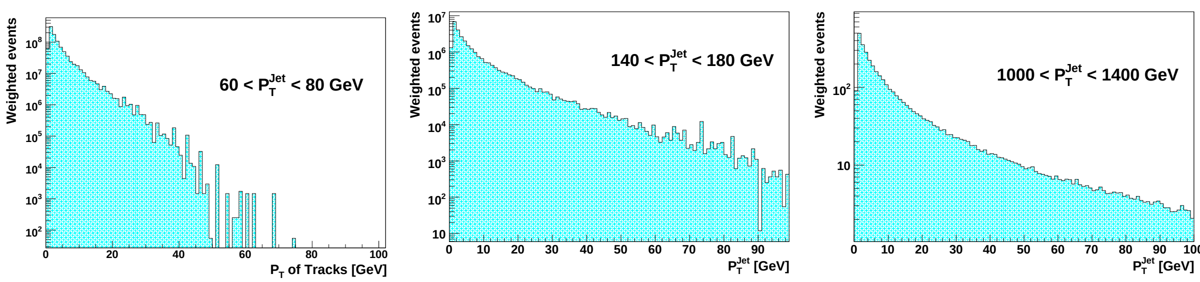

Figure 7.6. p_T distributions of tracks in a jet for selected jet p_T bins.

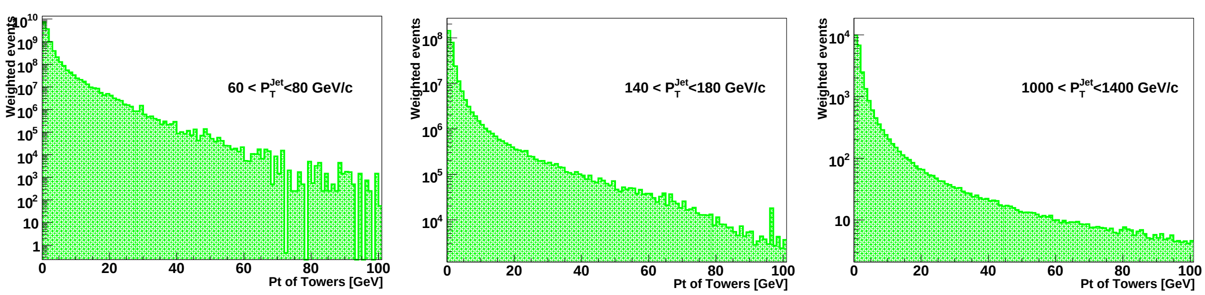

Figure 7.7. p_T distributions of calorimeter towers in a jet for selected jet p_T bins.

7.5 Jet Shapes: Results

The initial introduction to jet shapes was given in section 2.3.3. Briefly, the jet shape is defined as the average fraction of the jet transverse momentum within a cone of a given size r around the jet axis, $r = \sqrt{(y_i - y_j)^2 + (\phi_i - \phi_j)^2}$, where i refers to the particle, calorimeter tower or track, and j to the jet. As mentioned before jet shapes can be studied by using an integrated or a differential distribution. In the present study only two leading jets within $|y| < 1$ are considered per event. All particles and calorimeter towers within distance $R = \sqrt{(\Delta y)^2 + (\Delta\phi)^2} = 0.7$ from the jet axis are used. This large cone size ensures that most of the parent parton energy is included in the jet. In practice, the average jet shapes are measured, where the average is taken over all jets in the samples. Equation 2.17 for the integrated shapes (see Figure 2.13) becomes

$$\psi(r) = \frac{1}{N_{jets}} \sum_{jets} \frac{P_T(0,r)}{P_T(0,R)} \tag{7.3}$$

where $P_T(0,r)$ is the scalar sum of transverse momenta of all particles within the distance r from the jet axis with $\psi(r = R) \equiv 1$. The differential distribution, $\rho(r)$, was illustrated in Figure 2.12. It is defined as the fraction of the jet transverse momentum contained inside an annulus of inner radius $r - \delta r/2$ and outer radius $r + \delta r/2$ around the jet axis, such that $0 \leq r \leq R$. Similarly, for the differential jet shapes, $\rho(r)$, Equation 2.18 becomes

$$\rho(r) = \frac{1}{\delta r} \frac{1}{N_{jet}} \sum_{jets} \frac{P_T(r - \delta r/2, r + \delta r/2)}{P_T(0,R)}. \tag{7.4}$$

Above, N_{jet} denotes the total number of selected jets. In the numerator P_T is the sum of all particles, tracks or towers in the distance range $(r - \delta r/2, r + \delta r/2)$ from the jet axis. In the denominator, $P_T(0,R)$ is the scalar sum of transverse momenta of all the particles, tracks or towers within the cone of radius R. The jet shape is affected by fragmentation and gluon radition. However, at suffeciently high E_T^{jet} the most contribution is predicted to come from gluon emission of the primary parton and, therefore, is calculable in pQCD. To calculate the jet shapes, we made histograms of transverse momentum in a cone of the appropriate bin of r divided by the transverse momentum in the cone $R = 0.7$ for $r = 0.1, 0.2, \ldots, 0.7$. The mean value of these histograms was then plotted as function of r. The statistical uncertainty on each point was calculated as $rms/\sqrt{N}$, using the rms of the corresponding histogram and the number N of expected jets in the bin for luminosity of 10 pb^{-1}. For the integrated shape the uncertainties at different r points are partially correlated. We used 20000 events in each $\hat{p}_T$ bin. The samples have been combined according to the cross section weights.

7.5.1 Raw Jet Shapes

Figure 7.9 shows the differential jet shapes for PYTHIA events at generated and calorimeter levels (see Figures B.4, B.5 and Figure B.6 and B.7 in AppendixB for all P_T bins). Most of the momentum is concentrated at the small radius region. Jet shapes become narrower with the increasing P_T of the jet. Underlying event contribution as the fraction of jet P_T is larger at low P_T and at large radius. Integrated jet shapes in Figure 7.10 become narrower with increasing P_T for both particle and calorimeter levels (see also Figures in Appendix).

7.5.2 Jet Shape Corrections

Due to various detector effects, the measured (calorimeter) jet shapes are different than the true (particle) jet shapes. Due to the magnetic field of CMS, charged particles with $P_T < 0.9$ GeV do not reach the calorimeter. In addition showers from particles interacting with the detector material spread their energy over many calorimeter towers. The measured jet shapes with the calorimeter must be corrected to the hadron level for these detector effects. Correction factors were determined as a function of distance from the jet axis using MC events before and after the CMS detector simulation. For this approach to be valid, the MC simulation must describe the calorimeter response accurately. As will be discussed in Section 7.10 we plan to cross-check this assumption using tracking information. The corrections have been determined using unmatched jets and are applied as a function of distance from the jet axis.

The correction factors $D(r)$ and $I(r)$ for differential and integrated jet shapes are defined in Equations 7.5 and 7.6, respectively:

$$D(r) = \rho_{MC}^{PARTICLE}(r)/\rho_{MC}^{CAL}(r) \tag{7.5}$$

$$I(r) = \psi_{MC}^{PARTICLE}(r)/\psi_{MC}^{CAL}(r) \tag{7.6}$$

where calorimeter towers and generated particles have been used to reconstruct differential $\rho_{MC}^{CAL}(r)$, $\rho_{MC}^{PARTICLE}(r)$ and integrated jet shapes $\psi_{MC}^{CAL}(r)$, $\psi_{MC}^{PARTICLE}(r)$ in different bins of jet P_T. Measured calorimeter jet shapes are then used to determine the corrected differential jet shapes $\rho^{corrected}(r) = D(r) \cdot \rho^{CAL}(r)$ and integrated jet shapes $\psi^{corrected}(r) = I(r) \cdot \psi^{CAL}(r)$. The correction factors $D(r)$ in Figure 7.11 (see also Figures B.8 to Figure B.11 in Appendix B) do not show a significant dependence on jet P_T in the region $r < 0.5$. They vary between 0.6 and 1.3 as a function of r, and between 1.3-2 for the region $r > 0.5$. The correction factors for integrated jet shapes in Figure 7.12 (see also Figures in Appendix) vary from 0.9 to 1.06 for all radius and P_T bins. For the integrated distributions, the correction factors do not have a strong dependence on jet P_T.

7.5.3 Corrected Jet Shapes

The corrected differential and integrated jet shapes are shown in Figures 7.9 and 7.10 (see Figures B.4, B.5 and Figure B.6 and B.7 in AppendixB for all P_T bins).Close to the jet axis, the jet shape is dominated by collinear gluon emission, whereas at large distance from the jet axis, the jet shape reflects large angle gluon emissions, which can be calculated perturbatively. The jet shape $\psi(r)$ increases faster with r for jets at larger P_T indicating that these jets are more collimated.

7.5.4 Sensitivity of Jet Shapes to Underlying Event Tunes

Jet measurements are affected by the presence of multiple semi-hard interactions from other parton-parton pairs from the proton-proton collision of interest, i.e. the underlying event (UE) of the same collision. In addition, the physics environment at the LHC is also affected by additional minimum bias (MB) collisions of other proton pairs in the same bunch crossing as mentioned in chapter 2. Both effects limit the efficiency for reconstructing the hadron-level jets (and ultimately the parton-level jets) from the hard scattering (signal) and also add complex features to the already non-trivial detector jet signals. From the point of view of jet shapes measurement, the energy from the underlying event (UE) contributes to jets and impacts the jet shapes. To determine the sensitivity of jet shapes to the UE contribution, event samples were generated using PYTHIA DW which has a smaller UE contribution than PYTHIA with tune DWT, which is the CMS default setting (CMS Collaboration, CMS-Note-2006/067.). These tunes are different extrapolations to $\sqrt{s}$ = 14 TeV of the same tune at the Tevatron energy $\sqrt{s}$=1.8 TeV. The jet shapes for PYTHIA DWT and PYTHIA DW are shown in Figure 7.13 (see also Figures in Appendix) for the differential jet shapes and in Figure 7.14 (see also Figures in Appendix) for the integrated jet shapes. At low jet P_T, one can observe the difference in jet shapes due to the UE contribution. This comparions has been done in the transverse region (see Figure 2.7) where the sensitivity to the UE is higher for the dijet events.

7.5.5 Jet Shapes from ALPGEN Samples

We tested the corrections derived from PYTHIA on an independent sample generated using ALPGEN (Mangano, 2003). For this sample the parton showering and hadronization models are the same as used by PYTHIA. Figure 7.15 shows the differential jet shapes at particle and corrected calorimeter levels for ALPGEN multi-jet samples (see also Figures in Appendix). Figure 7.16 shows the corrected integrated jet shapes (see also Figures B.12 to B.15 in AppendixB). Correction factors determined from PYTHIA DWT events work reasonably well for ALPGEN, as expected since the parton showering and hadronization is done by PYTHIA.

7.5.6 Quark and Gluon Jet Shapes

Jet shapes are sensitive to quark and gluon jet contributions. Using parton information from PYTHIA we classified hadron level jets based on matching within $\Delta R < 0.5$ in (y, ϕ) space. The MC predicts that the measured jet shapes are dominated by contributions from gluon initiated jets at low jet P_T while contributions from quark initiated jets become important at high jet P_T. Figures 7.17 and 7.18 compare differential and integrated jet shapes for quarks and gluons with simulated data (see also Figures B.16 to B.19 in AppendixB). As expected, quark jets are narrower than the gluon jets due to the coupling strengths for gluon emission which depend on the color factors C_F=4/3 for radiating quarks and C_A=3 for gluons. Fraction of gluon jets in the sample is higher at lower jet P_T.

Figure 7.19 presents the P_T fraction contained in the jet cone $R = 0.7$ lying outside a cone of r = 0.2 as function of the jet P_T. Reconstructed calorimeter jets from the full CMS Monte Carlo simulation are compared with parton shower MC predictions for quark and gluon jets. Tables 7.2, 7.3 and 7.4 provide details of the calculation of statistical and systematic uncertainties for $1-\psi(r=0.2)$ in all P_T bins.

7.6 Systematic Uncertainties

The main sources of systematic uncertainties include:

- Jet energy scale
- Transverse shape of calorimeter showers
- Non-linearity of calorimeter response
- Jet fragmentation

The uncertainties arising from jet energy and position resolution, and from event selection cuts are expected to be negligible compared to the sources listed above and are not considered.

7.6.1 Jet Energy Scale

In the pp collisions hadrons experience scattering in their rest frame of momentum and the measurements of the processes often depend on the determination of the four-momenta of quarks and gluons produced in the hard scatter. The measurement of these four-momenta relies on the reconstruction of hadronic jets in the calorimeter, resulting from the quark or gluon fragmentation. The jets are corrected with the absolute corrections to transform the jet energy measured in the calorimeter into the energy corresponding to the underlying particle jet. After this correction the energy scale of a jet becomes independent from the detector. The jet corrections depend on the multiplicity and p_T spectrum of the particles inside a jet and on the response of the calorimeter to an individual particle. In general, jet corrections depend on the initial parton type, for example jets from gluons and from quarks have different multiplicities and on average gluon gives larger multiplicity, and therefore different physics processes may require different corrections. In the jet energy measurement and the correction processes there are systematical uncertainties. The systematics for jet energy scale (JES) include the uncertainties on the absolute jet energy corrections, calorimeter stability, underlying event and relative jet energy corrections.

The uncertainty on the jet energy scale (JES) will be determined from data. Current expectation of the JES uncertainty at start up is $\pm10\%$ (Bhatti, 2007). Changing the JES correction within its uncertainty changes the jet shapes as jets migrate between P_T bins. Jet shapes vary slowly with jet P_T and thus this effect is expected to be small. To determine the impact on the jet shapes, we changed the P_T of the jet by $\pm10\%$ and repeated the whole analysis. The comparison between the default JES corrections and the modified corrections is shown in Figure 7.20 (see also Figures B.20 and B.21 for differential jet shapes and Figures B.24 and B.25 for integrated jet shapes in AppendixB). The corresponding systematic uncertainties on the differential jet shape are 10% at r=0.1 and $< 5\%$ at r =0.2 for all jet P_T.At larger $r \geq 0.5$ they are $< 20\%$.

The uncertainties on the integrated jet shape are 10% at r=0.1, 5% at r=0.2 for P_T <100 GeV, and decrease as a function of r. They are $< 2\%$ at r=0.1 for $P_T > 100$ GeV and negligible at r >0.1, as shown in Figure 7.21 (see also Figures B.22 and B.23 for differential jet shapes and Figures B.26 and B.27 for integrated jet shapes in AppendixB). (The systematic uncertainty at r=0.7 is 0 by definition of the integrated jet shape.)

7.6.2 Jet Fragmentation

Because the calorimeter response depends on the energies of the particles in the jets, modeling of jet fragmentation contributes to the uncertainty on the corrected jet shapes. Uncertainties due to the fragmentation model can be estimated by comparing results obtained using PYTHIA and HERWIG++. The model of the underlying event used in HERWIG++ is described in (Bahr, 2008).

Particle level differential and integrated jet shapes in PYTHIA DWT and HERWIG++ 2.2 (Bahr,2008a) are shown in Figure 7.22 and Figure 7.23 (see also Figures B.28 and B.29 for differential jet shapes and Figures B.30 B.31 for integrated jet shapes in AppendixB), respectively. Their observed difference is less than 5% at r <0.3.

To determine the systematic uncertainty due to modeling of jet fragmentation we compared PYTHIA DWT and HERWIG++ differential jet shape correction factors, shown in Figure 7.24 (see also Figures B.32 and B.33 in AppendixB). They agree to $<$ 10% for $r \leq 0.2$, however, the differences can be as large as $30-40$% at $r \geq 0.5$. Note that the jet energy fraction at large r is small, which makes uncertainties on the differential jet shape measurement large in this region.

Comparisons of the integrated jet shape correction factors for PYTHIA DWT and HERWIG++ are shown in Figure 7.25 (see also Figures B.34 and B.35 for in AppendixB). They agree within5% (2%) at r=0.1 (0.2) for $60 < P_T < 80$ GeV. For $P_T > 80$ GeV the differences range between $5-10$% at r=0.1 and are less than 5% at r=0.2. These differences decrease with increasing radius r for all jet P_T.

The correction factors have been also compared for PYTHIA DWT and PYTHIA DW simulations. The differences are less than 20% at r=0.1 and $<$ 10% at $r = 0.2$. For differential jet shapes at large r, they can be as large as $20-30$%. For integrated jet shapes, they become smaller for the high P_T jets and decrease with increasing r. The comparisons of correction factors for PYTHIA DWT and PYTHIA DW are shown in Figure 7.26 for differential jet shapes and in Figure 7.27 for integrated jet shapes (see also Figures B.36 and B.37 for differential and integrated jet shapes, respectively in AppendixB.)

7.6.3 Non-linearity of Calorimeter Response and Transverse Shower Profile

The uncertainties due to CMS calorimeter simulation can be estimated by comparing track jet shapes with calorimeter jet shapes in simulated and collider data. Here we assume that track reconstruction inefficiently and fake rate are small in both data and MC and have negligible effect on track jet shapes. These assumptions will be verified by comparing the track multiplicity and track p_T distributions in data and MC after applying the track reconstruction inefficiency and fake rate as measured from data. In addition, it is assumed that any difference in calorimeter response to photons in data and MC is much smaller than possible difference in calorimeter response to hadrons.

The differential track jetshapes are compared to calorimeter jetshapes in Figure 7.28 (see also Figures B.38 and B.39 for differential jet shapes in AppendixB). Their ratios can be seen in Figure 7.28 (see also Figures B.40 and B.41 for differential jet shapes in AppendixB). We will measure the same ratio in data and determine the scale factor SF as defined below. This scale factor quantifies the difference between the data and the simulation and if it is ~ 1, we plan to scale the corrections derived from MC by SF and add the deviation from unity as systematic uncertainty. Analogous procedure can be done for the integrated jet shapes.

$$SF = \frac{R^{DATA}}{R^{MC}} \tag{7.7}$$

where

$$R^{MC} = \frac{TrackJetShape}{CaloJetShape}_{MC},\ R^{DATA} = \frac{TrackJetShape}{CaloJetShape}_{DATA} \tag{7.8}$$

7.6.4 Monte Carlo Estimate of Systematics Due to Calorimeter Response

As mentioned above, the systematic uncertainties can not be derived before real data is available. In the absence of data, we estimated the size of the uncertainty due to a possible difference in calorimeter simulation and the expected real calorimeter response using a simple model. We determined the calorimeter jet shape obtained using a parameterized calorimeter response to single pions and compared it to the full simulation. The differ-

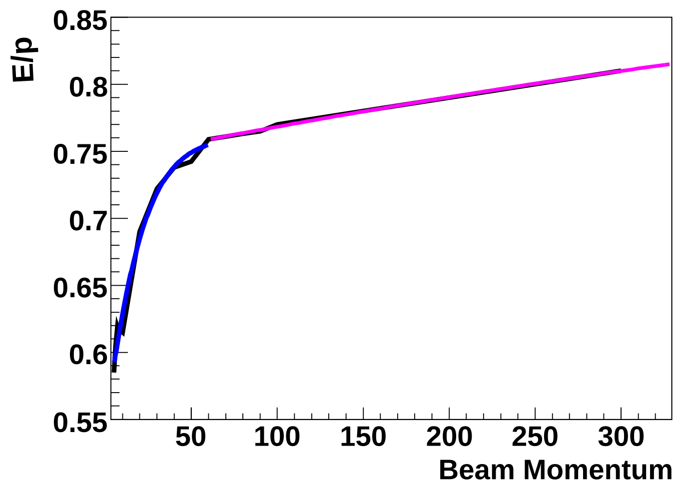

Figure 7.8. Single pion response from simulation.

ence in the two calorimeter jet shapes accounts for a) transverse spreading of the showers, b) material interactions and energy threshold effects in the calorimeter. It is a simplified model and thus only a fraction of this difference should be considered as systematic uncertainty. However, for the purpose of this paper we used the full difference as an estimate of the related systematics. In Section 7.6.5 we discuss the effect of ignoring the transverse shower spreading in the calorimeter. In Section 7.6.2 we discuss p_T dependent systematics for calorimeter response to single particles. Figure 7.8 shows the single pion response (in GeV) from the simulation. The E/p curve was fitted in two p_T sub-ranges ($p_T < 70$ GeV and $p_T > 70$ GeV) with the function given in the equation below:

$$f(x) = \frac{A}{1+Be^{-CX}} \tag{7.9}$$

We used variations of the E/p fit for estimating this part of the systematics.

7.6.5 Transverse Showering Spread

Calorimeter level shower shape is different than the particle level shape due to bending of charged particles in the magnetic field and to showering of particles in the calorimeter. To estimate the latter effect we used the parametrized E/p for single particle response to scale p_T of the particles. The scaled p_T was used to calculate new jet shapes, which take into account the E/p response but not the transverse shower spread. Response for the π^0, γ and e was taken as 1. Then we compared the calorimeter jet shapes obtained from a parameterized calorimeter response with calorimeter jet shapes obtained from full simulation. We consider the numbers below as upper limits on the expected uncertainties.

Figures 7.29 and 7.30 show the estimated impact of the transverse showering effect on differential and integrated jet shapes, respectively (see also Figures B.42 and B.43 for differential and Figures B.46 and B.47 for integrated jet shapes in AppendixB.). Figure 7.31 (Figure 7.32) shows the deviations from unity of the ratio of differential (integrated) jet shapes obtained using the parameterized response to those from full simulation (see also Figures B.44 and B.45 for differential and Figures B.48 and B.49 for integrated jet shapes in AppendixB.). Based on this comparison, we estimated the uncertainty for differential jet shapes as $< 40\%$ at r=0.1 and $< 20\%$ for r=0.2 at $60 < P_T < 80$ GeV, and $< 20\%$ for $r \leq 0.2$ at $80 < P_T < 100$ GeV. The deviation from unity at r=0.2 does not change much for jet $P_T >$100 GeV while at r=0.1 it decreases slowly as a function of jet P_T.

The transverse showering uncertainty for the integrated jet shapes is negligible for $r >$0.3 for all jet P_T. For $60 < P_T < 80$ GeV, the difference is 30% (10%) at r=0.1 (0.2) and decreases to 20% (10%) for r=0.1 (0.2) for 80 P_T <100 GeV jets. For jets with $P_T >$100 GeV, the difference is 10% at r=0.1 and negligible for $r >$0.1. In Figure 7.19, these differences are added in quadrature with the other sources of systematic uncertainty.

7.6.6 Linearity of the Calorimeter Response

The observed jet shape depends on the E/p response function for single particles. The uncertainty due to E/p simulation in the MC can be estimated by varying the single particle response function within its expected error.

As before, p_T of each track was scaled with the fitted E/p curve. Since no official estimate of uncertainty on E/p curve was available, we used an educated guess. We changed the E/p parameterization by $\pm$10% for p_T <50 GeV and by $\pm$5% for p_T >50 GeV and then we determined the new calorimeter jet shape. Figures 7.33 and 7.34 show the ”scaling difference” for differential and integrated jet shapes due to such $\pm 1\sigma$ variations of E/p (see also Figures B.50 and B.51 for differential and Figures B.52 and B.53 for integrated jet shapes in AppendixB.). For jets with 60< P_T <80 GeV, the differential jet shape changes by $< 2\%$ at the low radius (r=0.1) and $< 4\%$ at $r >$0.1 while the differences are negligible at r=0.1 for jet $P_T >$80 GeV. The integrated jet shapes are less affected by this scaling: $< 2\%$ at r=0.1, and negligible at $r > 0.1$.

7.7 Theory Comparison

As mentioned in chapter 2, jet shapes have been used to test perturbative QCD (pQCD) α_s^3 calculations (Abe, 1993; Abachi, 1995). It is the lowest order (LO) calculation which can be done for jet shapes, namely α_s^3 calculation. These leading order calculations involve only one additional parton in a jet.

Measurements of jet shapes can be compared to QCD calculations based on different approaches. These comparisons allow the study of the relative importance of parton radiation and fragmentation in the formation of a jet as well as the differences between quark and gluon jets. It should be noted that these two predictions refer to the hadron level. For these predictions, jets are searched for in the final state hadronic system using the same jet algorithm as in the simulated data.

For the LO (α_s^3) calculation, the program NLOJet++ (Nagy, 2002) is employed which would be completely sufficient for a simple comparison using the SISCone jet reconstruction algorithm with radius R=0.7. Renormalization factorization scales were set to $\mu = p_T$ as central and also $\mu = p_T/2$ and $\mu = 2p_T$ while seperation parameters were set to $R_{sep} = 1.3$ and $R_{sep} = 2$.

The PDFs for the NLOJet++ are taken from CTEQ6.6. The simulated MC event samples representing the collider data in this study have been generated with PYTHIA tune DWT at 14TeV. PYTHIA DWT is the CMS default setting (CMS Collaboration, CMS-Note-2006/067). Hovewer, private QCD samples were generated without UE parameter with the same PYTHIA tune DWT at the same center of mass energy in order to make hadron level to leading-order comparison. These samples employ the CTEQ (see Figure 7.38) 5 leading-order PDF set.

7.7.1 Corrections for Hadronization and the Underlying Event

NLO calculations can not be compared directly to calibrated calorimeter jets. In addition, the influence of the parton shower , hadronization and decays as well as the Underlying Event has to be taken into account and correction factors have to be applied to hadron level results in order to make reasonable comparison to the NLO result (in our case to the ”LO”). Unfortunately, this can not yet be done in a completely consistent manner for the NLOJet++ since most MC generation programs, do only allow for LO matrix elements to be coupled to parton showers and the subsequent hadronization.

In order to get the hadronization and the UE correction factors, private QCD(2→2) samples were generated without UE parameter. This is a necessary requirement for this comparison since the LO jet shapes does not contain hadronization and UE effect but particle level. Hence, the jet shapes have been derived from PYTHIA once for the partonic final state without Underlying Event and once for the hadronic final state, i.e. all stable particles, including the Underlying Event. The ratio of the latter to the former is then multiplied with the NLO jet cross section. The final results are shown as the ouncertainties. Figure 7.35 shows the particle level and LO (α_s^3) jet shapes with/without underlying events. The correction factors for the hadronization and underlying event derived from Figure 7.35 are shown in Figure 7.36 for the selected p_T bins.

We consider here the only central NLOJet++ predictions obtained for $\mu = p_T$ (see Figure 7.37). It shows how jet shapes agree well for particle level and LO+parton level after applied corrections to the LO calculation. A different choice of renormalization factorization scales (e.g. $\mu = p_T/2$ or $\mu = 2p_T$) only results in a few percent difference (see Figure 7.38) .

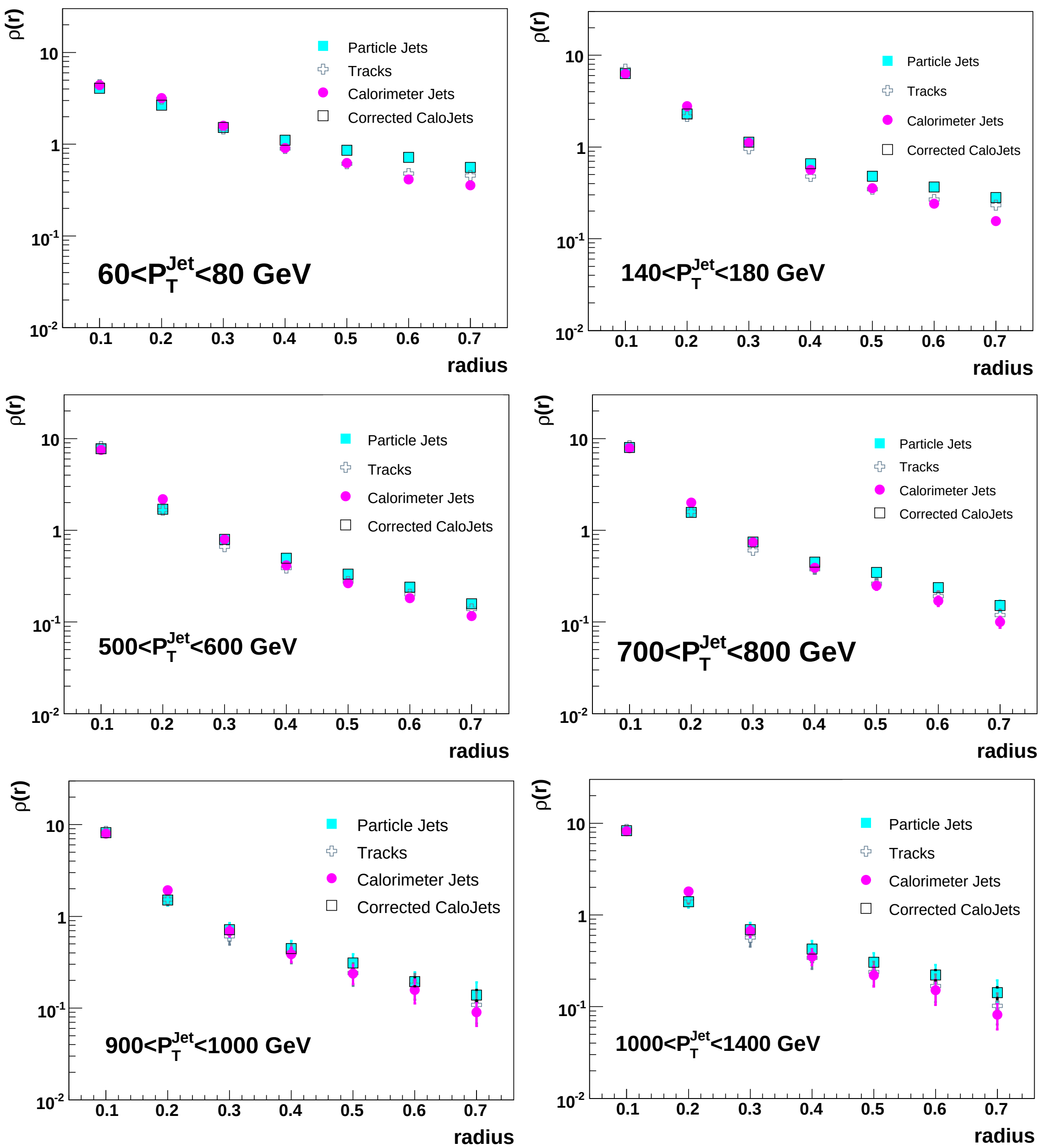

Figure 7.9. Differential jet shapes for selected p_T bins. Statistical errors are included.

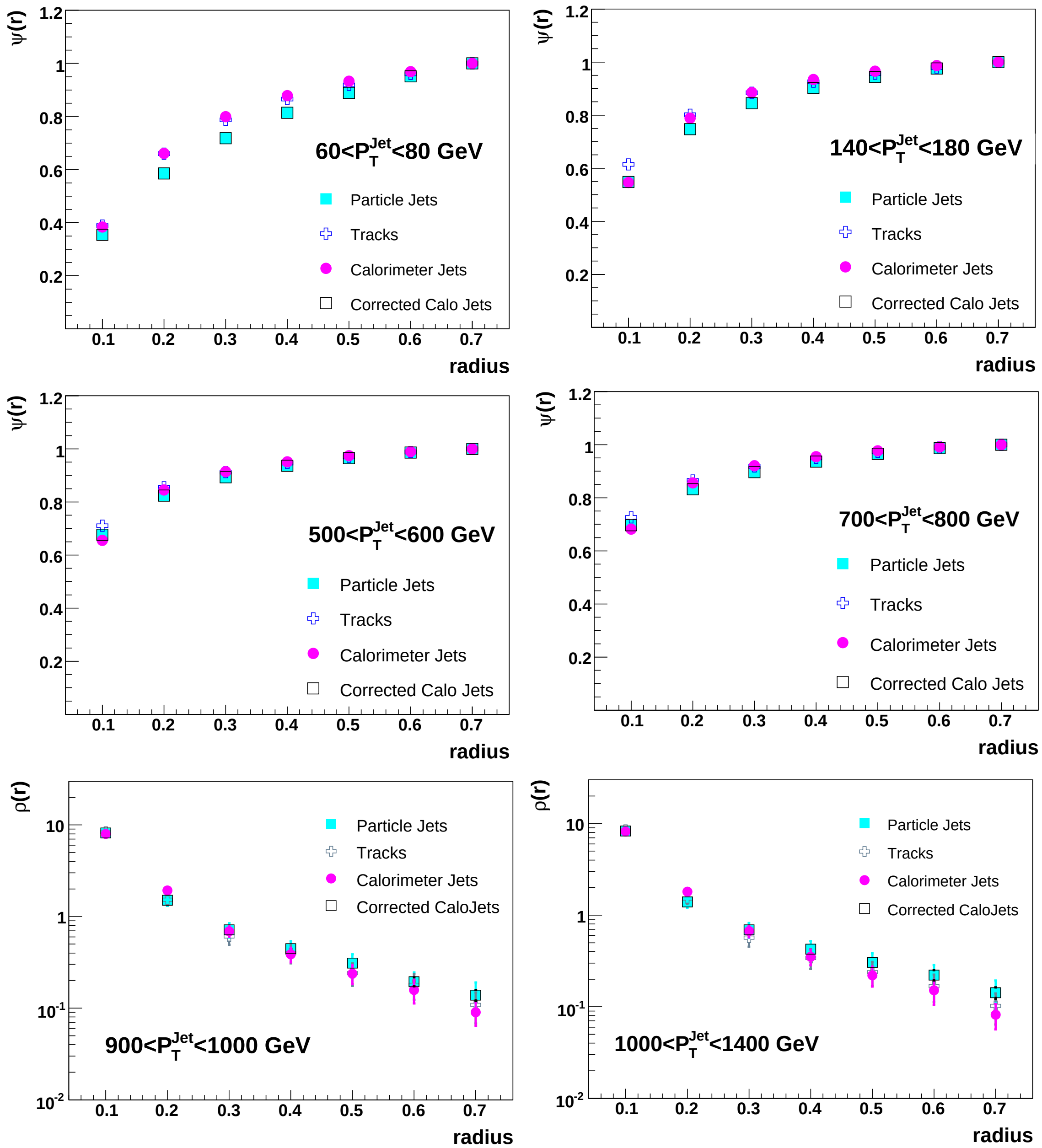

Figure 7.10. Integrated jet shapes for selected p_T bins. Statistical errors are included.

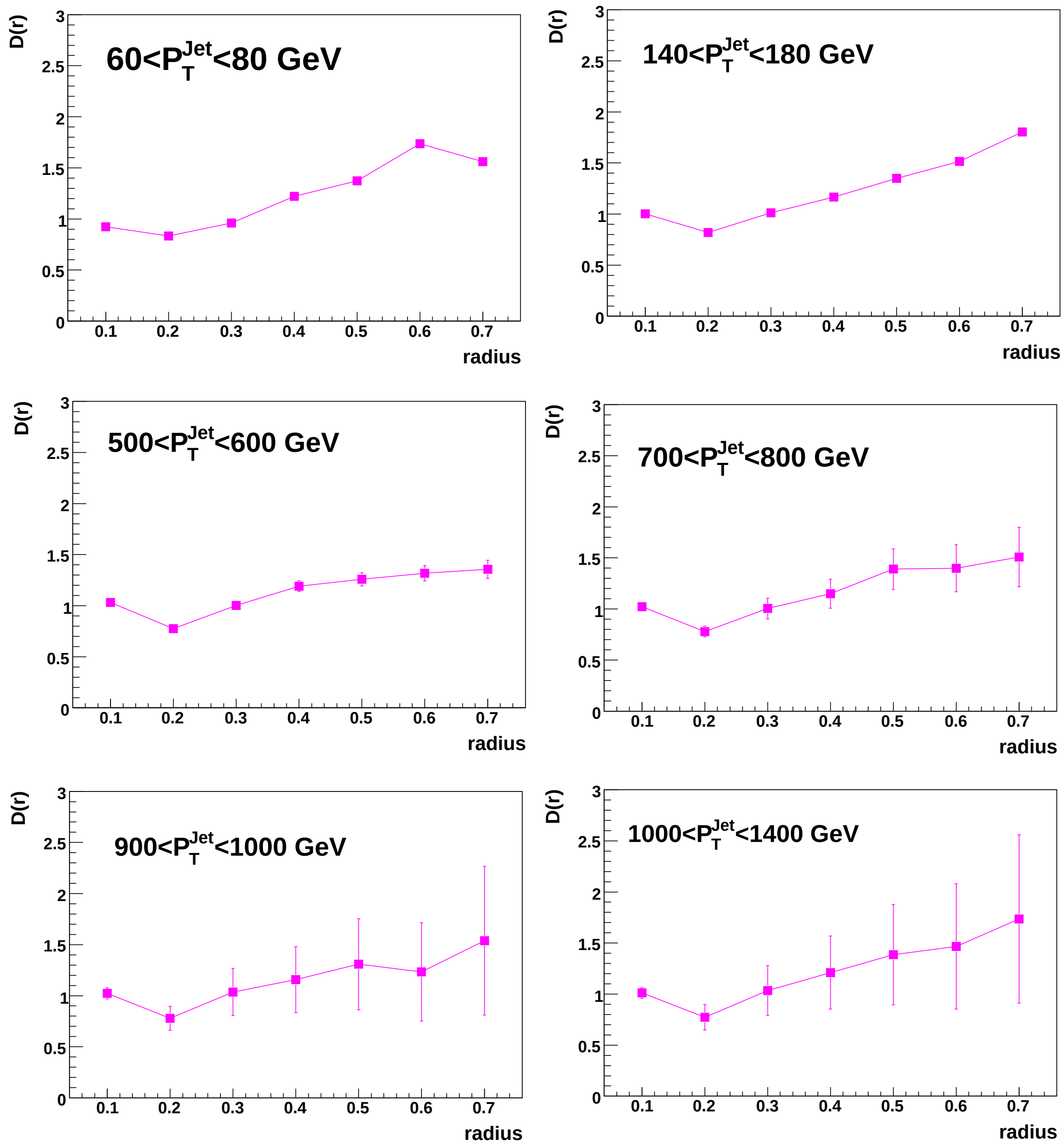

Figure 7.11. Correction factors for differential jet shapes for selected p_T bins. Statistical errors are included.

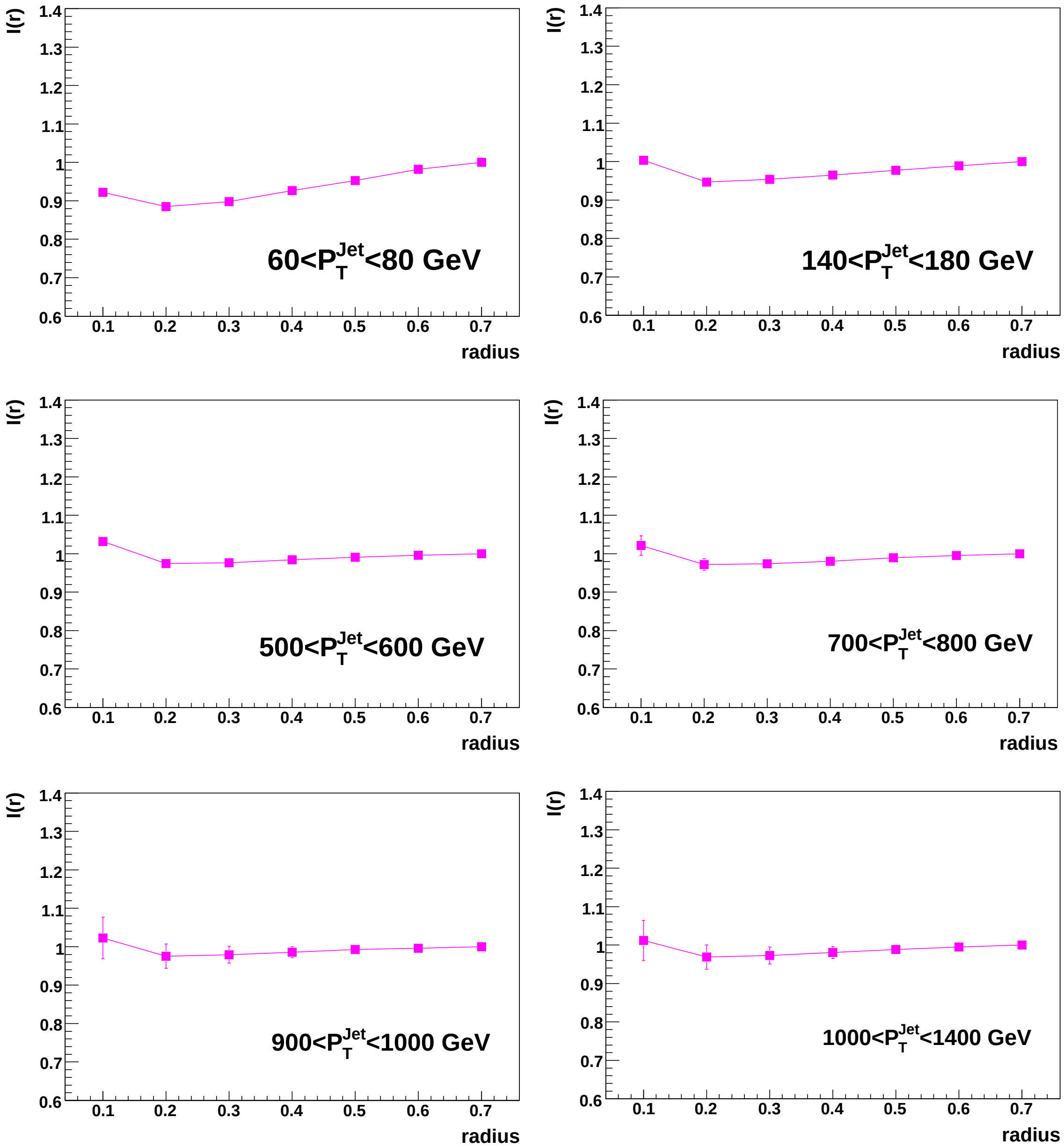

Figure 7.12. Correction factors for the integrated jet shapes for selected p_T bins. Statistical errors are included.

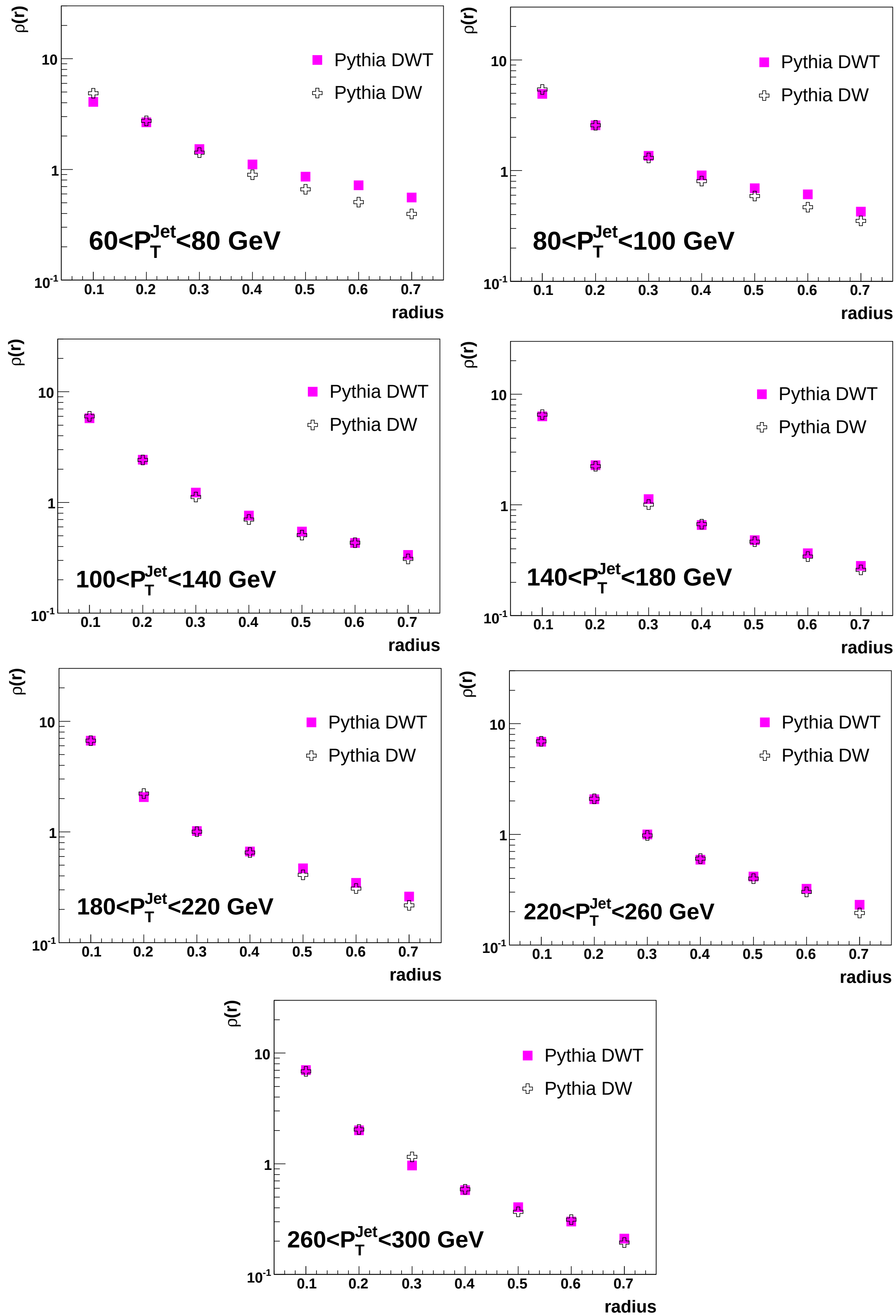

Figure 7.13. Comparison of differential jet shapes for PYHTIA tunes DWT and DW in selected p_T bins. Statistical errors are included.

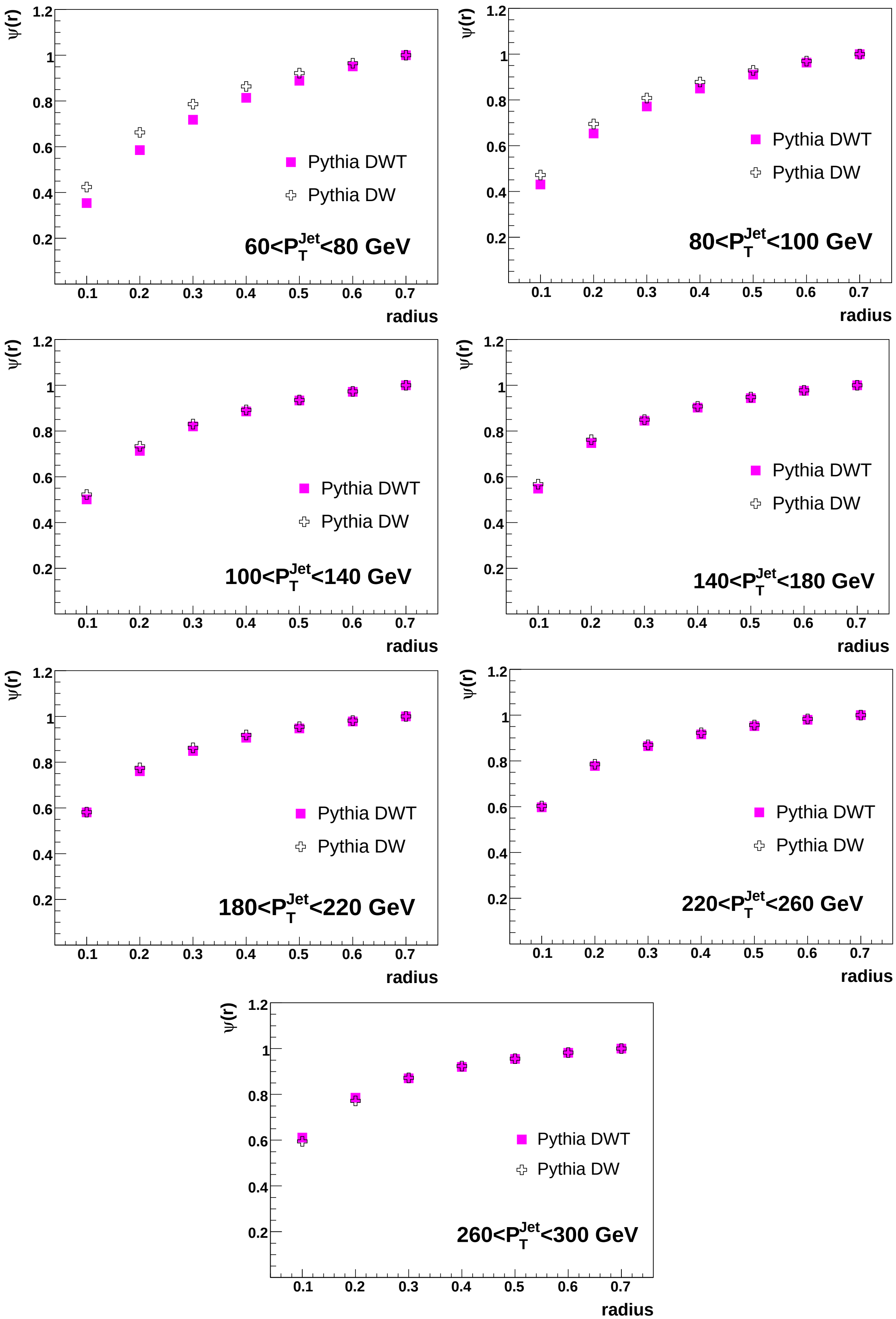

Figure 7.14. Comparison of integrated jet shapes for PYHTIA tunes DWT and DW in selected p_T bins. Statistical errors are included.

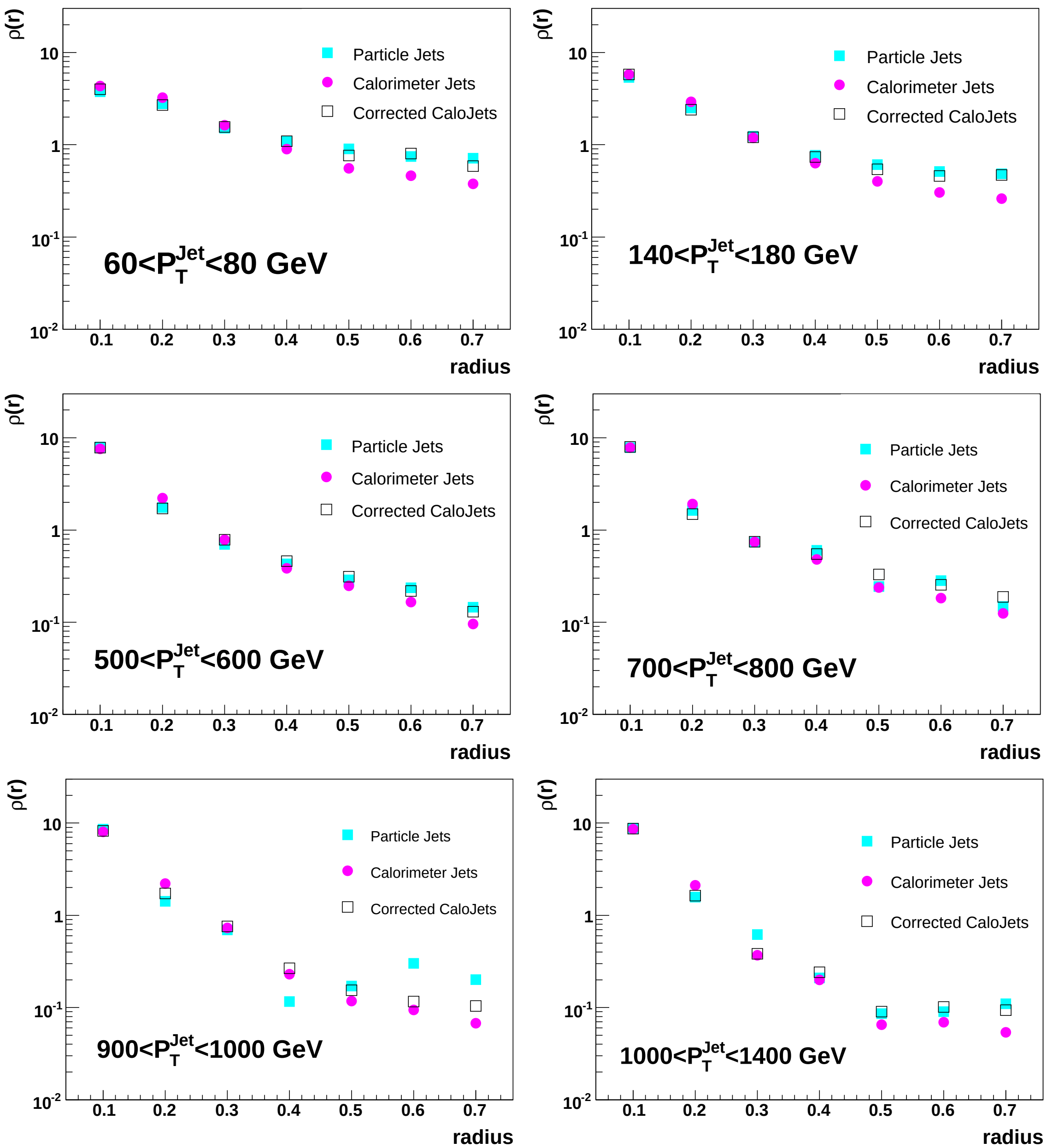

Figure 7.15. Differential jet shapes for selected p_T bins in multi-jet samples generated with ALPGEN. Calorimeter jets are corrected using corrections derived from PYTHIA samples. Statistical errors are included.

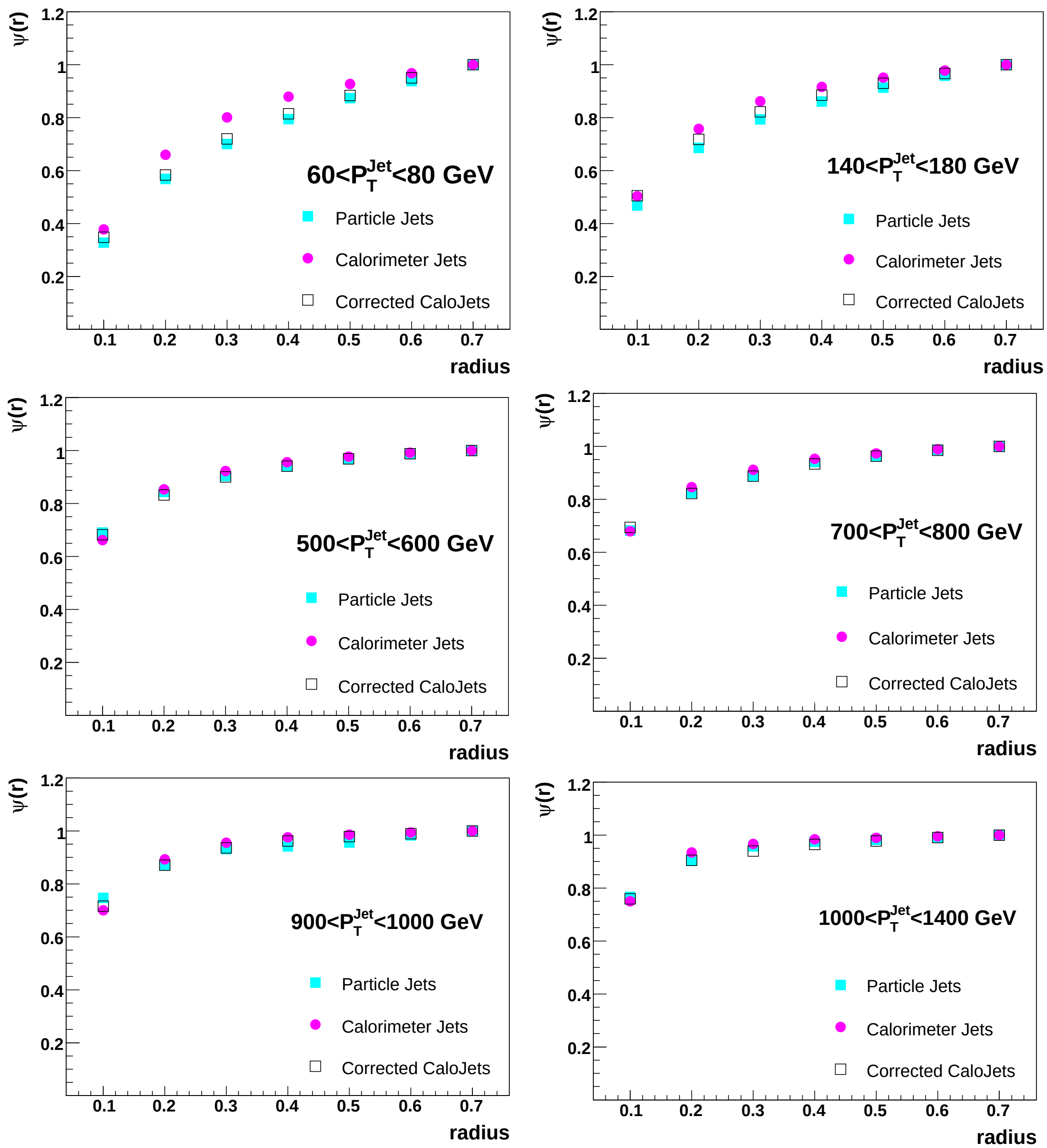

Figure 7.16. Integrated jet shapes for selected p_T bins in multijet samples generated with ALPGEN. Calorimeter jets are corrected using corrections derived from PYTHIA samples. Statistical errors are included.

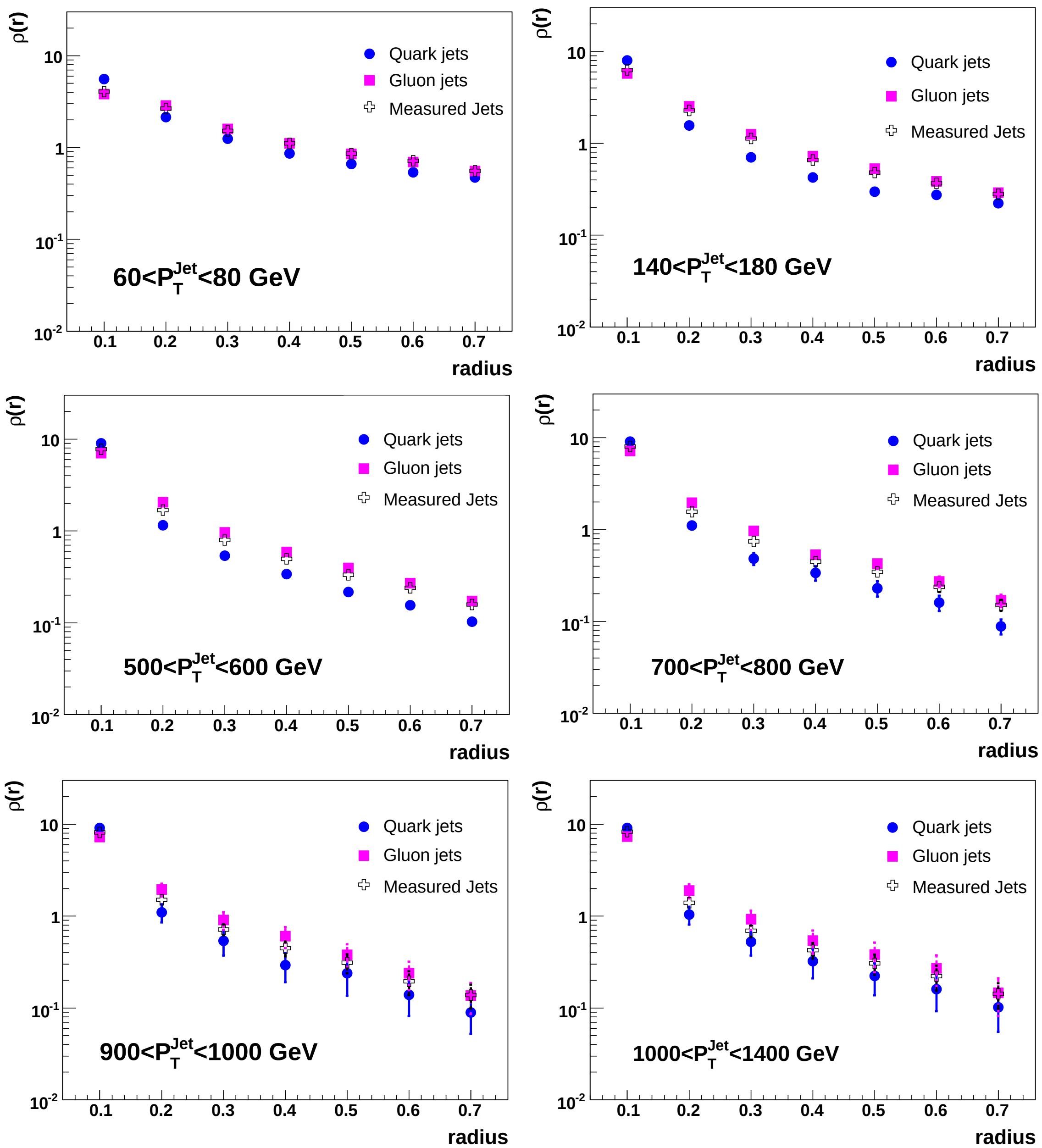

Figure 7.17. Comparison of quark and gluon differential jet shapes to simulated data in selected p_T bins. Statistical errors are included.

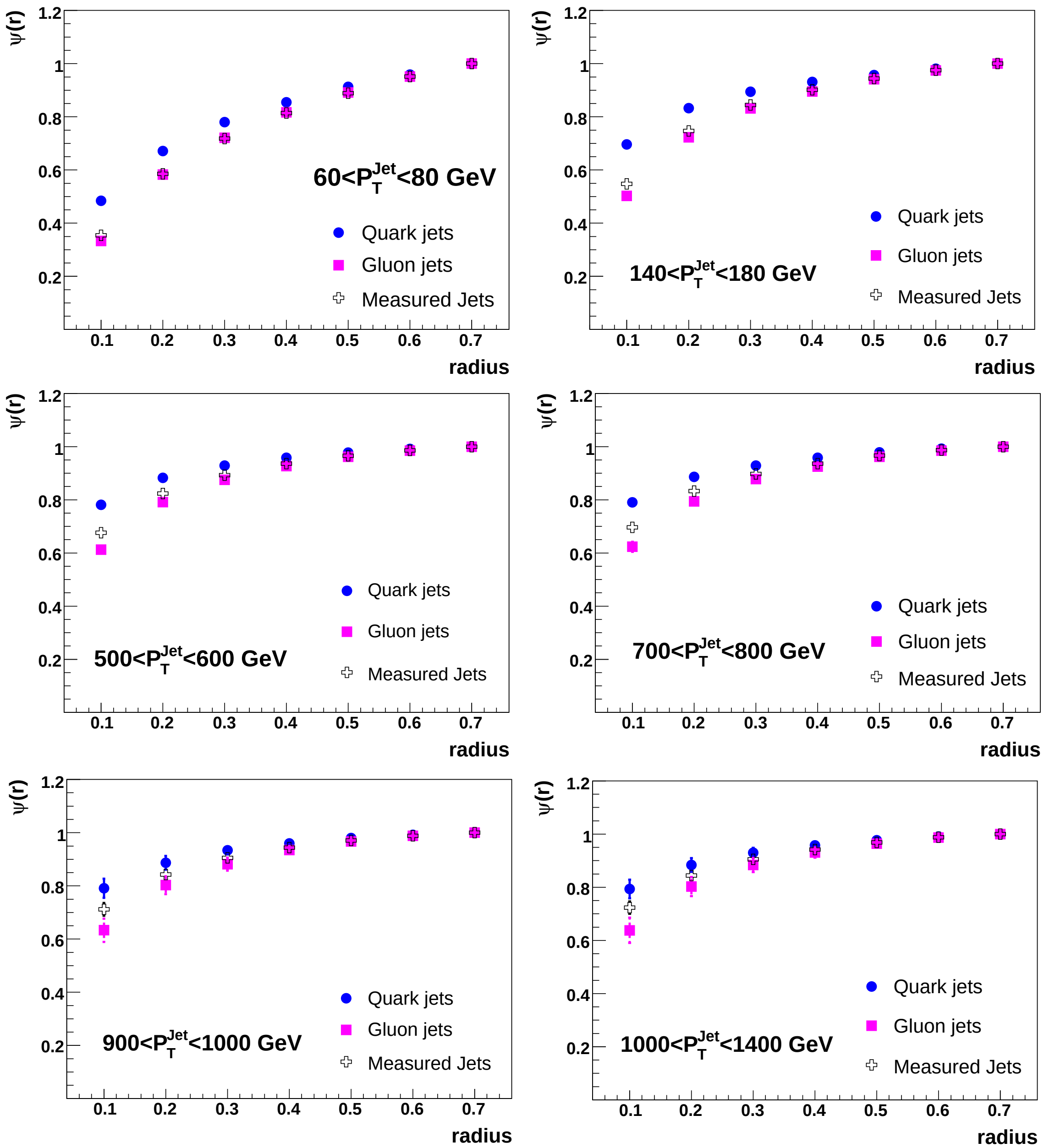

Figure 7.18. Comparison of quark and gluon integrated jet shapes to simulated data in selected p_T bins. Statistical errors are included.

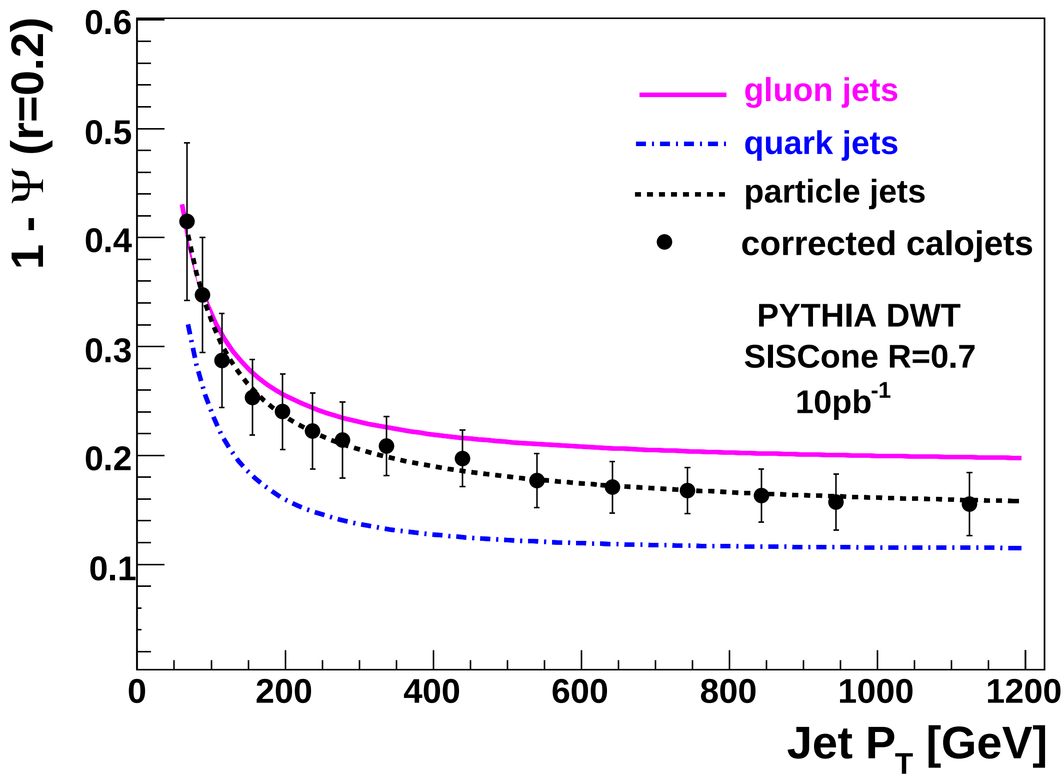

Figure 7.19. The fractional transverse momentum of a jet outside r=0.2, $1-\psi(0.2)$, as a function of the jet p_T for jets in the rapidity region $|y| < 1$. The reconstructed calorimeter jets, from PYTHIA Tune DWT (black points) are shown along with PYTHIA predictions for quark (dashed-dotted line) and gluon (solid line) initiated jets, and for all particle jets (dashed line). Systematic and statistical errors for the reconstructed calorimeter jets are added in quadrature. For the integrated shape the uncertainties at different r points are partially correlated.

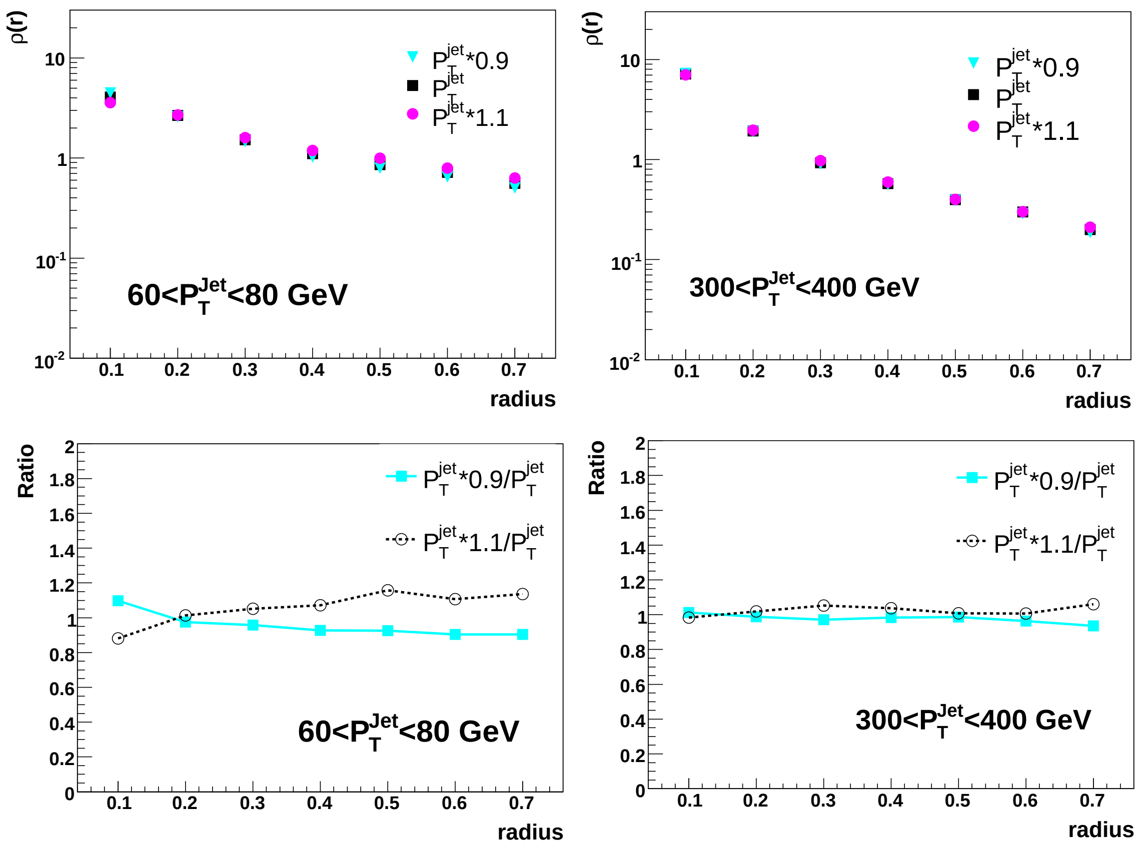

Figure 7.20. Differential jet shapes for ±10% change in energy scale (top) and fractional effect of changing jet energy scale (bottom), for selected p_T bins. Only statistical errors are included.

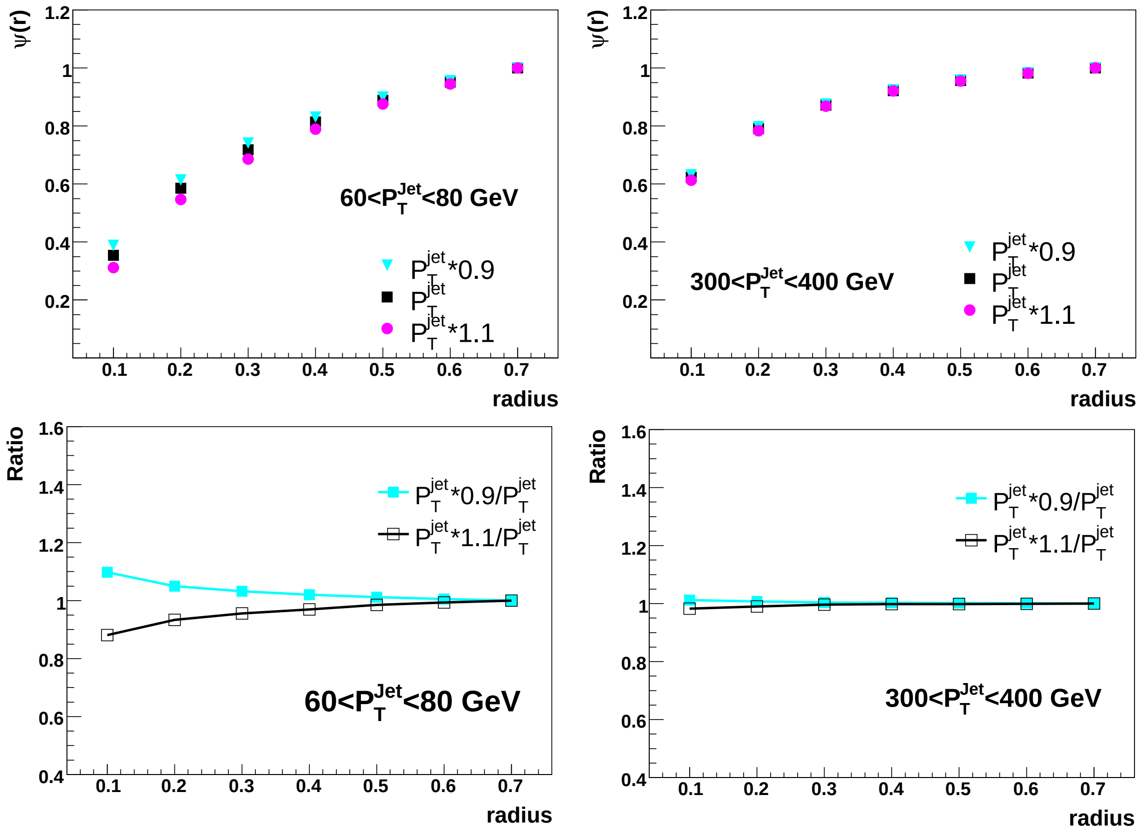

Figure 7.21. Integrated jet shapes for ±10% changes in energy scale (top) and fractional effect of changing the jet energy scale (bottom), for selected p_T bins. Only statistical errors are included.

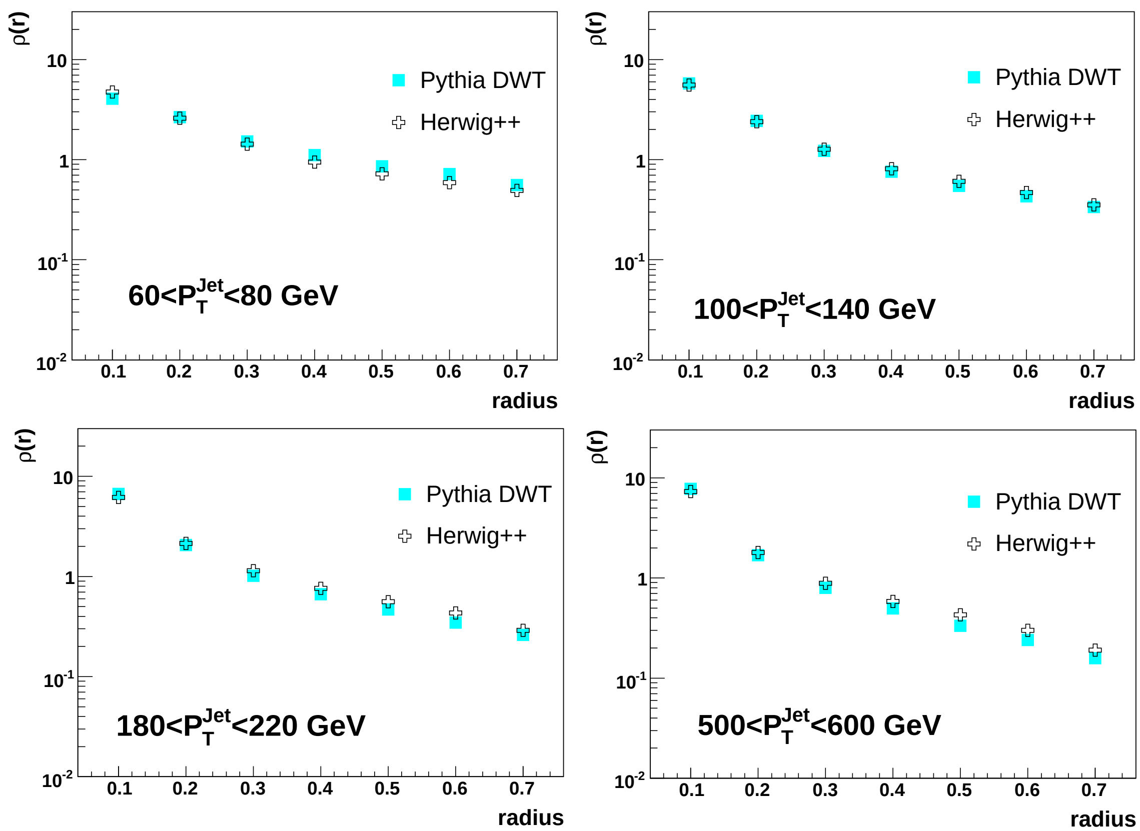

Figure 7.22 .Comparison of differential jet shapes from HERWIG++ and PYTHIA for selected p_T bins. Only statistical errors are included.

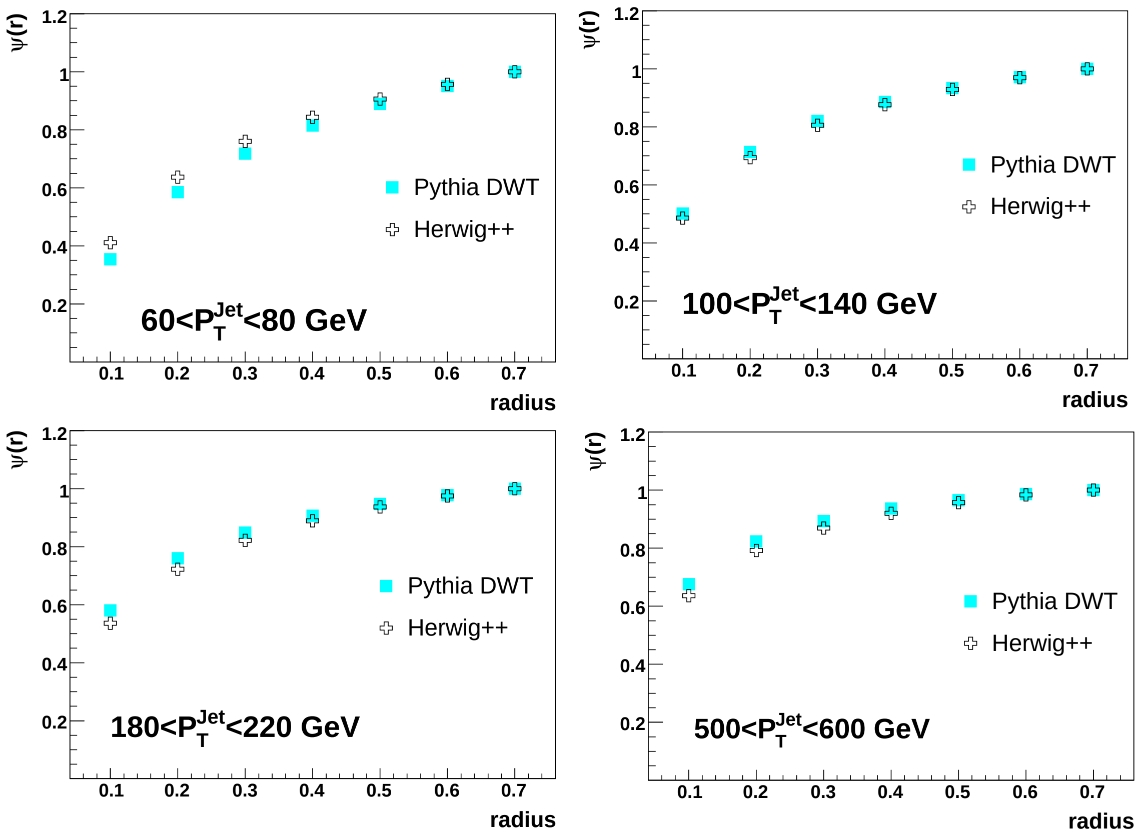

Figure 7.23. Comparison of integrated jet shapes from HERWIG++ and PYTHIA DWT for selected p_T bins. Only statistical errors are included.

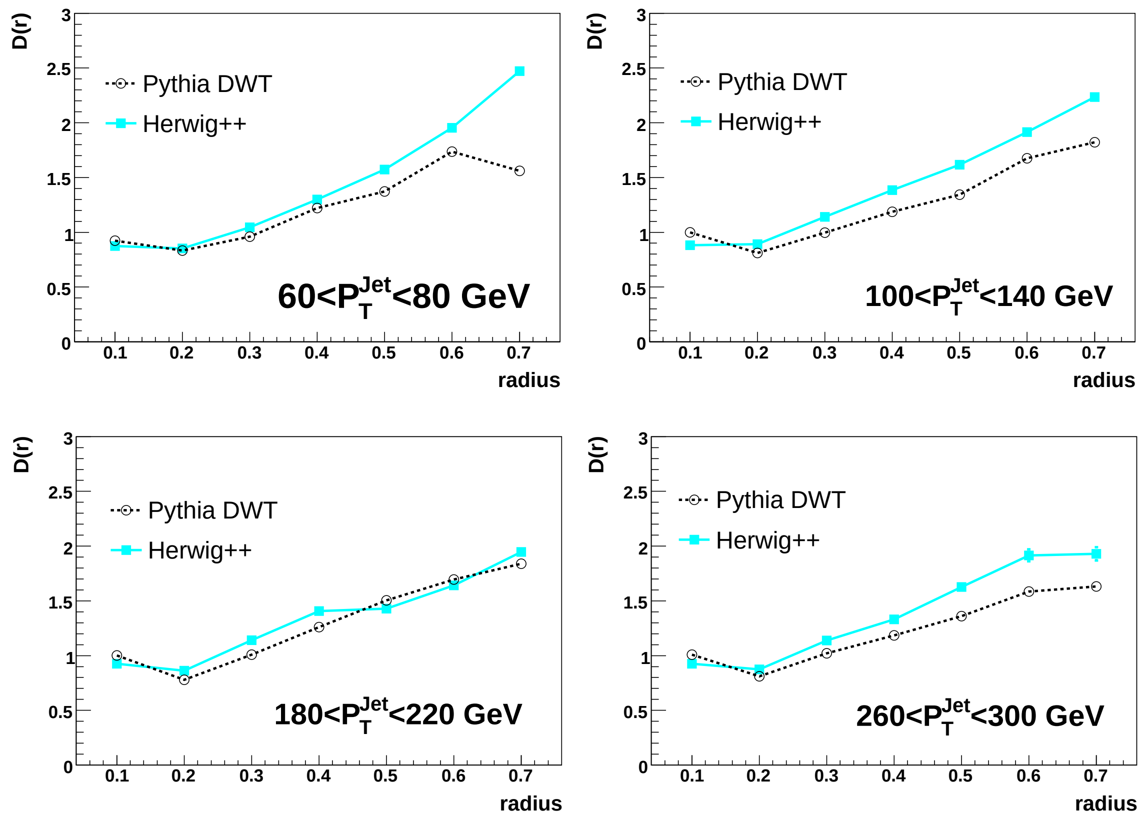

Figure 7.24. Comparison of the correction factors for PYTHIA DWT and HERWIG++ differential jet shapes. Only statistical errors are included.

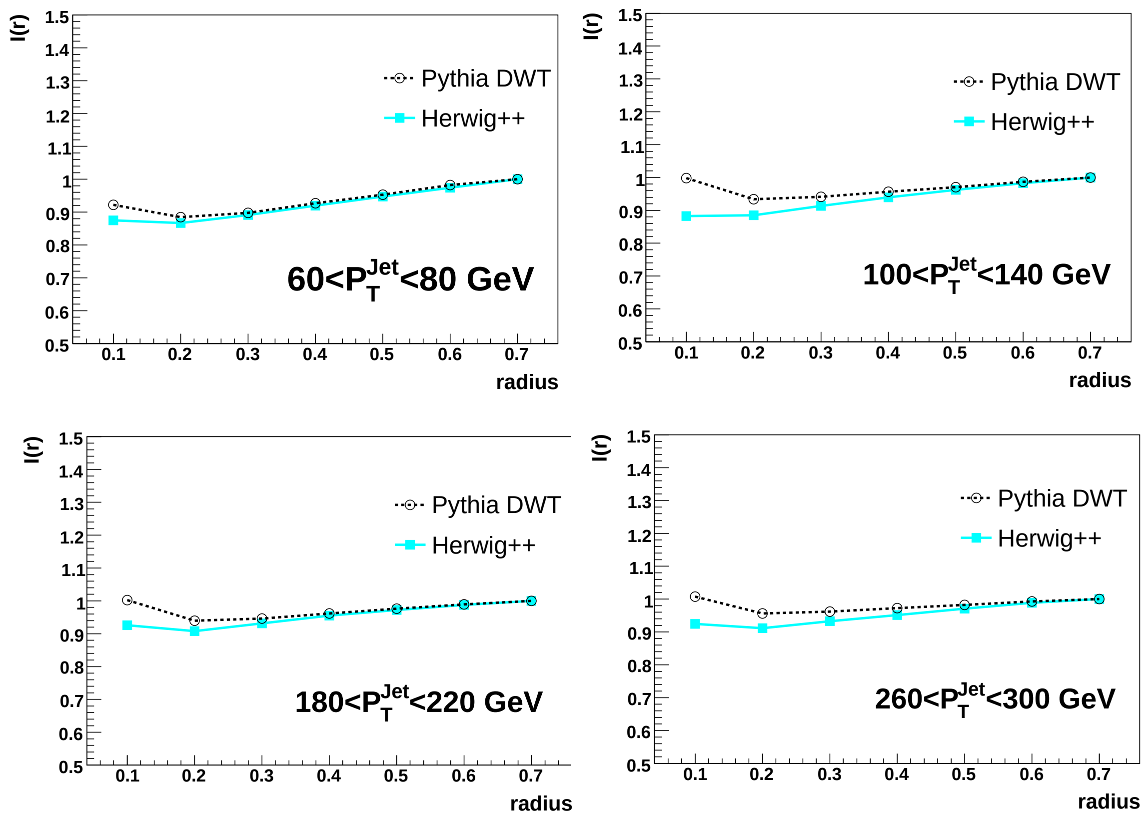

Figure 7.25. Comparison of the correction factors for PYTHIA DWT and HERWIG++ integrated jet shapes. Only statistical errors are included.

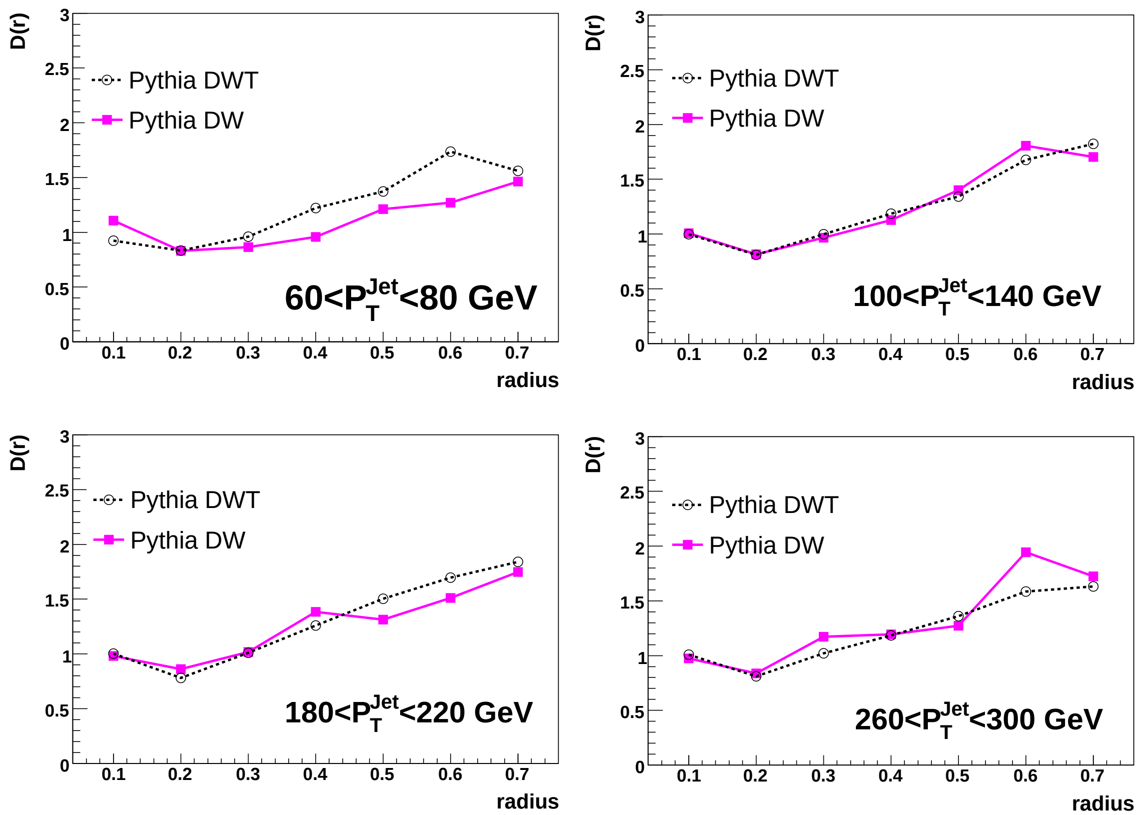

Figure 7.26. Comparison of the correction factors for PYTHIA DWT and DW differential jet shapes. Only statistical errors are included.

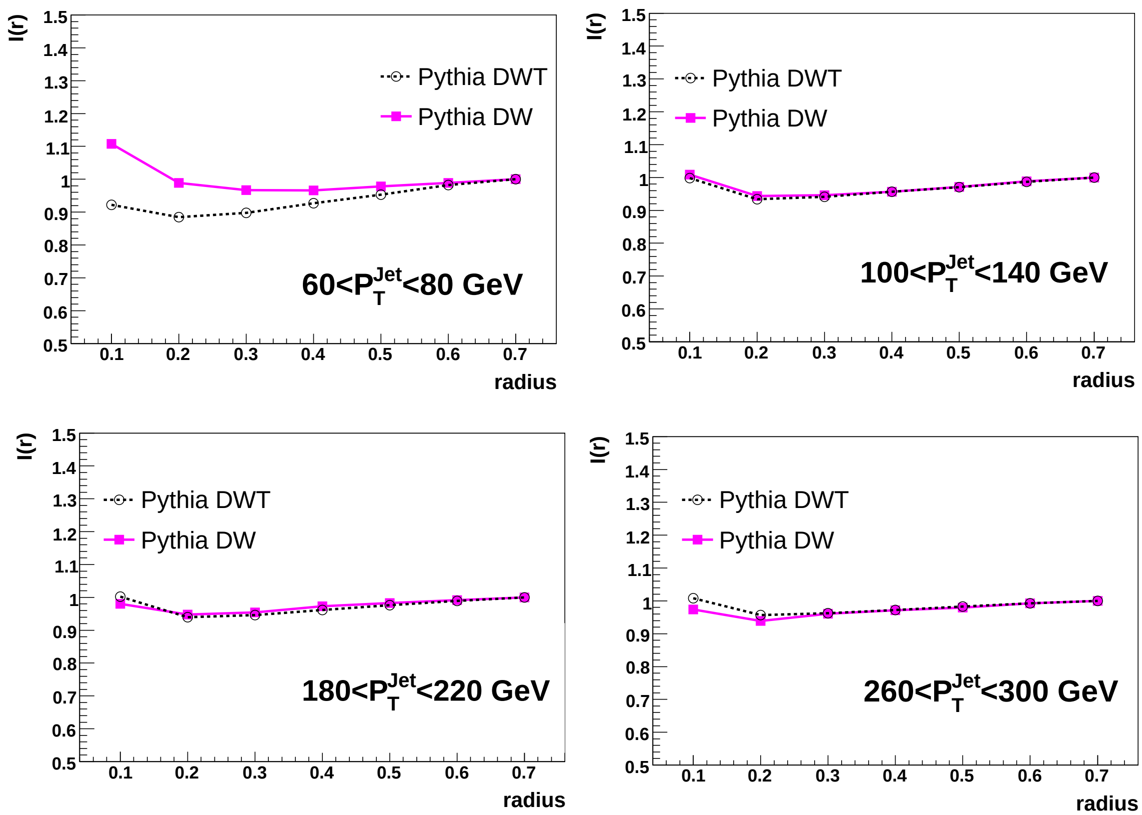

Figure 7.27. Comparison of the correction factors for PYTHIA DWT and DW integrated jet shapes. Only statistical errors are included.

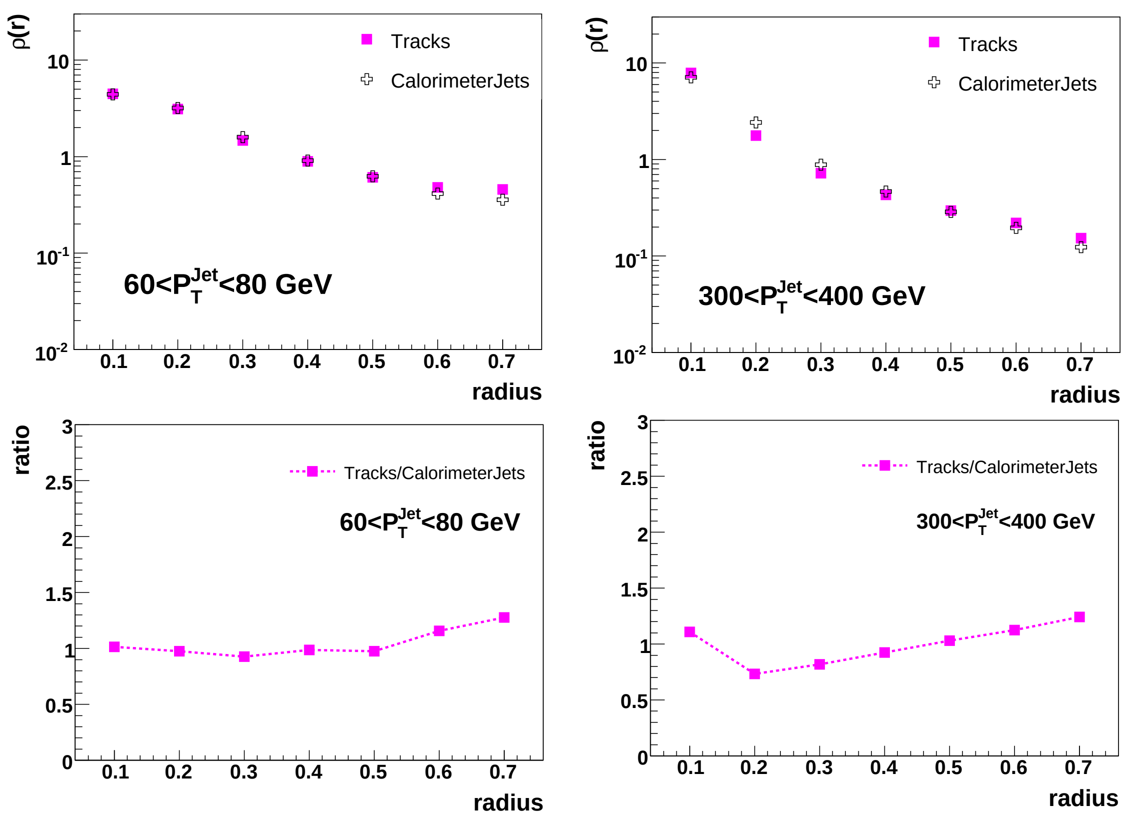

Figure 7.28. Comparison of the track jet shapes with the calorimeter jet shapes in simulated data (top) and their ratios (bottom) for selected p_T bins.

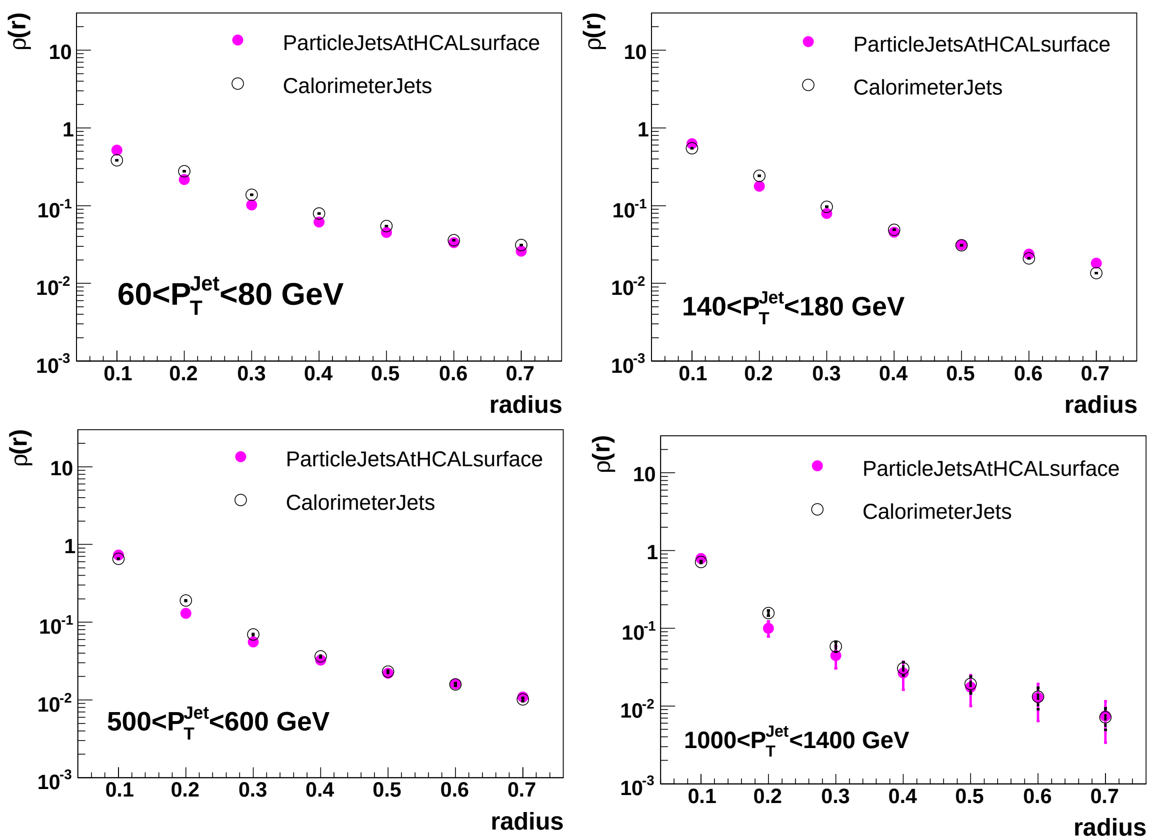

Figure 7.29. Effect of transverse showering spread for the differential jet shapes. Only statistical errors are included.

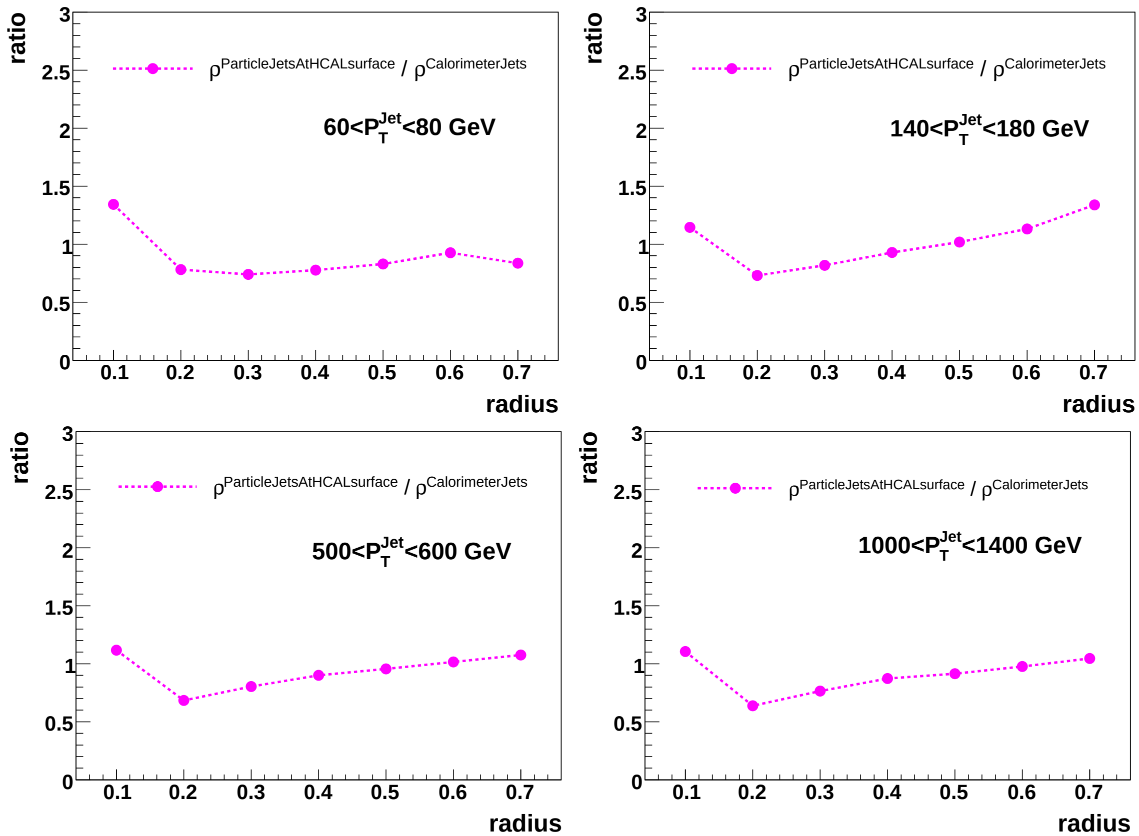

Figure 7.30. Ratio of the differential jet shapes obtained using the parameterized response (without transverse showering) to those from full simulation.

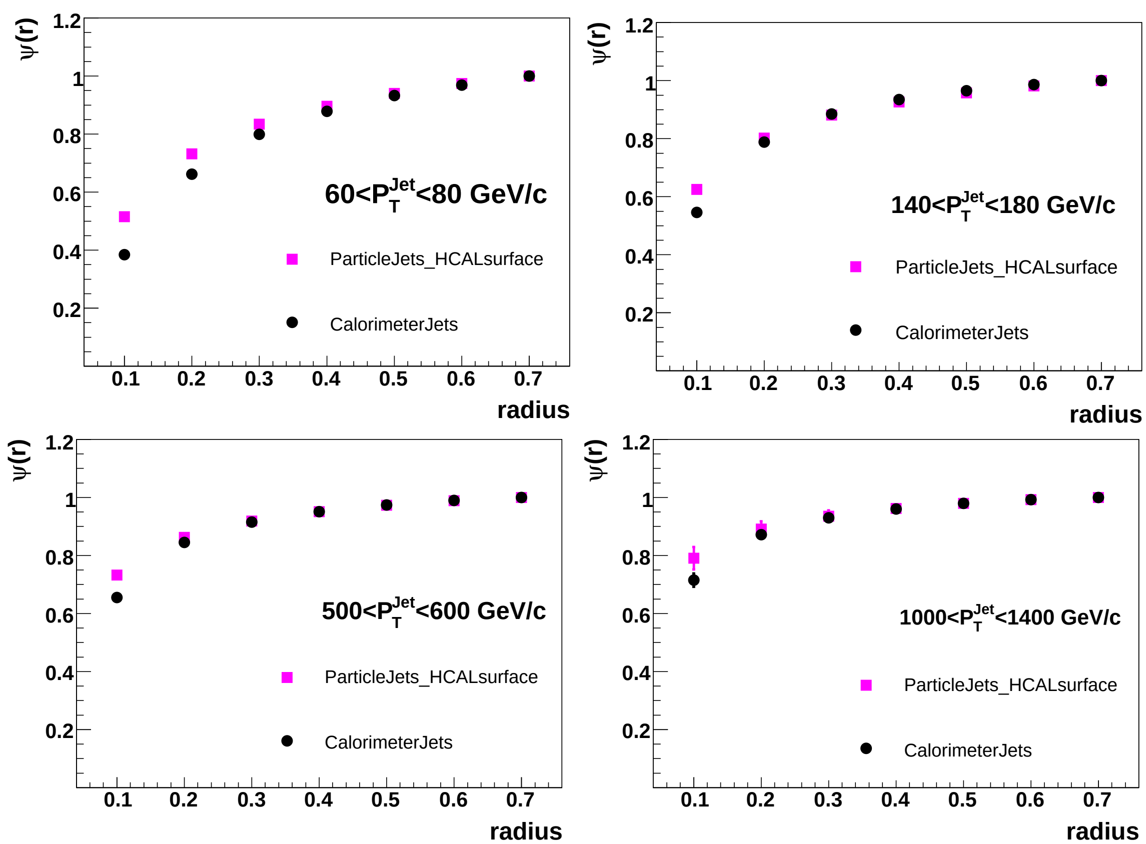

Figure 7.31. Effect of transverse showering spread for the integrated jet shapes. Only statistical errors are included.

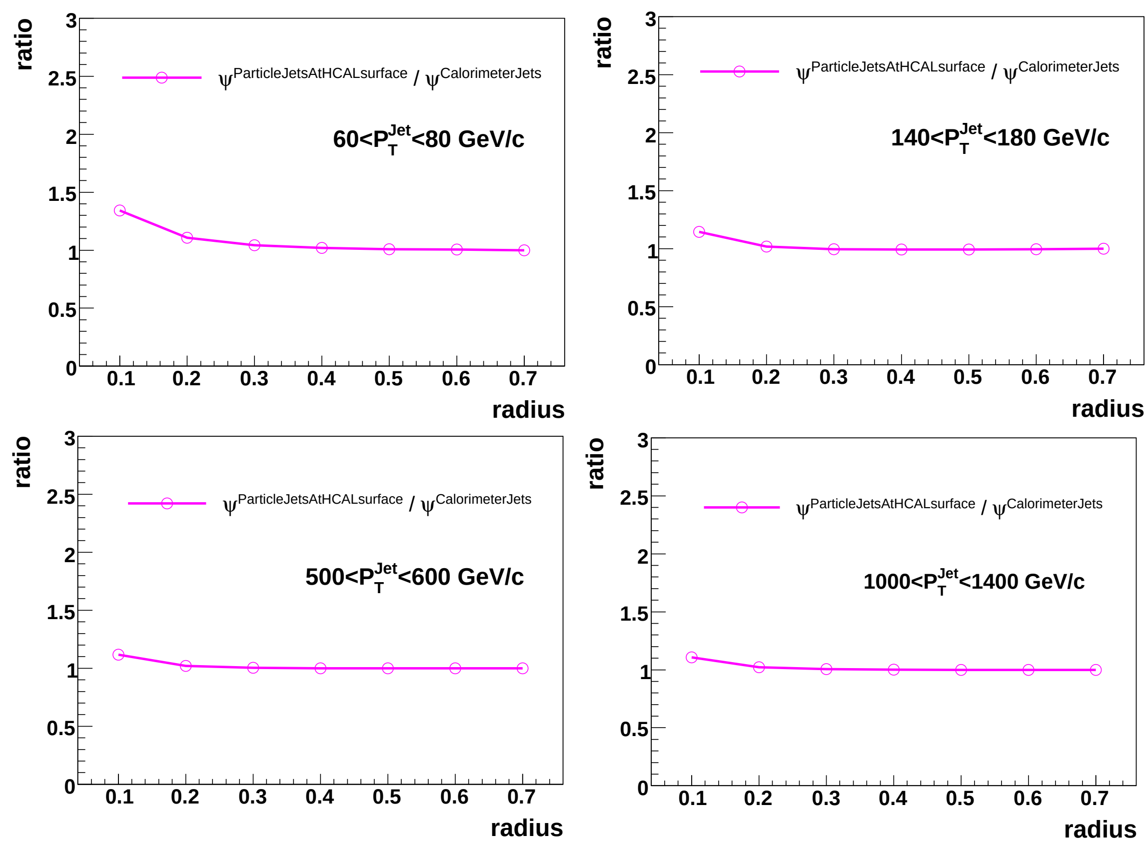

Figure 7.32. Ratio of the integrated jet shapes obtained using the parameterized response (without transverse showering) to those from full simulation.

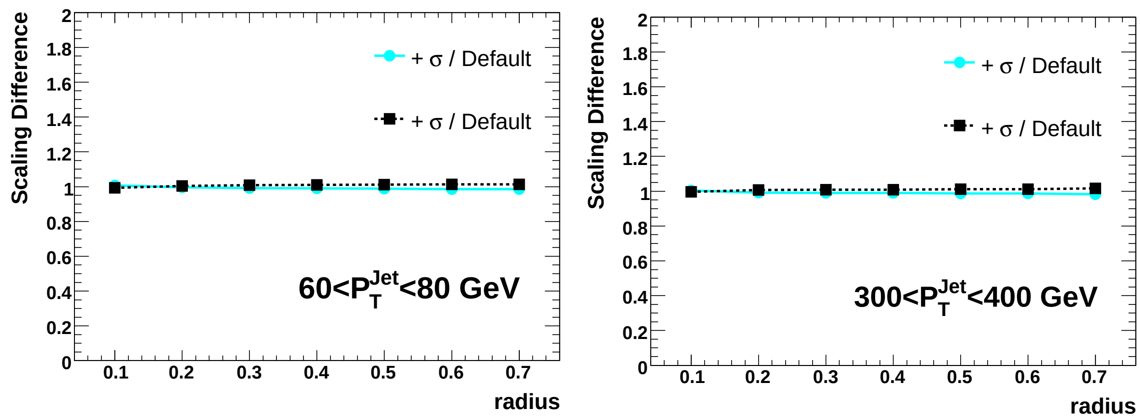

Figure 7.33. Scaling difference due to the E/p variation(see text) for the differential jet shapes for selected p_T bins.

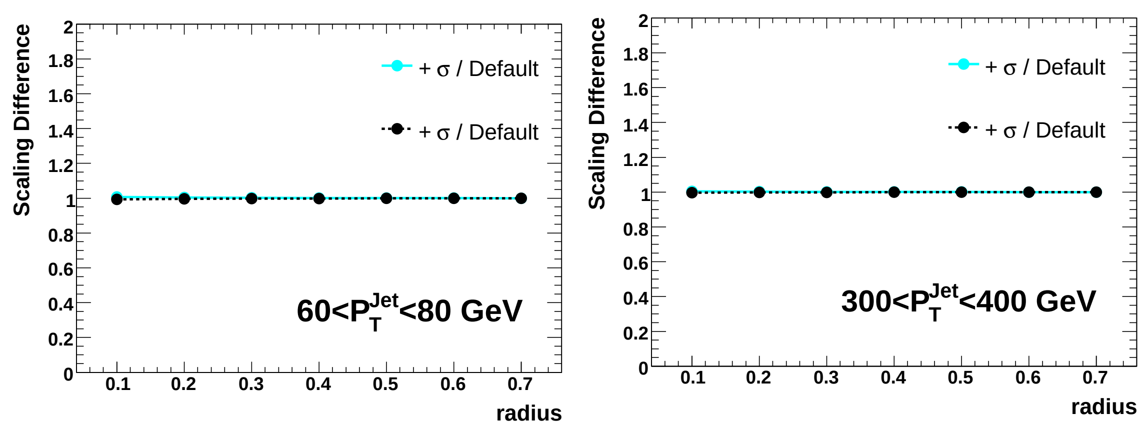

Figure 7.34. Scaling difference due to the E/p variation (see text) for the integrated jet shapes for selected p_T bins.

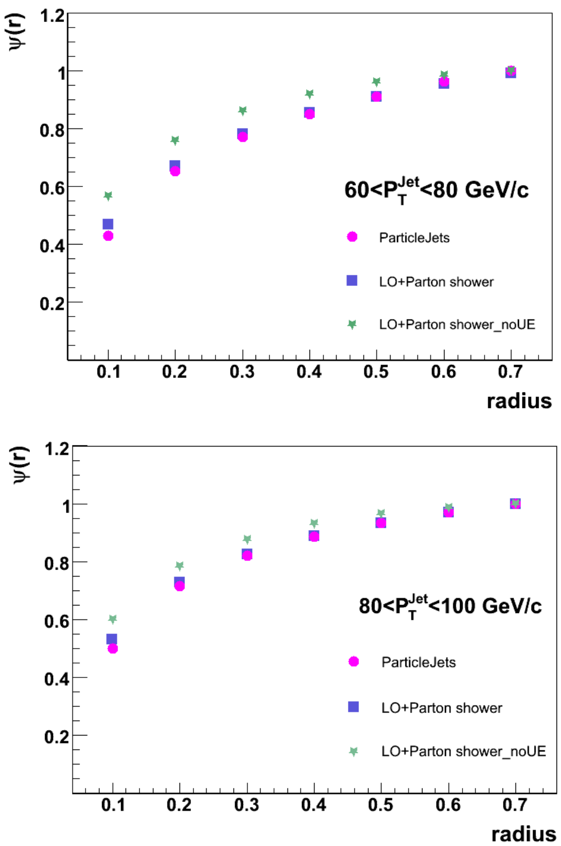

Figure 7.35. The figures show jet shapes for particle level and LO+parton shower prediction w/o UE for selected p_T bins.

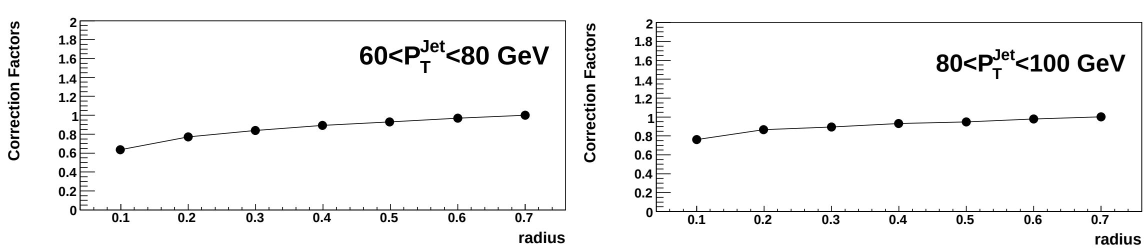

Figure 7.36. The figures show hadronization and underlying event correction factors derived from Figure 7.35; the ratio of particle level jet shapes to LO+parton shower jet shapes for selected p_T bins.

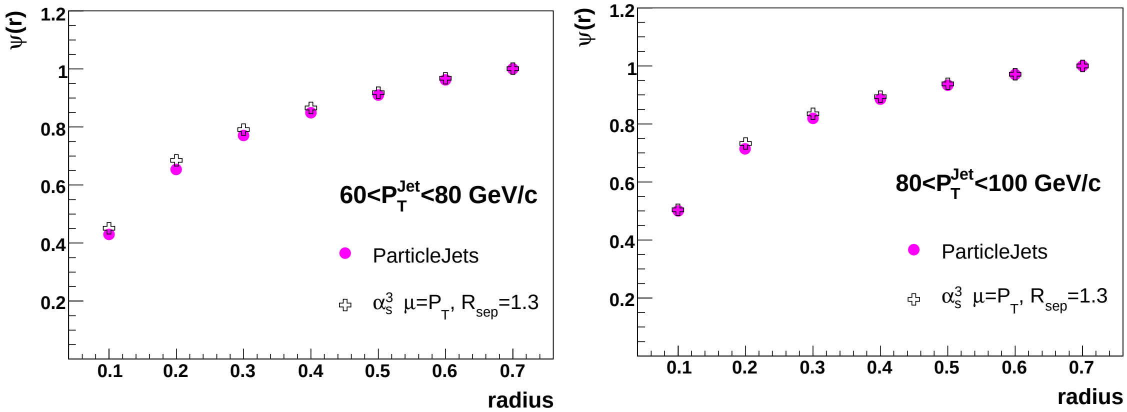

Figure 7.37. Jet shapes for particle level and corrected LO+parton shower prediction for selected p_T bins.

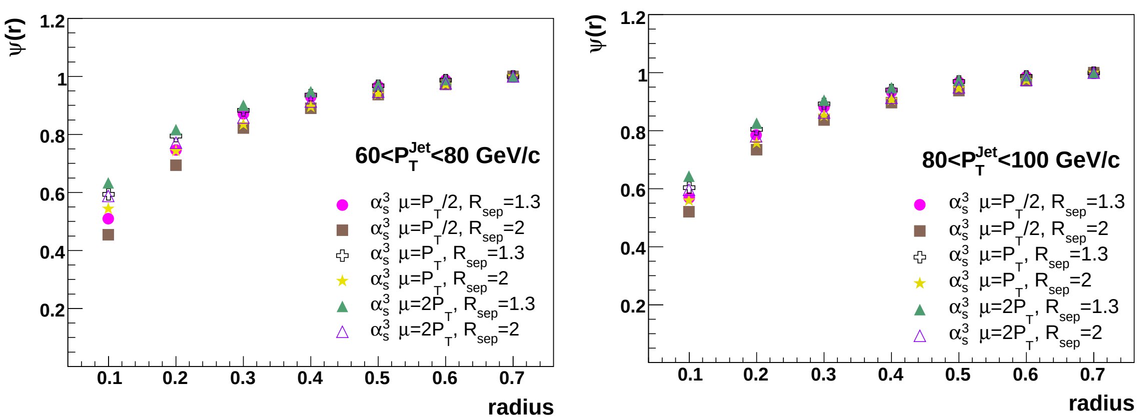

Figure 7.38. Only α_s^3 calculations. The jet shapes are shown for all renormalization scales and Rsep parameters for selected p_T bins.

Table 7.1. HLT thresholds and prescales

HLT threshold (GeV)	Prescale
30	10^5
60	10^4
110	10^2
150	10
200	1

Table 7.2. Number of jets before and after prescale, and mean and rms values of the p_T fraction histograms at r=0.2 in 10 pb^{-1} for all p_T jet bins which were analyzed. Statistical errors are listed for the corresponding jet p_T using prescaled event numbers. Here the σ is the statistical error bar which is derived from $\sigma = rms/\sqrt{(N_p)}$.

P_T (GeV)	N^{Jets}	$N^{Jets}_{prescaled}$ (N_p)	$Mean\ \psi(r = 0.2)$	rms	σ	$\sigma/Mean(\%)$
$60-80$	$1.311e+08$	1311.7	0.66	0.24	0.006	0.90
$80-100$	$2.803e+07$	2803.1	0.72	0.21	0.004	0.55
$100-140$	$1.328e+07$	132.8	0.76	0.20	0.017	2.31
$140-180$	$2.484e+06$	248498	0.78	0.20	0.0004	0.05
$180-220$	682348	682348	0.80	0.20	0.0002	0.02
$220-260$	256142	256142	0.81	0.21	0.0004	0.04
$260-300$	102488	102488	0.82	0.20	0.0006	0.07
$300-400$	83581.5	83581.5	0.83	0.21	0.0006	0.07
$400-500$	17589.5	17589.5	0.83	0.21	0.001	0.11
$500-600$	5282.8	5282.8	0.84	0.21	0.002	0.23
$600-700$	1909.3	1909.3	0.85	0.20	0.004	0.46
$700-800$	753.8	753.8	0.85	0.22	0.007	0.81
$800-900$	325.8	325.8	0.86	0.22	0.012	1.3
$900-1000$	159.2	159.2	0.86	0.21	0.016	1.87
$1000-1400$	158.1	158.1	0.87	0.21	0.016	1.83

Table 7.3. Different sources of systematics for $\psi(r = 0.2)$ listed as percentage contributions for all jet p_T bins for 10 pb^{-1} of integrated luminosity. Total systematics is a quadrature sum of fragmentation, jet energy scale, showering and E/p contributions.

P_T (GeV)	$Fragmentation(\%)$	$JES(\%)$	$Showering(\%)$	$E/p(\%)$	$TotalSys.(\%)$
60 – 80	1.82	5.78	10.7	0.39	12.3
80 – 100	2.20	5.5	5.4	0.33	8.06
100 – 140	4.85	1.38	2.4	0.30	5.58
140 – 180	4.18	1.0	1.6	0.26	4.62
180 – 220	3.10	0.81	0.7	0.24	3.29
220 – 260	4.22	0.96	1.1	0.23	4.49
260 – 300	4.48	0.13	1.8	0.23	4.85
300 – 400	3.23	0.83	0.7	0.21	3.42
400 – 500	2.35	0.92	2.0	0.19	3.23
500 – 600	4.71	0.68	2.0	0.18	5.19
600 – 700	1.69	0.44	1.3	0.16	2.19
700 – 800	2.85	0.51	1.7	0.16	3.40
800 – 900	2.17	0.39	1.3	0.15	2.56
900 – 1000	1.99	0.11	1.3	0.14	2.41
1000 – 1400	1.73	0.74	2.2	0.12	2.9

Table 7.4. Absolute error on $1-\psi(r=0.2)$ represents quadratic sum of systematic and statistical uncertainties for 10 pb^{-1} of integrated luminosity. $I(r=0.2)$ refers to the integrated correction factors at r=0.2.

P_T (GeV)	Raw $\psi(r=0.2)$	$I(r=0.2)$	$1-\psi(r=0.2)$	*AbsErr*
60 – 80	0.66	0.90	0.41	0.072
80 – 100	0.72	0.93	0.34	0.052
100 – 140	0.76	0.94	0.28	0.043
140 – 180	0.79	0.94	0.25	0.034
180 – 220	0.80	0.95	0.24	0.025
220 – 260	0.81	0.95	0.22	0.034
260 – 300	0.82	0.95	0.21	0.038
300 – 400	0.83	0.96	0.20	0.027
400 – 500	0.83	0.97	0.19	0.025
500 – 600	0.84	0.96	0.17	0.042
600 – 700	0.85	0.97	0.17	0.018
700 – 800	0.85	0.97	0.16	0.029
800 – 900	0.86	0.97	0.16	0.024
900 – 1000	0.86	0.96	0.15	0.025
1000 – 1400	0.87	0.97	0.15	0.028

8. CONCLUSION

In about a month from now the LHC will start operation, and CERN and experimental particle physics will enter a new epoch, hopefully the most glorious and fruitful of their history that will allow to study various undiscovered or yet unknown aspects of particle physics.

The studies presented in this thesis were performed for the CMS experiment, one of the two general-purpose detectors at the LHC. My thesis can be grouped into 3 parts.

The first part of my work, as presented in this thesis, a method to measure the amount of the dead material between the ECAL and HCAL calorimeters that effect the response of the particles has been described for CMS detector using the Test Beam 2006 data in the energy range 4-300 GeV. Investigation of the calorimeter uniformity was another study that has been carried out in this thesis. For this purpose 100 GeV π^- and μ^- beam events have been used.

The second part of my work was dedicated for the performances of the jet reconstruction algorithms in CMS. We presented detailed comparisons of performance between four jet reconstruction algorithms currently available in CMSSW with two radius parameter choices each: Iterative Cone, SISCone, and Midpoint Cone with R = 0.5 and 0.7, and Fast k_T with D = 0.4 and 0.6. The performance comparisons presented in this chapter include jet composition and shape distributions for dijets. All results are based on QCD dijet samples generated with CMSSW_1_5_2, thus providing a new baseline for the jet reconstruction. We find similar performance on the calorimeter level between algorithms with similar size parameter. The impact of the detector effects appears to be more pronounced than the algorithmic differences studied in this study. We also find that the SISCone algorithm performs as well or better than the Midpoint Cone, while known to be preferred theoretically. It seems worthwhile to mention that the use of the SISCone algorithm, implemented as an external package, by both CMS and ATLAS will go a long way towards the goal of direct comparisons of jet based measurements without the unnecessary uncertainties induced by the experiment-specific implementations; it is possible that this will be true for comparisons to the Tevatron results as well. Therefore it is strongly recommended to adopt SISCone as the default cone-based jet algorithm and consequently to include it in the reconstruction in future standard event processing at CMS. The k_T algorithm is infrared- and collinear safe to all orders of pQCD as well and complementary to the cone based algorithms. The execution time of Fast k_T is dramatically reduced w.r.t. earlier k_T implementations and it is therefore well suited for the high multiplicity environment of LHC pp collisions, in fact executing faster than all cone-based algorithms but Iterative Cone. We find that it performs as good or better than any other algorithm in this study and strongly encourage its use as an alternative to SISCone. Further studies will be conducted regarding the performance of all algorithms in events with high pileup and more realistic calorimeter noise.

On the last part of my thesis, jet shapes analysis for the pp collisions at 14TeV was carried out for the first time in CMS detector. Since these measurements are sensitive to different fragmentation and hadronization models various MC event generators were used to study the internal structure of jets. In this manner it is extremely important to understand the differences among the Monte Carlo event generator programs that can produce such high energetic jets. In particular, it is crucial to understand the uncertainties on this measurement based on different Monte Carlo event generators, and to see how the different approximations used in these programs produce differences in the observables which can be reconstructed in experiments. These generators implement a combined use of fixed order Matrix Element calculations and all order Parton Shower calculations. We used some of the most popular programs for hadron collisions simulation: PYTHIA and HERWIG++, which are probably the most widely used Leading Order event generators in high energy physics; and ALPGEN, which is a newer program that implements higher order tree level corrections for a number of processes. We compare the predictions of the Monte Carlo generators PYTHIA, HERWIG++, and ALPGEN by looking into the internal structure of jets using the transverse momentum. We investigated the differences among these generators using the transverse momentum distributions.

Finally, using PYTHIA and HERWIG++ MC simulations, we have investigated a technique to measure jet shapes in pp collisions for the two leading jets in the kinematic region 60 GeV$< p_T < 1.4$ TeV and $|y| < 1$. Particle level jet shapes were determined from calorimeter jets using corrections derived from PYTHIA MC events.

Several sources of systematic uncertainties were investigated, arising from jet energy calibration, jet fragmentation, calorimeter response and transverse showering, as function of jet p_T and distance from jet axis r. The systematic uncertainty is dominated by overall jet energy scale, jet fragmentation and calorimeter simulation effects. The total systematic uncertainty at r=0.2 is 12% at p_T=60 GeV, decreasing to 4% at jet p_T=1 TeV.

As expected in QCD, jet shapes are observed to become narrower with increasing jet p_T. Different underlying event tunes (PYTHIA DWT and PYTHIA DW) were studied. PYTHIA DW tends to produce narrower jet shapes in the low p_T region. QCD predicts different shapes of jets originating from quarks and gluons. A measurement of the jet shapes in the context of the PYTHIA Monte Carlo gives an estimate of the fraction of gluon initiated jets in data as a function of jet p_T.

It can be concluded from the summarized results and related uncertainties that systematic uncertainties are under control and allow an early measurement of jet shapes at CMS.

REFERENCES

ABACHI, S. et al., D0 Collaboration, Transverse energy distributions within jets in pp collisions at $\sqrt{s}$ = 1.8 TeV, Phys. Lett. B357 (1995) 500-508.

ABDULLIN, S. et al, Eur. Phys. J. C 53 (2008) 139.

ABE F. et al., CDF Collaboration, A Measurement of jet shapes in $p\bar{p}$ collisions at $\sqrt{s}$ = 1.8 TeV, Phys. Rev. Lett. 70 (1993), 713-717.

ABREU, P. et al., DELPHI Collab., Phys. C70 (1996) 179;

ABULENCIA, A. et al., CDF Collaboration, Phys. Rev. D78:072005 (2008).

ACKERSTA, K. et al., OPAL Collab., Eur. Phys. J. C1 479 (1998).

ACOSTA, D. E. et al., CDF Collaboration, Study of jet shapes in inclusive jet production in $p\bar{p}$ collisions at $\sqrt{s}$ = 1.96 TeV, Phys. Rev. D71 (2005) 112002, arXiv:hep-ex/0505013.

___________, 2004 CDF Collaboration, Phys. Rev. D 70, 072002 (2004), arXiv:hep-ex/0404004.

ACTON, P. D. et al. OPAL Collab., Phys. C58 (1993) 387;

ADAMS, M. et al, Nucl. Instrum. Methods A511 (2003) 311.

ADLOFF, C. et al., H1 Collaboration, Measurements of transverse energy flow in deep inelastic scattering at HERA, Eur. Phys. J. C12 (2000) 595-607, arXiv:hep-ex/9907027.

AFFOLDER, A. A. et al. (CDF Collaboration), Phys. Rev. D 65, 092002 (2002).

AKERS, R. et al., OPAL Collab., Zeit. f. Phys. C63 (1994) 197.

___________, 1995 OPAL Collab., Phys. C68 (1995) 179;

ALEXANDER, G. et al., OPAL Collab., Phys. Lett. B265 (1991) 462;

___________, 1996 OPAL Collab., Phys. C69 (1996) 543;

ALICE Collaboration, ALICE: Technical Proposal for A Large Ion Col lider Experiment at the CERN LHC, CERN-LHCC-95-71.

ALTARELLI, G. and Parisi, G. Nucl. Phys. B 126, 298 (1977)

AMATO, S. et al., LHCb Collaboration, LHCb Technical Proposal, CERN-LHCC-98-4.

ARMSTRONG, W. W. et al., ATLAS Collaboration, ATLAS: Technical Proposal for a General-Purpose pp Experiment at the Large Hadron Col lider at CERN, CERN-LHCC-94-43.

ARCHAYA, B. S. et al, The CMS Outer Calorimeter, CMS NOTE-2006/127.

BAHR, M. et al., Underlying events in Herwig++, arXiv:0809.2669, 2008.

__________, 2008a Herwig++ 2.2 Release Note, arXiv:0804.3053, 2008.

__________, 2008b Simulation of multiple partonic interactions in Herwig++, JHEP 07 (2008) 076, arXiv:0803.3633.

BLAZEY, G. et al., Run II Jet Physics. hep-ex/0005012, 2000..

BUTTERWORTH, J. M., Couchman, J. P., Cox, B. E., Waugh, B. M., KtJet: A C++ implementation of the kt clustering algorithm , Comp. Phys. Comm. vol 153/1 85-96 (2003).

BHATTI, A. et al., Plans for Jet Energy Corrections at CMS. CMSAN-2007/055.

__________, 2008 "Performance of the SISCone Jet Clustering Algorithm", CMS AN 2008-002.

__________, 2009 Offset Energy Correction for Cone Jets, CMS PAS, vol. JME-09-003, 2009.

BAYATIAN, G. L. and et al.: 1998,CMS Tracker Project Technical Design Report, CERN/LHCC-98-6.

__________, 2000, CMS, Addendum to the CMS Tracker TDR, CERN-LHCC-2000-016.

__________, 1997a, CMS, The Electromagnetic Calorimeter Technical Design Report, CERN-LHCC-97-33.

__________, 1997b, CMS: The Hadron Calorimeter Technical Design Report, CERN-LHCC-97-31.

__________, 1997c, CMS Magnet Technical Design Report, CERN/LHCC-97-10.

__________, 1997d, CMS Muons Technical Design Report, CERN/LHCC-97-32.

__________, 2007, CMS Physics Technical Design Report (Vol II), J. Phys. G: Nucl. Part. Phys. 34, 995 (2007).

__________, 2006, CMS Physics Technical Design Report (Vol I), http://cmsdoc.cern.ch/cms/cpt/tdr/ptdr1 final colour.pdf (02/02/2006)

BJORKEN, J. D., Phys. Rev. 179, 1547 (1969)]

BREIDENBACH, M. et al., Phys. Rev. Lett. 23, 935 (1969);

BREITWEG, J. et al., ZEUS Collaboration, Measurement of jet shapes in high-Q**2 deep inelastic scattering at HERA, Eur. Phys. J. C8 (1999) 367-380, arXiv:hep-ex/9804001.

BRUNING, O. (Ed.) et al., LHC Design Report. Vol. I: The LHC Main Ring, CERN-2004-003-V-1.

BUSKULIC, D. et al., ALEPH Collaboration, Phys. Lett. B384 (1996) 353.

CACCIARI, M., Salam, G. P., Dispelling the N3 myth for the Kt jet-finder , Phys.Lett. B641 57-61 (2006).

CAMPBELL, J. M., Huston, J. W. and Stirling, W. J., Rept. Prog. Phys. 70, 89 (2007), arXiv:hep-ph/0611148.

CATANI, S., Dokshitzer, Y. L., Seymour, M. H., and Webber, B. R., Nucl. Phys. B 406 (1993) 187;

CHATRCHYAN, S. et al., The CMS Collaboration, 2008 JINST 3 S08004.

CORCELLA, G. et al., HERWIG 6.5: an event generator for Hadron Emission Reactions With Interfering Gluons (including supersymmetric processes). JHEP, 0101:010, 2001.

DAQ and High-Level Trigger Technical Design Report, CERN/LHCC 2002-026 (2002).

DELLACQUA, A. et al., GEANT-4: An Object oriented toolkit for simulation in HEP. CERN-DRDC-94-29.

DEMINA, R. et al., Calorimeter Energy Thresholds for Jet Reconstruction in CMS, CMS NOTE 2006-020 (2006).

DISSERTORI, G., Knowles, I. and Schmelling, M., Quantum Chromodynamics, High Energy Experiments and Theory, International Series of Monographs on Physics Nr. 115, Oxford University Press, 2003.

DOBBS, M. A. et al., Les Houches guidebook to Monte Carlo generators for hadron collider physics. hep-ph/0403045, 2004.

DOKSHITZER, Y. L., Phys. JETP 46 (1977) 641-653.

DOKSHITZER, Y. L., Leder, G. D., Moretti, S. and Webber, B. R., JHEP 9708, 001 (1997) [hep-ph/9707323].

ELLIS, S., Kunszt, Z. and Soper, D., Phys. Rev Lett. 69, 1496 (1992); Phys. Rev. Lett. 64, 2121 (1990); Phys. Rev. D40, 2188 (1989); Phys. Rev. Lett. 62, 726 (1989).

___________, 1992 Jets at hadron colliders at order α_s^3: A Look inside, Phys. Rev. Lett. 69 (1992) 3615-3618, arXiv:hep-ph/9208249.

ELLIS, S. D., arXiv:hep-ph/9306280, 1993.

ELLIS, S. D. and Soper, D. E., Phys. Rev. D 48 (1993) 3160, hep-ph/9305266.

ELLIS, R. K., Stirling, W. J. and Webber, B. R., QCD and Collider Physics, Cambridge Monographs on Particle Physics, Nuclear Physics and Cosmology, CUP, 1996.

FIELD, R. D. for the CDF Collaboration, FERMILAB-CONF-06-409-E, Presented at 33rd International Conference on High Energy Physics (ICHEP 06), Moscow, Russia, 26 Jul - 2 Aug 2006.

FRIEDMAN, J. L. and Kendall, H. I., Ann. Rev. Nucl. Part. Science 22, 203 (1972).

FRIXIONE, S. and Webber, B. R., JHEP 0206, 029 (2002) arXiv:hep-ph/0204244.

GRIBOV, V. N. and Lipatov, L. N., Sov. J. Nucl. Phys. 15 (1972) 438-450.

GIELE, W.T. , Glover, E.W.N. and Kosower, D.A. Nucl. Phys. B403 (1993) 633.

__________, 1994 Phys. Rev. Lett. 73, 2019 (1994), arXiv:hep-ph/9403347.

GIANOTTI, F., Phys. Rept. 403, 379 (2004).

GRIFFITHS, David. Introduction to Elementary Particles, 2004. ISBN 0-471-60386-4]

HARRIS, R., Kousouris, K., MC Truth L2 L3 Factorized Jet Corrections at CMS CMS AN-2008/003.

HEISTER, A., Kodolova, O. et al., Measurement of Jets with the CMS Detector at the LHC, 2006. CMS NOTE 2006-036.

KODOLOVA O., Jet Energy Measurements at CMS, HCP-2005 Les-Diablerets, 9 July, 2005

KURT, P., Bhatti, A. and Zielinski, M., Transverse Momentum Distribution within Jets in pp Collisions at 14 TeV, CMS PAS QCD-005 - CMS AN 2008/024.

KURT, P. for the CMS Collaboration, Jet Shapes at CMS, CERN-CMS-CR-2009-004.

LIPATOV, L. N., Sov. J. Nucl. Phys. 20 (1975) 94-102.

LISTER, A., Measurement of b-quark jet shapes at CDF, PhD Thesis, TS2006-003.

MANGANO, M. L. , Moretti, M., Piccinini, F., Pittau, R. and Polosa, A. D., ALPGEN, a generator for hard multiparton processes in hadronic collisions, JHEP 07 (2003) 001, arXiv:hep-ph/0206293.

NAGY, Z., Phys. Rev. Lett. 88, 122003 (2002), arXiv:hep-ph/0110315; Phys. Rev. D 68, 094002 (2003) arXiv:hep-ph/0307268.

__________, 2002a, Three-jet cross sections in hadron hadron collisions at next-to-leading order, Phys. Rev. Lett. 88 (2002) 122003, arXiv:hep-ph/0110315.

PDG. Phys. Rev. D. 1 (2002).

PERKINS, Donald H. Hochenergiephysik, 1991. ISBN 3-89319-236-0.

PUMPLIN, J. et al., JHEP07, 012 (2002) [arXiv:hep-ph/0201195];

SEYMOUR, M. H., Jet shapes in hadron collisions: Higher orders, resummation and hadronization, Nucl. Phys. B513 (1998) 269-300, arXiv:hep-ph/9707338.

SHIFMAN, M., Handbook of QCD, vol. 2* 887-971, Pub. World Scientific Publisher, Singapore, New York, 2001.

SJOSTRAND, T., Mrenna, S. and Skands, P., PYTHIA 6.4 physics and manual, JHEP 0605, 026 (2006).

STERMAN, G., QCD and Jets, these TASI lectures. arxive:hep-ph/0412013, 2004.

St*ö*ckli, F., Effects of QCD Radiation on Higgs Production at the Large Hadron Collider, PhD Thesis, TS2008-024.

Tevatron-for-LHC Report of the QCD Working Group, FERMILAB-CONF-06-359, Oct 2006 [arXiv:hep-ph/0610012].

THE CMS COLLABORATION, Technical Design Report, CERN/LHCC 2000-038 (2000); http://cmsdoc.cern.ch/cms/TDR/TRIGGER-public/trigger.html (15/12/2000).

__________, 2006 The Underlying Event at LHC. CMS-Note-2006/067.

__________, 2007 J. Phys. G: Nucl. Part. Phys. 34 2307-2455.

__________, 2009a Jet energy calibration with photon+jet events, CMS PAS, vol. JME-09-004, 2009.

__________, 2009b Determination of the jet energy scale using $Z \to e^+e^- + jet\ p_T$ balance and a procedure for combining data driven corrections", CMS PAS, vol. JME-09-005, 2009.

THE PARTICLE DATA GROUP. Particle Physics Booklet - July 2006, 2006. LBL-61033.

THORNE, R. S., Martin, A. D. and Stirling, W. J. [arXiv:hep-ph/0606244], 2006.

WIGMANS, R., 1998, Nucl. Inst. Meth. A265, 273.

__________, 2000, Calorimetry, Energy Measurement in Particle Physics, Oxford University Press.

WOBISCH, M. and Wengler, T. hep-ph/9907280; M. Wobisch, Measurement and QCD analysis of jet cross sections in deep-inelastic positron proton collisions at s = 300GeV.

YAO, W.-M. et al., Review of Particle Physics. Journal of Physics G, 33:1+, 2006.

YAZGAN, E., PhD Thesis, TS2007-011.

CURRICULUM VITAE

Pelin Kurt was born on April 29, 1977, Tarsus, Mersin, Turkey. She graduated from the Chemistry Technical High School in the spring of 1994. She attended the Çukurova University, and graduated with bachelor degree in physics in the fall of 2000. Her interest in physics sciences persisted and she joined the Niğde University, Turkey, and accepted a research assistantship to study experimental nuclear physics under the supervision of Prof. Dr. Sefa Ertürk. On the beginning of fall 2003 she started for her PhD studies in the field of high energy particle physics under the supervision of Assoc. Prof. Dr. İsa Dumanoğlu. At the completion of this dissertation, Pelin Kurt considers to continue her activity in the research and academia field.

A. Jet Kinematics

A.1 Kinematics at Hadron Colliders

In performing parton model calculations for hadronic collisions like in Eq. (15), the partonic c.m. frame is not the same as the hadronic c.m. frame, e. g. the lab frame for the collider. Consider a collision between two hadrons of A and B of four-momenta $P_A = (E_A, 0, 0, p_A)$ and $P_B = (E_A, 0, 0, -p_A)$ in the lab frame. The two partons participating the subprocess have momenta $p_1 = x_1 P_A$ and $p_2 = x_2 P_B$. The parton system thus moves in the lab frame with a four-momentum

$$P_{cm} = [(x_1 + x_2)E, A, 0, 0, (x_1 - x_2)p_A] \ (E_A \approx p_A) \tag{A.1}$$

or with a speed $\beta_{cm} = (x_1 - x_2)/(x_1 + x_2)$, or with a rapidity

$$y_{cm} = \frac{1}{2} ln \frac{x_1}{x_2} \tag{A.2}$$

Denote the total hadronic center of mass energy by $S = 4E_A^2$ and the partonic center of mass energy by s, we have

$$s = \tau S, \qquad \tau = x_1 x_2 = \frac{s}{S} \tag{A.3}$$

The parton energy fractions are thus given by

$$x_{1,2} = \sqrt{\tau} e^{\pm y_{cm}} \tag{A.4}$$

One always encounters the integration over the energy fractions as in equation(15). With this variable change, one has

$$\int_{\tau_0}^{1} dx_1 \int_{\tau_0/x_1}^{1} dx_2 = \int_{\tau_0}^{1} d\tau \int_{\frac{1}{2} ln\tau}^{-\frac{1}{2} ln\tau} dy_{cm} \tag{A.5}$$

The variable τ characterizes the (invariant) mass of the reaction, with $\tau_0 = m_{res}^2/S$ and m_{res} is the threshold for the parton level final state (sum over the masses in the final state); while y_{cm} specifies the longitudinal boost of the partonic c.m. frame with respect to the lab frame. It turns out that the $\tau - y_{cm}$ variables are better for numerical evaluations. Consider a final state particle of momentum $p^\mu = (E, \vec{p})$ in the lab frame. Since the c.m. frame of the two colliding partons is a *priori* undetermined with respect to the lab frame, the scattering polar angle θ in these two frames is not a good observable to describe theory and the experiment. It would be thus more desirable to seek for kinematical variables that are invariant under unknown longitudinal boosts.

Transverse Momentum and the Azimuthal Angle: Since the ambiguous motion between the parton c.m. frame and the hadron lab frame is along the longitudinal beam direction ($\vec{z}$), variables involving only the transverse components are invaraint under longitudinal boosts. It is thus convenient to write the phase space element in the cylindrical coordinate as

$$\frac{d^3\vec{p}}{E} = dp_x dp_y \frac{dp_z}{E} = p_T dp_T d\phi \frac{dp_z}{E} \tag{A.6}$$

where ϕ is the azimuthal angle about the $\vec{z}$ axis, and

$$p_T = \sqrt{p_x^2 p_y^2} = p \sin\theta \tag{A.7}$$

is the transverse momentum. It is obvious that both p_T and ϕ are boost-invariant, so is dp_z/E The rapidity of a particle of momentum p^μ is defined to be

$$y = \frac{1}{2} ln \frac{E + p_z}{E - p_z} = \frac{1}{2} ln \frac{1 + \beta_z}{1 - \beta_z} \tag{A.8}$$

where $\beta_z = p_z/E = \beta \cos\theta$ is the z-component of the particles velocity. In the The advantage of using rapidity is that under an arbitrary boost along the z -axis, rapidity differences remain invariant, i.e. they directly measure relative scattering angles in the partonic c.m. frame

Consider the rapidity in a boosted frame (say the parton c.m. frame), and perform the Lorentz transformation,

$$y = \frac{1}{2} ln \frac{E' + p_z'}{E' - p_z'} = \frac{1}{2} ln \frac{(1 - \beta_0)(E + p_z)}{(1 + \beta_0)(E - p_z)} = y - y_0 \tag{A.9}$$

In the massless limit, E $\approx |\vec{p}|$, so that

$$y = \frac{1}{2} ln \frac{(1 + \cos\theta)}{(1 - \cos\theta)} = ln \cot\frac{\theta}{2} \equiv \eta \tag{A.10}$$

where η is the pseudo-rapidity, which has one-to-one correspondence with the scattering polar angle $\pi \geq \theta \geq 0$ for $-\infty < \eta < \infty$. It is desirable to use the kinematical variables p_T, η, ϕ to describe events in hadronic collisions.

B. Figures for All Jet p_T Bins

B.1 Figures for Number of Particles, Tracks, Towers for Selected Jet P_T Bins

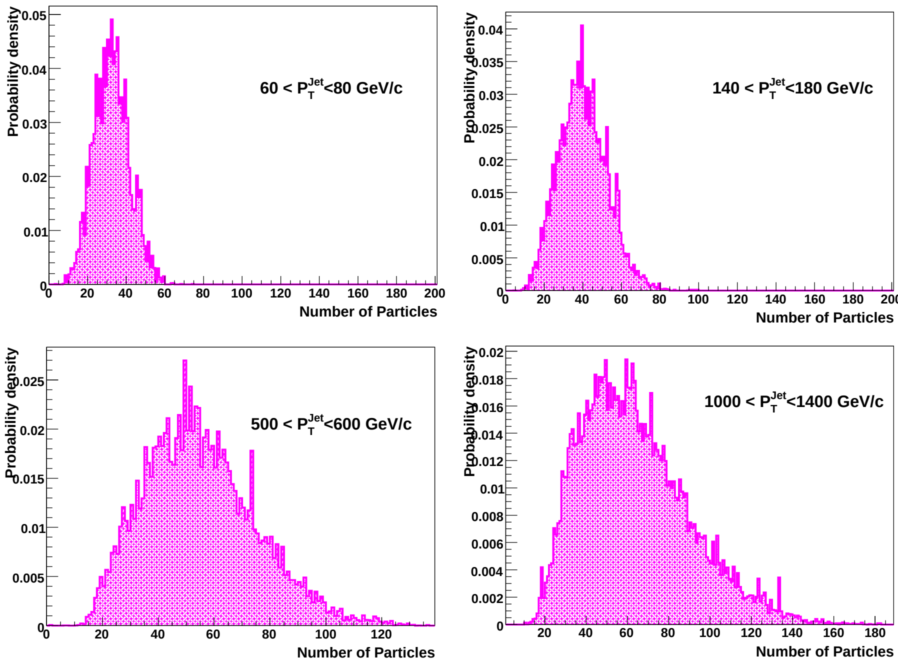

Figure B.1. Multiplicity distributions of particles in a jet for selected p_T bins.

B.2 Figures for All Jet p_T Bins

In the following pages we present an expanded set of figures for all jet p_T bins.

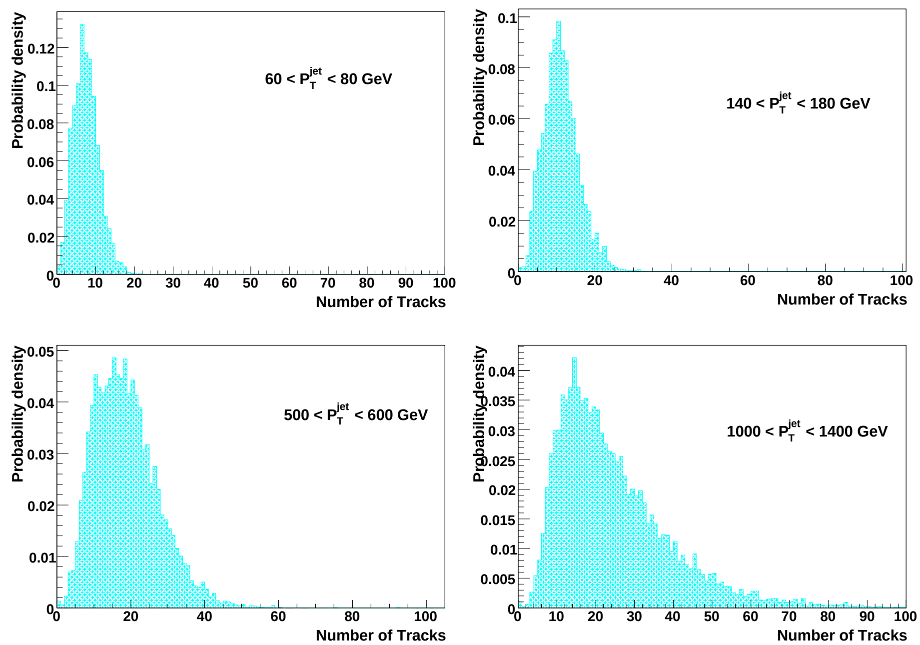

Figure B.2. Multiplicity distributions of tracks in a jet for selected jet p_T bins.

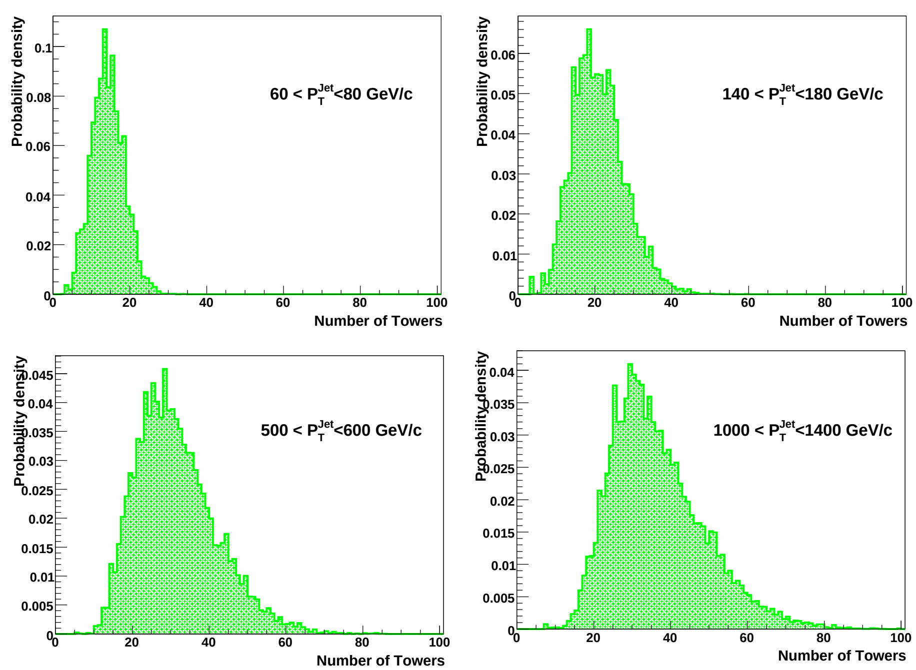

Figure B.3. Multiplicity distributions of calorimeter towers in a jet for selected jet p_T bins.

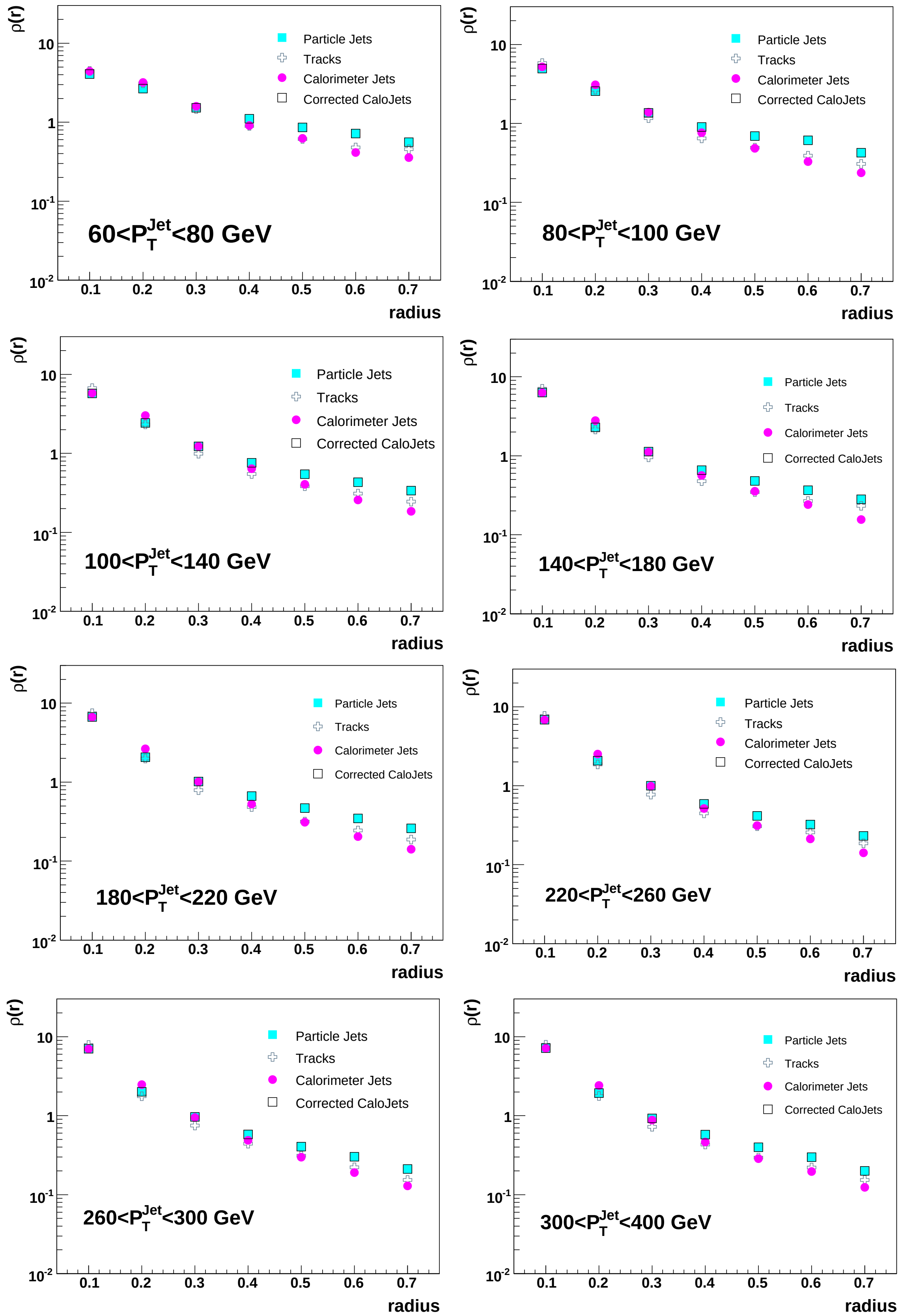

Figure B.4. Differential jet shapes for selected p_T bins. Statistical errors are included.

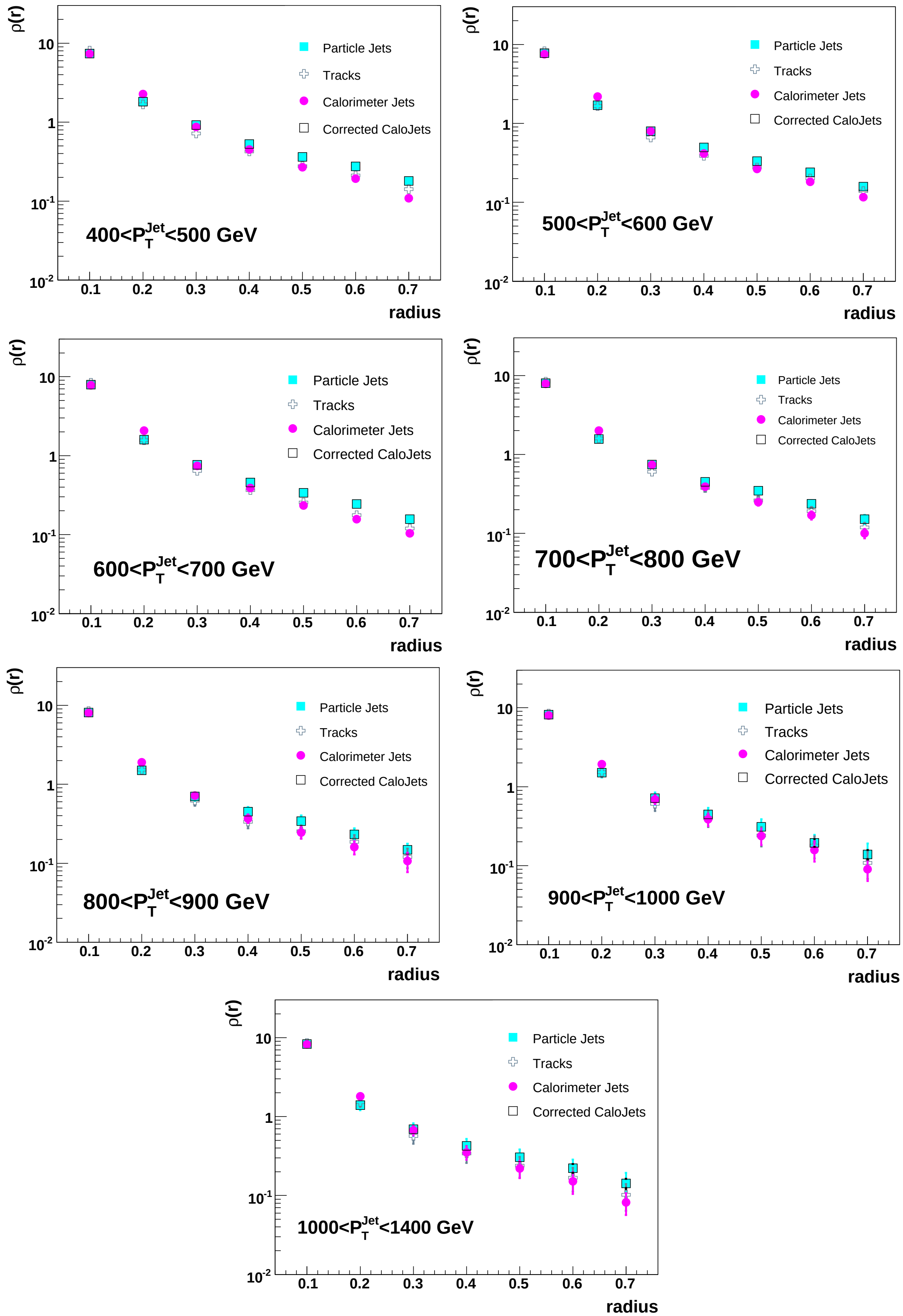

Figure B.5. Differential jet shapes for selected p_T bins. Statistical errors are included.

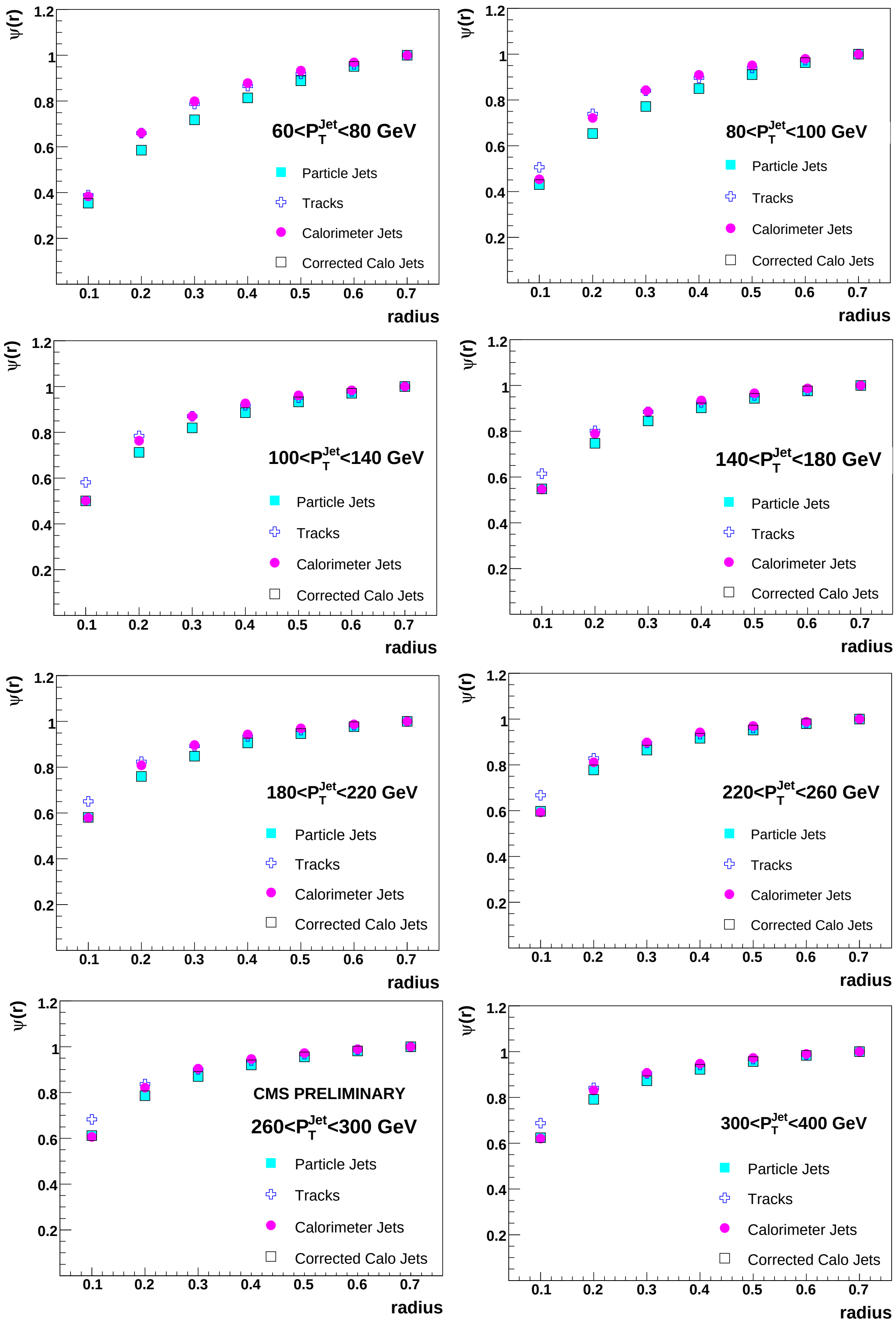

Figure B.6 .Integrated jet shapes for selected p_T bins. Statistical errors are included.

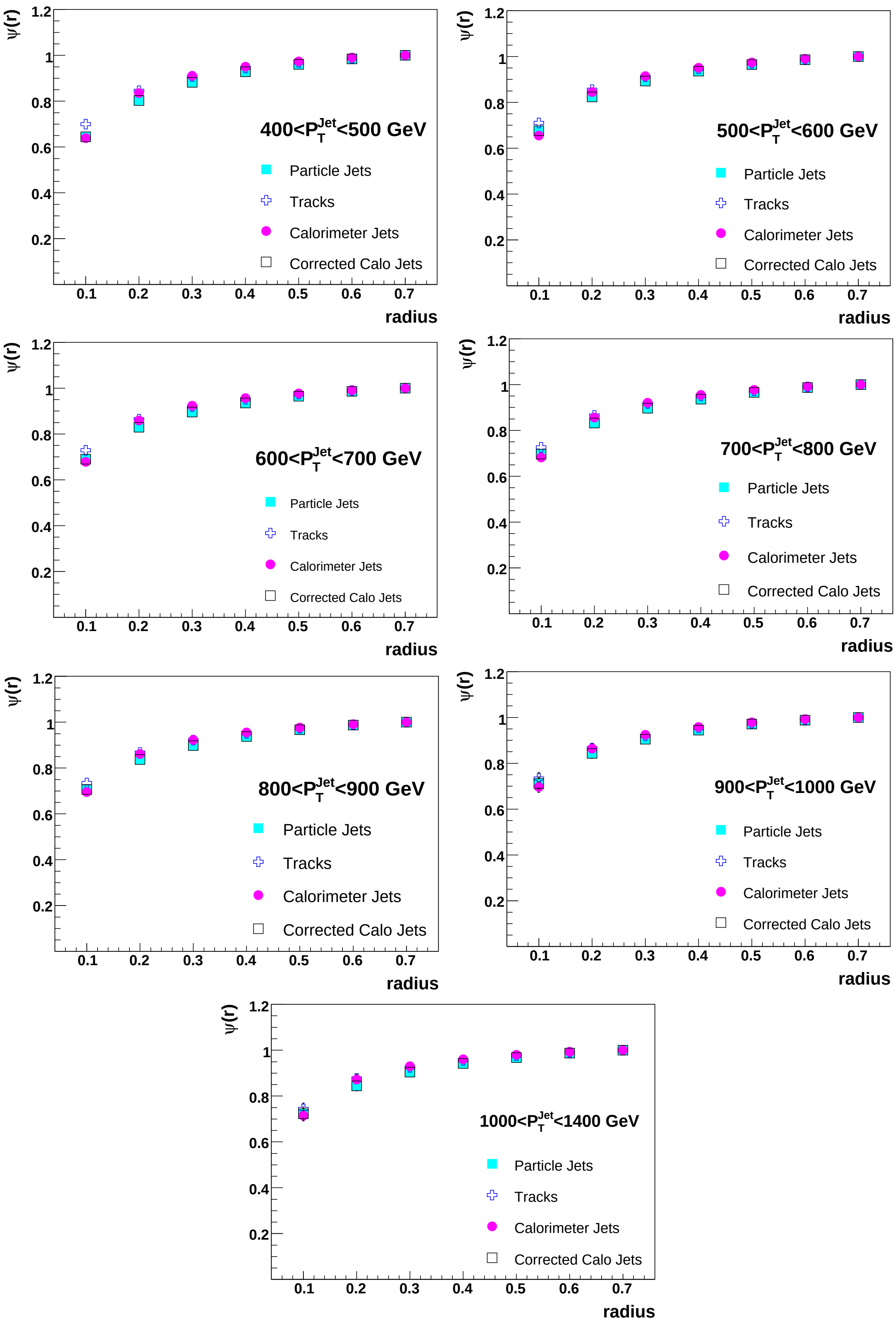

Figure B.7. Integrated jet shapes for selected p_T bins. Statistical errors are included.

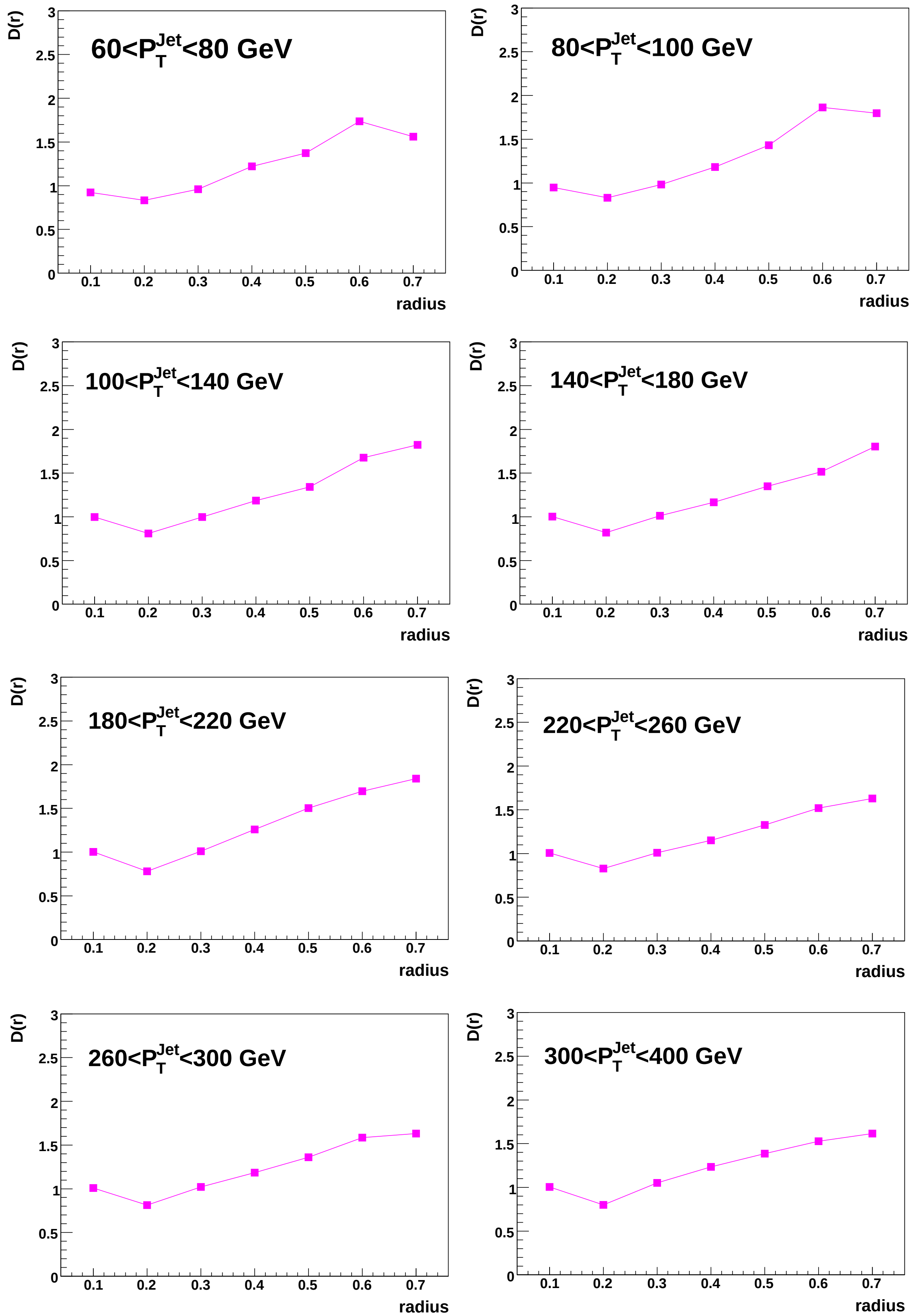

Figure B.8. Correction factors for differential jet shapes for selected p_T bins. Statistical errors are included.

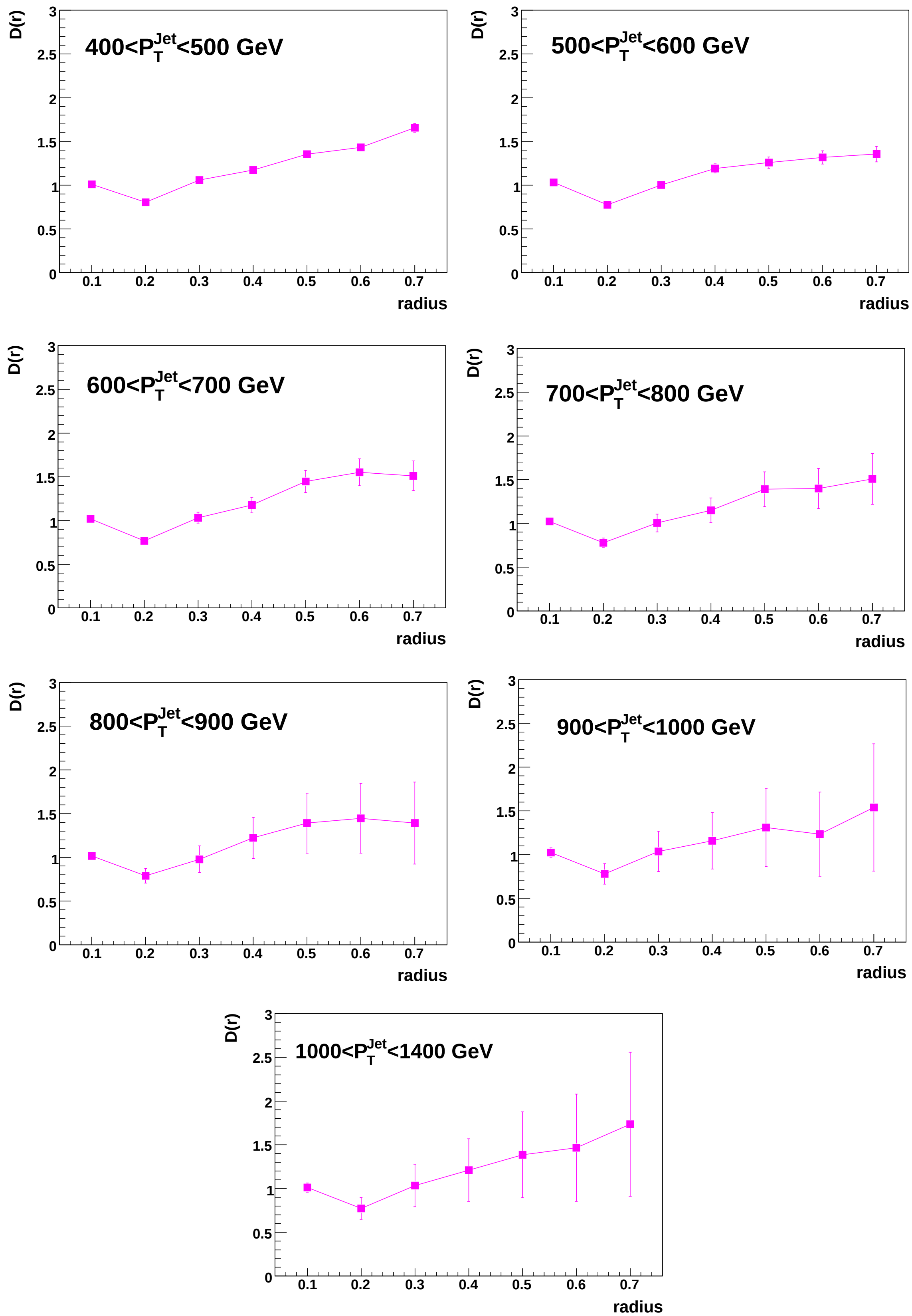

Figure B.9 .Correction factors for differential jet shapes for selected p_T bins. Statistical errors are included.

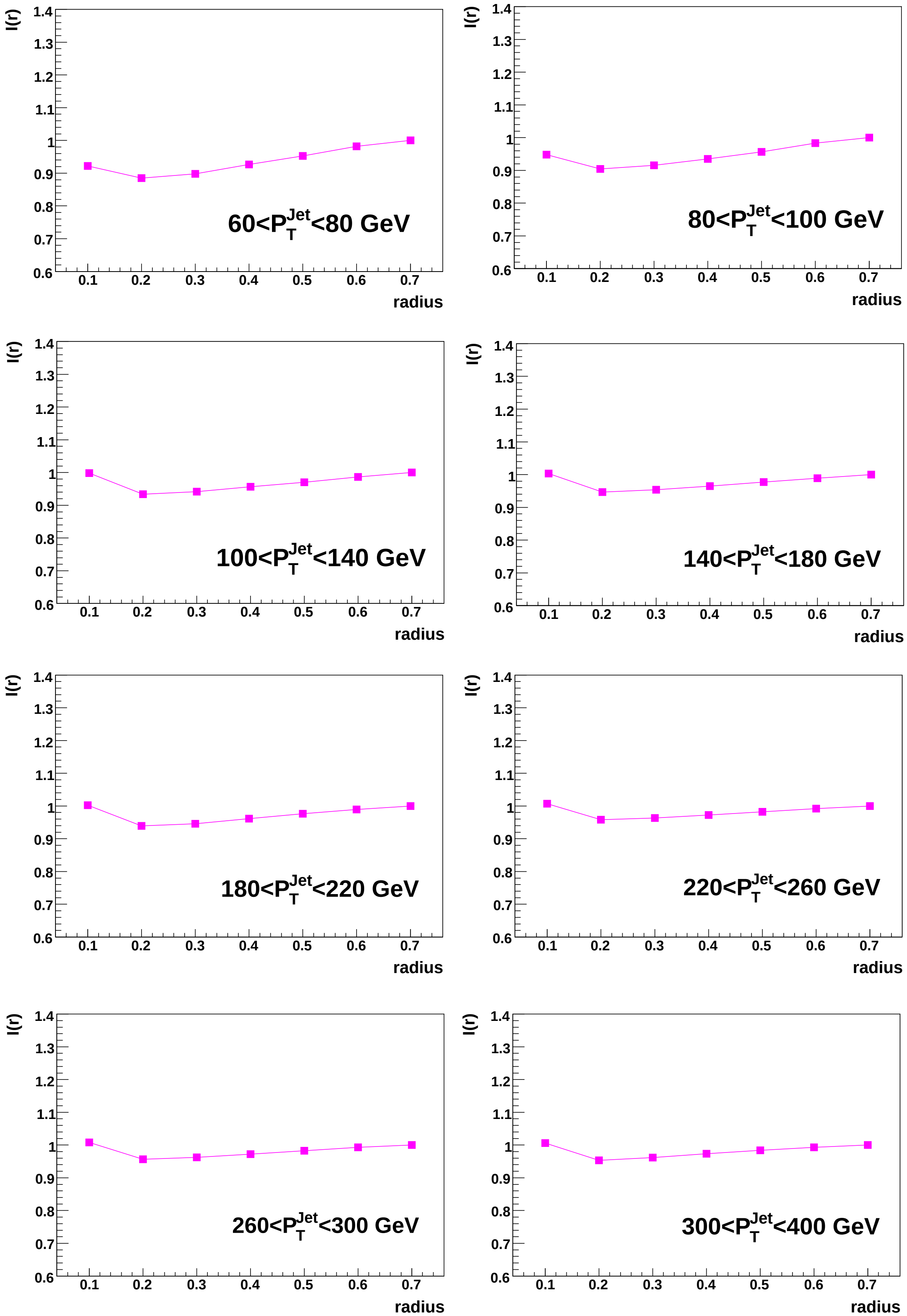

Figure B.10. Correction factors for integrated jet shapes for selected p_T bins. Statistical errors are included.

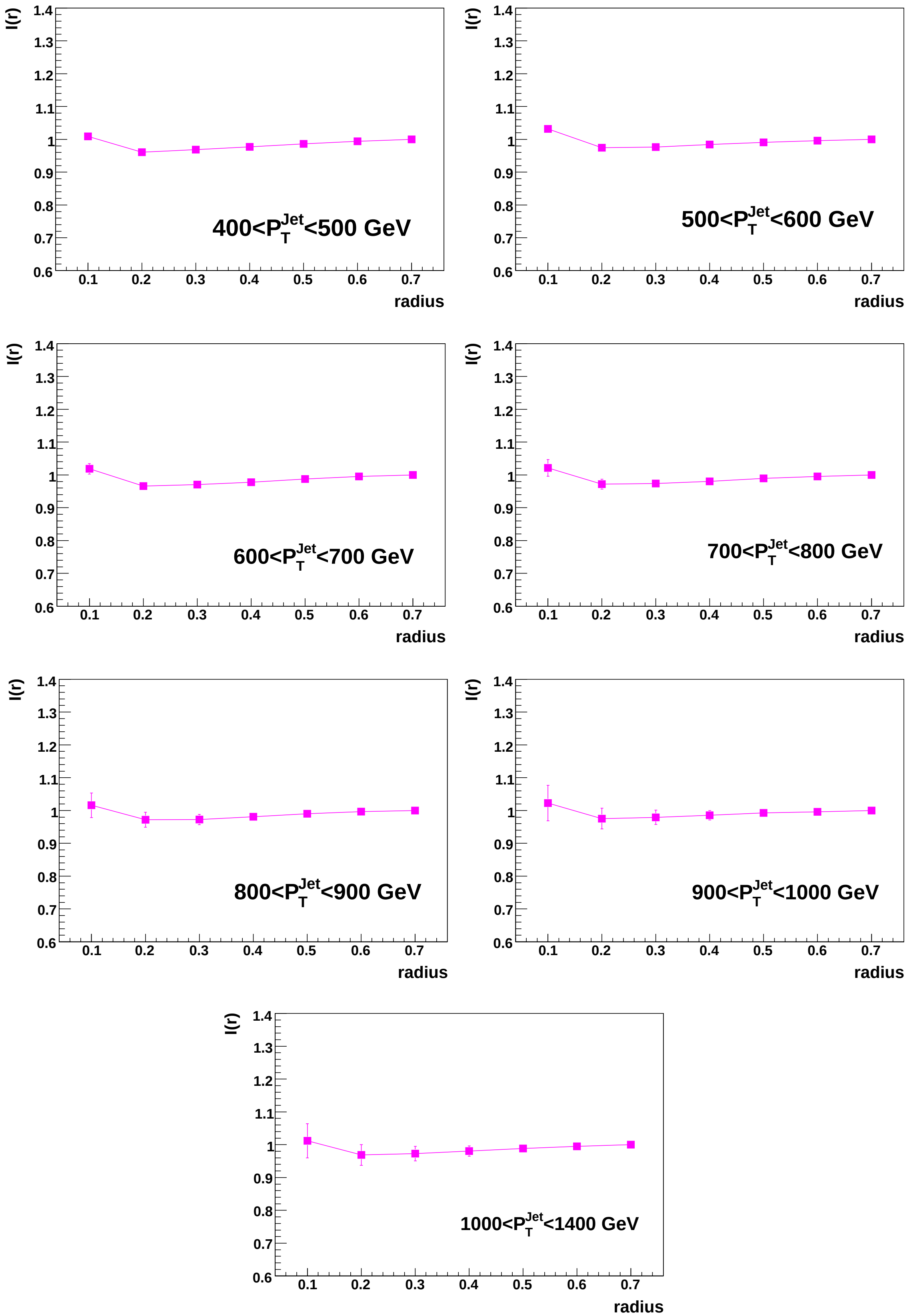

Figure B.11. Correction factors for integrated jet shapes for selected p_T bins. Statistical errors are included.

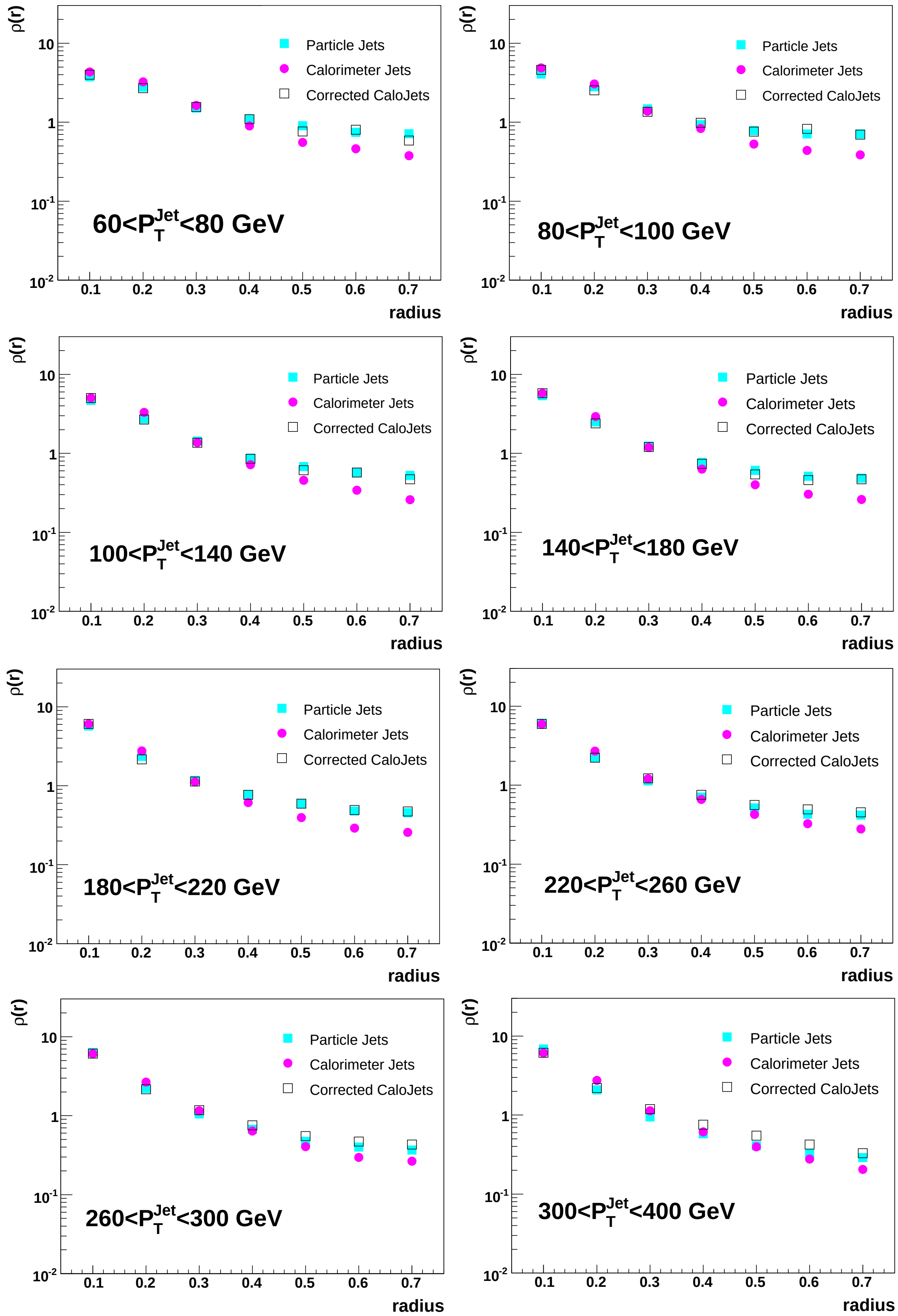

Figure B.12. Differential jet shapes for selected p_T bins in multijet samples generated with ALPGEN. Statistical errors are included.

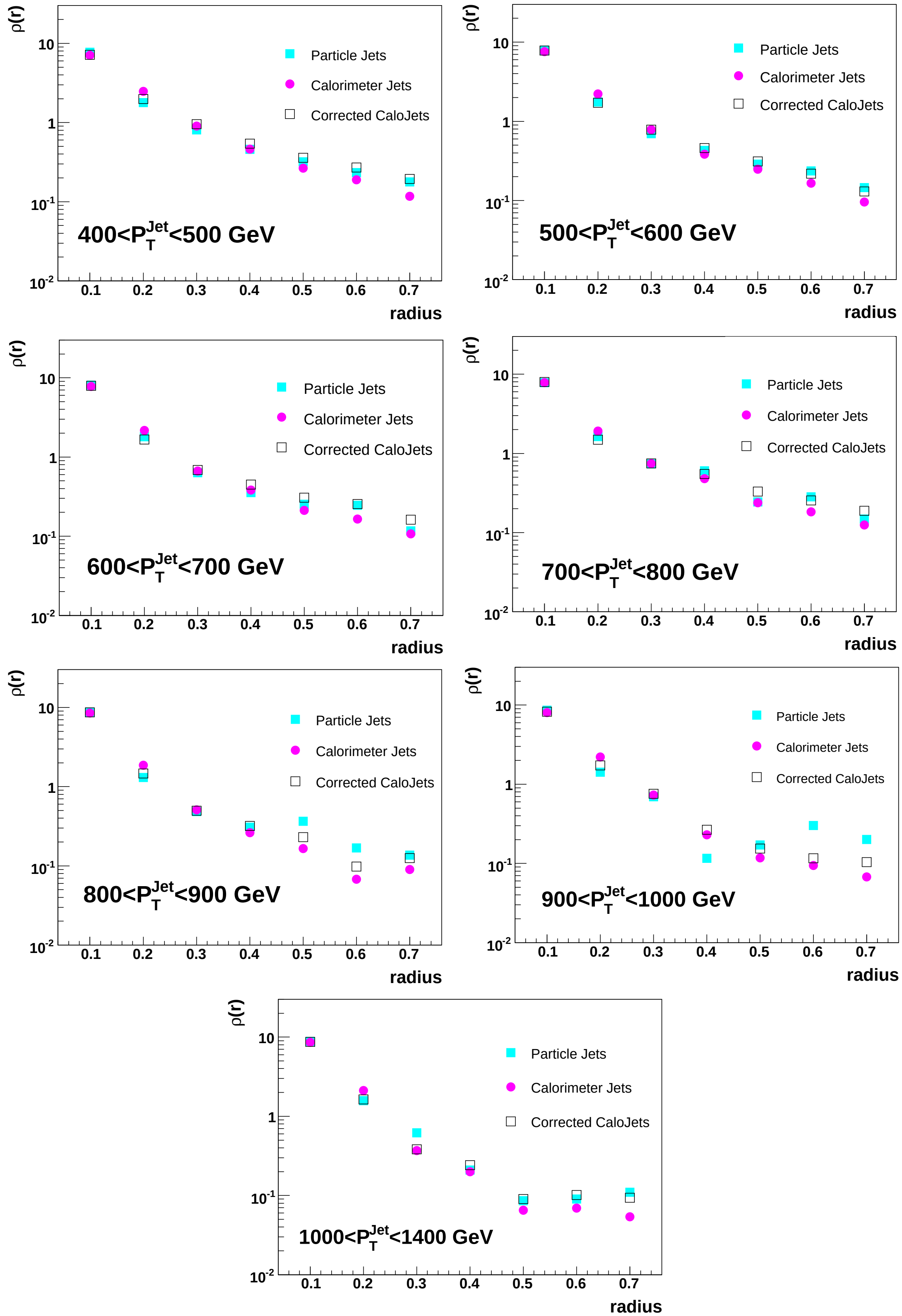

Figure B.13. Differential jet shapes for selected p_T bins in multijet samples generated with ALPGEN.

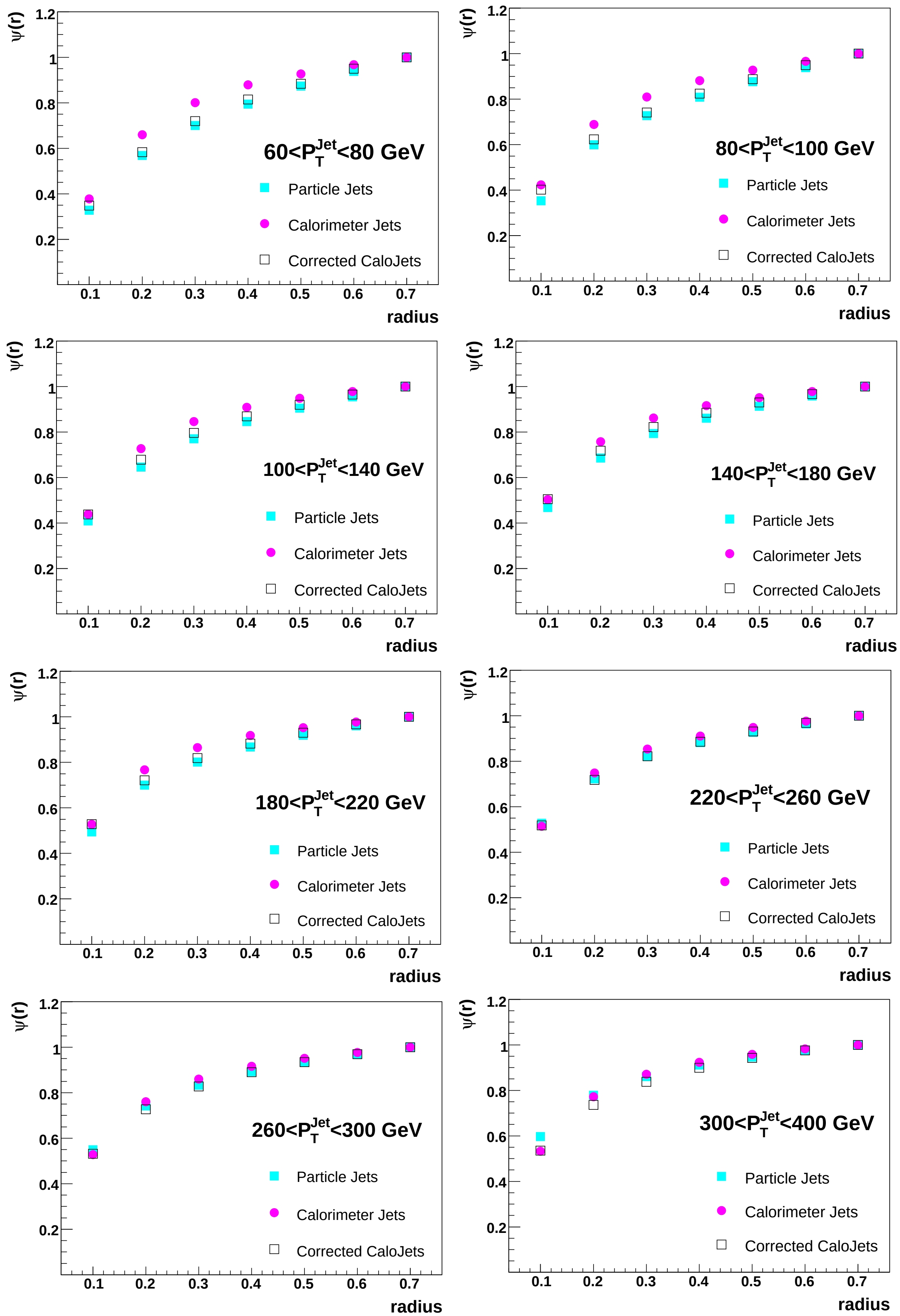

Figure B.14. Integrated jet shapes for selected p_T bins in multijet samples generated with ALPGEN.

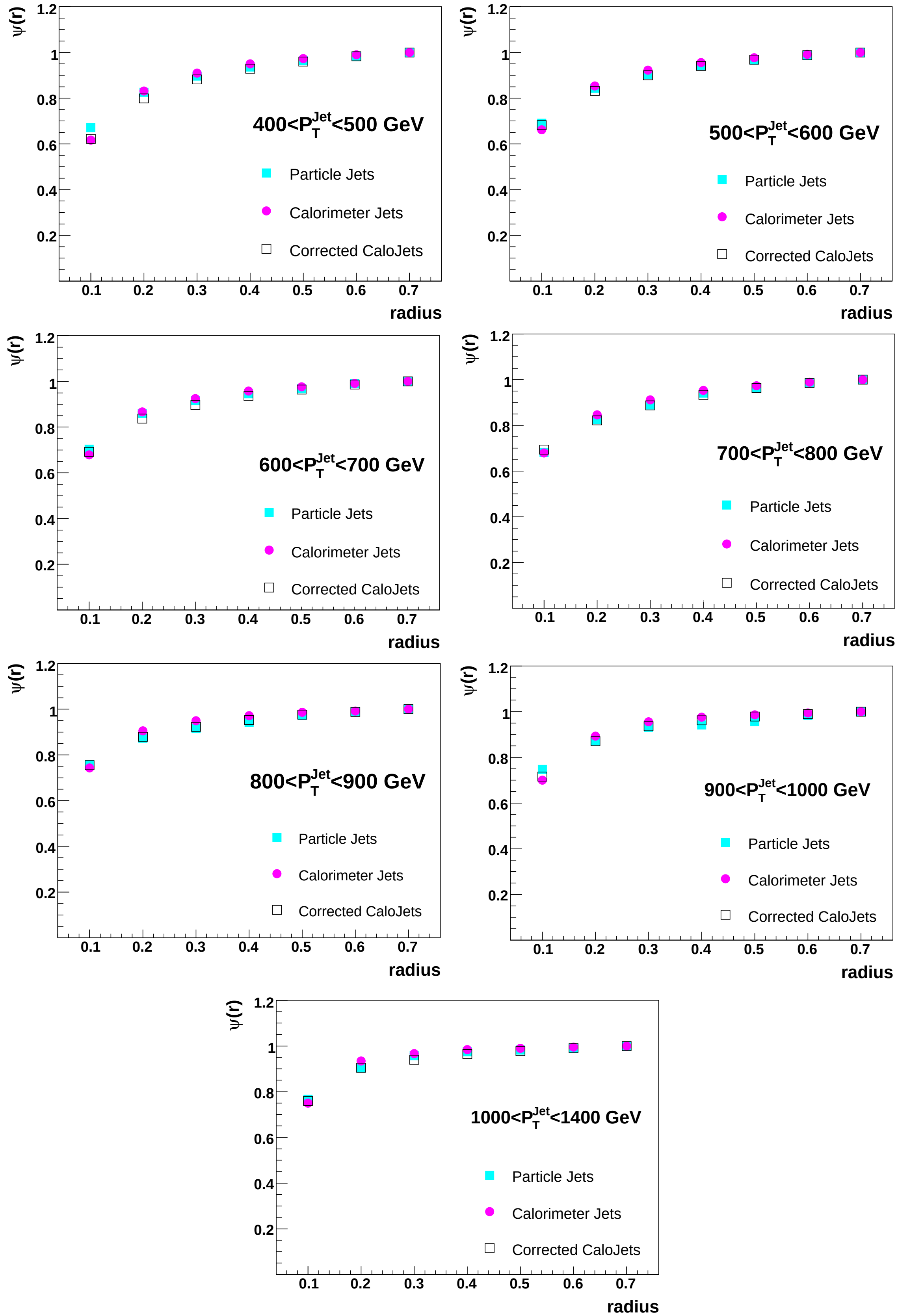

Figure B.15. Integrated jet shapes for selected p_T bins in multijet samples generated with ALPGEN.

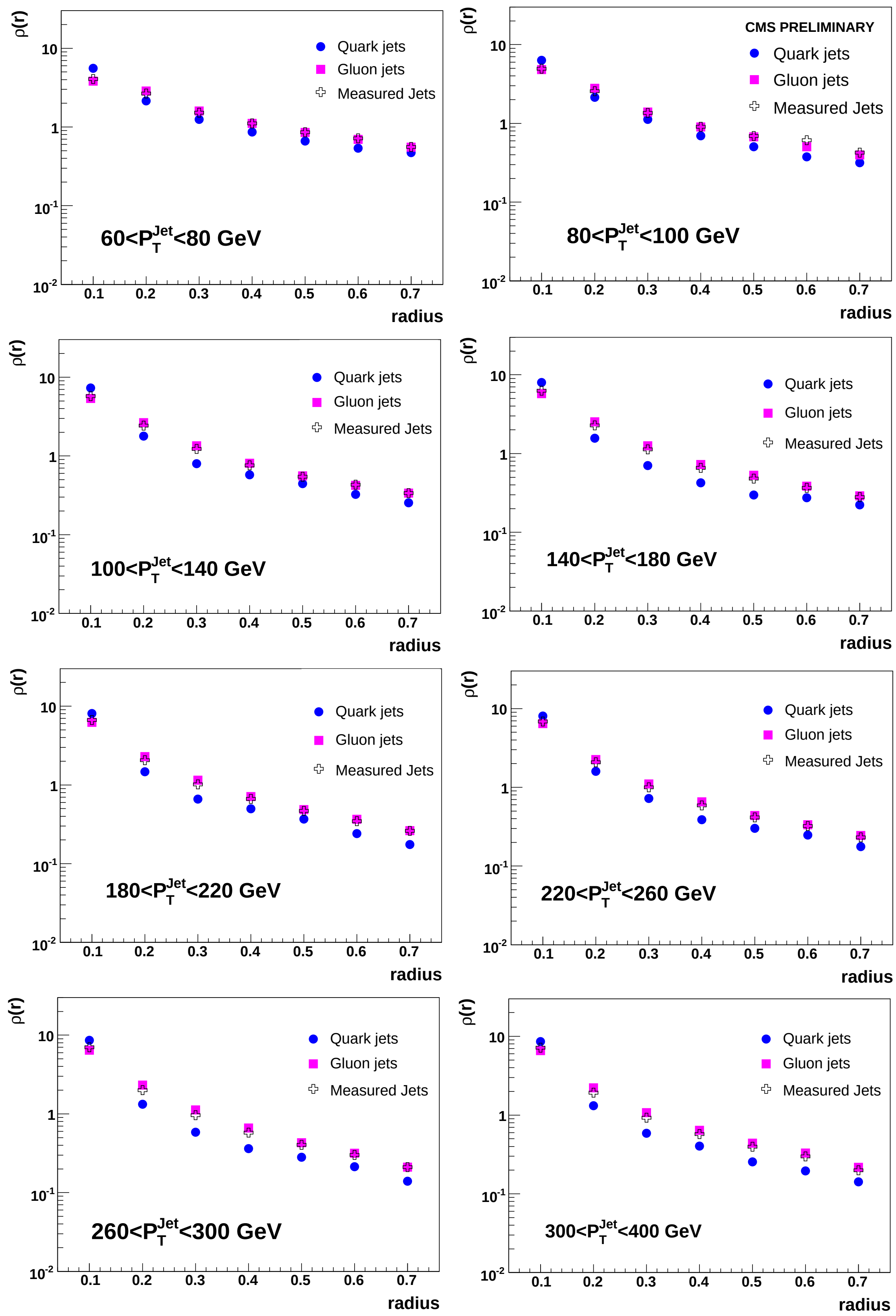

Figure B.16. Comparison of quark and gluon differential jet shapes to simulated data in selected p_T bins. Statistical errors are included.

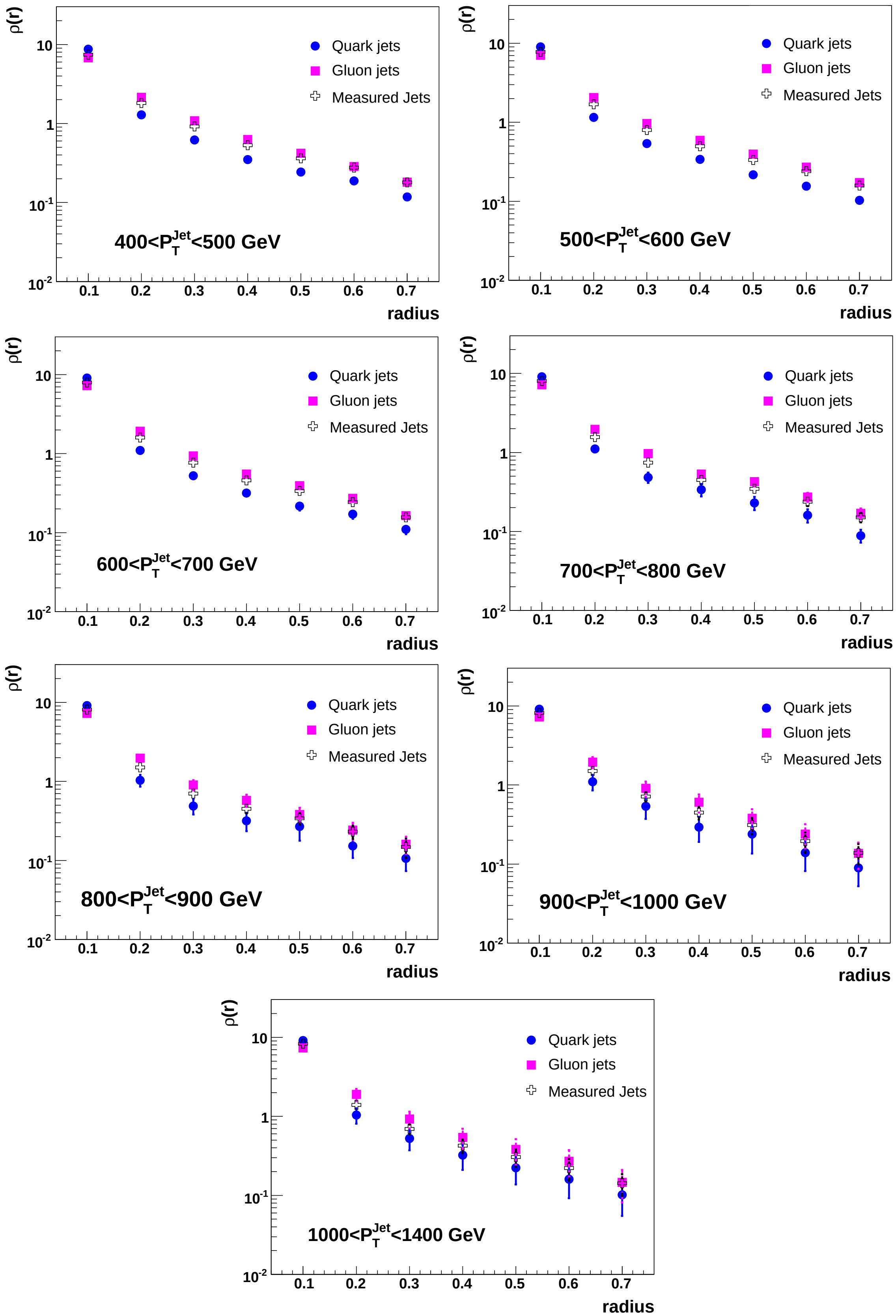

Figure B.17. Comparison of quark and gluon differential jet shapes to simulated data in selected p_T bins. Statistical errors are included.

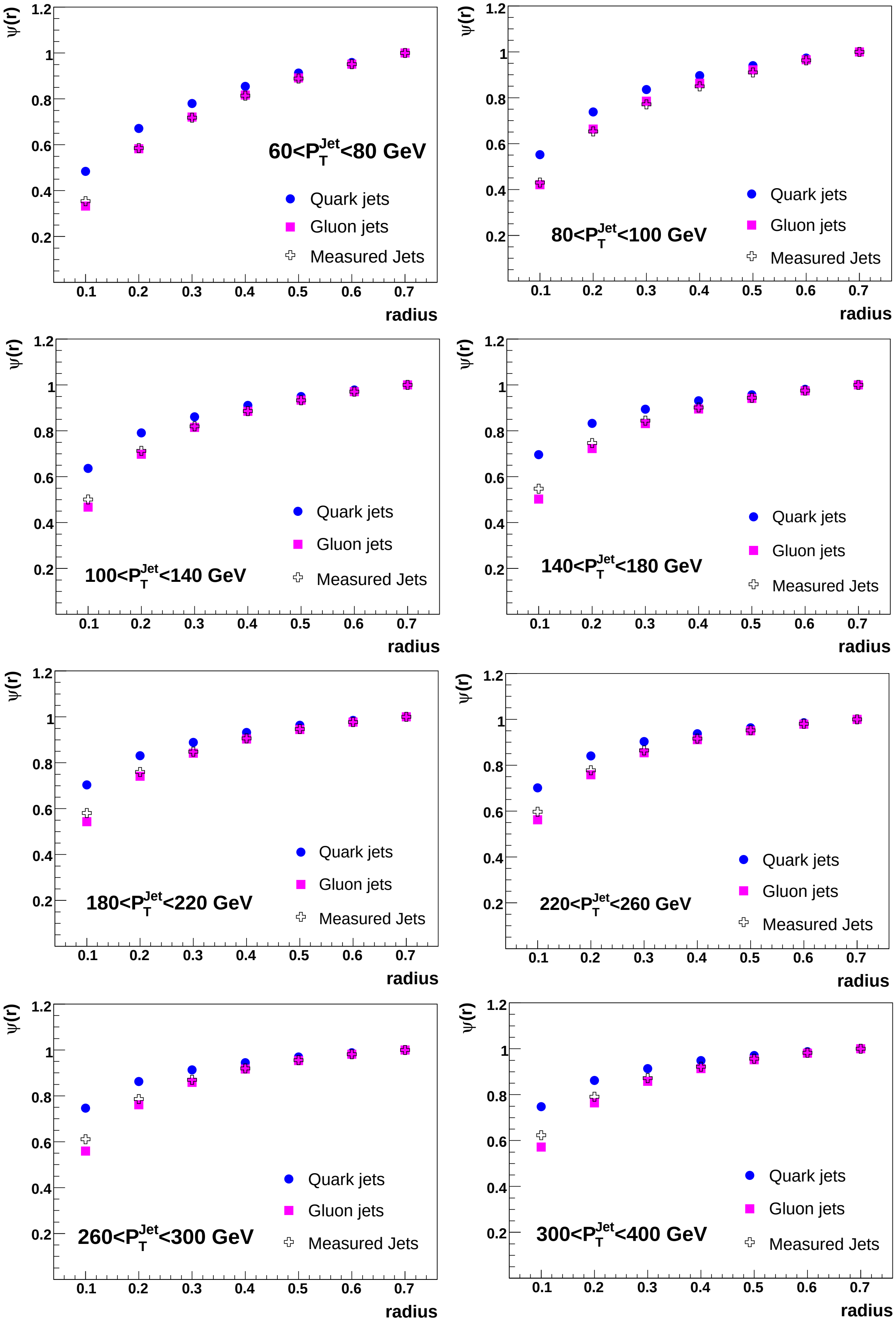

Figure B.18. Comparison of quark and gluon integrated jet shapes to simulated data in selected P_T bins. Statistical errors are included.

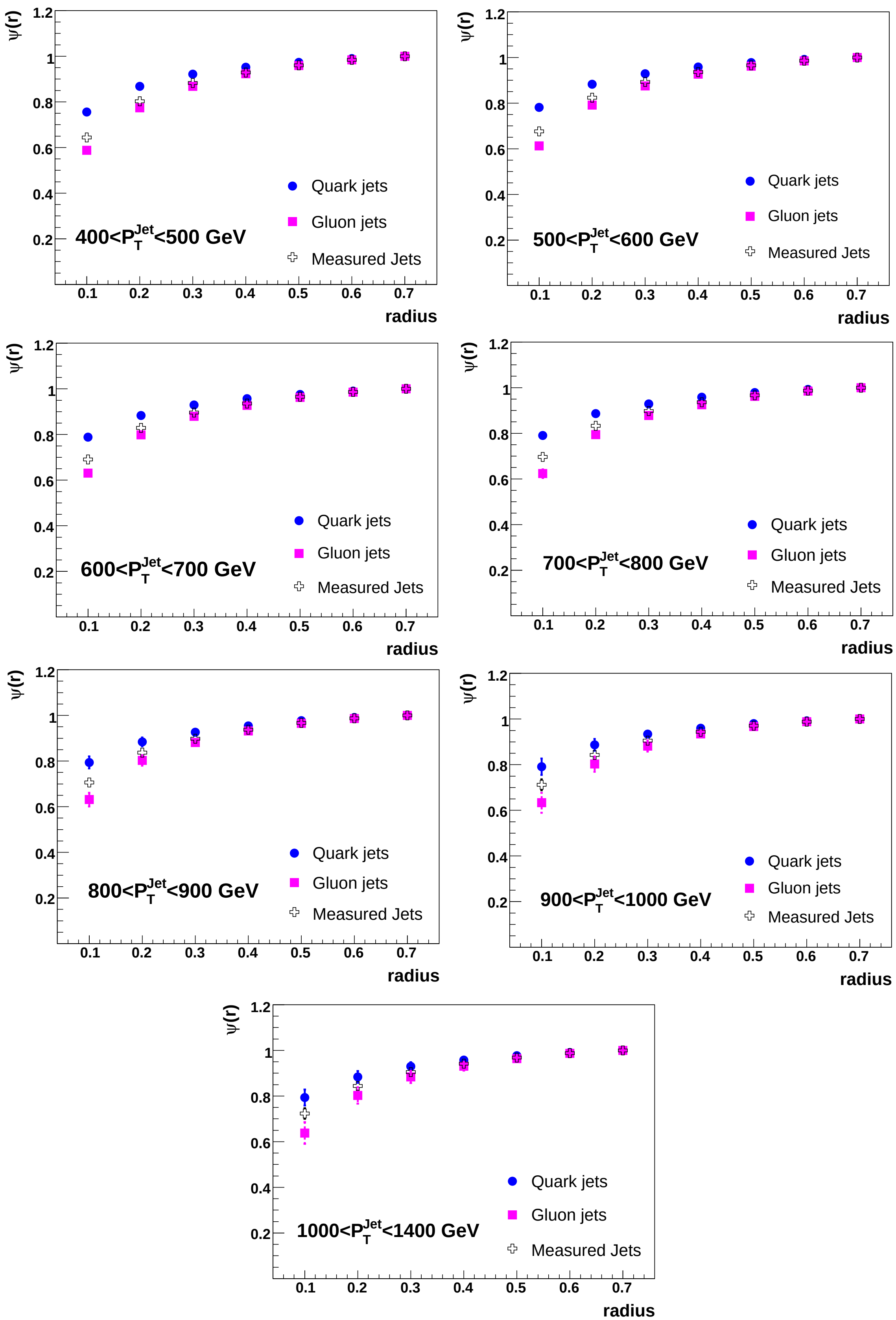

Figure B.19. Comparison of quark and gluon integrated jet shapes to simulated data in selected p_T bins. Statistical errors are included.

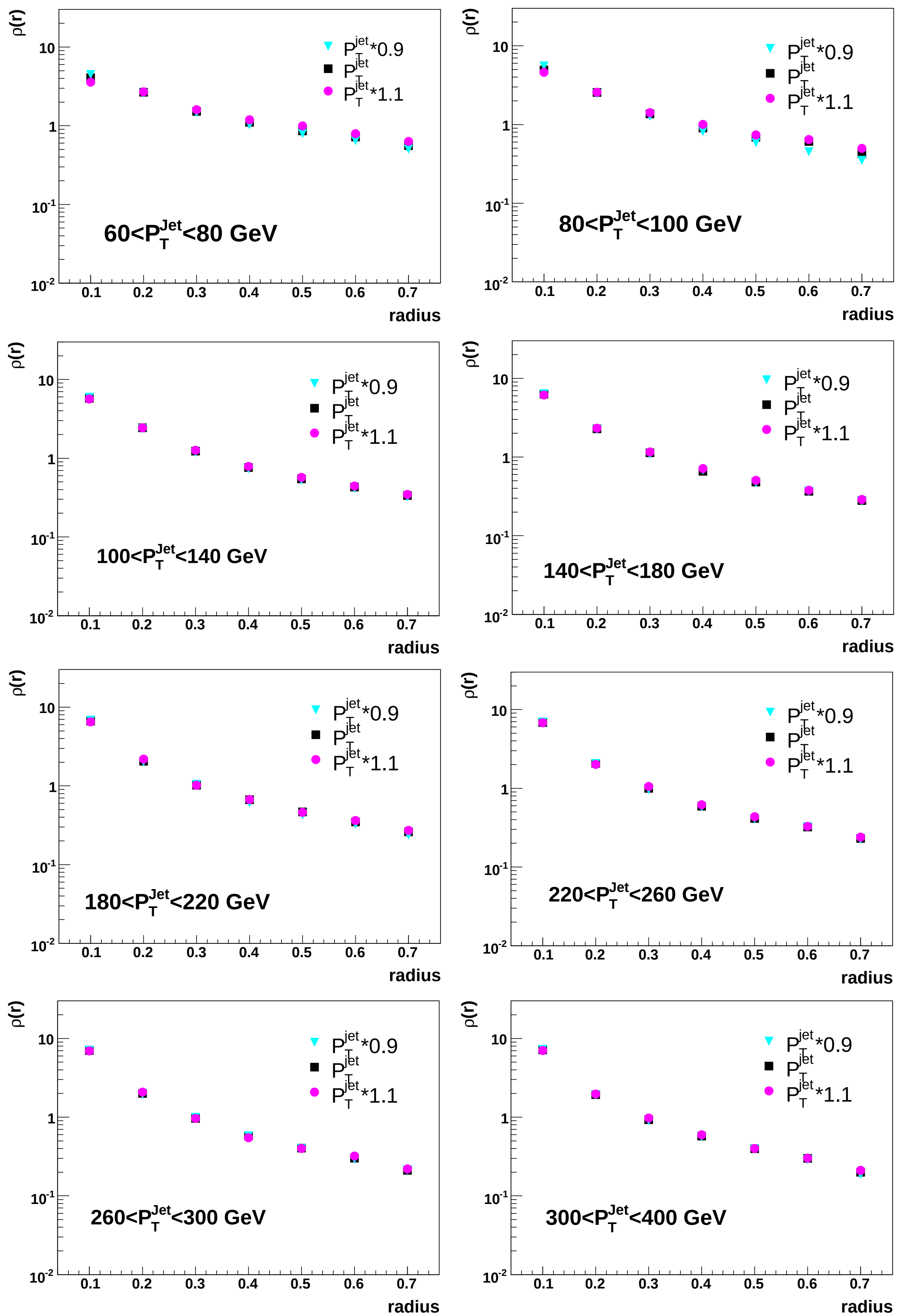

Figure B.20. Differential jet shapes for ± 10% changes in energy scale for selected p_T bins. Statistical errors are included.

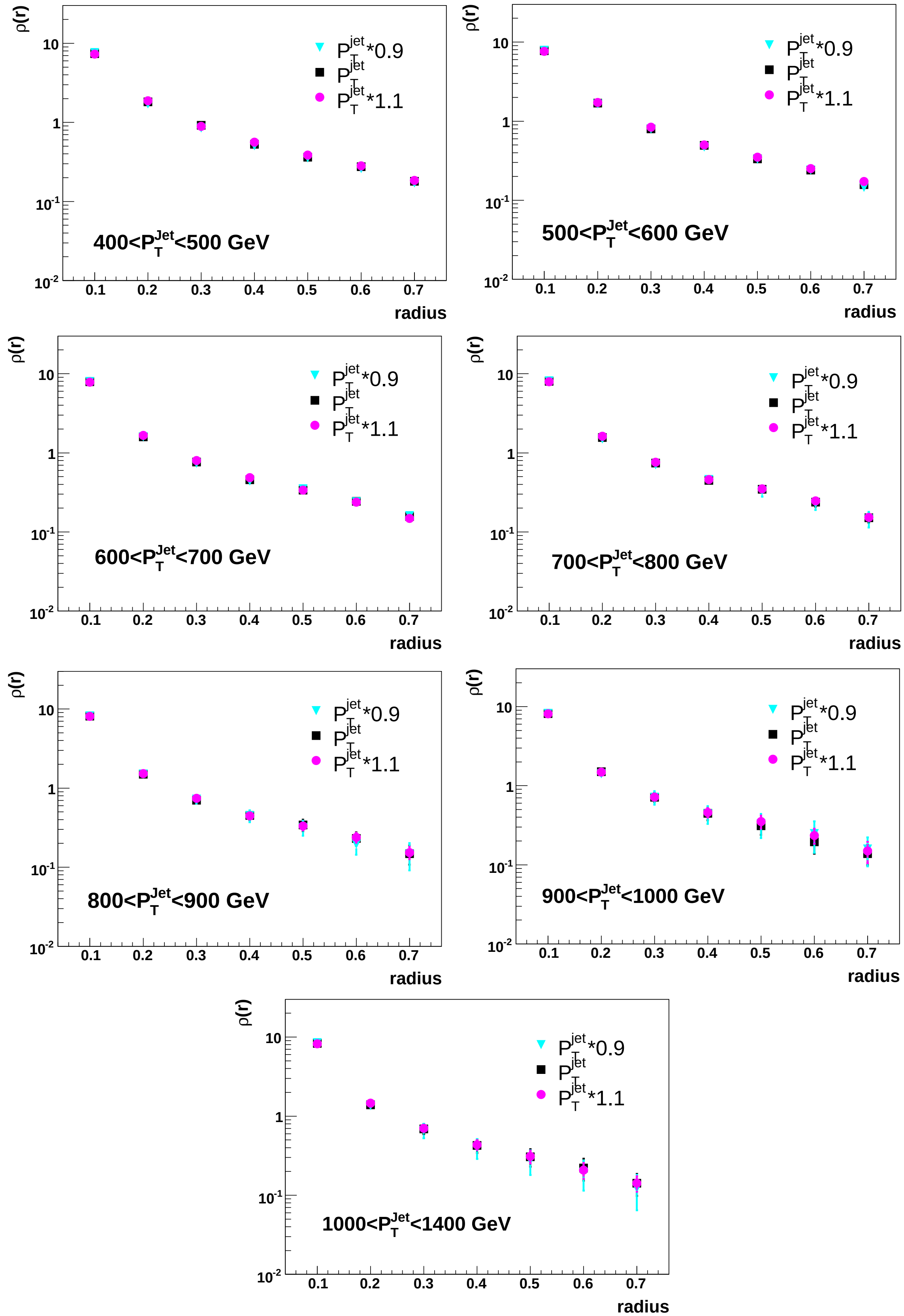

Figure B.21. Differential jet shapes for $\pm 10\%$ changes in energy scale for selected p_T bins. Statistical errors are included.

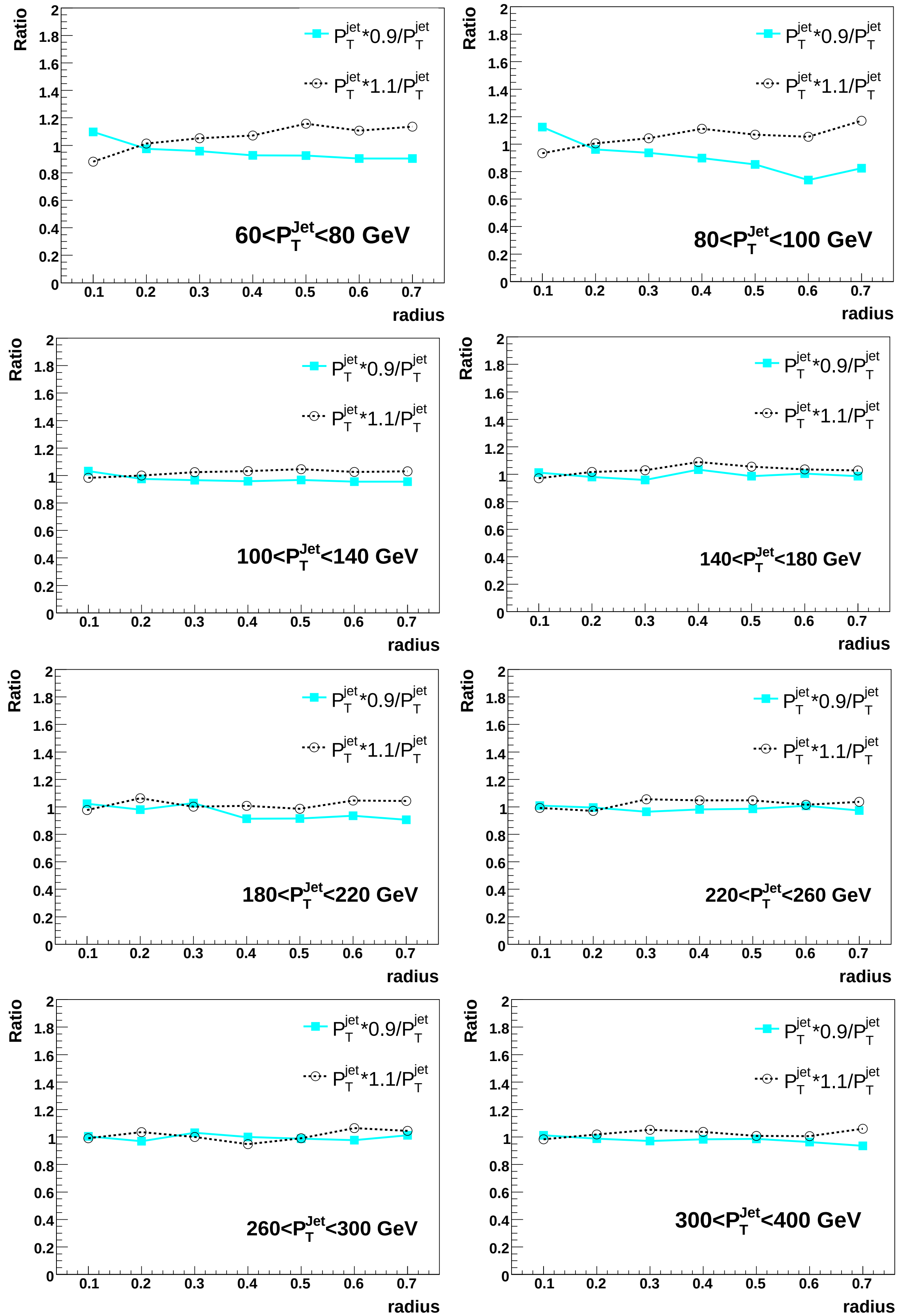

Figure B.22. Effect of changing jet energy scale for differential jet shapes for selected p_T bins. Only statistical errors are included.

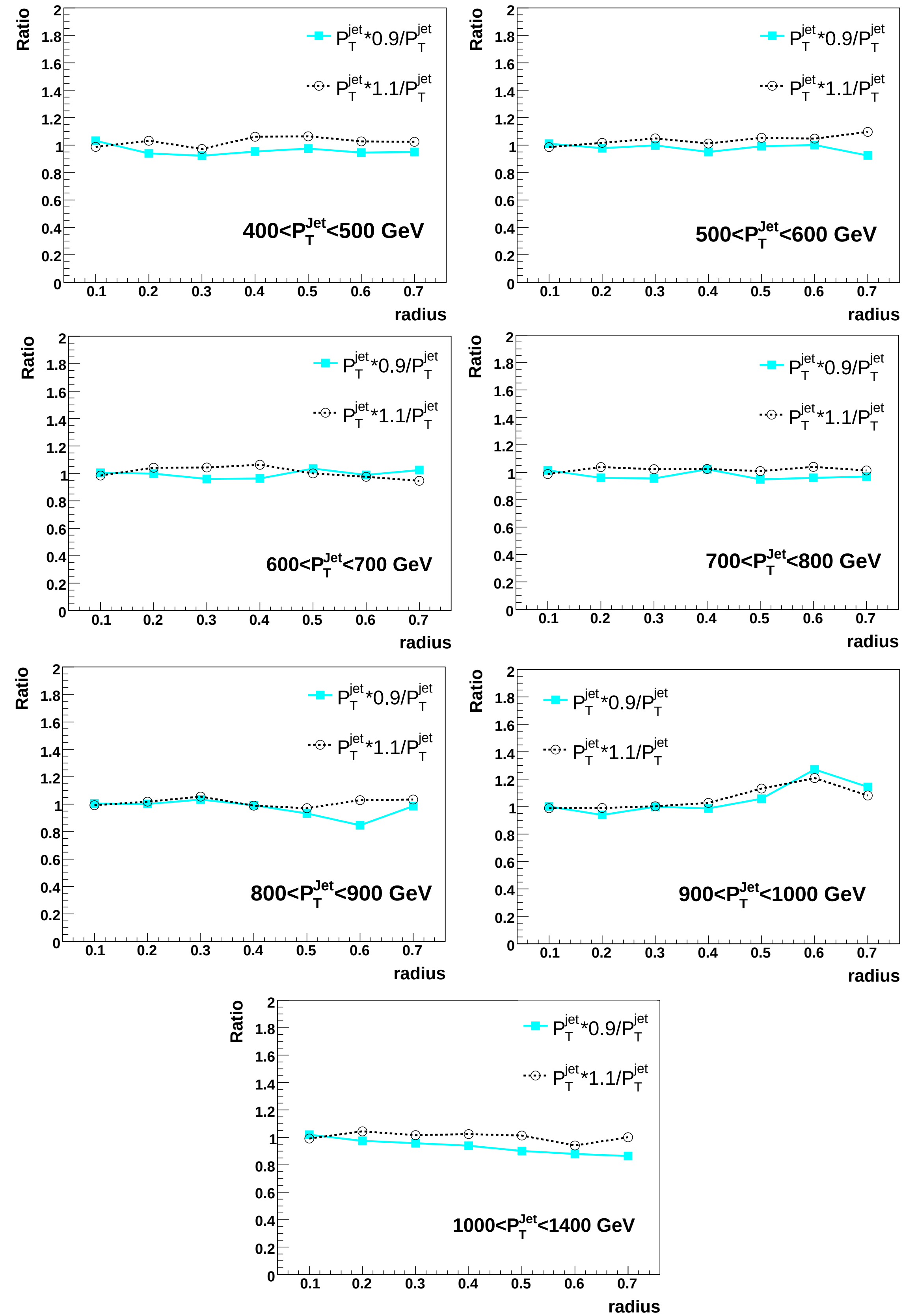

Figure B.23. Effect of changing jet energy scale for differential jet shapes for selected p_T bins. Only statistical errors are included.

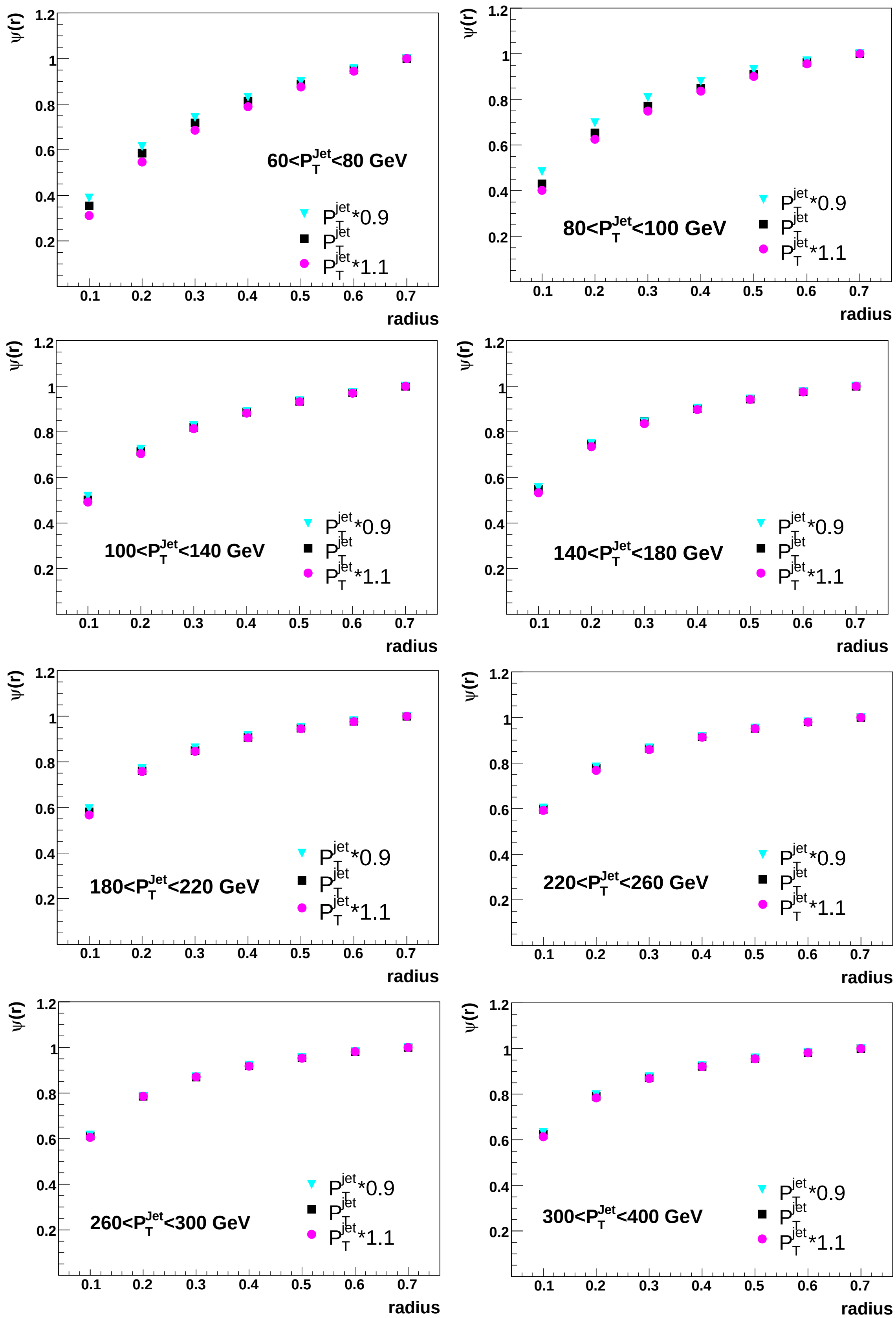

Figure B.24. Integrated jet shapes for ±10% changes in energy scale for selected p_T bins. Statistical errors are included.

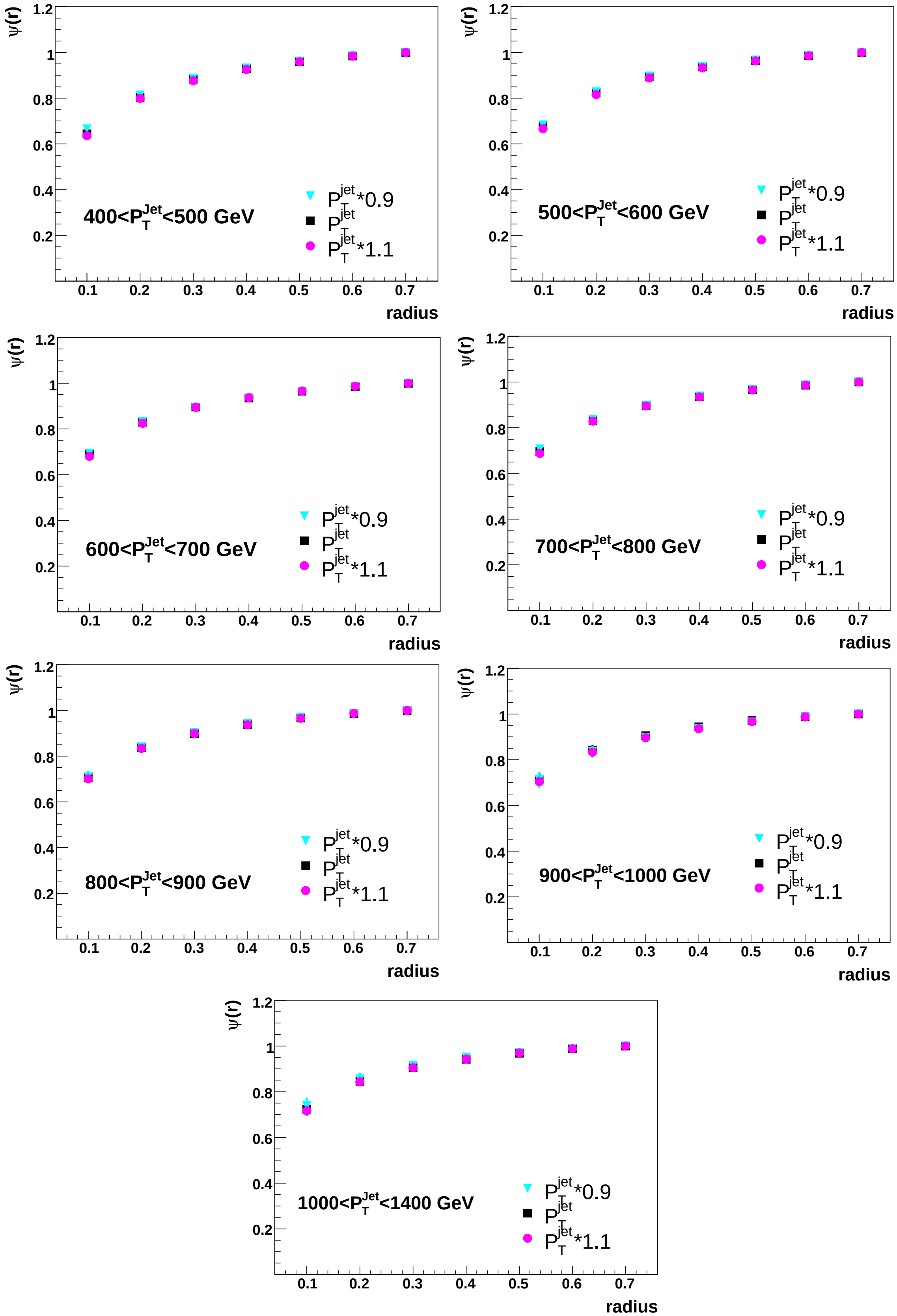

Figure B.25. Integrated jet shapes for ±10% changes in energy scale for selected p_T bins. Statistical errors are included.

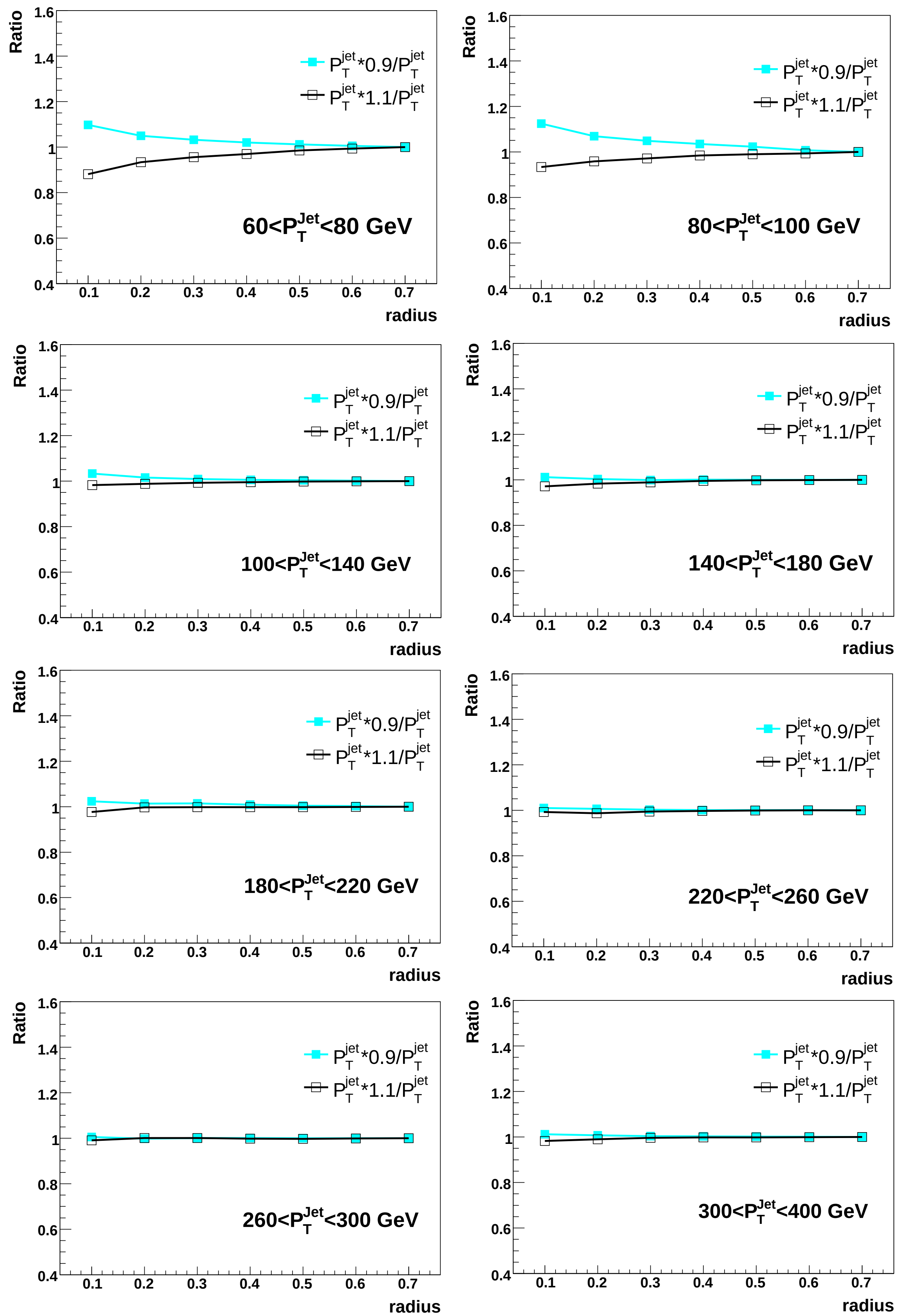

Figure B.26. Effect of changing jet energy scale for integrated jet shapes for selected p_T bins. Only statistical errors are included.

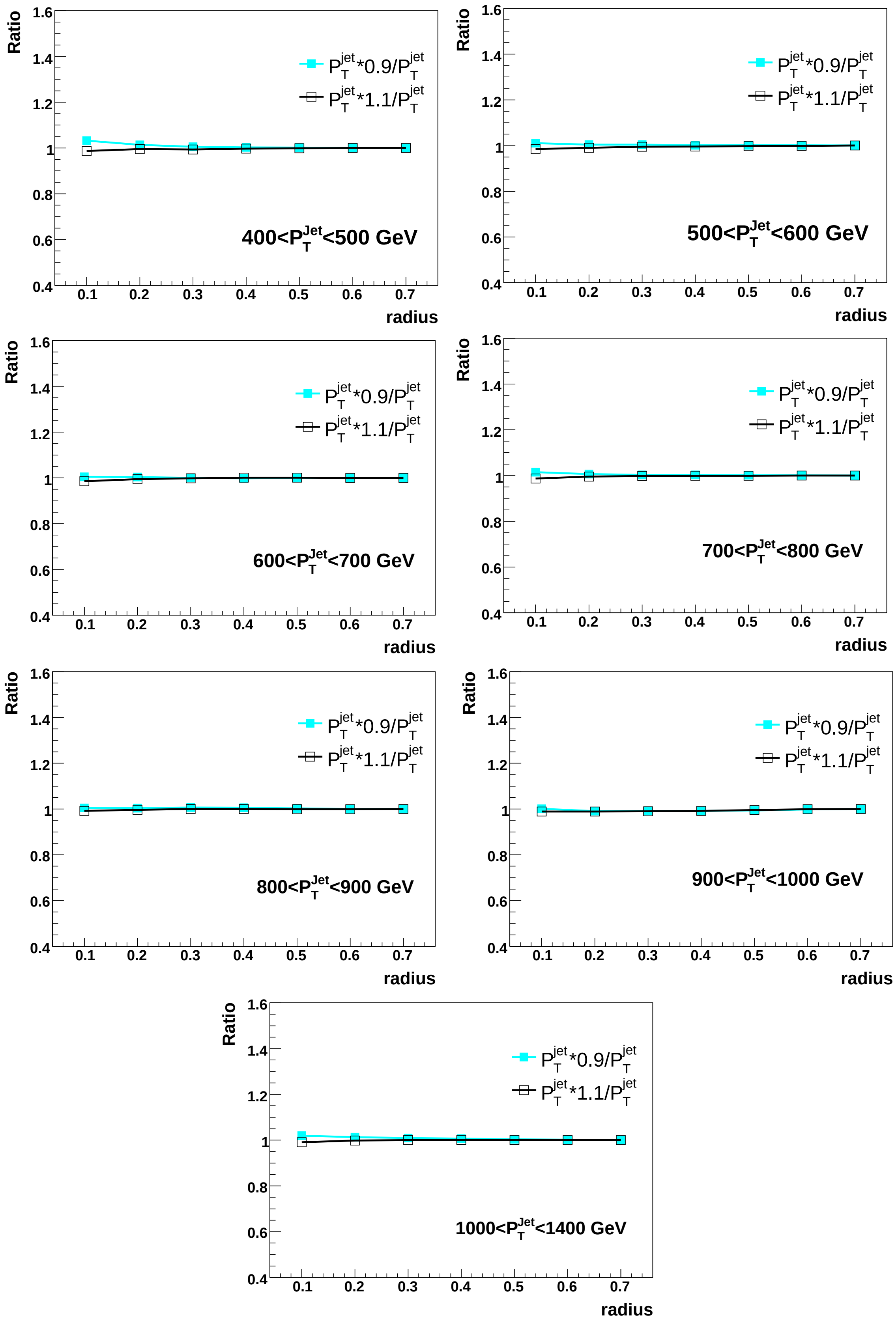

Figure B.27. Effect of changing jet energy scale for integrated jet shapes for selected p_T bins. Only statistical errors are included.

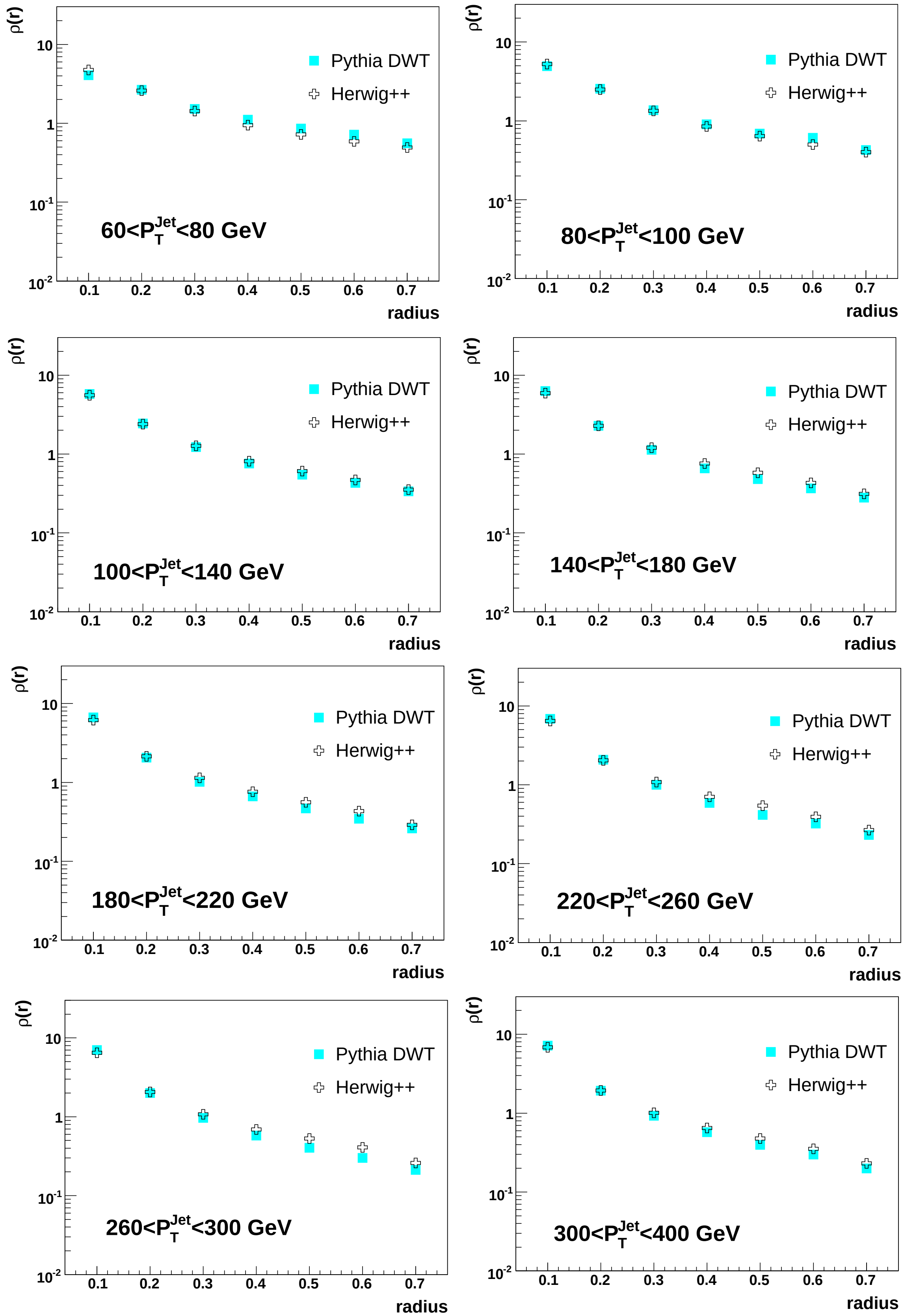

Figure B.28. Comparison of particle level differential jet shapes from HERWIG++ and PYTHIA for selected p_T bins. Statistical errors are included.

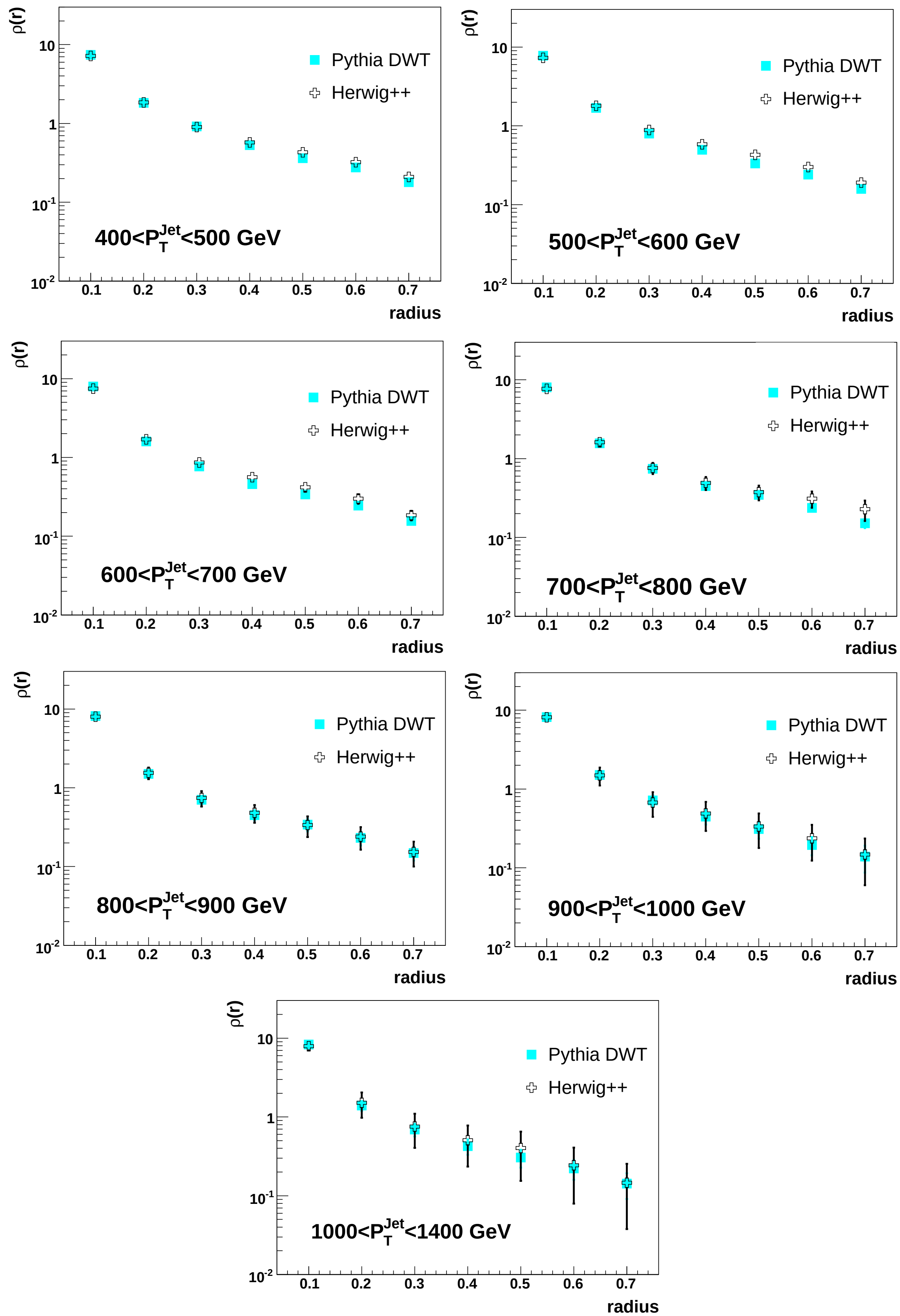

Figure B.29. Comparison of particle level differential jet shapes from HERWIG++ and PYTHIA for selected p_T bins. Statistical errors are included.

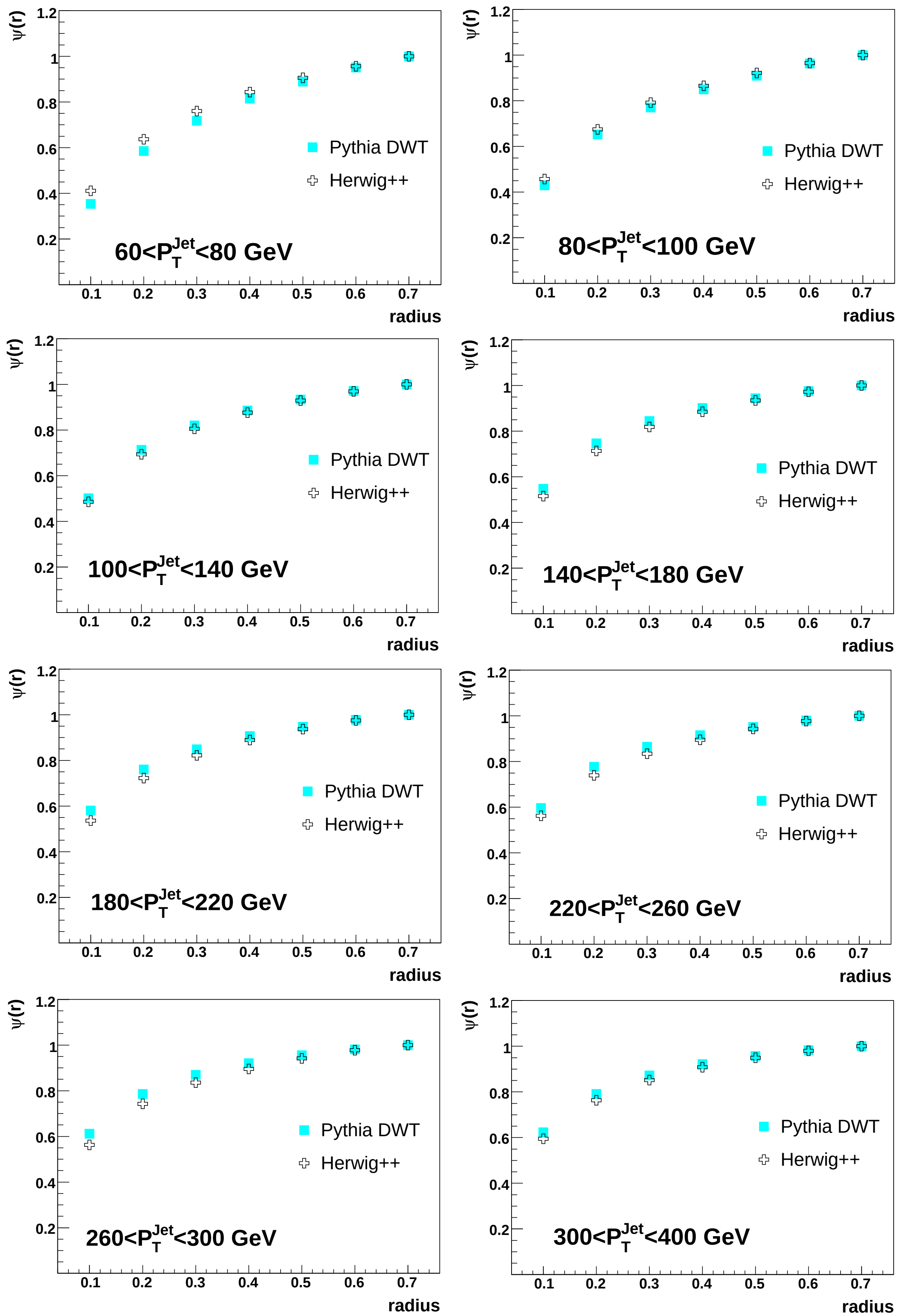

Figure B.30. Comparison of particle level integrated jet shapes from HERWIG++ and PYTHIA for selected p_T bins. Statistical errors are included.

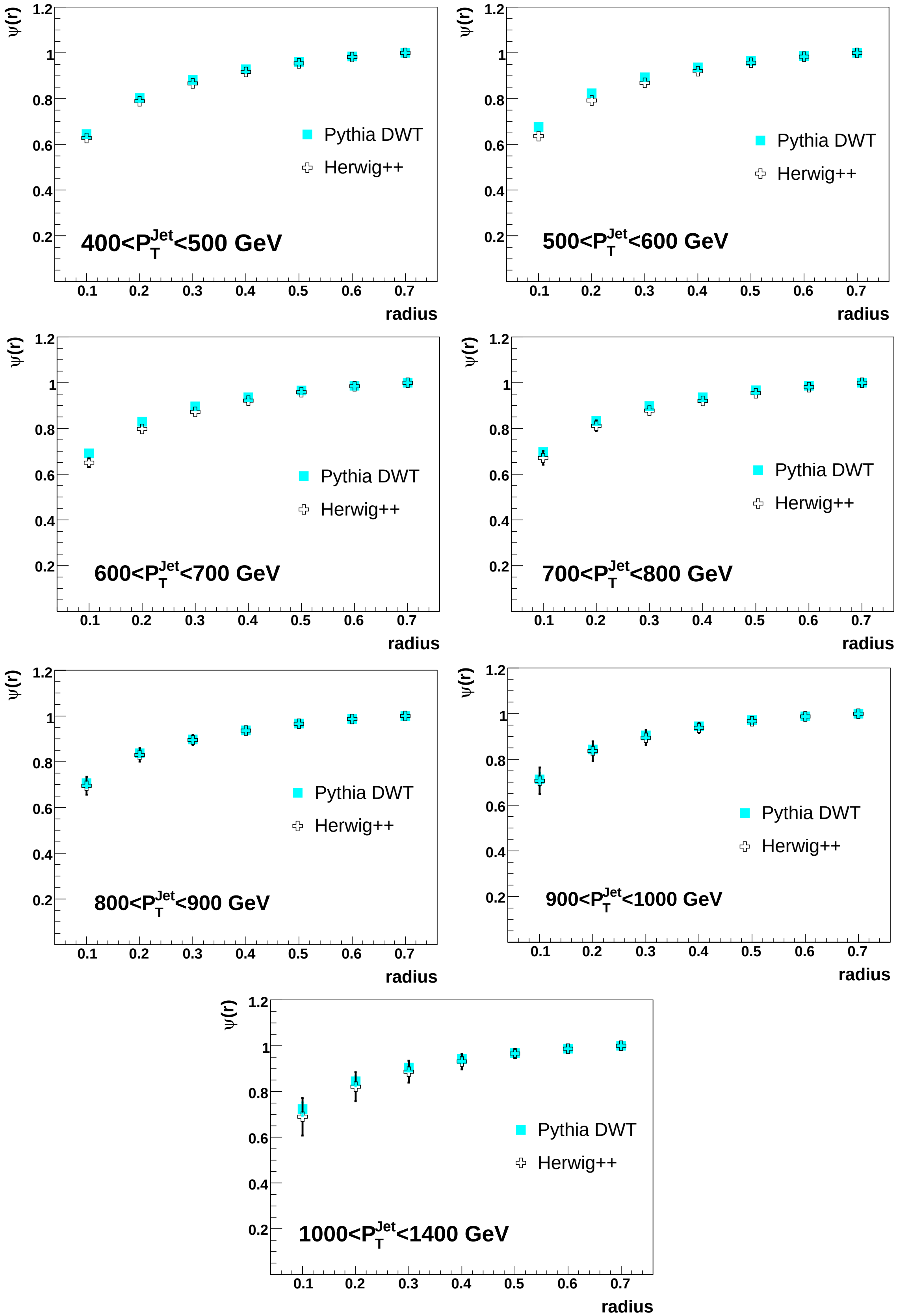

Figure B.31. Comparison of particle level integrated jet shapes from HERWIG++ and PYTHIA for selected p_T bins. Statistical errors are included.

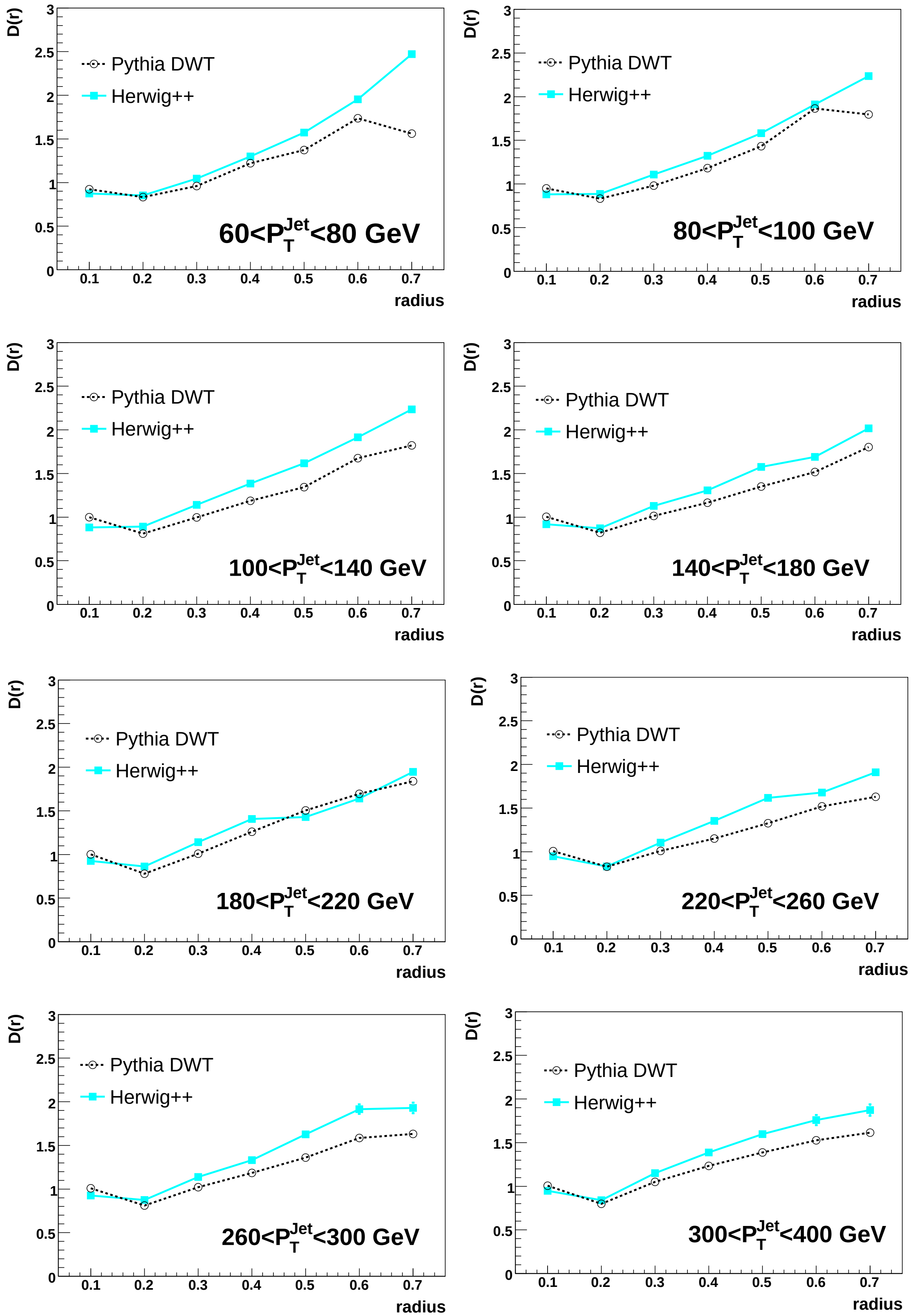

Figure B.32. Comparison of the correction factors for differential jet shapes using PYTHIA DWT and HERWIG++. Statistical errors are included.

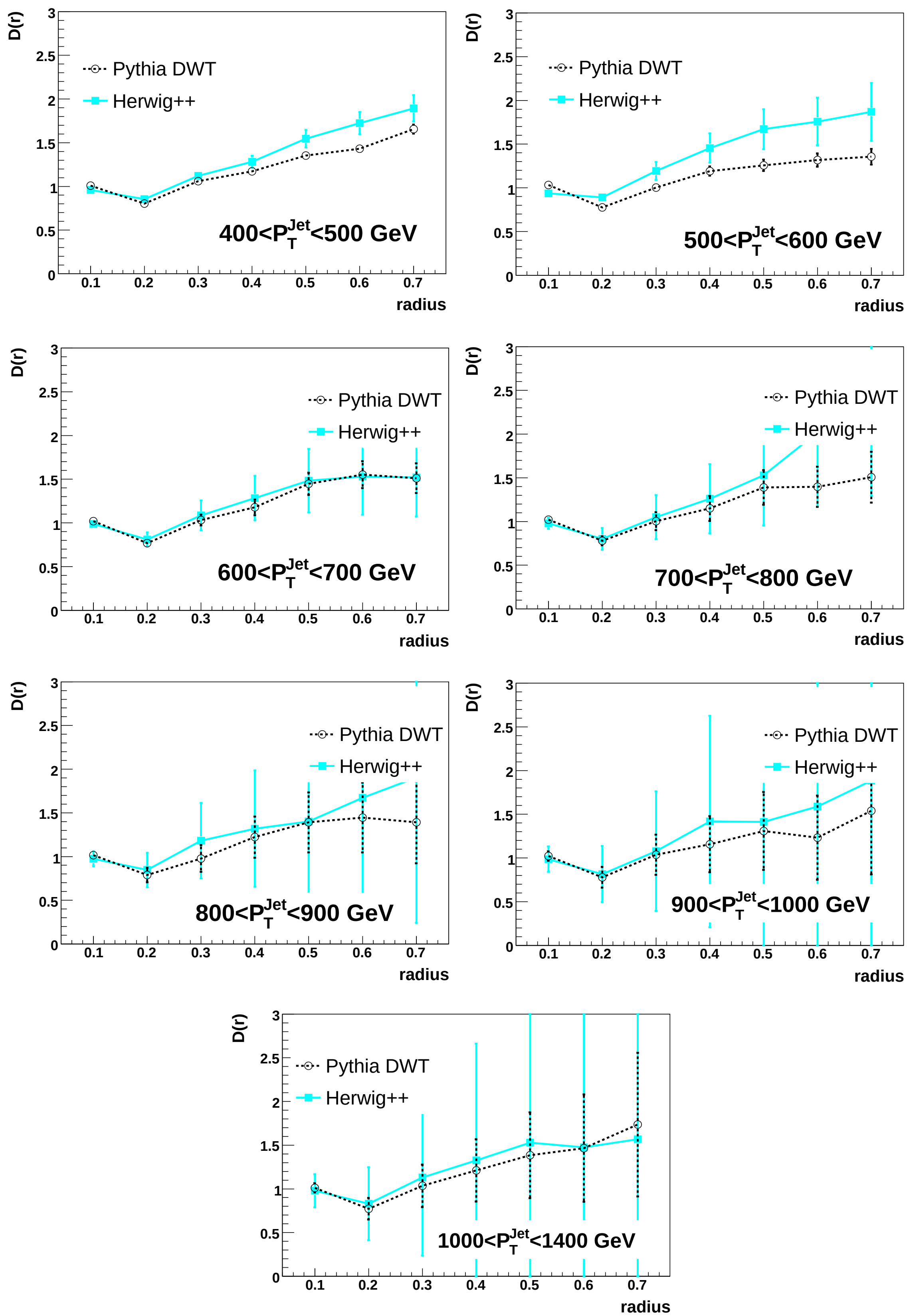

Figure B.33. Comparison of the correction factors for using differential jet shapes using PYTHIA DWT and HERWIG++. Statistical errors are included.

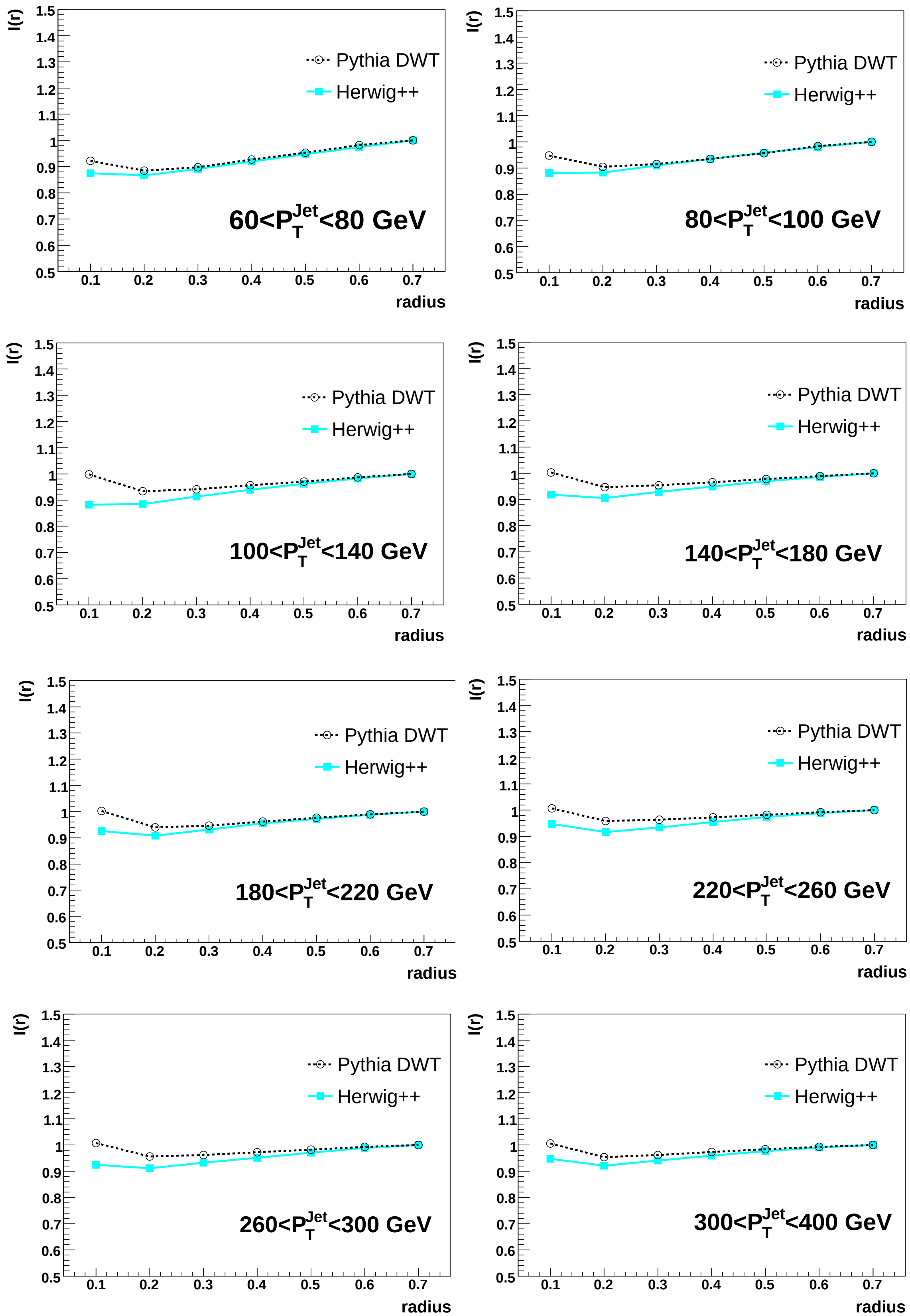

Figure B.34. Comparison of the correction factors for integrated jet shapes using PYTHIA DWT and HERWIG++. Statistical errors are included.

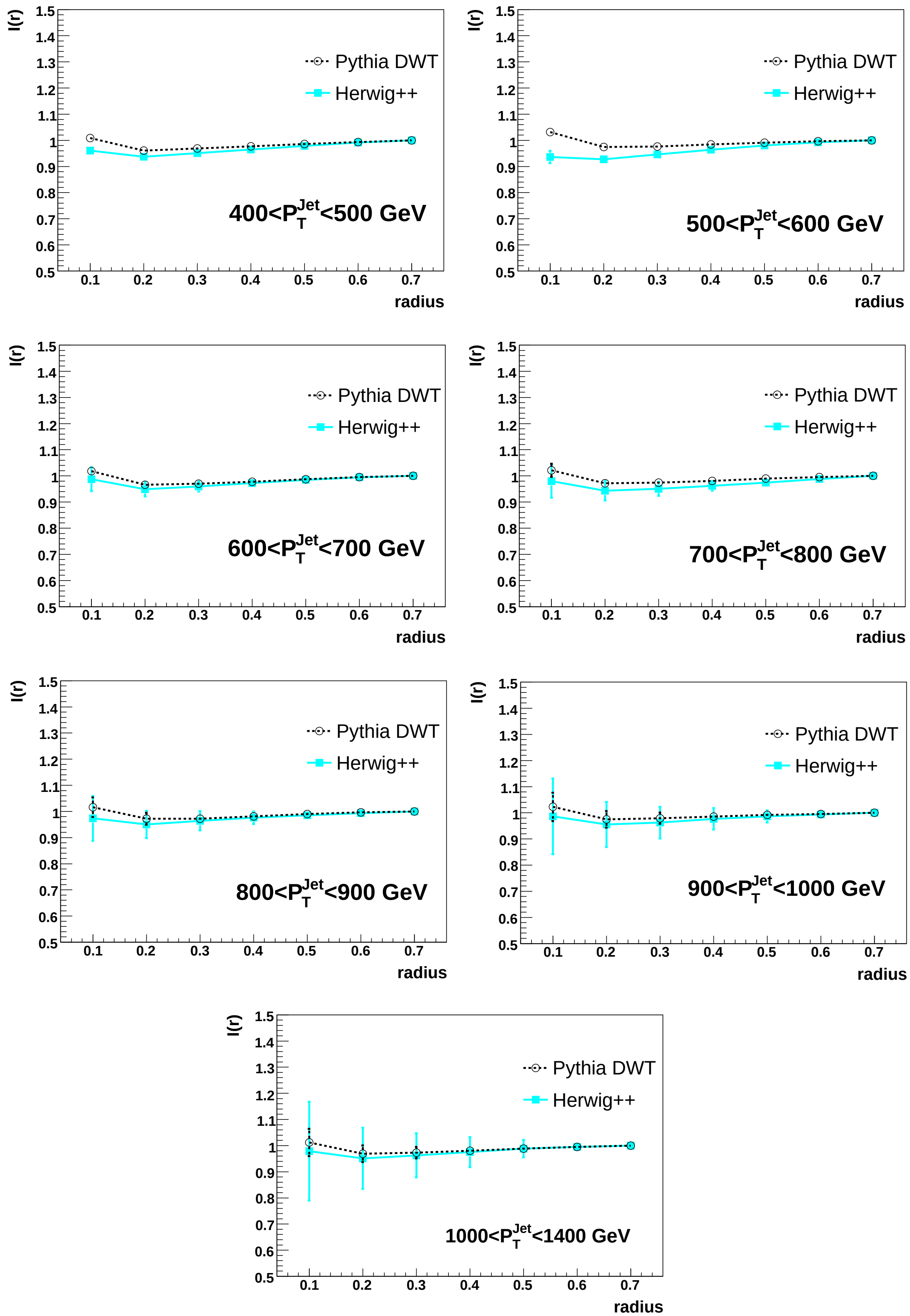

Figure B.35. Comparison of the correction factors for integrated jet shapes using PYTHIA DWT and HERWIG++. Statistical errors are included.

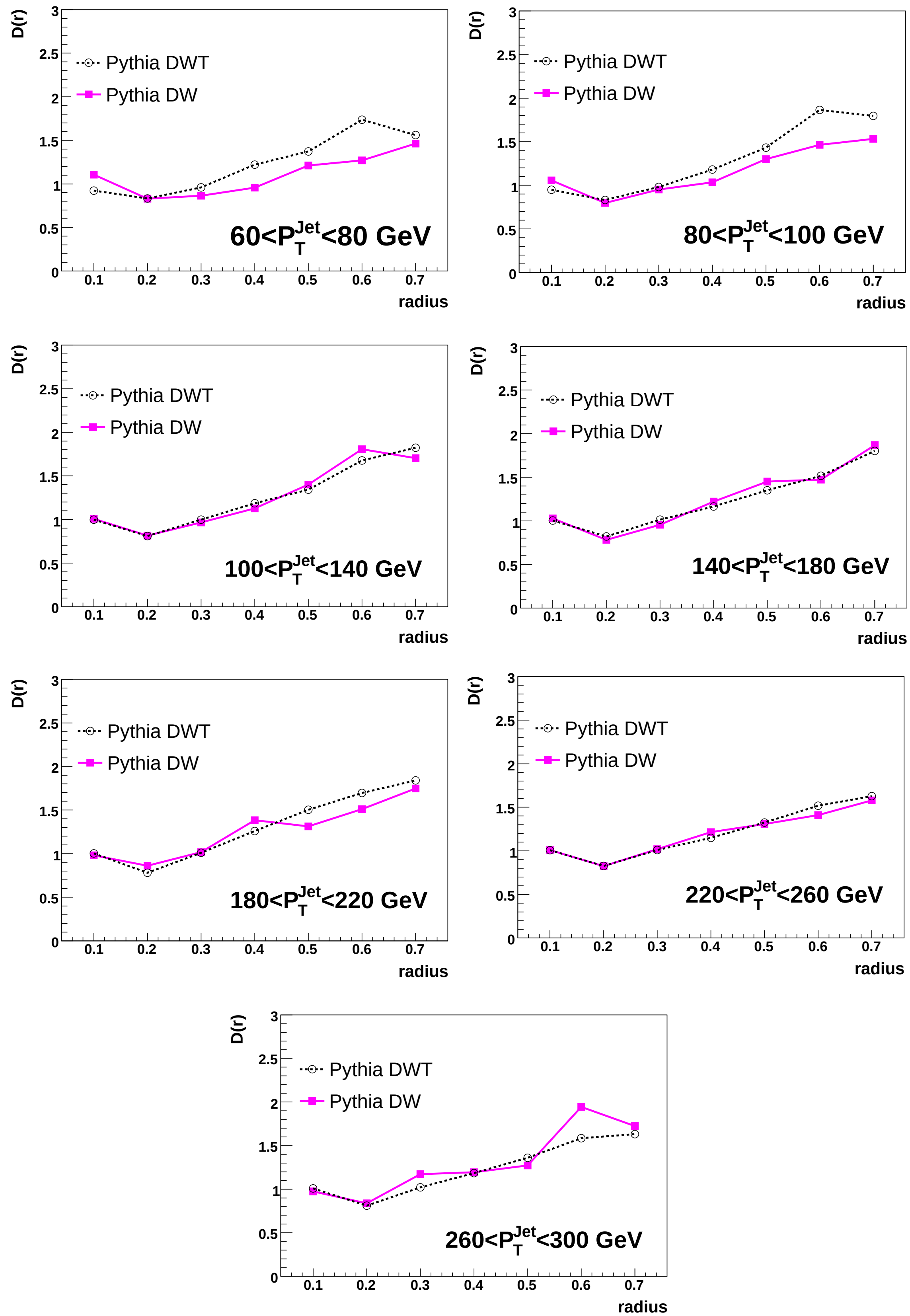

Figure B.36. Comparison of the correction factors for differential jet shapes using PYTHIA DWT and DW tunes. Statistical errors are included.

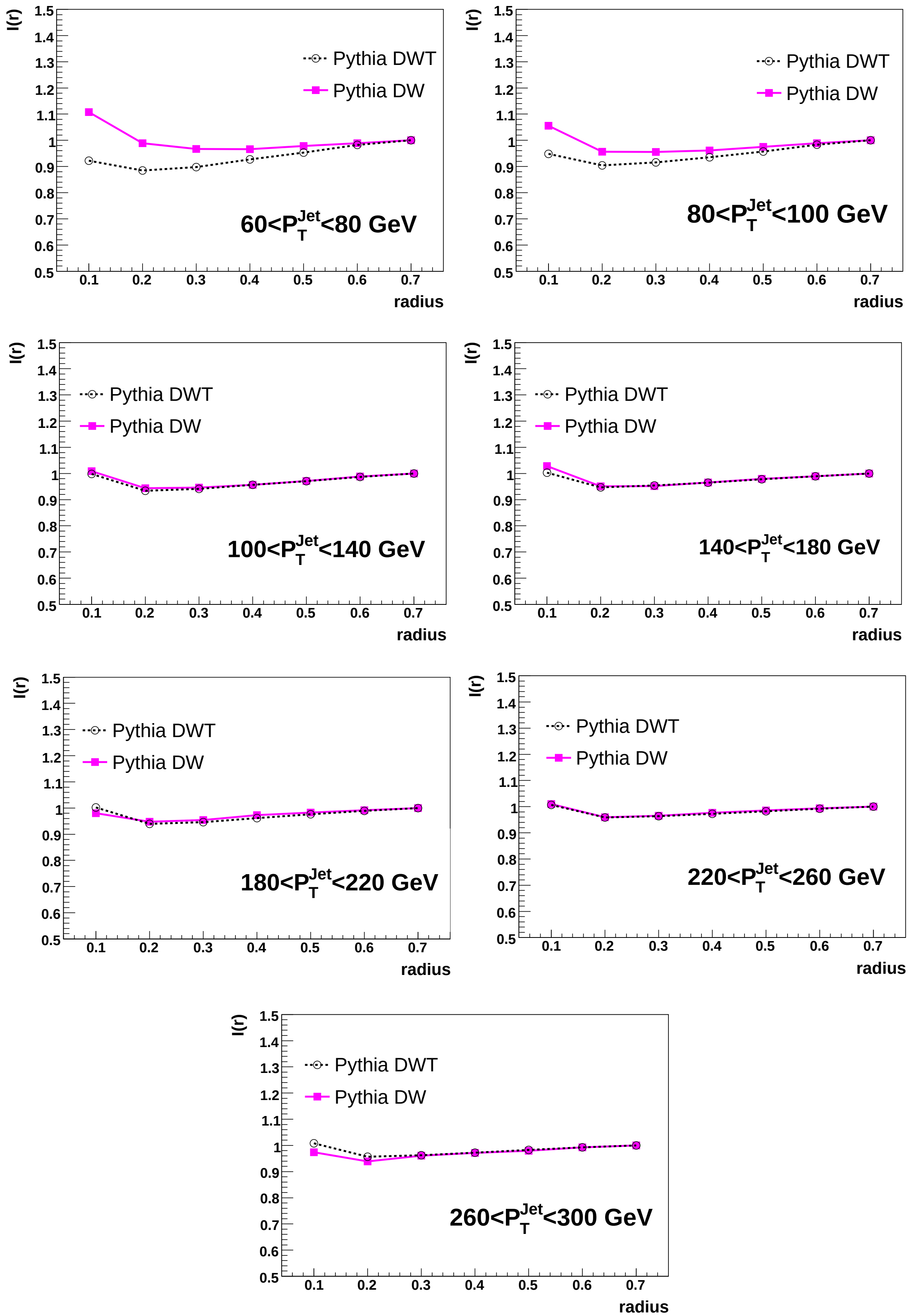

Figure B.37. Comparison of the correction factors for integrated jet shapes using PYTHIA DWT and DW tunes. Statistical errors are included.

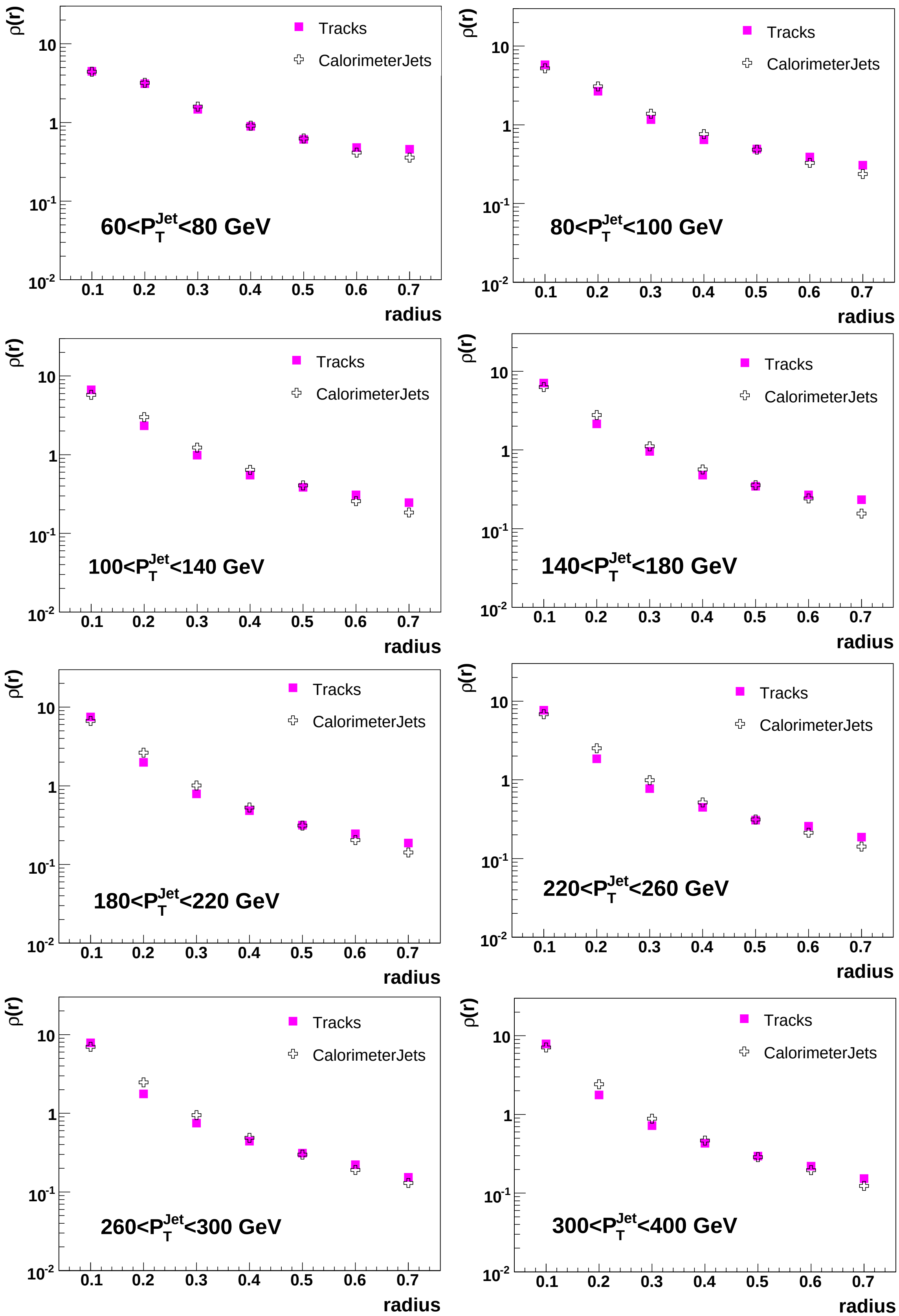

Figure B.38. Comparison of the differential track jet shapes to the calorimeter jet shapes in simulated data for selected p_T bins. Statistical errors are included.

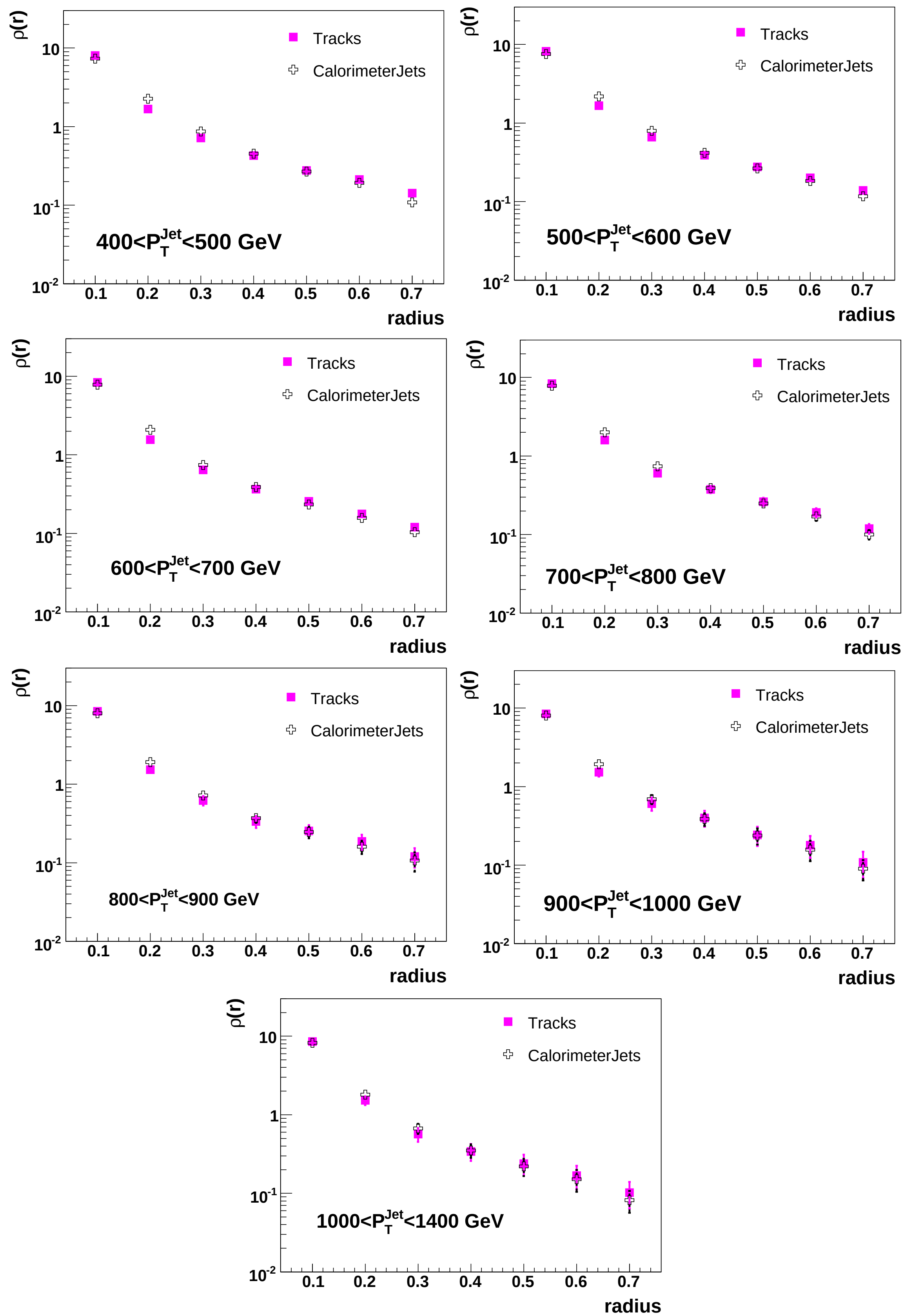

Figure B.39. Comparison of the differential track jet shapes to the calorimeter jet shapes in simulated data for selected p_T bins. Statistical errors are included.

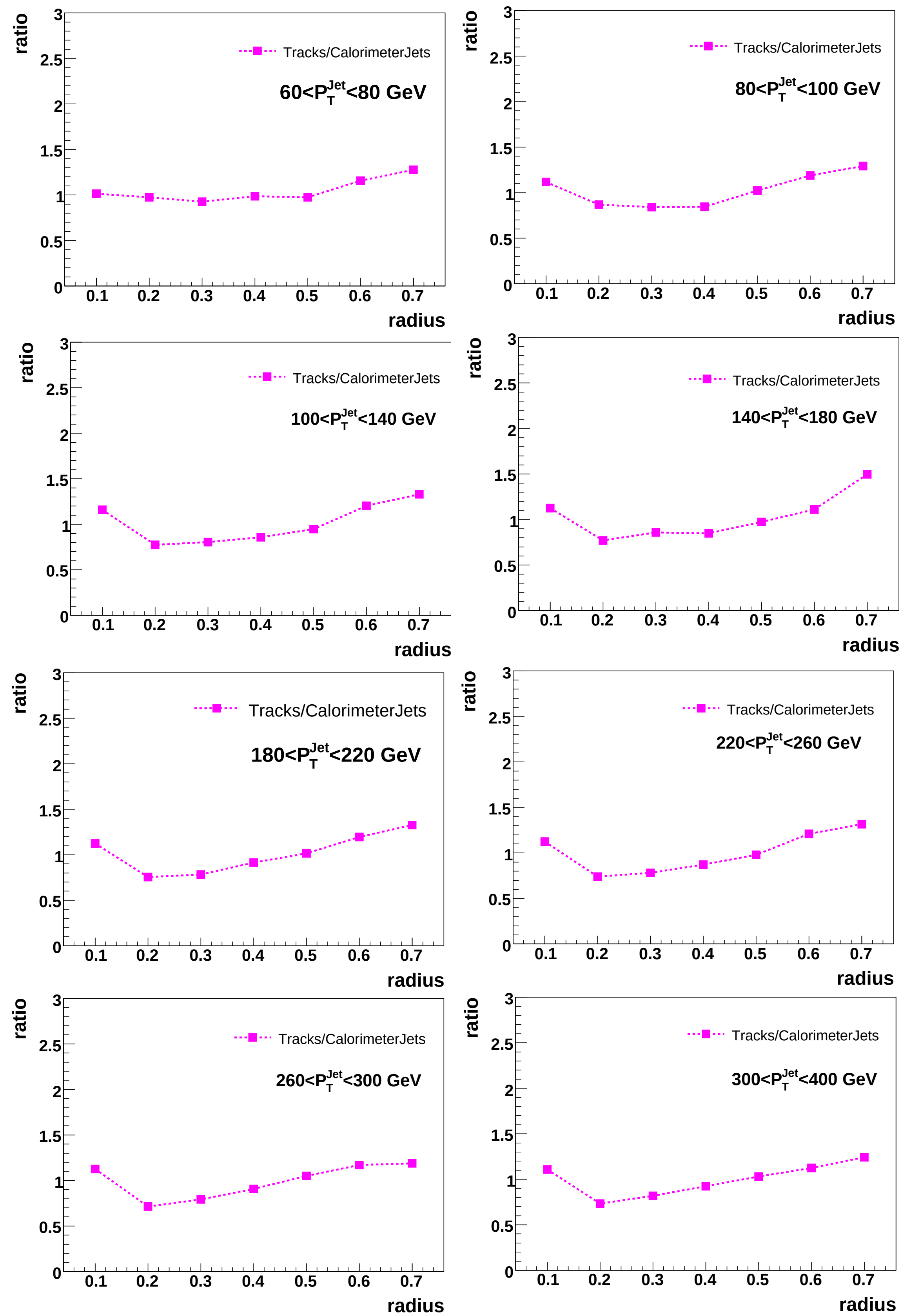

Figure B.40. Ratio of the track differential jet shapes to the calorimeter jet shapes in simulated data for selected p_T bins. Statistical errors are included.

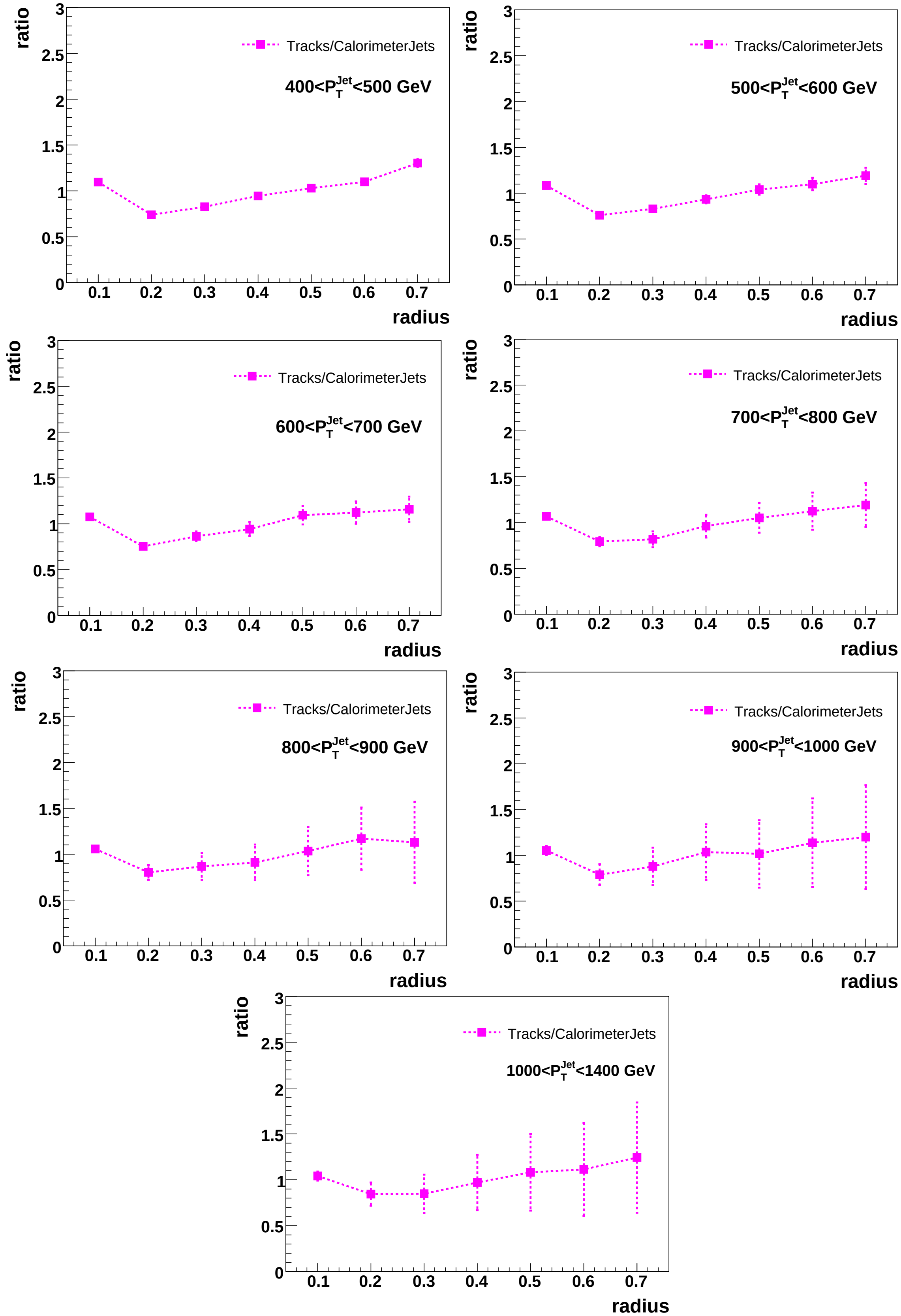

Figure B.41. Ratio of the track integrated jet shapes to the calorimeter jet shapes in simulated data for selected p_T bins. Statistical errors are included.

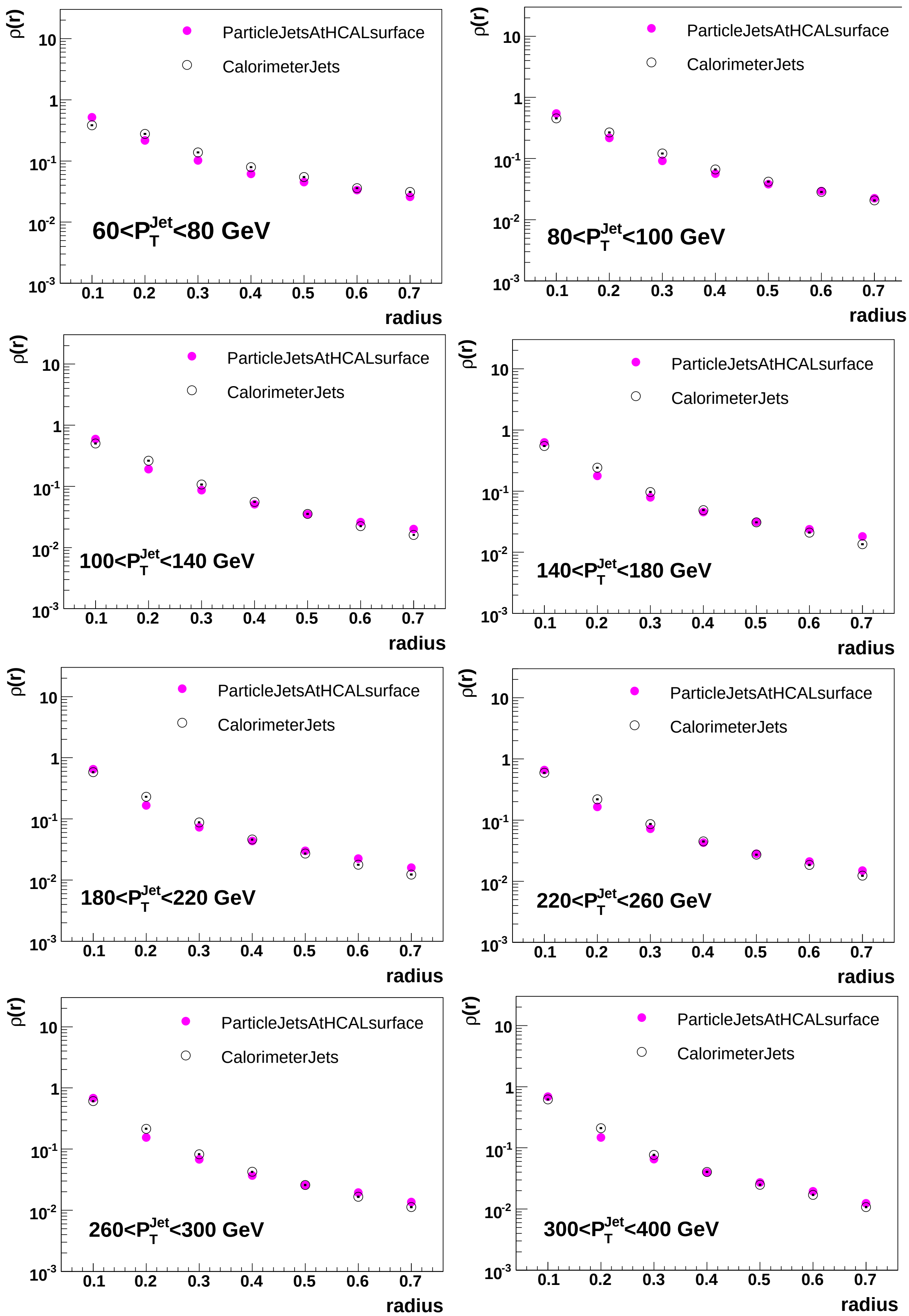

Figure B.42. Effect of the transverse showering spread for the differential jet shapes. Only statistical errors are included.

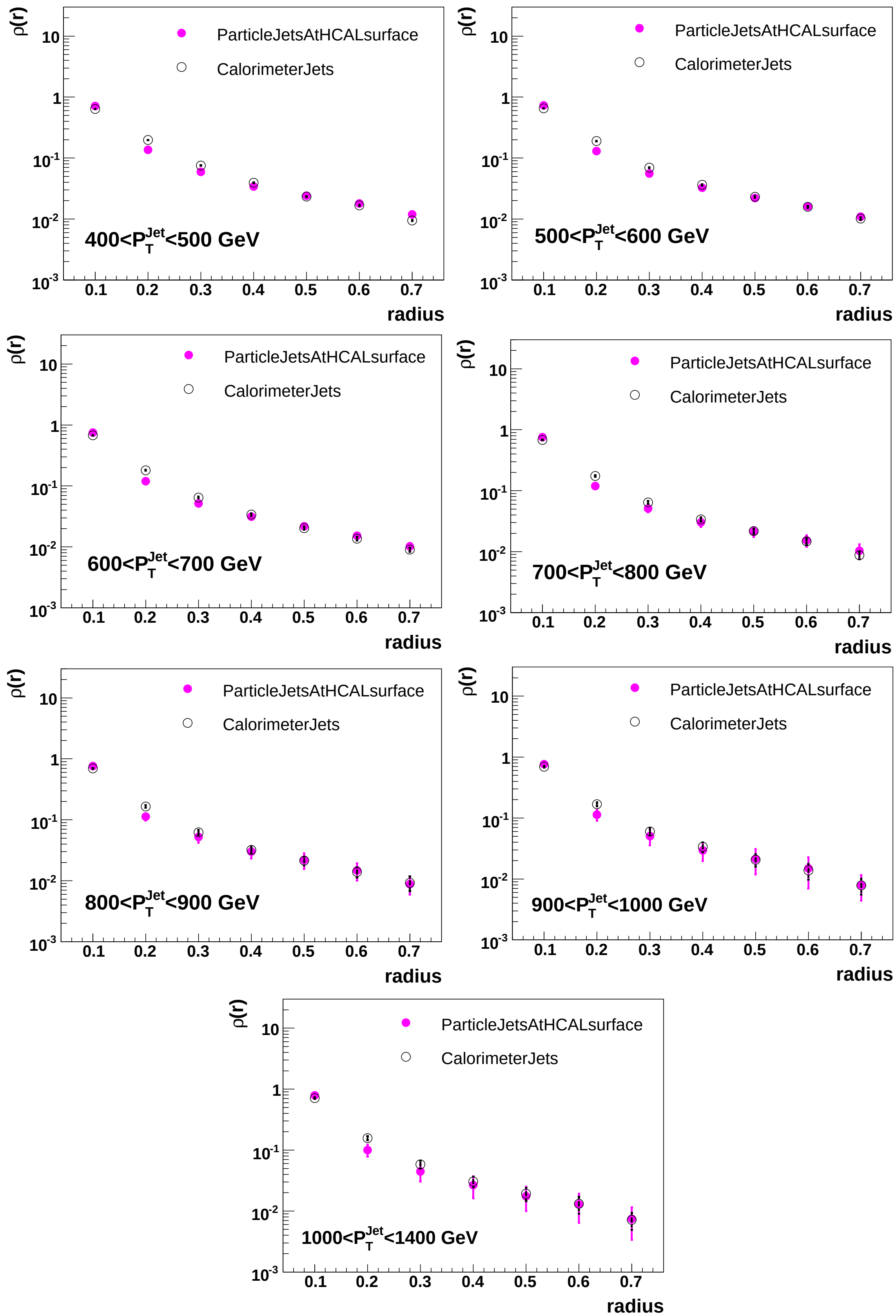

Figure B.43. Effect of the transverse showering spread for the differential jet shapes. Only statistical errors are included.

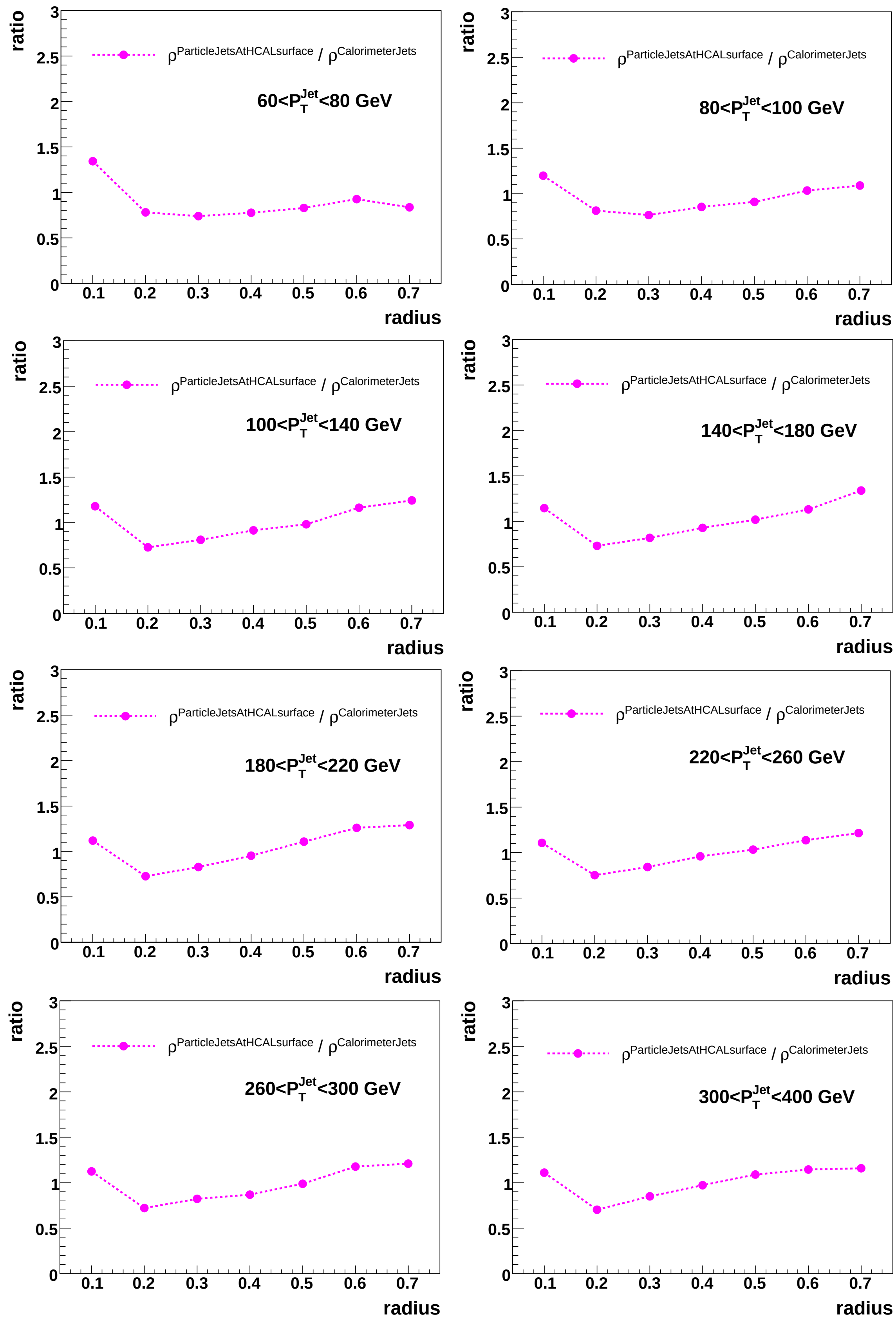

Figure B.44. Ratio of the differential jet shapes obtained using parameterized response (without transverse showering) to those from full simulation.

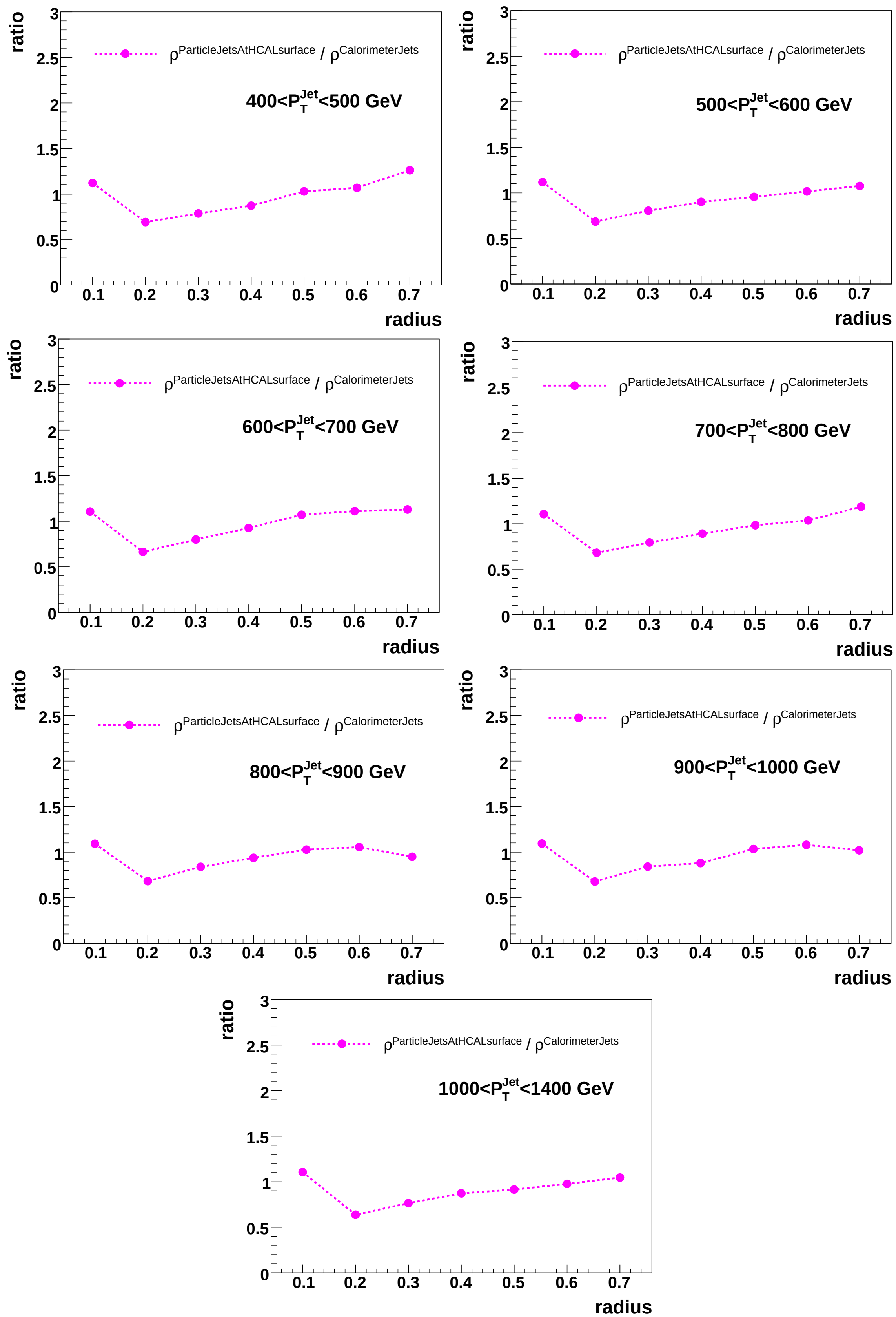

Figure B.45. Ratio of the differential jet shapes obtained using parameterized response (without transverse showering) to those from full simulation.

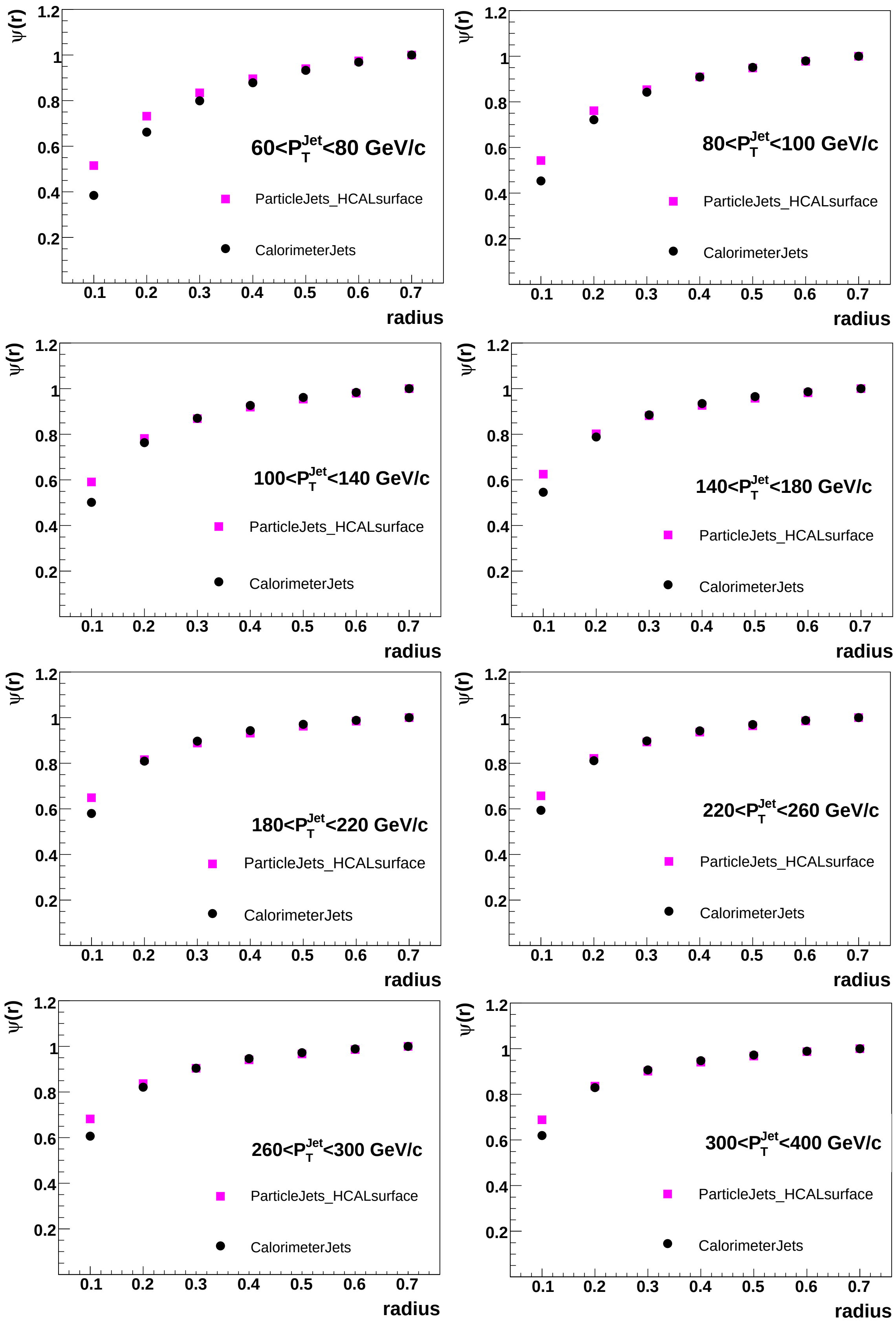

Figure B.46. Effect of the transverse showering spread for the integrated jet shapes. Only statistical errors are included.

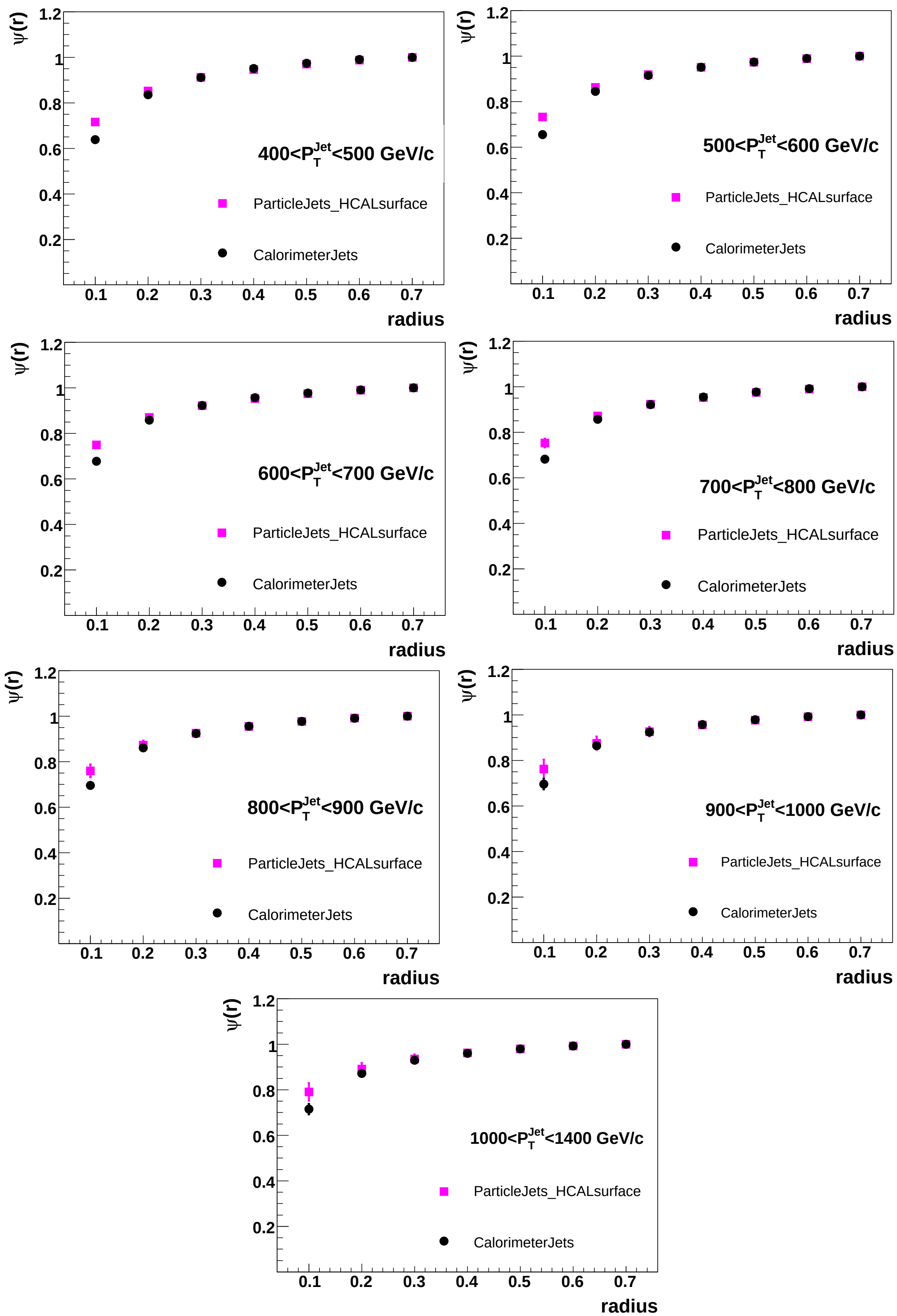

Figure B.47. Effect of the transverse showering spread for the integrated jet shapes. Only statistical errors are included.

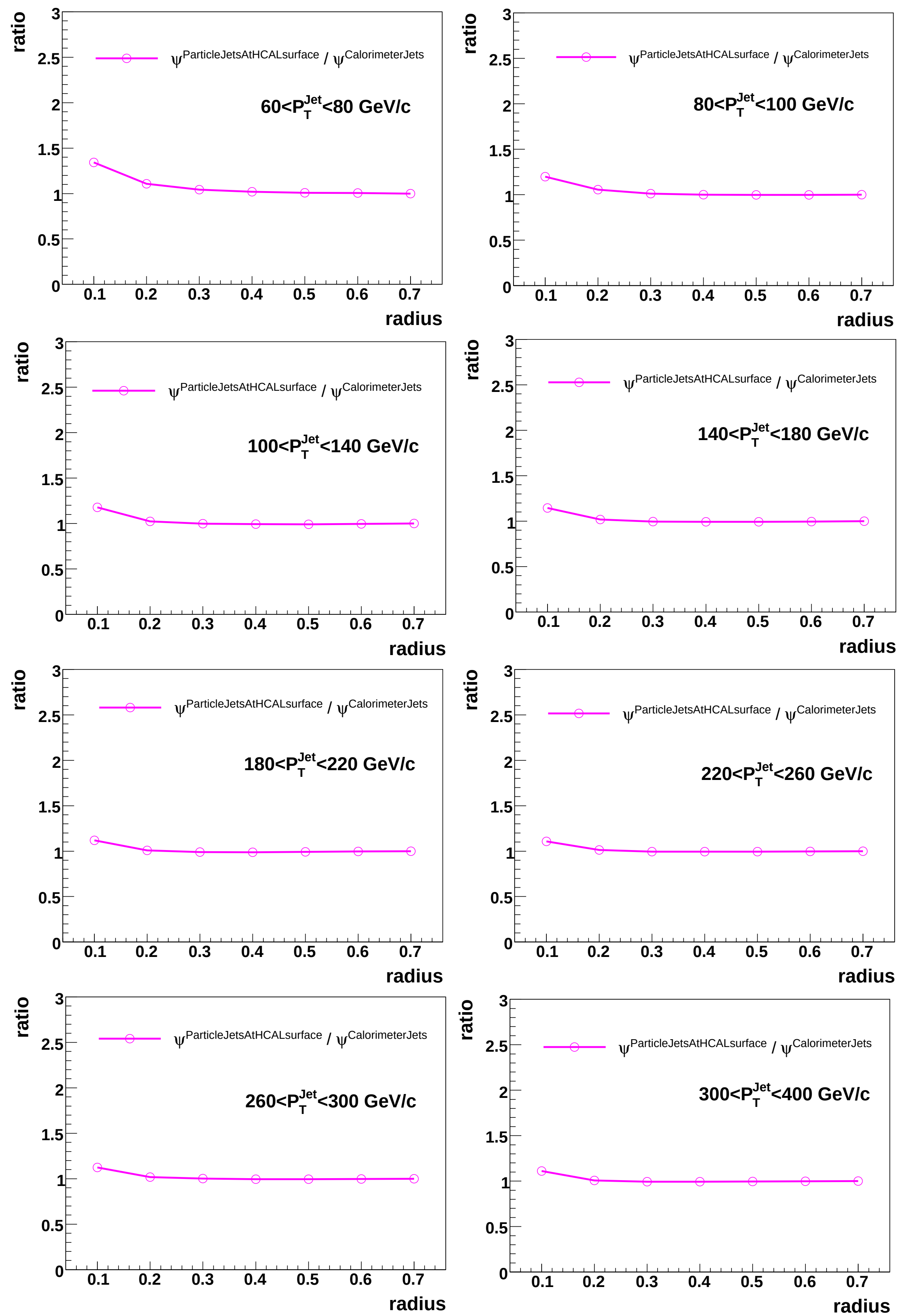

Figure B.48. Ratio of the integrated jet shapes obtained using parameterized response (without transverse showering) to those from full simulation.

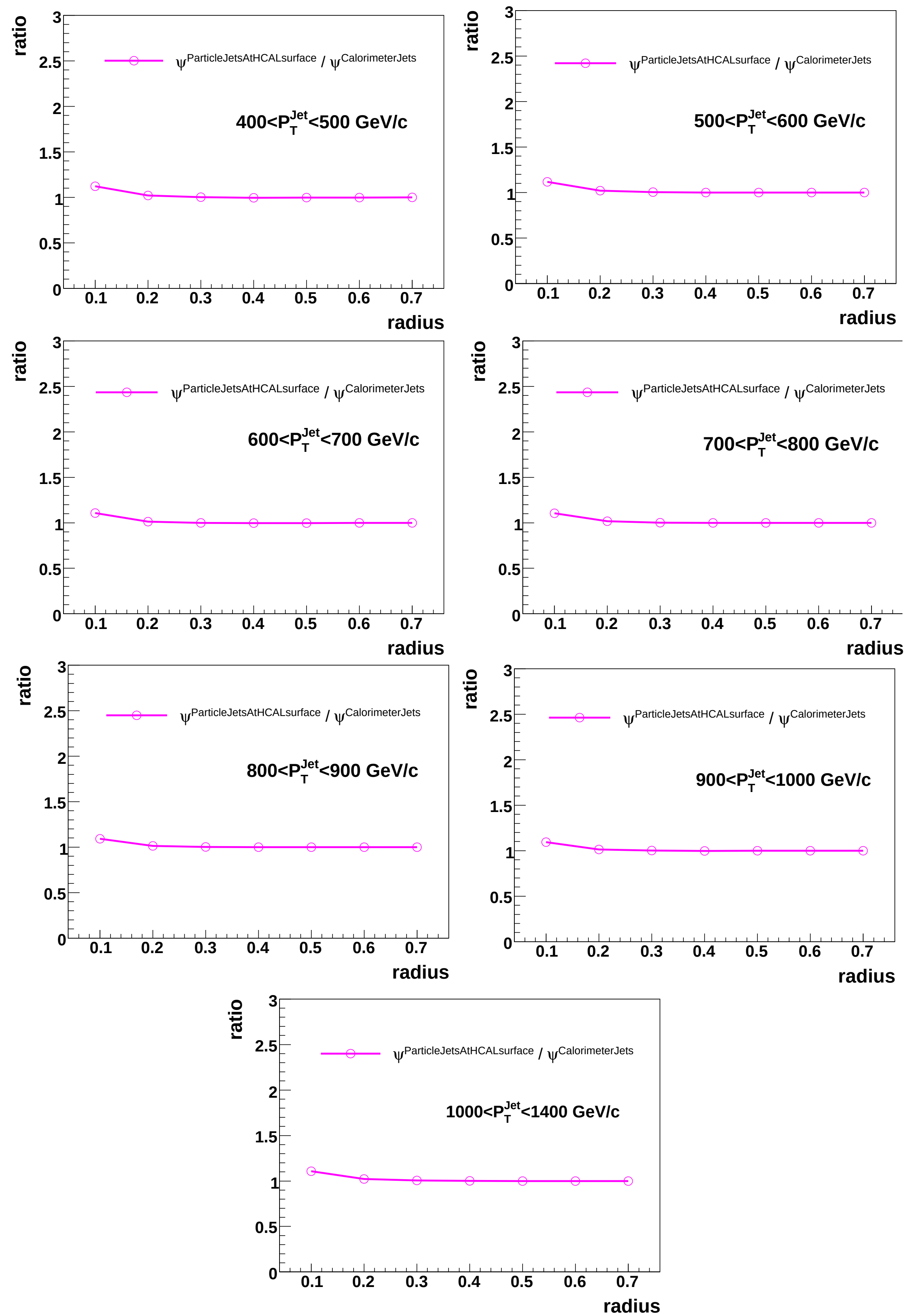

Figure B.49. Ratio of the the integrated jet shapes obtained using parameterized response (without transverse showering) to those from full simulation.

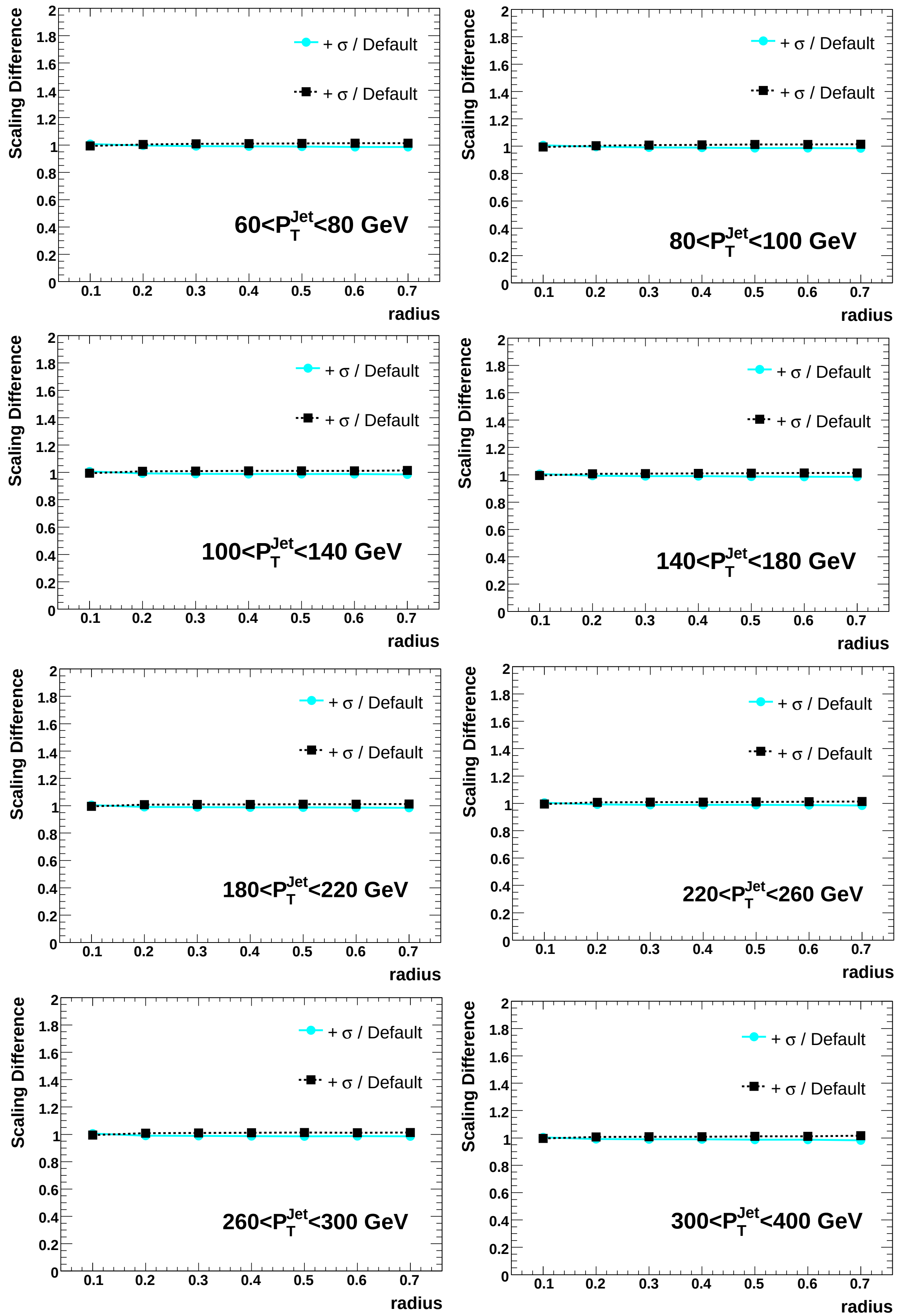

Figure B.50. The scaling difference due to $\pm 1\sigma$ variation of E/p for differential jet shapes for selected p_T bins.

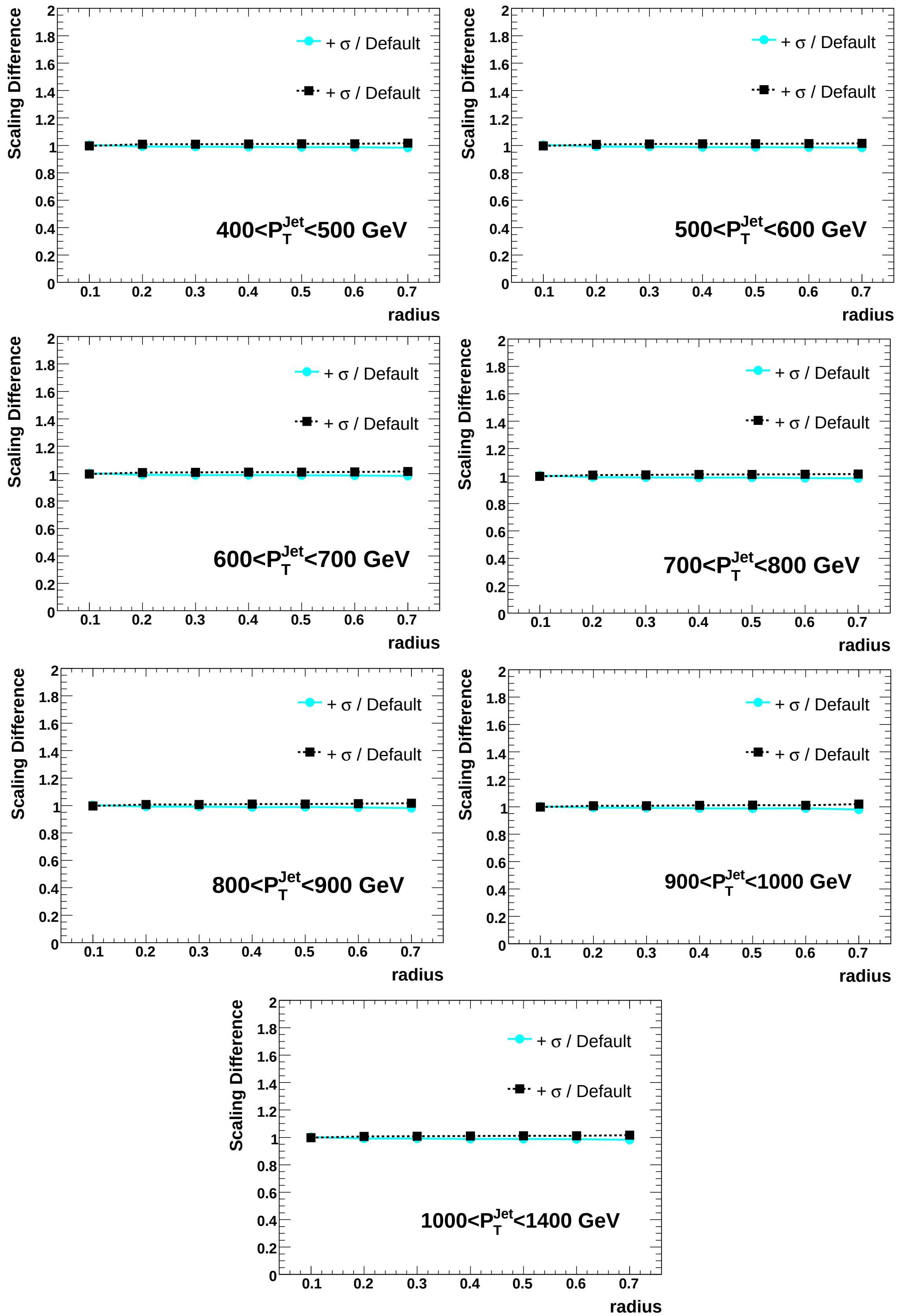

Figure B.51. The difference due to $\pm 1\sigma$ variation of E/p for differential jet shapes for selected p_T bins.

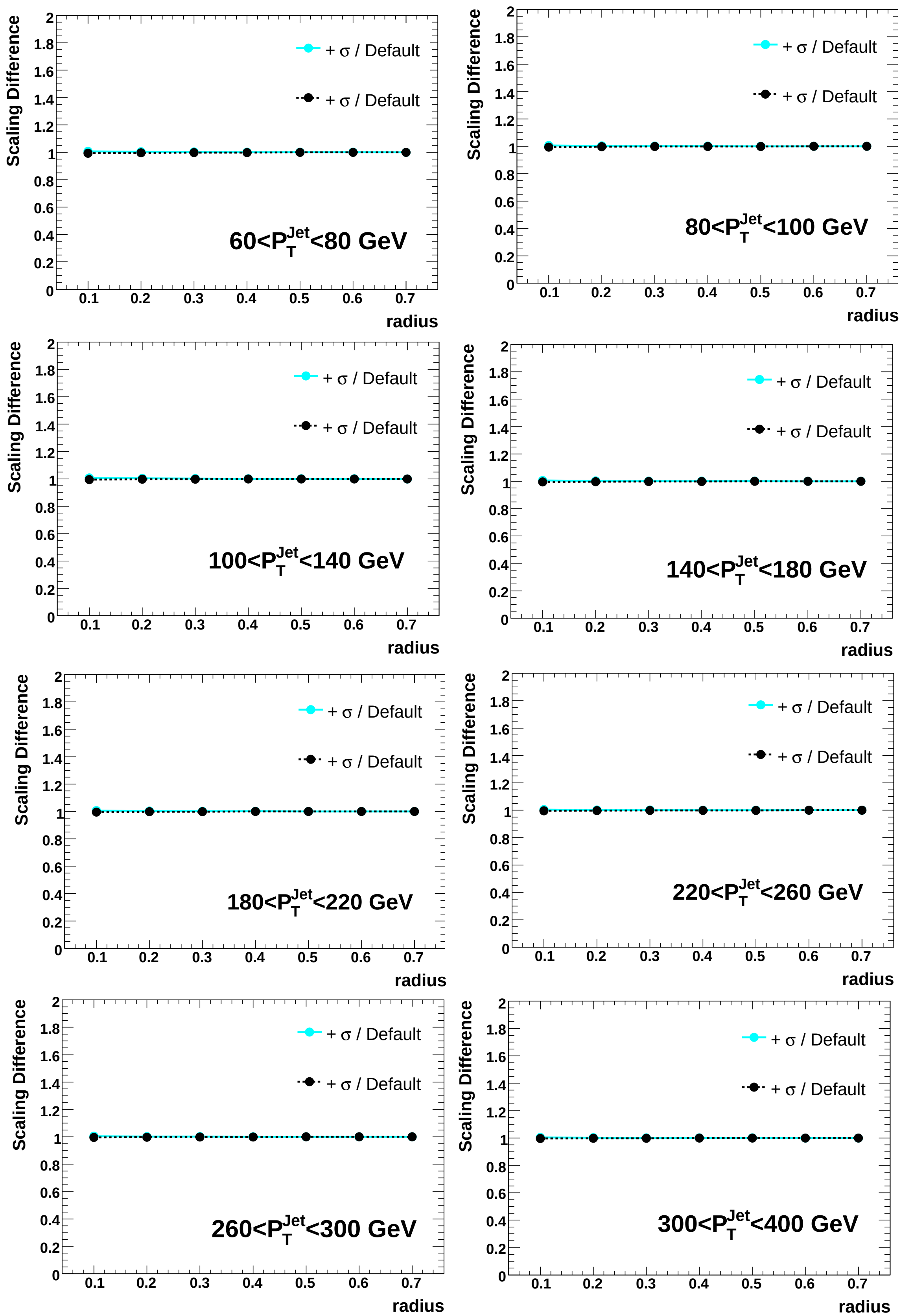

Figure B.52. The scaling difference due to $\pm 1\sigma$ variation of E/p for integrated jet shapes for selected p_T bins.

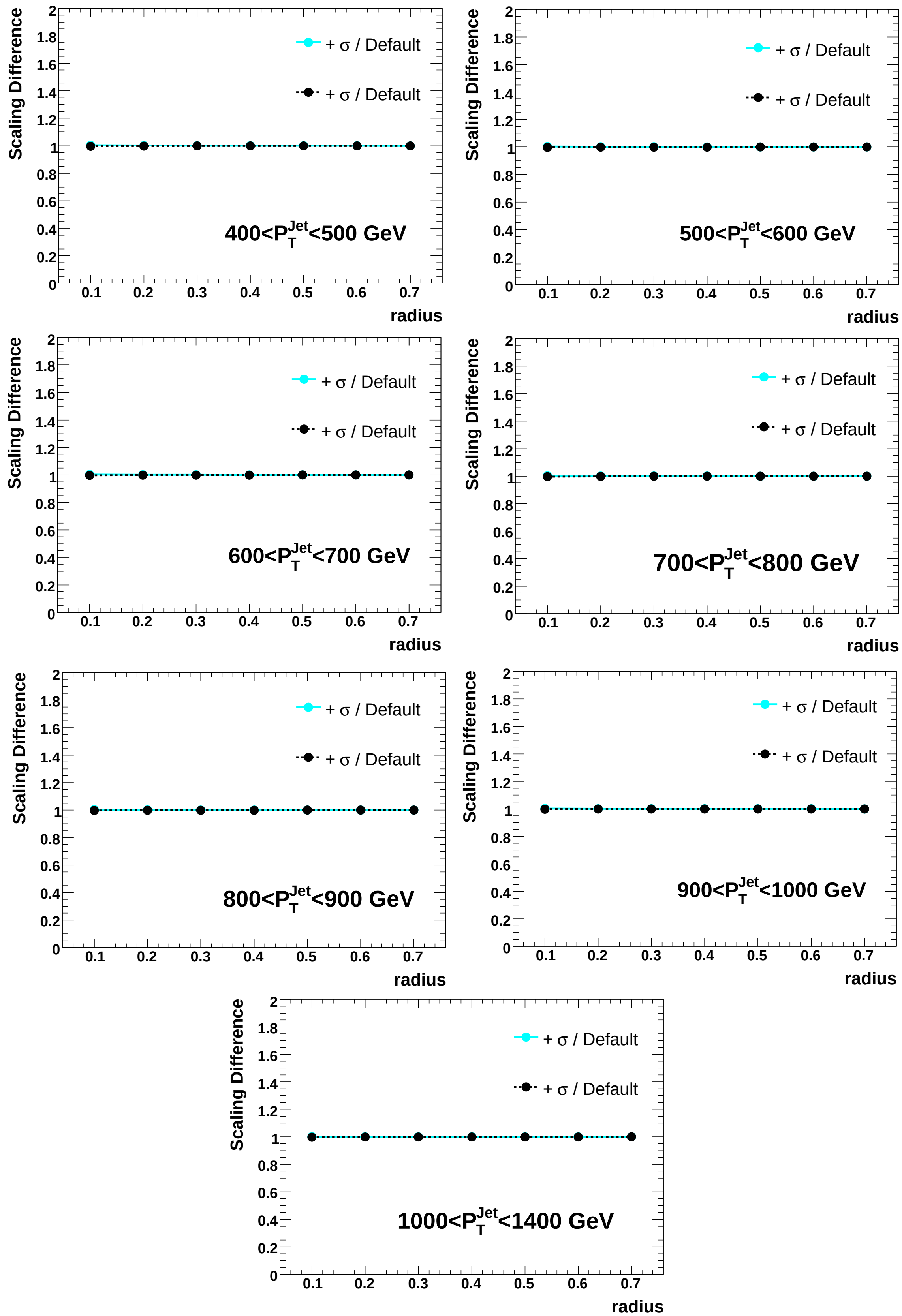

Figure B.53. The scaling difference due to $\pm 1\sigma$ variation of E/p for integrated jet shapes for selected p_T bins.